FINAL REPORT

Studies on Carbon FRP (CFRP) Prestressed Concrete Bridge Columns and Piles in Marine Environment

Principal investigator
M. AROCKIASAMY, Ph.D., P.E.
Professor and Director

Ahmed Amer, Ph.D., P.E.
Research Associate

Submitted to:
Florida Department of Transportation

under:
WPI No. 0510698 and Contract No. B9076

Monitored by:
Structural Research Center
Florida Department of Transportation
2007 E. Paul Dirac Drive
Tallahassee, FL 32304

Center for Infrastructure and Constructed Facilities
Department of Ocean Engineering
FLORIDA ATLANTIC UNIVERSITY
Boca Raton, Florida-33431

November 1998

TECHNICAL REPORT STANDARD TITLE PAGE

1. Report No.	2. Government Accession No.	3. Recipient's Catalog No.

4. Title and Subtitle
Studies on Carbon FRP (CFRP) Prestressed Concrete Bridge Columns and Piles in Marine Environment

5. Report Date
November 1998

6. Performing Organization Code

7. Authors
M. Arockiasamy and Ahmed Amer

8. Performing Organization Report No.

9. Performing Organization Name and Address
Florida Atlantic University
Center for Infrastructure and Constructed Facilities
Department of Ocean Engineering
Boca Ration, Florida 33431

10. Work Unit No.

11. Contract or Grant No.
WPI 0510698

12. Sponsoring Agency Name and Address
Florida Department of Transportation
605 Suwannee Street
Tallahassee, Florida 32399-0466

13. Type of Report and Period Covered
Final Report

14. Sponsoring Agency Code
B-9076

15. Supplementary Notes

Prepared in cooperation with the Federal Highway Administration

16. Abstract

The main objective of this study was to investigate the feasibility of using concrete piles pretensioned with Carbon Fiber Reinforced Plastics (CFRP) tendons. The study reviews the available literature on mechanical properties of CFRP reinforcement, durability of FRP rods and tendons, service and ultimate load, and time dependent behavior of FRP reinforced concrete columns, existing models on confined concrete reinforced with steel ties and hoops, and pile driving. An experimental program was carried out to study the durability of CFRP tendons exposed to air, seawater and alkaline solutions for different time duration. The ultimate strength analysis of CFRP reinforced concrete slender columns was made utilizing the moment magnification method and the CFRP stress – strain characteristics. An experimental investigation on the ultimate load behavior of eight CFRP reinforced concrete slender columns was carried out and the results compared with the theoretical values.

An analytical and experimental investigation was made on the long term behavior of CFRP reinforced concrete beams and columns under sustained loading. Four concrete beams and four concrete columns were subjected to sustained uniform load intensity for two years. A method to predict the total deformations of CFRP reinforced concrete members at any time is proposed considering the instantaneous and time dependent deformations.

The feasibility of using pretensioned concrete piles with CFRP tendons in marine environment was examined based on analytical and experimental studies. Prior to fabrication and driving the test piles, an investigation of the pile driving site and equipment was made in order to determine the pile driving stresses using the wave equation analysis. The design, instrumentation, fabrication and driving of pretensioned concrete piles with CFRP tendons were carried out successfully in the study. The pile driving test results of the CFRP pretensioned concrete piles are discussed and compared with those of the concrete piles pretensioned with steel. The load deformation characteristics of the concrete columns are established for different CFRP hoop spacing based on testing eleven concrete column specimens. The strength enhancement due to the CFRP hoops is evaluated using a proposed stress vs. strain model for confined concrete.

17. Key Words
composites, carbon FRP, prestressed concrete, reinforced concrete, durability, columns, ultimate strength, creep, piles, confinement, time dependent deformations, bridges

18. Distribution Statement
No restrictions. This document is available to the public through the National Technical Information Service, Springfield, Virginia 22161

19. Security Classif. (of this report)	20. Security Classif. (of this page)	21. No. of Pages	22. Price
Unclassified	Unclassified	294	

Form DOT F 1700.7 (8-89)

UNIT CONVERSION TABLE

To convert from	To	Multiply by
inch	Centimeter	2.54
square inch	Square centimeter	6.4516
kip	KiloNewton (kN)	4.44747
kip/sq. in. (ksi)	kN/sq. m (kPa)	6,894.28
kip-foot	kN-meter	1.3556

DISCLAIMER

The opinions, findings and conclusions expressed in this publication are those of the authors who are responsible for the facts and accuracy of the data presented herein. The contents do not necessarily reflect the views or the policies of the Florida Department of Transportation or the Federal Highway Administration. This report does not constitute a standard, specification or regulation.

The report is prepared in cooperation with the Florida Department of Transportation and the Federal Highway Administration.

ACKNOWLEDGMENTS

The authors wish to express their sincere thanks to Dr. Mohsen A. Shahawy, Chief Structures Analyst, Florida Department of Transportation, for his excellent suggestions, discussions and constructive criticisms throughout the project. They wish to express their appreciation to Dr. S. E. Dunn, Professor and Chairman, Department of Ocean Engineering, and Dr. J. Jurewicz, Dean, College of Engineering, Florida Atlantic University for their continued interest and encouragement.

The valuable assistance and contributions to the experimental and analytical work from Graduate Students, Messrs. Wei Xia, Senthil Chidambram, Rama Kumar Potturu, and Scott Gemmel, Florida Atlantic University are gratefully acknowledged.

SUMMARY

The main objective of this study was to investigate the feasibility of using concrete piles pretensioned with Carbon Fiber Reinforced Plastics (CFRP) tendons. The study reviews the available literature on mechanical properties of CFRP reinforcement, durability of FRP rods and tendons, service, ultimate load and time dependent behavior of FRP reinforced concrete columns, existing models on confined concrete reinforced with steel ties and hoops, and pile driving. An experimental program was carried out to study the durability of CFRP tendons exposed to air, seawater and alkaline solutions for different time duration. The ultimate strength analysis of CFRP reinforced concrete slender columns was made utilizing the moment magnification method and the CFRP stress – strain characteristics. An experimental investigation on the ultimate load behavior of eight CFRP reinforced concrete slender columns was carried out and the results compared with the theoretical values.

An analytical and experimental investigation was made on the long term behavior of CFRP reinforced concrete beams and columns under sustained loading. Four concrete beams and four concrete columns were subjected to sustained uniform load intensity for two years. A method to predict the total deformations of CFRP reinforced concrete members at any time is proposed considering the instantaneous and time dependent deformations.

The feasibility of using pretensioned concrete piles with CFRP tendons in marine environment was examined based on analytical and experimental studies. Prior to fabrication and driving the test piles, an investigation of the pile driving site and equipment was made in order to determine the pile driving stresses using the wave equation analysis. The design, instrumentation, fabrication and driving of pretensioned concrete piles with CFRP tendons were carried out successfully in the study. The pile driving test results of the CFRP pretensioned concrete piles are discussed and compared with those of the concrete piles pretensioned with steel.

The load deformation characteristics of the concrete columns are established for different CFRP hoop spacing based on testing eleven concrete column specimens. The strength enhancement due to the CFRP hoops is evaluated using a proposed stress vs. strain model for confined concrete.

TABLE OF CONTENTS

CHAPTER 1 INTRODUCTION

CHAPTER 2 LITERATURE REVIEW

CHAPTER 3 DURABILITY STUDIES ON CFRP CABLES

CHAPTER 4 ULTIMATE STRENGTH ANALYSIS OF CFRP REINFORCED CONCRETE SLENDER COLUMNS

CHAPTER 5 EXPERIMENTAL STUDIES ON ULTIMATE LOAD BEHAVIOR OF CFRP REINFORCED CONCRETE SLENDER COLUMNS

5.5 EXPERIMENTAL RESULTS AND DISCUSSIONS

CHAPTER 6 EXPERIMENTAL PROGRAM FOR TIME DEPENDENT DEFORMATIONS OF CFRP REINFORCED CONCRETE BEAMS AND COLUMNS

6.2 MATERIALS

6.3 CFRP REINFORCED CONCRETE BEAMS

6.4 CFRP REINFORCED CONCRETE COLUMNS

CHAPTER 7 ANALYSIS OF TIME DEPENDENT DEFORMATIONS OF CFRP REINFORCED CONCRETE BEAMS AND COLUMNS

7.2 ANALYTICAL PREDICTION OF THE LONG TERM DEFORMATION OF THE CONCRETE BEAMS REINFORCED WITH CARBON FRP

CHAPTER 8 COMPARISON OF ANALYTICAL AND EXPERIMENTAL TIME DEPENDENT DEFORMATIONS

CHAPTER 9 PRE-DRIVING STUDIES ON CFRP PRETENSIONED CONCRETE PILES

CHAPTER 10 DESIGN, INSTRUMENTATION AND FABRICATION OF CFRP PRETENSIONED CONCRETE PILES

CHAPTER 11 CFRP PRESTRESSED CONCRETE PILE DRIVING AND TESTING

CHAPTER 12 CONFINEMENT EFFECTS IN REINFORCED CONCRETE COLUMNS WITH CFRP HOOP REINFORCEMENT

CHAPTER 13 SUMMARY AND CONCLUSIONS

LIST OF FIGURES

LIST OF TABLES

CHAPTER 1

INTRODUCTION

1.1 BACKGROUND

The use of the FRP composites was first recognized for the military and aerospace applications. Lately, FRP composites was considered as a suitable alternative to steel reinforcement in reinforced concrete in view of its high strength, light weight and excellent corrosion resistance. Extensive studies and research were conducted in Canada, Europe, Japan and USA in the areas of materials and structures. A wide range of FRP rods, bars, strands and cables are now available commercially. The FRP bars are made from high strength continuous fibers (carbon, glass, aramid, etc.) bound together with a resin using pultrusion process.

Concrete piles pretensioned with steel are prone to corrosion in marine environment. The extent of steel corrosion and the resulting concrete degradation reduce the useful service life of the structures. Continuing use of concrete piles prestressed with steel is very costly both in initial costs and subsequent maintenance. The development of FRP composites with improved physical properties provides new opportunities for innovative solution to overcome the concrete deterioration problems particularly in the splash zone. The high tensile strength and excellent corrosion resistance of carbon fiber reinforced plastics (CFRP) make them suitable for prestressing the concrete piles for use in marine environment.

Bridges in Florida are exposed to harsh environment characterized by a wide range of temperature and humidity. They are subjected to cyclic load effects and impact in addition to sustained dead load. Durability and time dependent deformations of concrete members reinforced / prestressed with CFRP composites need careful evaluation before application in bridges.

Many assumptions made in designing members with steel reinforcement may not be valid in the design of members reinforced with CFRP. For instance, the assumption of moment redistribution at ultimate conditions is not valid since the CFRP cables, which are linearly elastic up to failure and have no yield point unlike steel reinforcement. Design principles for concrete columns reinforced with CFRP are not yet fully formulated and lately significant research effort is focused on formulation of design concepts.

Extensive research has been carried out in the area of confinement, mainly concrete confined with steel ties, hoops or spirals and jackets. It has been established that the lateral confinement would enhance both the strength and ductility of reinforced concrete members due to the development of triaxial stress field within the confined concrete. Very limited technical literature has been published related to confinement effects of CFRP hoops in concrete columns.

1.2 OBJECTIVES AND SCOPE

The objectives of the study are the following:

i) Determination of mechanical properties and durability of CFRP cables.
ii) Investigation of the ultimate strength behavior of CFRP reinforced concrete slender columns.
iii) Study of the time dependent deformations of CFRP reinforced concrete beams and columns.
iv) Study of feasibility of fabrication of concrete piles pretensioned with CFRP tendons.
v) Investigation of the driveability of CFRP pretensioned concrete piles.
vi) Determination of the confinement effects of CFRP hoops in reinforced concrete columns.

Chapter 2 reviews the available literature on mechanical properties of CFRP reinforcement, durability of FRP rods and tendons, service, ultimate load and time dependent behavior of FRP reinforced concrete columns, existing models on confined concrete reinforced with steel ties and hoops, and pile driving. **Chapter 3** presents the experimental studies on durability on CFRP tendons exposed to air, seawater and alkaline solutions for different time duration.

Chapter 4 presents the ultimate strength analysis of CFRP reinforced concrete slender columns based on moment magnification method. **Chapter 5** presents the experimental investigation on the ultimate load behavior of the CFRP reinforced concrete slender columns, and comparison of results with the theoretical analysis.

Chapter 6 describes the experimental program to study the long term behavior of CFRP reinforced concrete beams and columns under sustained loading. **Chapter 7** presents the analytical procedure for computing the total deformation of CFRP reinforced concrete members at any time considering the instantaneous and time dependent deformations. **Chapter 8** compares the experimental and analytical results for the beams and columns reinforced with CFRP.

The main objective of the studies is to investigate the feasibility of pretensioned concrete piles with CFRP tendons. Prior to fabrication and driving the test piles, an investigation of the pile driving site and equipment was made in order to determine the pile driving stresses using the wave equation analysis and the results presented in **Chapter 9**. The design, instrumentation and fabrication of pretensioned concrete piles with CFRP tendons are presented in **Chapter 10.** The pile driving test results of the CFRP pretensioned concrete piles are discussed and presented in **Chapter 11**.

Chapter 12 presents the preparation, instrumentation and testing of the reinforced concrete column specimens with CFRP hoops. The load deformation characteristics of the concrete columns are established for different CFRP hoop spacings and the strength enhancement due to the CFRP hoops is evaluated using a proposed stress vs strain model. **Chapter 13** summarizes the main findings and conclusions of the studies.

CHAPTER 2

LITERATURE REVIEW

2.1 INTRODUCTION

The use of the FRP composites was recognized as early as 1940's for the military and aerospace applications. In the late 1980's, FRP was considered as a suitable alternative to steel reinforcement in reinforced concrete in view of its high strength, light weight and corrosion resistance. Extensive studies and research were conducted in Canada, Europe, Japan and USA in 1990's. A wide range of FRP rods, bars, strands and cables are now available commercially. The FRP bars are made from high strength continuous fibers (carbon, glass, aramid, etc.) bounded together with a resin using pultrusion process.

This chapter presents a brief summary of the state-of-the-art on the mechanical properties and durability of reinforced / prestressed concrete members with CFRP composites. This chapter will also summarize the ultimate load and time dependent behavior of FRP reinforced concrete columns and behavior of pretensioned concrete piles with FRP tendons.

2.2 MECHANICAL PROPERTIES

Carbon FRP is one type of Continuous Fiber Reinforcing Material (CFRM), consisting of fiber and matrix resin binder. The classification of the CFRM is shown in Fig. 2.1 [JSCE, 1993]. Carbon fiber is made from either petroleum or coal pitch and polyacrylonitril, commercially classified as pitch and PAN carbon. Each fiber is between 5 to 20 μm in diameter, and is aggregate of imperfect fine graphite crystals.

Resins are of different types and classified by the heat-resisting properties and the basic physical properties. The different types of resins are, for example, denaturated epoxy resin, heat-resisting epoxy resin and bismaleic amid resin. The polymer matrix serves several critical functions beyond simply holding the reinforcement in place. It acts as an environmental barrier against environmental effects and also protects the fiber surface from corrosion or abrasion. It also contributes to the load carrying capacity of the reinforcement.

The CFRP tendons used in the present study are made up of PAN carbon fiber and epoxy resin manufactured by Toho Rayon Co., Ltd. The basic properties of the carbon fiber and resin are presented in Tables 2.1 and 2.2 [Tokyo Rope, 1993]. Carbon reinforcement offers a higher tensile strength, higher Young's modulus, and lower elongation than the other FRP’s. CFRP tendon properties are shown in Fig. 2.2. The physical properties of different reinforcing / prestressing bars are given in Table 2.3 [ACI , 1996]. FRP bars and tendons exhibit a high tensile strength compared to steel reinforcement as shown in Table 2.3 and do not exhibit any yielding before failure.

Table 2.1 Basic physical properties of carbon fiber [Tokyo rope, 1989]

Raw material	Tensile strength	Tensile modulus	Elongation at break
Carbon fiber	370 kgf/mm^2	24,000 kgf/mm^2	1.5 %

Note: 1kgf = 9.81 N

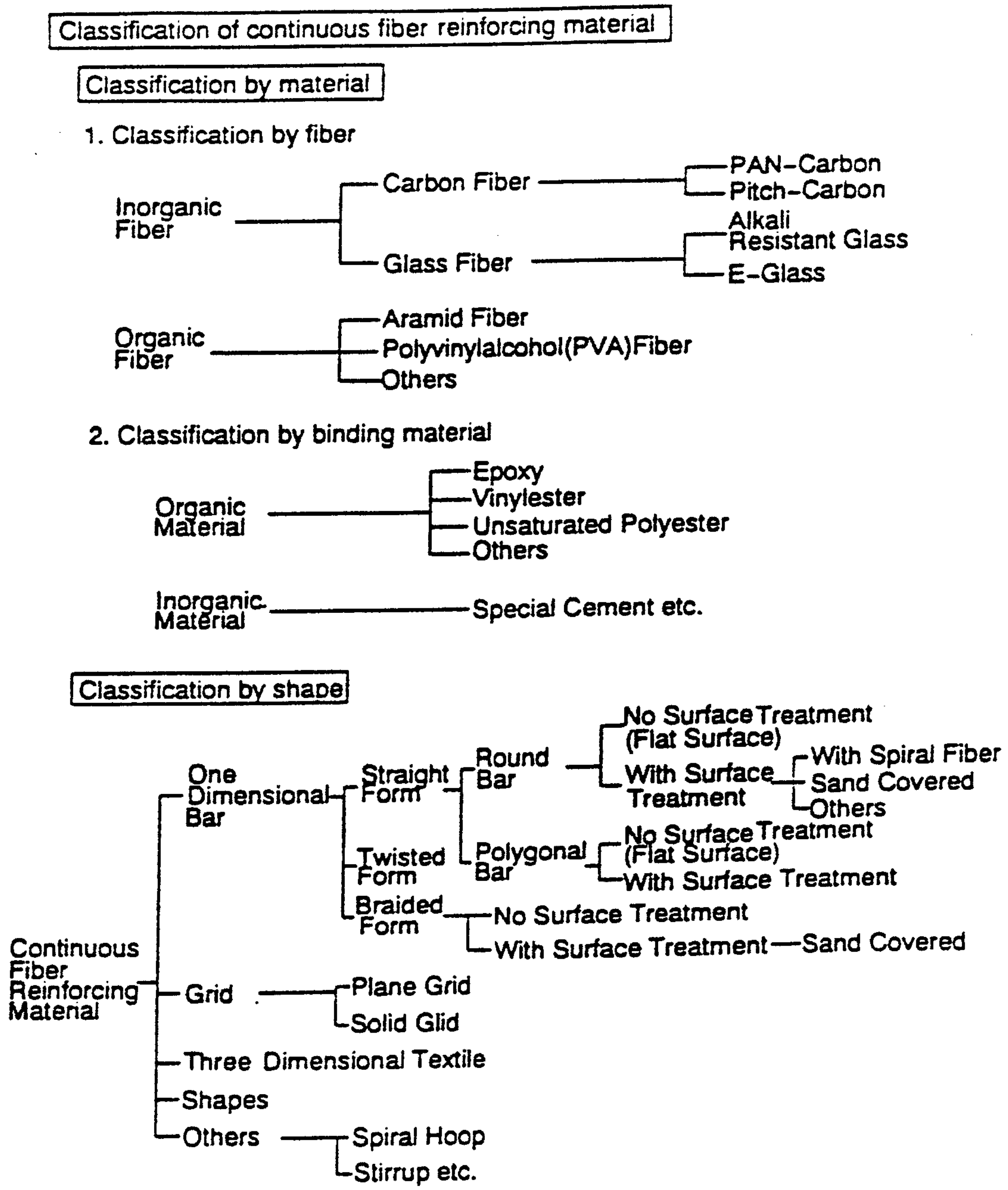

Figure 2.1 **Classification of continuous fiber reinforcing material**

Table 2.2 Basic physical properties of resins [Tokyo rope, 1989]

Heat resisting grade	Resins	Tensile strength (kgf/mm^2)	Tensile modulus (kgf/mm^2)	Elongation at break (%)
130^0C type	Denaturated epoxy resin	9.0	360	4.2
180^0C type	Heat-resisting epoxy resin	7.0	400	1.7
240^0C type	Bismaleic amid resin	8.0	360	2.5

Note: 1kgf = 9.81 N

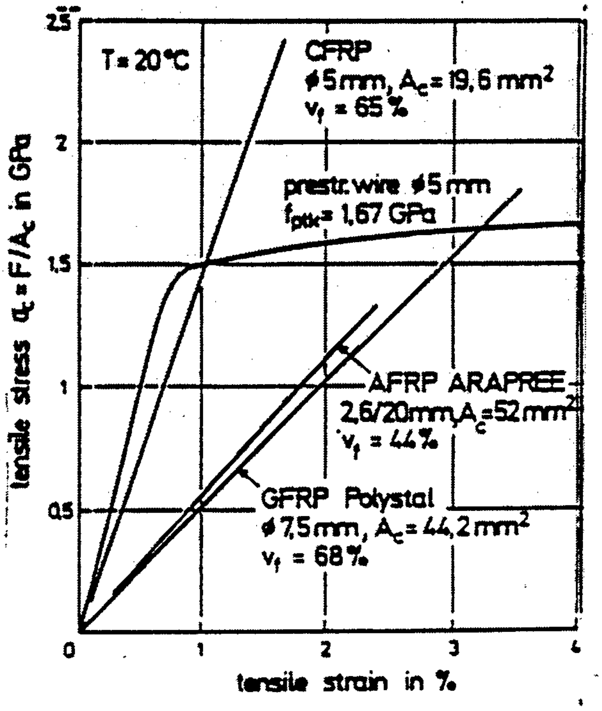

Fig. 2.2 Tensile stress-strain behavior of various reinforcements

(V_f =Volume fraction, ϕ = diameter)

Table 2.3 Comparison of the physical properties [ACI, 1996]

	Steel reinforcing bar	Steel tendon	GFRP bar	GFRP tendon	CFRP tendon	AFRP tendon
Tensile strength, MPa (ksi)	480-690 (70-100)	1380-1860 (200-270)	520-1210 (75-175)	1380-1720 (200-250)	1650-2410 (240-350)	1170-2070 (170-300)
Yield strength, MPa (ksi)	275-410 (40-60)	1040-1380 (150-203)		Not	Applicable	
Tensile elastic modulus, GPa (ksi)	200 (29,000)	186-200 (27,000-29,000)	40-55 (6000-8000)	48-62 (7000-9000)	150-165 (22,000-24,000)	48-76 (7000-11,000)
Ultimate elongation, mm / mm	> 0.10	> 0.04	0.035-0.05	0.03-0.045	0.01-0.015	0.02-0.026
Compressive strength, MPa (ksi)	275-410 (40-60)	N/A	310-480 (45-70)	N/A	N/A	N/A
Coefficient of thermal expansion (10^{-6}/ F)	6.5	6.5	5.5	5.5	0.0	-0.5
Specific gravity	7.9	7.9	1.5-2.0	2.4	1.5-1.6	1.25

2.3 DURABILITY

Katsuki and Uomoto [1995] conducted alkali penetration tests on FRP rods and observed that degradation was more pronounced in glass FRP (GFRP) rods due to very thin layer of the resin and poor alkali resistance of the glass fibers. Alkali cannot penetrate into CFRP and AFRP rods due to high alkali resistance offered by the carbon and aramid fibers.

Arockiasamy, et al. [1994] studied the chemical resistance of tensioned and untensioned Arapree cables subjected to wet/dry cycles in alkaline solution and seawater. A thermal controller was used to elevate the temperature of the chemical solution to accelerate the test. Ultimate tensile tests indicated no significant strength reduction due to exposure to alkaline solution and seawater.

Katawaki, et al. [1992] performed studies on the durability of advanced composites for applications to prestressed concrete bridges. They selected the splash zone (marine atmospheric location) as the typical corrosive environment. The materials include carbon fiber, aramid fiber, and glass fiber composites. The deterioration was measured as a function of the exposure duration and was found that the carbon and aramid fiber composite materials have strength characteristics comparable to steel and exhibit excellent anti-corrosion properties required for maritime structures. Exposure to marine environment caused cracks in the glass fiber composite material.

Sen. et al. [1991, 1993] conducted durability tests on fiberglass pretensioned concrete beams. They determined the effect of wet/dry cycles on the ductility and ultimate load capacity of identical steel and fiberglass pretensioned specimens and evaluated the relative durability of pre-cracked and uncracked specimens. The results of the studies indicated that the particular fiberglass tendons used in this study are not good in resisting corrosion. There were no visual signs of the deterioration of the fiberglass pretensioned beams prior to sudden failure of the beams.

Sen. et al. [1995] conducted durability studies on beams pretensioned with aramid and carbon FRP tendons. The pretensioned beams were subject to outdoor exposure, wet/dry cycles in salt water to simulate tidal effects and a combination of wet/dry cycles in salt water and thermal cycling. The test results indicate that outdoor exposures have relatively minor effect on the strength and serviceability of the beams. AFRP pretensioned beams showed little deterioration of strength and serviceability when subjected to wet/dry cycles in salt water. CFRP pretensioned beams showed a somewhat greater reduction in ultimate capacity. AFRP pretensioned beams displayed significant strength loss when exposed to tidal and thermal cycling. In contrast, the same environment had no effect on the strength and serviceability of CFRP pretensioned beams.

2.4 SERVICE AND ULTIMATE LOAD BEHAVIOR OF FRP REINFORCED CONCRETE COLUMNS

Very limited published literature is available on the behavior of CFRP reinforced/ prestressed concrete columns under service and ultimate loads. Sen. et al. [1992] carried out experimental studies on four concrete columns pretensioned with fiberglass tendons under axial and eccentric loads. The response of fiberglass pretensioned columns was similar to that of conventional steel pretensioned columns. Saeed and Noel [1994] reported studies on concrete columns reinforced with fiber reinforced plastic rebars. In this study, equations similar to those proposed by ACI Building Code for steel reinforced concrete columns were developed for FRP reinforced concrete columns. A theoretical interactive diagram was constructed for FRP concrete columns.

Priestley and Seible [1992] reported studies on column seismic retrofit using fiberglass/epoxy jackets. The concept of retrofitting bridge columns to enhance flexural and shear performance using fiberglass/epoxy composite jackets in critical regions is discussed and the results include those on three large-scale flexural columns with longitudinal reinforcement lapped in the flexural plastic hinge region and four shear columns tested under double bending. The experimental results indicate that properly designed composite jackets can inhibit lap-splice failures in hinge regions and provide sufficient shear strength to columns deficient in shear strength to ensure ductile flexural response.

2.5 TIME DEPENDENT BEHAVIOR OF CONCRETE MEMBERS REINFORCED WITH FRP

2.5.1 Creep of concrete

A typical stress-strain curve for concrete is shown in Fig. 2.3. Generally, it is assumed that the stress is proportional to the strain under the service load conditions. The strain occurring during the application of the stress is referred to as the instantaneous strain and expressed as follows:

$$\varepsilon_c(t_0) = \frac{\sigma_c(t_0)}{E_c(t_0)} \tag{2.1}$$

where t_0 = time of application of the stress

$\sigma_c(t_0)$ = compressive stress in concrete at age t_0

$E_c(t_0)$ = modulus of elasticity of concrete at age t_0

Under sustained stress, the strain increases with time due to the creep and the total strain at time t is the sum of the instantaneous and the creep strains (Fig. 2.4).

$$\varepsilon_c(t) = \frac{\sigma_c(t_0)}{E_c(t_0)}[1 + \varphi(t, t_0)] \tag{2.2}$$

where $\varphi(t,t_0)$ = creep coefficient from time t_0 to t.

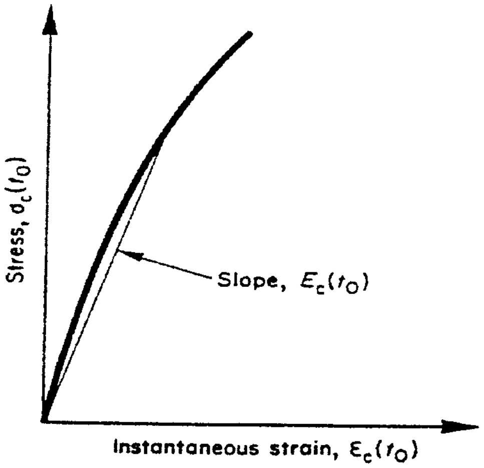

Fig. 2.3 Compressive stress-strain curve for the concrete

The coefficient φ represents the ratio of the creep strain to the instantaneous strain. Its magnitude increases with the load application at an early stage and increased period (t-t_0) during which time the stress is sustained. Creep deformations for concrete depend on the magnitude of the applied stress, concrete strength, shape and size of the member, and the atmospheric conditions. With elapsing time, creep decreases with time and ceases after 2 to 5 years and attains a final value of about 1.2 to 3 times the instantaneous strain.

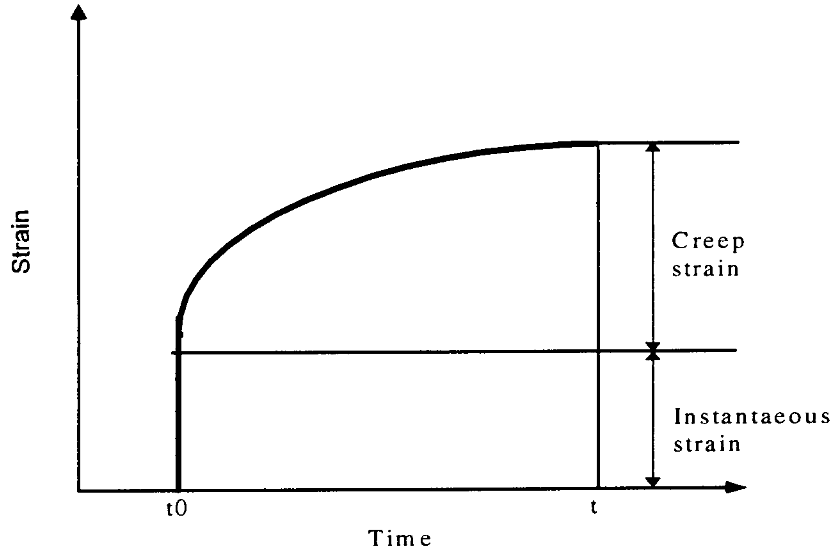

Fig. 2.4 Creep of concrete under the effect of sustained stress

2.5.2 Shrinkage of concrete

Drying of concrete in air results in shrinkage, while concrete exposed to moisture increases in volume. When the change in volume by shrinkage or swelling is restrained, internal stresses develop within concrete. In reinforced concrete structures, the restraint may be caused by the reinforcing steel, the supports or differential volume changes in various parts of the structure. Stresses caused by shrinkage are generally reduced by the creep of concrete. Although shrinkage and creep may not be independent phenomena, it can be assumed that superposition of strains is valid and hence the total strain is given by the following:

$$\text{Total stain } (\varepsilon_t) = \text{elastic strain } (\varepsilon_e) + \text{creep strain } (\varepsilon_c) + \text{shrinkage } (\varepsilon_{sh}) \qquad (2.3)$$

2.5.3 Relaxation of Prestressed Tendons

The effect of creep on prestressing tendons is commonly evaluated by a relaxation test in which a tendon is stretched and maintained at a constant length and temperature and the loss in tension is measured over a long period. The relaxation under constant strain as in a constant-length test is referred to as intrinsic relaxation. The relaxation of the CFRP tendons was observed to be insignificant.

2.5.4 Studies on time-dependent behavior

Only very limited published information on long term studies of carbon FRP reinforced concrete members is available. Extensive long term studies have been published on steel reinforced concrete members. The literature review presented in this section includes mainly the work published on creep and shrinkage of concrete and very limited studies on FRP reinforced concrete members.

Bazant, et al. [1982] reported that a poor prediction of creep and shrinkage causes excessive deflection and cracking, which endangers the serviceability of the structure. Creep and shrinkage deformations are usually several times larger than instantaneous deformations in concrete structures. These deformations produce cracking, damage and excessive deflections, which affect the durability, economy and long-term safety of concrete structures.

Balaguru and Nawy [1982] presented an analytical method to calculate the time dependent stresses and strains in reinforced concrete columns. It was concluded that time dependent stress redistribution substantially increases the steel stresses, hence should be considered in the design of the columns. Samra [1995] presented an approach for the evaluation of the effects of axial loading on steel reinforced concrete columns under sustained service stresses. The results of the theoretical approach correlate well with experimental tests conducted on specimens in the laboratory, and with deformations of columns measured in the Water Tower Place and Lake Point Tower in Chicago.

Currier et al. [1995] conducted tests and compared the long term deflection of CFRP, AFRP and fiberglass pretensioned concrete beams with steel reinforced concrete members under uniform sustained dead loads. The results indicate that the deflections of beams reinforced with FRP are smaller than the predicted values and within the acceptable levels for steel tendons.

Amer [1993] studied the relative creep and shrinkage losses in identical steel and fiberglass prestressed concrete columns under sustained axial loading. The shortening in fiberglass specimens was higher than those in the steel specimens. The strain variation with time for the concrete columns reinforced with fiberglass at different stress levels is shown in Fig. 2.5.

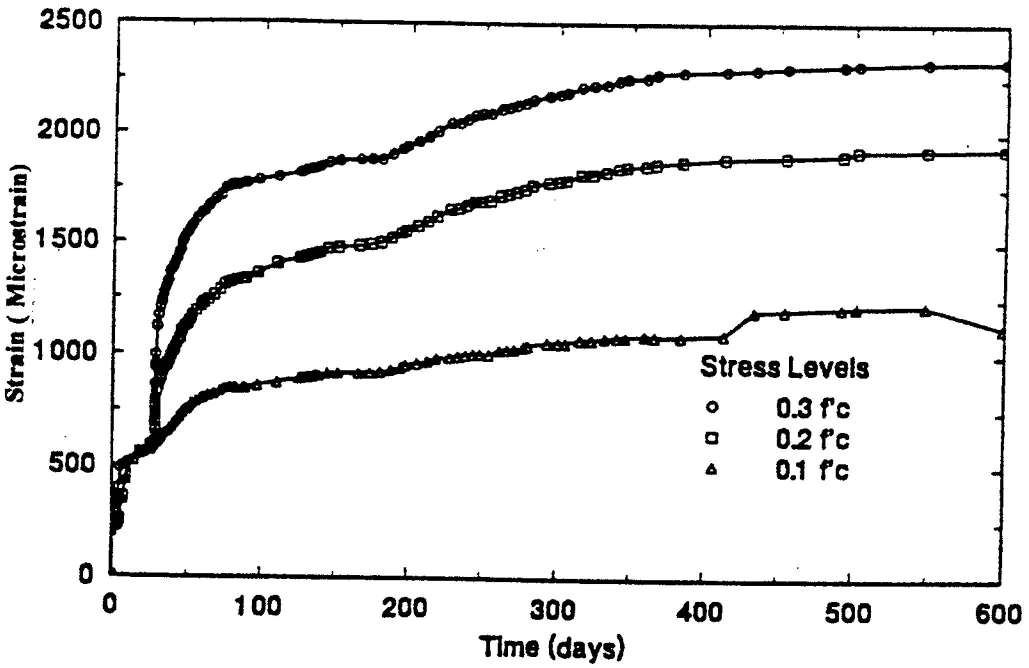

Fig. 2.5 Variation of compressive strain in columns with time [Amer, 1993]

Issa and Amer [1995] observed a considerable loss of prestress due to creep and shrinkage from the long term studies on fiberglass prestressed concrete specimens. It was observed that prestress losses in fiberglass specimens are considerably lower than those in steel specimens due to the low modulus of elasticity of fiberglass. Prestress creep losses increase with the increase in axial compression for both fiberglass and steel specimens.

2.6 EXISTING MODELS ON CONFINED CONCRETE

Extensive research was carried out in the area of confinement, mainly concrete confined with steel ties, hoops or spirals as well as jackets. Also, it has been proved that the lateral confinement will enhance the properties of the concrete members. The success of the lateral confinement is due to the development of triaxial stress field within the confined concrete and the containment of the concrete.

2.6.1 Confined concrete with steel spirals

The most commonly used equation (Eqn. 2.4) was developed for predicting the axial compressive strength enhancement of confined concrete [Richart et al.,1928] based on failure tests on 100 x 200 mm normal-weight concrete cylinders with varying intensities of lateral fluid pressure. The experimental data indicated that the axial strength and ductility of the concrete increase with the increased lateral pressure. The confined concrete strength is given by :

$$f'_{cc} = f'_c + 4.1\sigma_p \qquad \text{.............................. (2.4)}$$

where

f'_{cc} = ultimate compressive strength of confined concrete (MPa)

f'_c = ultimate compressive strength of concrete cylinder (MPa)

σ_p = lateral pressure (MPa)

Tests were also conducted on a series of spiral reinforced normal-weight concrete cylindrical columns having unconfined compressive strengths ranging from approximately 14 to 21 MPa [Richart et al., 1929]. The steel spiral confinement was affected by the amount of axial deformation experienced by the specimen. The constant 4.1 in the Eqn. 2.4, was estimated as 4.8, and later revised to 4.2 by Considere [1936]. Talbot [1936] reported that the constant may vary between 2.8 and 4.0 depending on the mix proportions and materials used in the concrete member. Tests conducted on several spirally confined concrete members (150 x 300 mm) under concentric compression, indicated that the confinement enhances axial strength by approximately 50 % and ultimate axial strain by 75 % compared to the corresponding unconfined concrete [Chan, 1955].

Morales et al. [1982] investigated the steel spiral reinforced columns subjected to short-term concentric compression. It was found that the static modulus of elasticity of the confined concrete did not significantly differ from that of the corresponding unconfined concrete. They also concluded that the transverse to axial strain ratio decreased with increased effective confinement for any concrete strength. The following expressions are suggested to predict the maximum stress and the corresponding strain:

$$f'_{cc} = 0.85f'_c + 4.0\sigma_p(1 - s/d_c) \qquad \text{.............. (2.5)}$$

$$\varepsilon'_{cc} = 0.0025 + \frac{250\sigma_{sp}(1 - s/d_c)}{\left(f'_c\right)^2} \qquad \text{.............. (2.6)}$$

where 250 is a dimensional constant in psi (equal to 1.72 MPa) and

A_{sp} = area of cross section of lateral reinforcement

f_{sy} = yield strength of the lateral reinforcement

d_c = lateral dimension of the column

s = spacing of the lateral reinforcement

ε'_{cc} = axial strain of confined concrete corresponding to f'_{cc}

ε'_c = axial strain of concrete corresponding to f'_c

Ahmad and Shah [1982] developed a model to predict the stress-strain relationships of confined concrete depending on the properties of the hoop reinforcement and the constitutive relationship of plain concrete. The tests were conducted on normal weight and light weight confined concrete cylinders of various compressive strengths under concentric compression. They proposed an expression for the full trace of the compressive stress-strain diagram in the form of a polynomial fraction, where the values for compressive strength and corresponding strain were based on the octahedral theory. Another unified stress-strain approach was developed for confined concrete applicable to both circular and rectangular shaped transverse reinforcement [Mander et al., 1984].

2.6.2 Confined concrete with FRP spiral

The performance of the concrete specimens jacketed with glass FRP shells both in uniaxial compression and tension tests was investigated by Fardis and Khalili [1981]. An analytical model for the performance enhancement was described using a circumferential stiffness parameter. The hyperbolic equation to trace the behavior of a confined specimen subjected to increasing axial compression is given by

$$f_c = \frac{E_c(\varepsilon_c)}{1+\varepsilon_c\left(\frac{E_c}{f'_{cc}} - \frac{1}{\varepsilon'_{cc}}\right)} \qquad \text{.....................} (2.7)$$

$$\varepsilon'_{cc} = 0.002 + 0.001\frac{E_{frp}t_{frp}}{d_c f'_c} \qquad \text{.....................} (2.7a)$$

$$f'_{cc} = f'_c\left[1 + 4.1\frac{f_{frp}t_{frp}}{d_c f'_c}\right] \qquad \text{.....................} (2.7b)$$

Equation 2.7b is identical to that proposed by Richart et al. [1928].

Where E_c = modulus of elasticity of the concrete

E_{frp} = modulus of elasticity of the lateral FRP reinforcement

t_{frp} = thickness of the FRP jacket

f_{frp} = ultimate strength of the FRP

A comparative investigation was conducted by Ahmad et al. [1991] on the effectiveness of glass FRP versus spiral steel confinement. Tests were conducted on 33 FRP confined normal weight concrete cylinders under concentric compression. An expression was developed for glass FRP confined concrete using a modified version of the stress-strain equation developed by Ahmad and Shah [1982] for predicting the stress-strain curves for concrete confined with steel spirals (Eqn. 2.8).

$$f_c = \left\{ \frac{A\left(\varepsilon_c / \varepsilon_c^{'}\right) + (B-1)\left(\varepsilon_c / \varepsilon_c^{'}\right)^2}{1 + (A-2)\left(\varepsilon_c / \varepsilon_c^{'}\right) + B\left(\varepsilon_c / \varepsilon_c^{'}\right)^2} \right\} f_c^{'} \qquad \text{…………… (2.8)}$$

A and B are material constants and Eqn. 2.8 was modified by using f'_{cc} and ε'_{cc} in place of f'_c and ε'_c for determining the stress-strain curves for the concrete confined with glass FRP.

Saadatmanesh et al. [1993] used the approach proposed by Mander et al. [1988] to compute the effective lateral confining pressure resulting from FRP tapes wrapped on to circular or rectangular columns. The analytical method was in turn used to quantify the gain in strength and ductility of retrofitted columns subjected to combined flexural and axial loading. Taniguchi et al. [1993] modified an existing stress-strain model for steel-confined concrete for the case of FRP-confined concrete, which showed a good agreement with experimental data obtained from concrete cylinders wrapped with FRP.

Howie and Karbhari [1994] reported the test results based on a variety of carbon fiber jacketed systems. Failure sequences are documented and related to structural behavior for each system. The results of this study show that the best possible orientation of the external composite wrap is one which contains a large amount of hoop reinforcement. This is demonstrated by the strength increases of wrapped cylinders compared to unwrapped cylinders, the radial confining stress and the large strain at failure.

Thirty 152.5 x 305 mm cylindrical specimens were tested, in which 24 were concrete filled FRP tubes. Results of the uniaxial compression tests are compared with the available confinement models [Mirmiran and Shahawy, 1996]. The unique characteristics of confinement with fiber composites contribute to decrease in the dilatation tendency of concrete.

2.7 PILE DRIVING TESTS

Extensive research work has been carried out on concrete piles pretensioned with steel. Driving tests are quite common both in research as well as routine field tests [Fellenius, 1988]. Concrete piles (610 mm square section) were driven with a single acting Kobe K45 diesel hammer in the alluvium soil to a depth of around 30 m (98.5 ft.) . The average measured hammer energy for the last 1.5 m (5 feet) of penetration was around 100 kN-m (74.4 kip-ft.) [Thomas, et al., 1984]. Tests have been reported on the concrete piles pretensioned with steel to support the Edison Bridge, Lee County, Florida [GRL & Associates, 1991]. Each pile had a 762 mm (30 in.) square cross section with a length varying from 21.64 m to 23.16 m (71 ft. to 76 ft.). The piles driven using Conmaco 300 E5 single acting air hammer were instrumented and monitored using PDA.

Only limited published literature is available in the area of FRP pretensioned concrete piles. Piles pretensioned with fiberglass reinforced tendons were successfully driven in dense sands [Sen et al., 1991]. Four concrete piles of 254 mm (10 in.) square cross section and 7.62 m (25 ft) long were driven using 13.36 kN (3 kips) drop hammer with an average drop height of 1.83 m (6 ft.). The driving stresses were monitored using PDA and by an independent data acquisition system. However, the long term durability study indicated that fiberglass tendons suffered degradation under wet/dry cycles. The section and 13.72 m (45 ft) long prestressed with graphite cable is presented by Iyer [1994]. These piles were intrumented by Goble, Rausche, Likens & Associates (GRL) to evaluate the performance of the piles during driving.

CHAPTER 3

DURABILITY STUDIES ON CFRP CABLES

3.1 INTRODUCTION

Bridges in Florida are exposed to harsh environment characterized by a wide range of temperature and humidity. They are subjected to cyclic load effects and impact in addition to sustained dead load. Corrosion resistance and durability of CFRP composites need careful evaluation before application in bridges. This chapter presents the experimental studies on durability of CFRP cables. The CFRP tensioned / untensioned specimens exposed to air, seawater and alkaline for different durations were tested to determine the durability characteristics. The tensile strength and elastic modulus of both tensioned and untensioned CFRP cables were determined to evaluate any degradation in the properties due to exposure to harsh environment.

3.2 EXPERIMENTAL SETUP FOR EXPOSURE TO WET / DRY CYCLES

3.2.1 Untensioned specimens

Two polycarbonate tanks were used, one for seawater and the other for alkali solution. Two metallic tanks were set next to each other connected with the polycarbonate tank. The seawater and alkali solution were pumped back and forth between the polycarbonate tanks and metallic tanks to simulate the wet/dry cycle. The investigation was carried out on three groups of untensioned specimens (Table 3.1) - one immersed in seawater, one in alkali solution and the other one exposed to air.

3.2.2 Tensioned specimens

Three steel self-straining frames were used (Fig. 3.1) for tensioning the CFRP specimens. A polycarbonate tank was placed in the middle of the self-straining frame to store seawater or alkali solution. The wet/dry cycle was similar to that used for the untensioned cables. The CFRP cables were passed through the holes provided in the tank and then laid in place in the self-straining frame to ensure that the cables would not be in contact with the edges of the holes in the frame to prevent any possible damage during the tensioning operation. CFRP cables were tensioned by a movable hydraulic jack at one end and anchored at the other. The CFRP specimens were loaded to 98 kN, which is approximately 65% of the ultimate load and the stress level maintained for periods of 3, 6 and 9 months.

The seawater was transported from the Atlantic Ocean and the tank filled with fresh seawater at regular intervals. The alkaline solution was made by mixing sodium hydroxide and calcium hydroxide solutions. The pH value was maintained at 13-14. The sodium hydroxide solution was prepared from 40 grams NaOH flake mixed with 1000 cm^3 of water. The calcium hydroxide solution was made up from 1 g $Ca(OH)_2$ powder mixed with 1000 cm^3 of water.

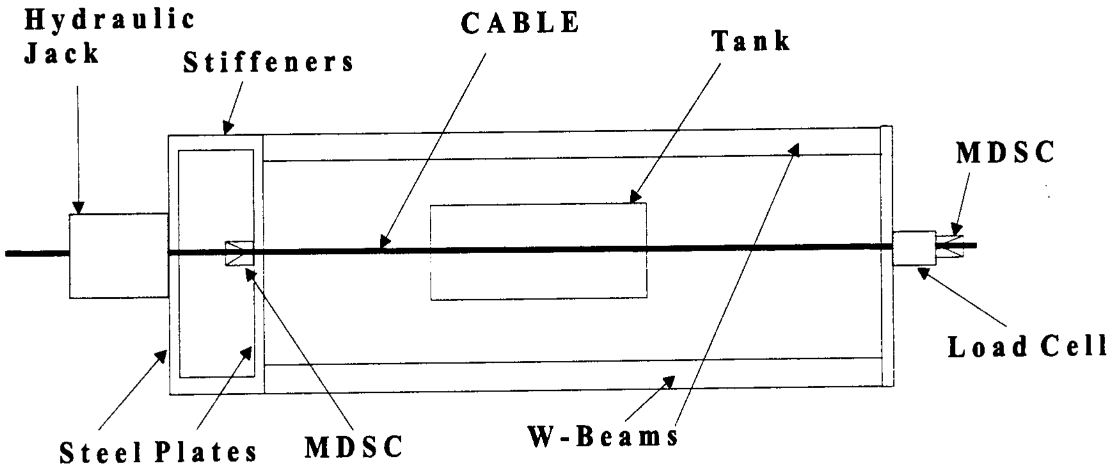

Fig. 3.1 Schematic of test frame and tank for durability study of the tensioned cables

Table 3.1 CFRP cable exposure periods

Number of cables	Exposure to air	Exposure to sea water	Exposure to alkaline solutions
Twenty-four (tensioned)	2 for 6 months 5 for 15 months 1 for 17 months	2 for 3 months 3 for 6 months 3 for 9 months	4 for 3 months 2 for 6 months 2 for 9 months
Twenty-four (untensioned)	8 control specimens	8 for 9 months	8 for 9 months

3.3 TENSILE STRENGTH OF CFRP TENDONS

3.3.1 Tension test setup

A pretensioning steel frame was used for testing the tendons (Fig. 3.2). An end protection frame was fabricated and bolted to the frame end. It consists of three 6.35 mm thick steel plates bolted together. Five steel cover plates of size 609.6 mm x 762 mm x 6.35 mm were used to contain the broken pieces of the CFRP cables at failure within the test frame (Fig. 3.3).

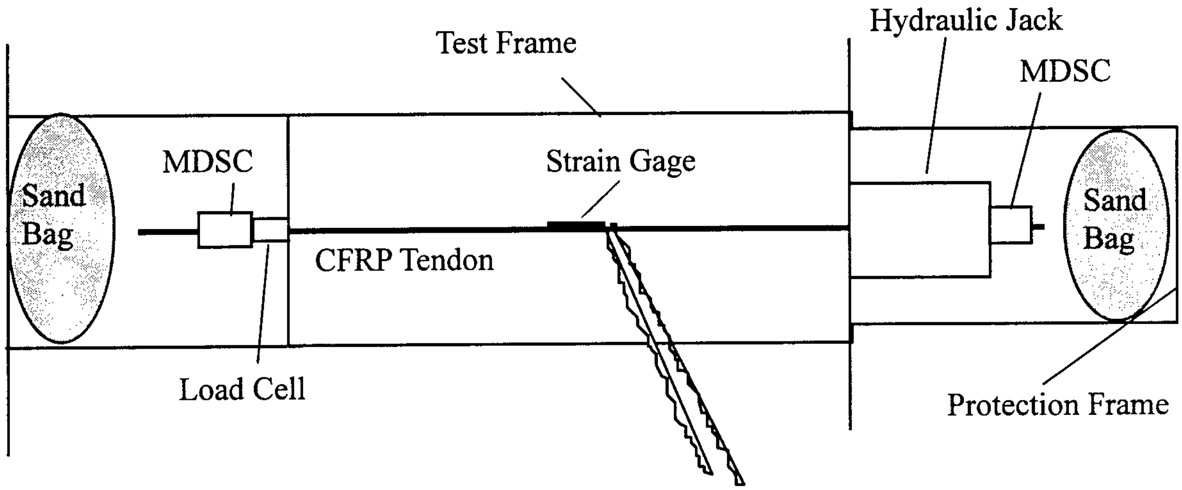

Fig. 3.2 Tensile strength test setup

3.3.2 Tensile strength test

CFRP tendons (tensioned/untensioned) exposed to air/seawater/alkali environments were tested to failure in the test frame (Fig. 3.2). The rust on the MDSC heads was sanded off to make sure the anchorage would not slide during the tension test. A strain gage was attached to the CFRP tendon (Fig. 3.4) and a load cell installed at the dead end of CFRP tendon between the wedge and end plate (Fig. 3.5). The hydraulic jack was set at the other end of the cable and secured by the wedge (Fig. 3.6). The load cell and strain gage were connected to a data acquisition system (System 4000). Tensile load was applied at increments of 22.24 kN and cable elongation measured at the jacking end at regular intervals. After applying a load of 0.70 times the ultimate load, the test tendon was covered with steel plates and the applied load increased steadily until failure (Fig. 3.3). At the ultimate load, tendons ruptured with a very loud noise. Fig. 3.7 shows the ruptured pieces of the tendon after failure.

3.3.3 Results and discussions

3.3.3.1 Ultimate strength of CFRP tendons under different corrosive environments

3.3.3.1.1 CFRP tendons exposed to air

The results of the tensile strength tests of the tensioned/untensioned CFRP tendons exposed to air are given in Table 3.2. The tensile strength of tendons exposed to air with different exposure periods is shown in Fig. 3.8. The test data show that the tensile strength of specimens is not affected by exposure periods.

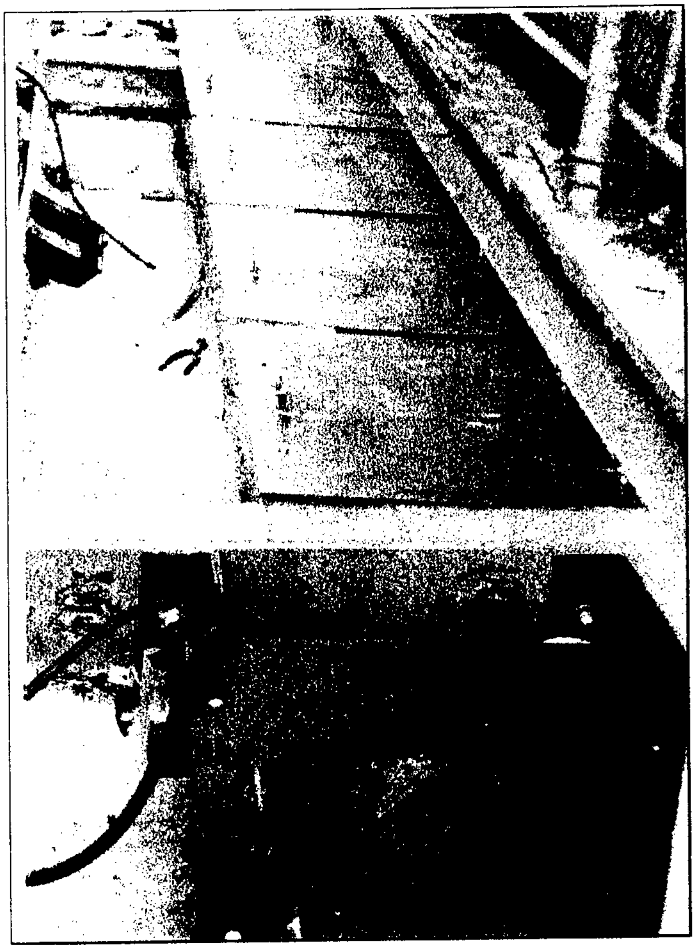

Fig. 3.3 Tensile strength testing frame

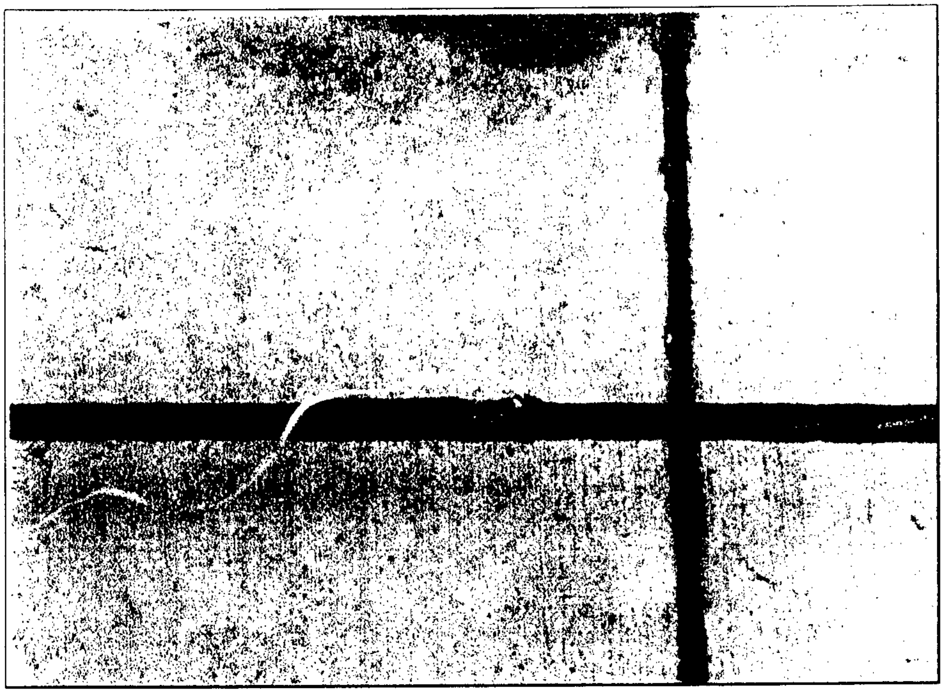

Fig. 3.4 Strain gage installed on the CFRP tendon

Fig. 3.5 Load cell setup on one end of CFRP specimens

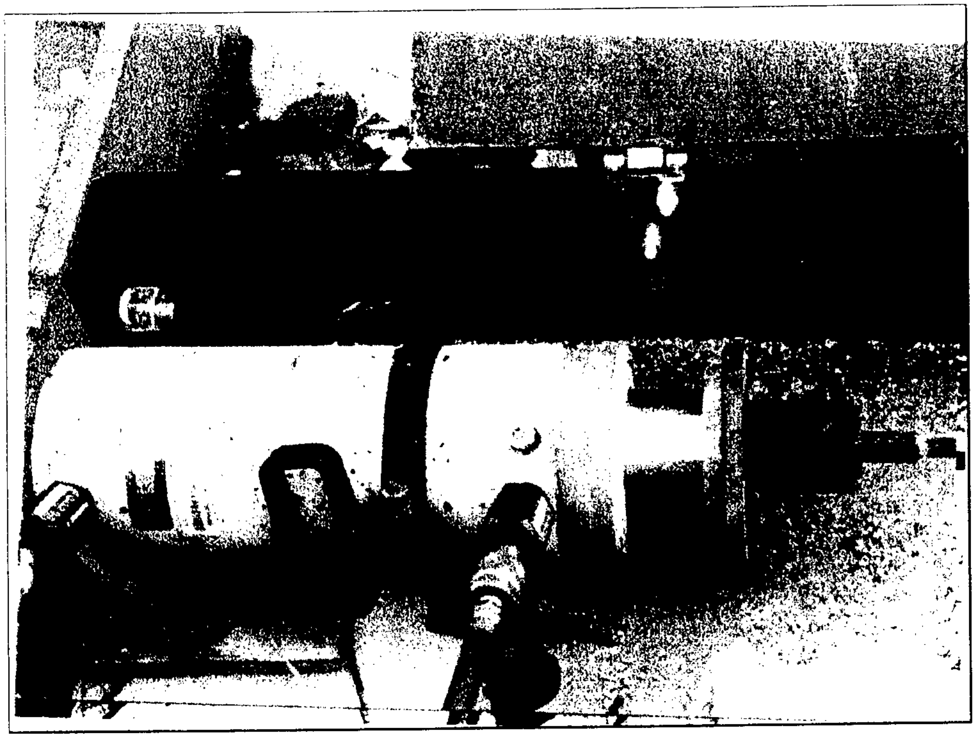

Fig. 3.6 Hydraulic jack for tensioning the CFRP specimens

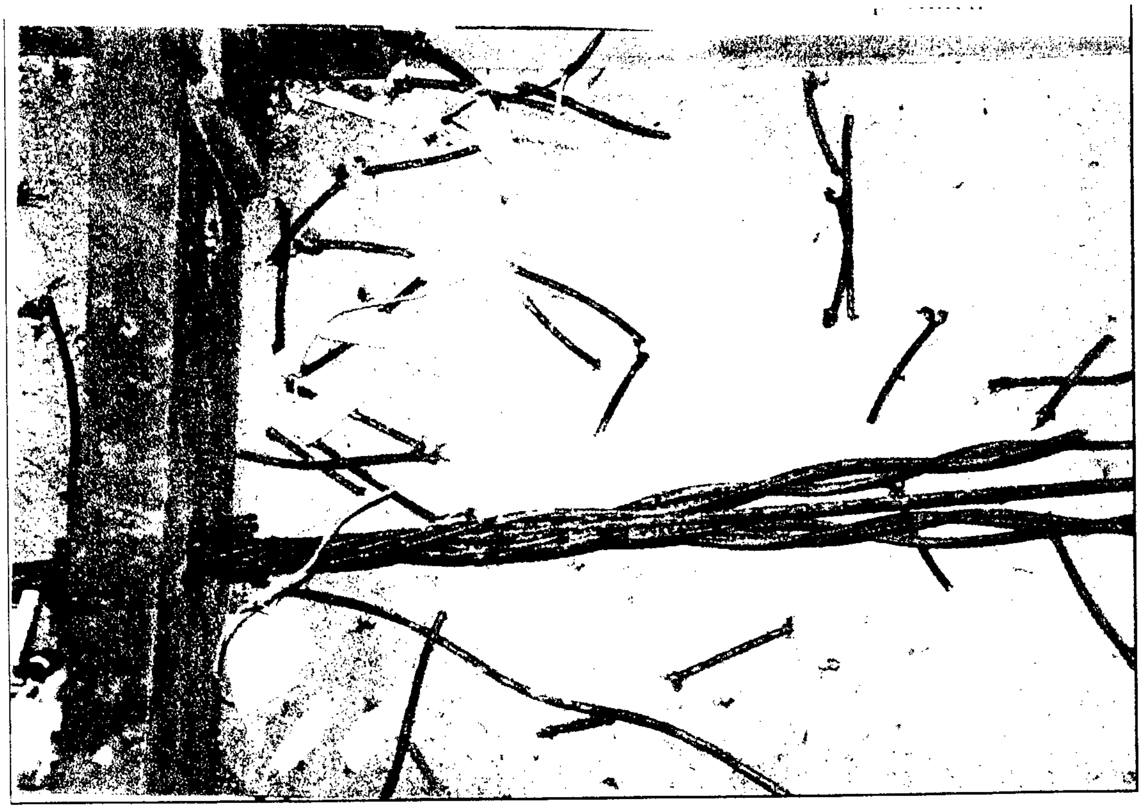

Fig. 3.7 Overview of ruptured pieces of CFRP tendon after failure

Table 3.2 Test results of CFRP specimens exposed to air

Tendon designation (Tensioned)	Ultimate load (kN)	Exposure period (months)	Average strength (N/mm^2)	Cable number (Untensioned)	Ultimate load (kN)	Average strength (N/mm^2)
T1	151.23	6	2057	U1	159.10	2069
T2	161.37	6		U2	167.76	
T3	167.02	15	2057	U3	144.96	
T4	159.68	15				
T5	151.14	15				
T6	150.15	15				
T7	153.45	15				
T8	154.97	17	2039			

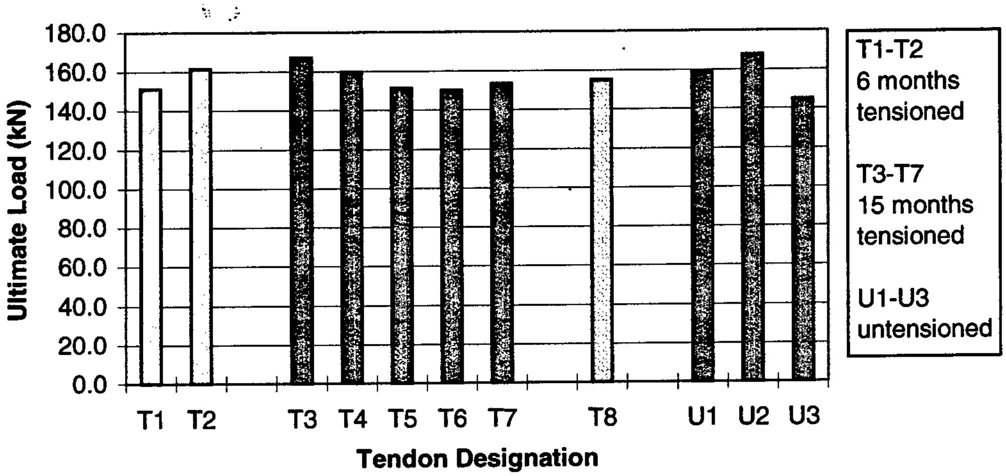

Fig. 3.8 Ultimate load of CFRP specimens exposed to air

3.3.3.1.2 CFRP specimens exposed to seawater

The ultimate loads of the tensioned/untensioned CFRP tendons exposed to seawater are shown in Fig. 3.9. The tensile strengths of specimens exposed to seawater do not show any strength reduction. It is interesting to observe that strength of tensioned specimens after different exposure periods to seawater was higher by about 8% than that of untensioned specimens.

3.3.3.1.3 CFRP tendons exposed to alkali solution

The ultimate loads of the tensioned/untensioned CFRP specimens exposed to alkali solution are shown in Fig. 3.10. From the test data, the CFRP tendons subjected to different periods of immersion in alkali solution do not show any strength reduction.

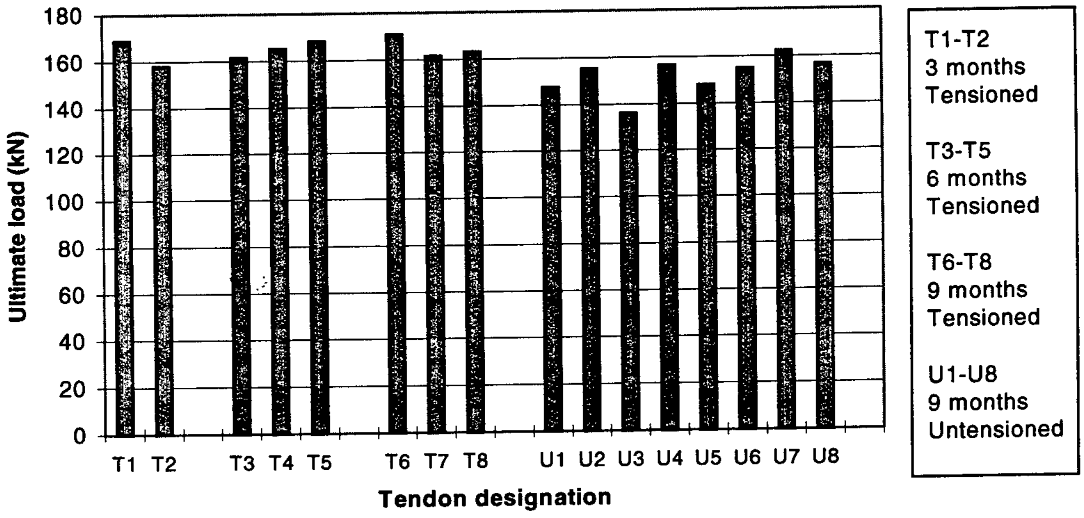

Fig. 3.9 Ultimate loads of CFRP specimens exposed to seawater

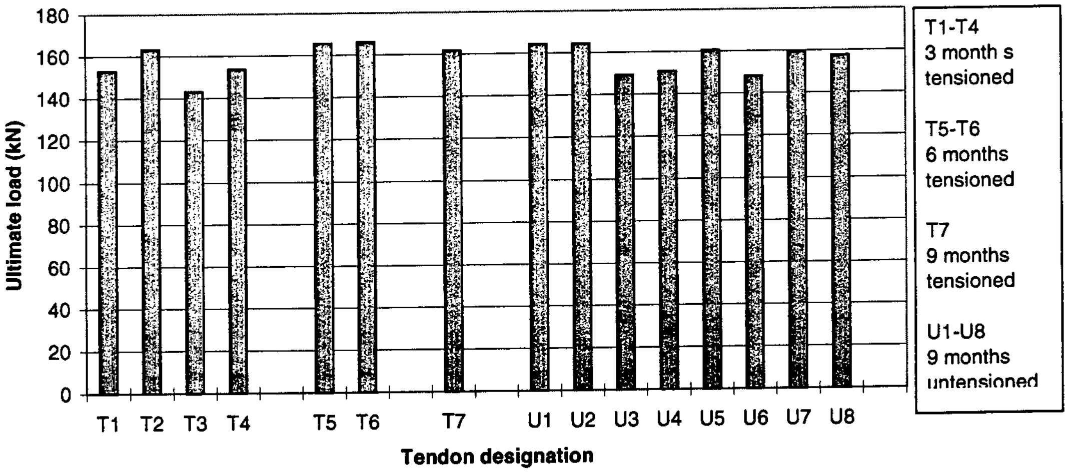

Fig. 3.10 Ultimate loads of CFRP specimens exposed to alkali solution

3.3.3.2 Discussions

The data from the tensile strength tests of specimens exposed to air, seawater and alkali solution show that the ultimate loads of CFRP tendons vary from 145 kN to 170 kN. The average ultimate loads of tensioned and untensioned specimens are 160 kN and 155 kN respectively. The average ultimate tensile strength of specimens is 2071 MPa, which is lower by 5% of the reported value of 2181 MPa by the manufacturer. The tendons subjected to sustained tension and exposed to seawater and alkaline solution do not show any strength reduction (Figs. 3.11 and 3.12).

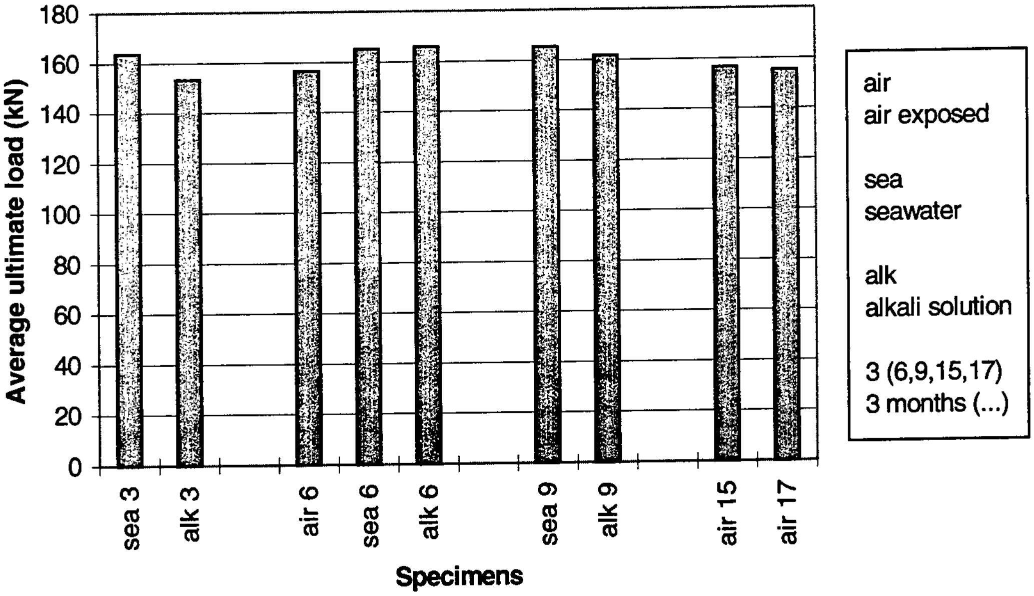

Fig. 3.11 Ultimate loads of tensioned CFRP specimens under different environments

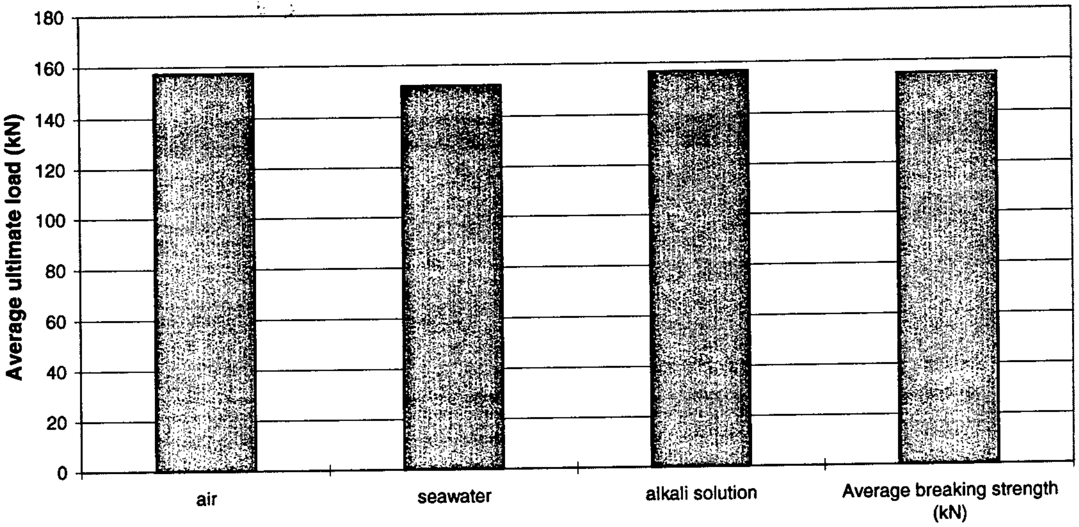

Fig. 3.12 Ultimate loads of untensioned CFRP specimens under different environments

3.4 MODULUS OF ELASTICITY

Elastic modulus of CFRP Tendons was determined when they were stressed to 65% ultimate load before subjecting them to sustained tension and exposure to seawater and alkaline solution. Fig. 3.13 shows the stress vs. strain relationship of CFRP tendons. The average elastic modulus is 133.41 GPa, which is slightly smaller than the reported value of 136.52 GPa by the manufacturer. This value is significantly less than the elastic modulus of high strength steel (200.0 GPa).

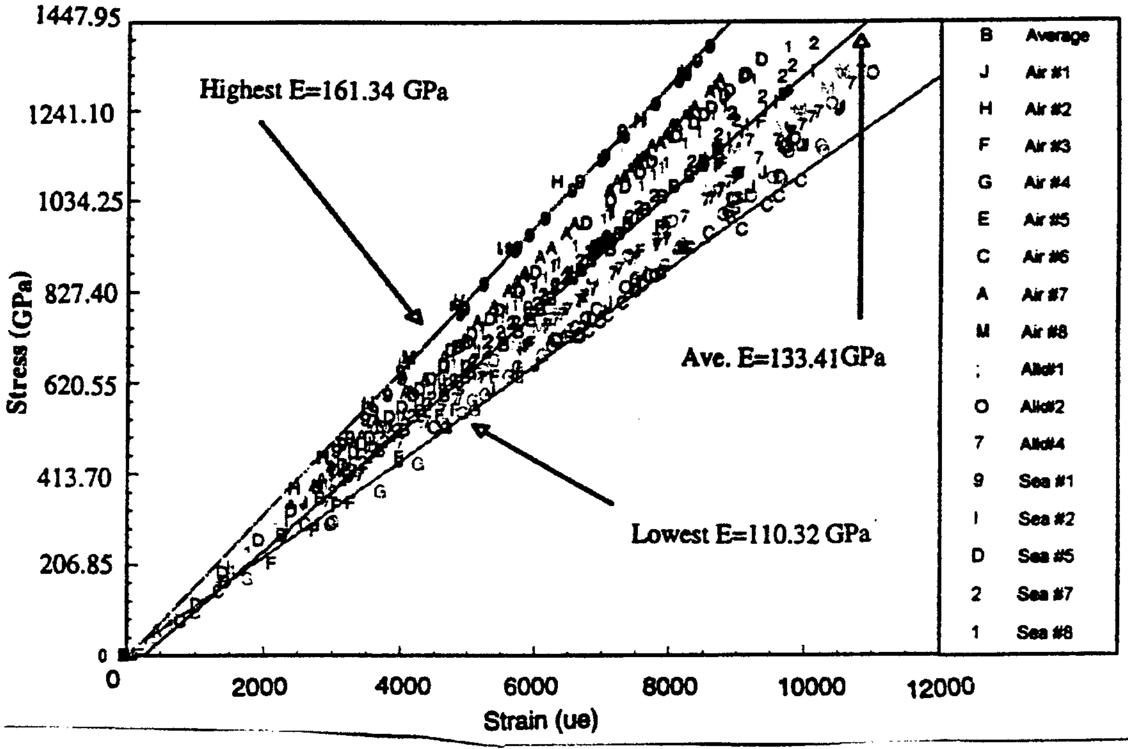

Fig. 3.13 Stress vs. strain for CFRP specimens

CHAPTER 4

ULTIMATE STRENGTH ANALYSIS OF CFRP REINFORCED CONCRETE SLENDER COLUMNS

4.1 INTRODUCTION

The strength of a slender column is affected by many factors such as column length, end-restraint conditions, distribution of bending moment, and bracing condition of the column. The current methods of stability analysis of slender column tend to be too complex for everyday design-office use. The ACI code provisions recommend using the moment magnification method in the analysis of steel reinforced concrete columns. The ultimate strength analysis of CFRP reinforced concrete columns is presented in this chapter. A computer program based on the moment magnification method has been developed to perform the analysis under combined axial load and bending moment. The linear elastic stress strain properties of CFRP cables and parabolic stress strain relationship of concrete are taken into account in the analytical formulation. Chapter 5 presents the experimental study on eight CFRP reinforced concrete columns under eccentric loads (Fig. 4.1) and comparison of results with the theoretical values. The slenderness ratio for the test columns ($kl_u/r=53$) exceeds the slenderness limits, $kl_u/r \leq 22$.

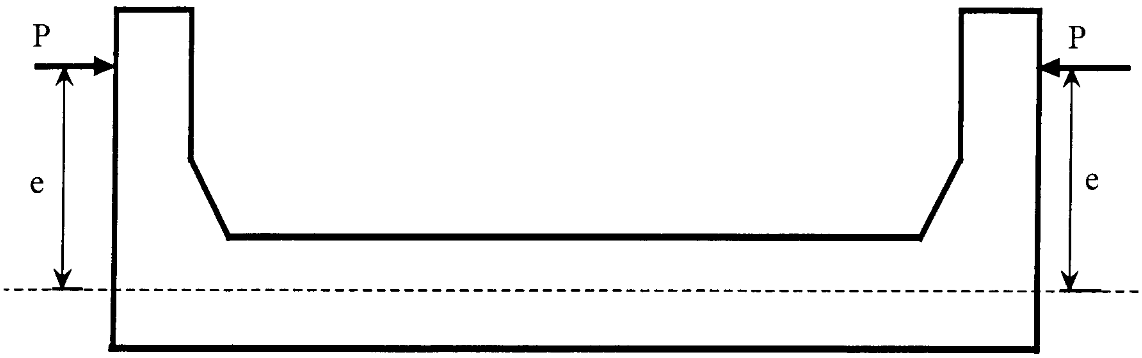

Fig. 4.1 Experimental test setup

4.2 LOAD AT FIRST CRACK

The first crack in the column initiates when the concrete tensile stress reaches the modulus of rupture. The first crack load of the column is calculated based on the following:

$$\frac{P_{cr}}{A_c} - \frac{(P_{cr}e + M_o)y}{I_g} = -f_r \qquad (4.1)$$

$$\Rightarrow \qquad P_{cr} = \frac{M_o y - f_r I_g}{I_g / A_c - ey} \qquad (4.2)$$

Where

e = the eccentricity of load

P_{cr} = the first crack load

f_r = the modulus of rupture of the concrete

A_c = the area of the cross section of column

M_o = the moment due to the self weight of the column

y = the distance of the bottom fiber from neutral axis

I_g = the moment of inertia of gross concrete section about centroidal axis, neglecting the reinforcement

4.3 ULTIMATE STRENGTH ANALYSIS OF CFRP REINFORCED CONCRETE SLENDER COLUMNS

4.3.1 Method of analysis

The strain distribution across the cross section of the column is assumed to be linear and the strains in the CFRP cables and the surrounding concrete are the same prior to the cracking of the concrete or the rupture of the cables. Concrete in the tension zone of the section is neglected in the flexural analysis and the tension reinforcement contributes to the total tensile force. Fig. 4.2 shows the typical distribution of strain across the depth of the column and equivalent stress block

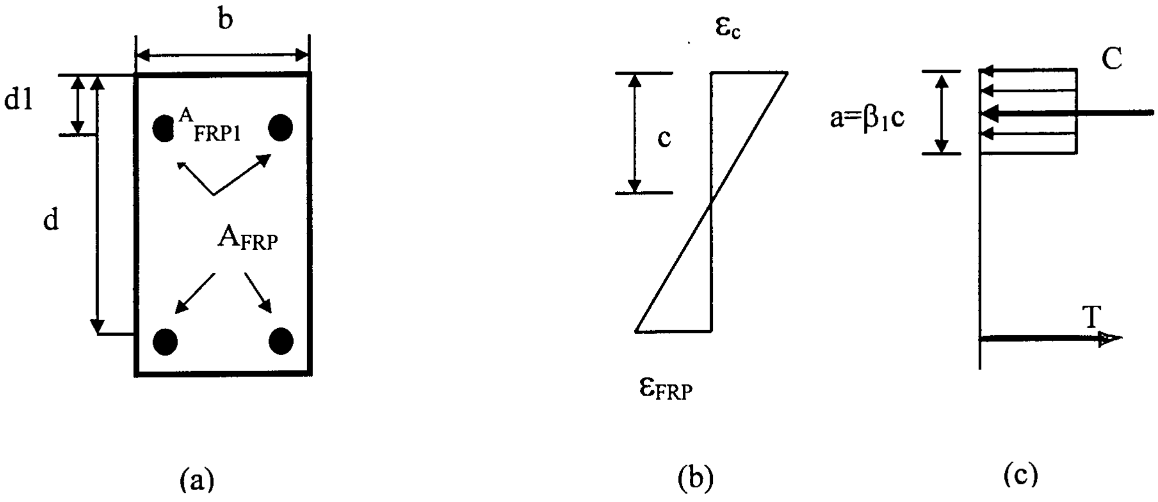

Fig. 4.2 Typical distribution of the stress and strain across the depth of the column: (a) Reinforcement details; (b) Strain distribution; (c) Equivalent stress block.

Since the slenderness ratio of the columns ($kl_u/r = 53.33$) is greater than ACI limits of 22, the buckling effects are considered in the analysis. The design of the member is based on an external magnified moment given by

$$M_c = P_n * (e + Deflection * \delta_b) \tag{4.3}$$

Where $\delta_b = \dfrac{C_m}{1 - P_u / P_c} \geq 1$, $\quad P_c = \dfrac{\pi^2 EI}{(kl_u)^2}$, $\quad EI = \dfrac{E_c I_g / 2.5}{1 + \beta_d}$

In the present study, C_m=1.0, β_d is zero in the absence of factored external dead load moment and there is no side sway moment. The deflection of the column computed from first principles consists of three parts: i) deflection due to eccentric axial loading, ii) deflection due to self weight of the enlarged ends of column, and iii) deflection due to self weight of part of the column with uniform cross section.

For a section with a known geometry and eccentricity e, compression block depth a is assumed and the value of the neutral axis depth c computed using the stress block depth factor, β_1. Using the basic principles of equilibrium of internal couples and strain compatibility, the stresses f_{FRP} and f_{FRP1} in the CFRP cables in the tension and compression zones are computed to determine the axial load P_n and internal nominal bending moment M_n (Eqns. 4.4-4.9).

The externally applied moment given by Eqn. 4.3 is checked with the internal nominal bending moment in the column. If they are not equal, the iterative computation is repeated until convergence is achieved. If the calculated external moment is larger than the internal nominal moment, then the assumed value for c and the corresponding depth, a of the compression block are less than the actual depth. A larger value of c is assumed and the iterative procedure repeated until convergence.

4.3.2 Computation of axial load P_n and nominal bending moment M_n

The following three possible strain distributions across the column depth (Fig. 4.3) are considered when the column is subjected to eccentric loading: i) compressive strains throughout the cross section; c > d, ii) one layer of CFRP cables in tension; c < d and iii) the CFRP cables in both layers in tension; c < d1.

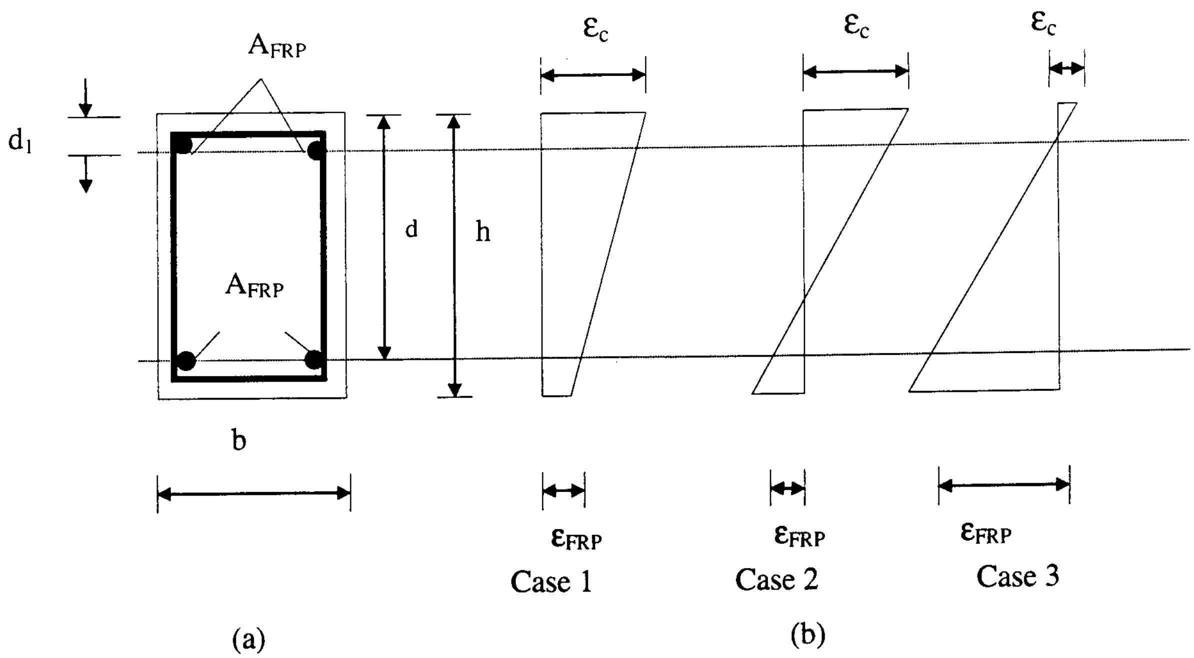

Fig. 4.3 Column geometry and strain distributions
(a) Cross section; (b) Case 1; Case 2; Case 3

Case 1: $c>d$ ------ all CFRP cables in compression

$$P_n = 0.85\, f_c\text{'}ba + A_{FRP}\, f_{FRP} + A_{FRP1}\, f_{FRP1} \tag{4.4}$$

$$M_n = 0.85\, f_c\text{'}ba(h/2-a/2) - A_{FRP}\, f_{FRP}(d-h/2) + A_{FRP1}\, f_{FRP1}(h/2-d_1) \tag{4.5}$$

Case 2: $d_1 \le c < d$ ------ only one layer of CFRP cables in tension

$$P_n = 0.85\, f_c\text{'}ba - A_{FRP}\, f_{FRP} + A_{FRP1}\, f_{FRP1} \tag{4.6}$$

$$M_n = 0.85\, f_c\text{'}ba(h/2-a/2) + A_{FRP}\, f_{FRP}(d-h/2) + A_{FRP1}\, f_{FRP1}(h/2-d_1) \tag{4.7}$$

Case 3: $c<d1$ ------ all CFRP cables in tension

$$P_n = 0.85\, f_c\text{'}ba - A_{FRP}\, f_{FRP} - A_{FRP1}\, f_{FRP1} \tag{4.8}$$

$$M_n = 0.85\, f_c\text{'}ba(h/2-a/2) + A_{FRP}\, f_{FRP}(d-h/2) + A_{FRP1}\, f_{FRP1}(d_1-h/2) \tag{4.9}$$

where

$c = a/\beta_1$, $\quad f_{FRP} = \varepsilon_c * E_{FRP} * |d-c|/c$, $f_{FRP1} = \varepsilon_c * E_{FRP} * |c-d_1|/c$

in which $\varepsilon_c = 0.003$.

4.3.3 Deflections

When the bending moment in the column is large, column cracking would be considered and the effective moment of inertia (I_e) of the column should be used in the calculation of deflection.

$$Ie = Icr + (\frac{Mcr}{Ma})^3 * (Ig - Icr) \tag{4.10}$$

The deflection of the column consists of three parts:

Deflection 1 = deflection due to eccentric axial loading

Deflection 2 = deflection due to self weight of the enlarged ends of column

Deflection 3 = deflection due to self weight of portion of the column with uniform cross section

Deflection = deflection 1 + deflection 2 + deflection 3.

4.4 COMPUTER PROGRAM FOR ULTIMATE LOAD ANALYSIS

A computer program has been developed to perform the analysis of CFRP reinforced concrete slender columns subjected to combined axial load and bending moment. The linear elastic stress-strain properties of CFRP cables and parabolic stress strain relationship of concrete are taken into account in the analytical formulation. The computer program is developed using Visual C++ language.

The program consists of three parts (Fig. 4.4):

- Input details of the columns, including the dimensions, reinforcement arrangement, and the loading condition and the related coefficients
- Computation of the first crack load of the column
- Determination of the ultimate load of the column

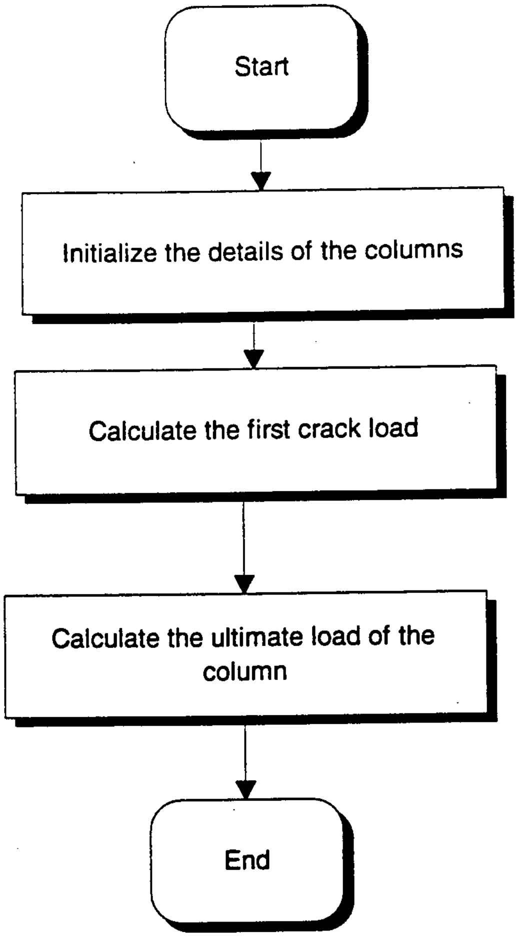

Fig. 4.4 General flowchart of the computer program

4.4.1 Initialization of the details of the column

The input to the first part of the program includes the detailed information of the column, including the dimensions, the arrangement of the reinforcement, the properties of the CFRP reinforcement, concrete, loading condition, eccentricity, etc. Figs. 4.5 and 4.6 show the interface for data input and the results are shown in Fig. 4.7.

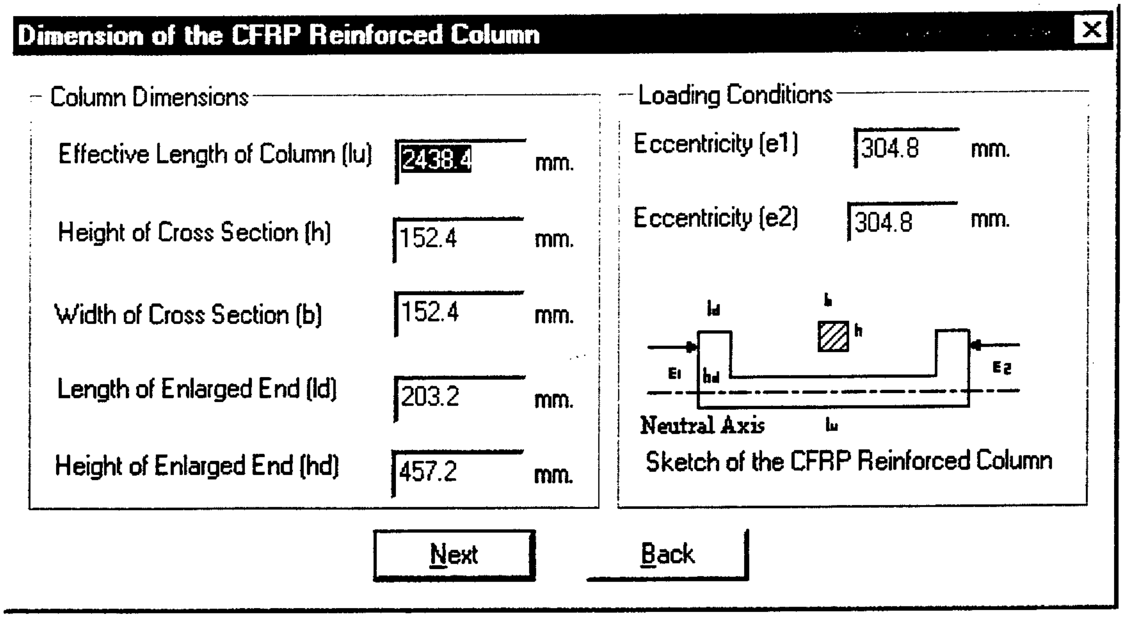
Dimension of the CFRP Reinforced Column

Column Dimensions

Effective Length of Column (lu) 2438.4 mm.

Height of Cross Section (h) 152.4 mm.

Width of Cross Section (b) 152.4 mm.

Length of Enlarged End (ld) 203.2 mm.

Height of Enlarged End (hd) 457.2 mm.

Loading Conditions

Eccentricity (e1) 304.8 mm.

Eccentricity (e2) 304.8 mm.

Fig. 4.5 Input window for column dimensions and loading condition

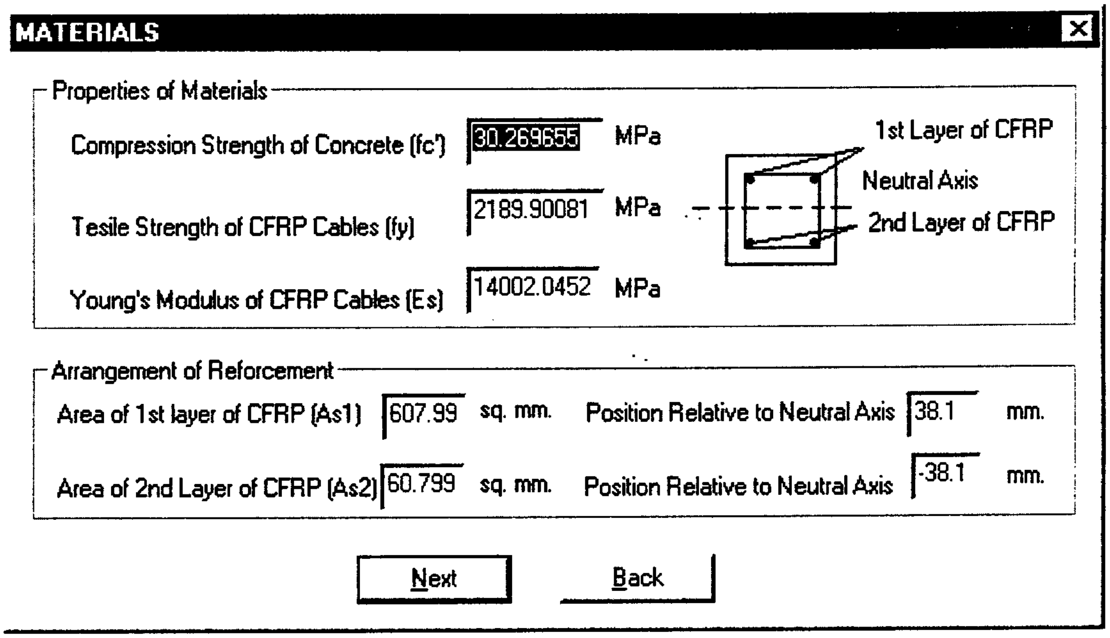
MATERIALS

Properties of Materials

Compression Strength of Concrete (fc') 30.269655 MPa

Tesile Strength of CFRP Cables (fy) 2189.90081 MPa

Young's Modulus of CFRP Cables (Es) 14002.0452 MPa

Arrangement of Reforcement

Area of 1st layer of CFRP (As1) 607.99 sq. mm. Position Relative to Neutral Axis 38.1 mm.

Area of 2nd Layer of CFRP (As2) 60.799 sq. mm. Position Relative to Neutral Axis -38.1 mm.

Fig. 4.6 Input window for properties of materials

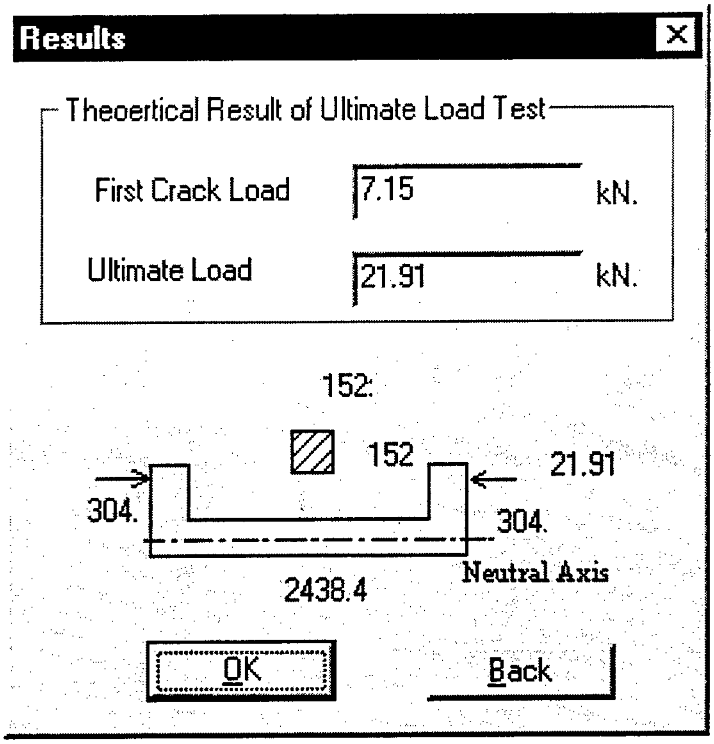

Results

Theoertical Result of Ultimate Load Test

First Crack Load 7.15 kN.

Ultimate Load 21.91 kN.

Fig. 4.7 Results window

4.5 SAMPLE CALCULATION

A typical calculation of nominal axial load and bending moment of a concrete column reinforced with CFRP tendon (CFRP 1 x 7, 7.5 mm ϕ) is presented below. The main parameters including the mechanical properties are as follows:

Effective cross sectional area (A_{FRP})	30.4 mm^2
Tensile strength (fu)	2.19 GPa
Tensile modulus of elasticity(E_{FRP})	140 GPa
Effective depth (d)	114 mm
Cover to compression reinforcement (d_1)	38 mm
Concrete strength (f'_c)	30.23 MPa

Fig. 4.8 shows the interaction diagram of the CFRP-reinforced concrete column.

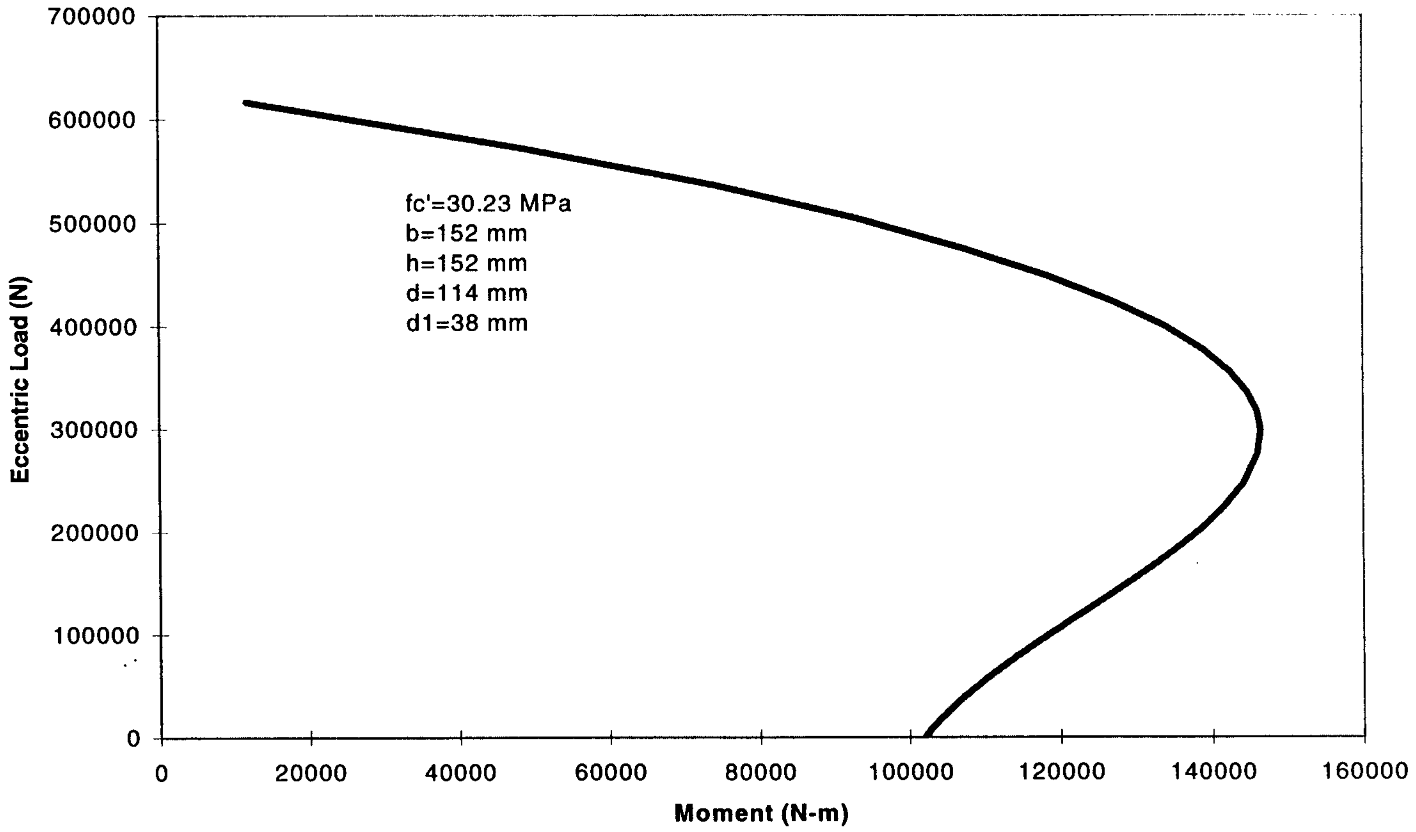

Fig. 4.8 CFRP reinforced concrete column interaction diagram

CHAPTER 5

EXPERIMENTAL STUDIES ON ULTIMATE LOAD BEHAVIOR OF CFRP REINFORCED CONCRETE SLENDER COLUMNS

5.1 INTRODUCTION

Design principles for concrete columns reinforced with CFRP are not yet fully formulated and lately significant research is focused on formulation of design concepts. Many assumptions which are made in designing members with steel reinforcement may not be valid in design of members reinforced with CFRP. This chapter presents the experimental investigation on the ultimate load behavior of the CFRP reinforced concrete slender columns, and comparison of results with the theoretical analysis based on the assumptions and formulations outlined in Chapter 4.

5.2 FABRICATION OF CFRP REINFORCED CONCRETE COLUMNS

Eight CFRP reinforced concrete columns of size approximately 152 mm x 152 mm x 2438 mm were cast in two groups, four columns in each group. In the first group of columns, each column was reinforced with four 7.5 mm diameter longitudinal CFRP bars and #3 steel stirrups (Fig. 5.1). The spacing of the stirrups is 152 mm in the middle (Fig. 5.2) and 76 mm at the ends (Fig. 5.3) of the columns. All the columns were provided with enlarged ends to facilitate application of eccentric load at the ends (Fig.5.3). Two embedded strain gages were attached along the top and bottom of the CFRP cables to monitor the strains (Fig. 5.4). Figs. 5.5 and 5.6 show the CFRP reinforcement arranged in place, the form work and reinforcement placement. Figs. 5.7 and 5.8 show the column during casting and in formwork after casting. The reinforcements of the columns in the second group were similar to those of the first group except for the stirrup size of 102 mm x 102 mm. Standard concrete cylinders were cast at the same time, three with the first group and four with the second. Tables 5.1a, 5.1b and 5.1c summarize the concrete strengths, the dimensions of the test columns and properties of CFRP reinforcement.

Table 5.1a Summary of concrete strengths

	f_c' (MPa) (minimum design strength)	f_c' (MPa) (actual strength after 28 days)
First set (Set I)	27.58	30.23
Second set (Set II)	34.49	42.76

Table 5.1b Dimensions of the CFRP reinforced concrete columns

Column #	f_c' (MPa)	b (mm)	h (mm)	d (mm)	d_l (mm)	e (mm)
1	30.23	152	152	109	44	305
2	30.23	152	154	95	31	127
3	30.23	152	149	87	40	66
4	30.23	149	149	106	38	33
5	42.76	152	156	117	41	305
6	42.76	152	152	119	46	124.5
7	42.76	152	152	110	37	63.5
8	42.76	152	152	114	38	38.1

Note: f_c' = concrete strength based on 28 days standard cylinder test

b = width of the column; h = height of the column;

d = effective depth of CFRP reinforcement; e = loading eccentricity;

d_l = the depth to the CFRP reinforcement in compression zone

Table 5.1c Properties of the carbon FRP bars

Item	Property	
Carbon fiber	Tensile strength	2110 MPa
	Tensile modulus	137 GPa
	Elongation at break	1.50%
Matrix resin	Type of resin	Denaturated epoxy resin
	Tensile strength	51.5 MPa
	Elongation at break	4.20%
Carbon FRP reinforcement	Diameter of the rod	7.5 mm (0.3 in.)
	Effective cross sectional area	30.4 mm2 (0.0477 in.2)
	Modulus of elasticity	137 GPa (19.9 x 103 ksi.)

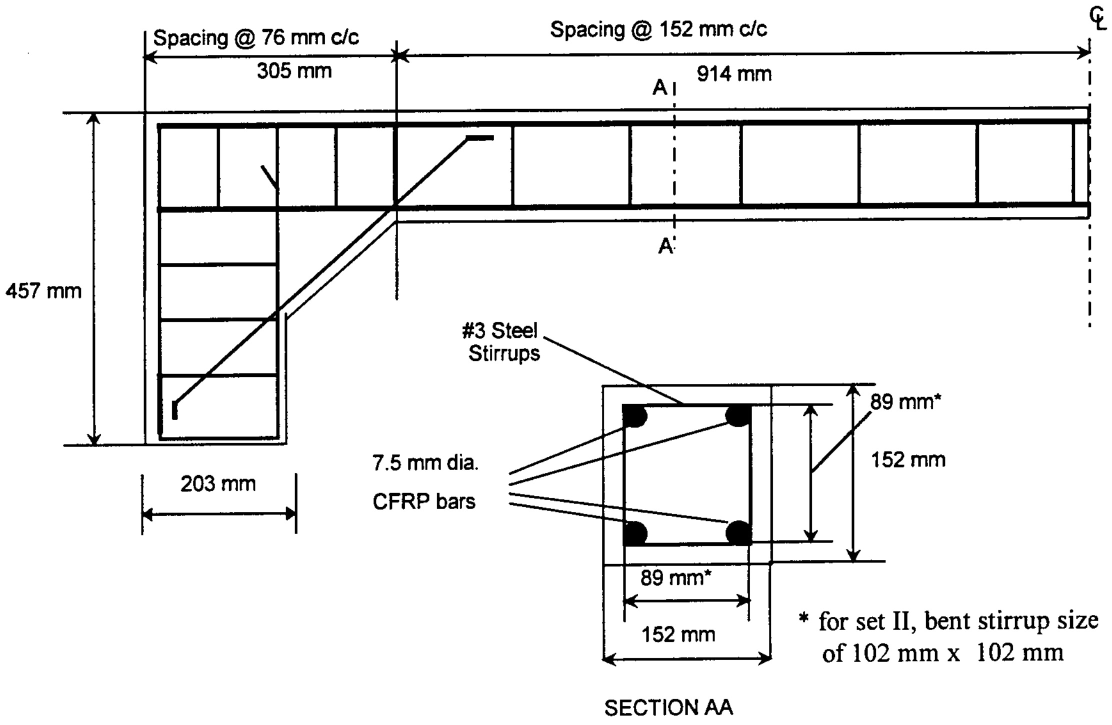

Fig. 5.1 Reinforcement details of concrete columns (Sets I and II) – Table 5.1.b

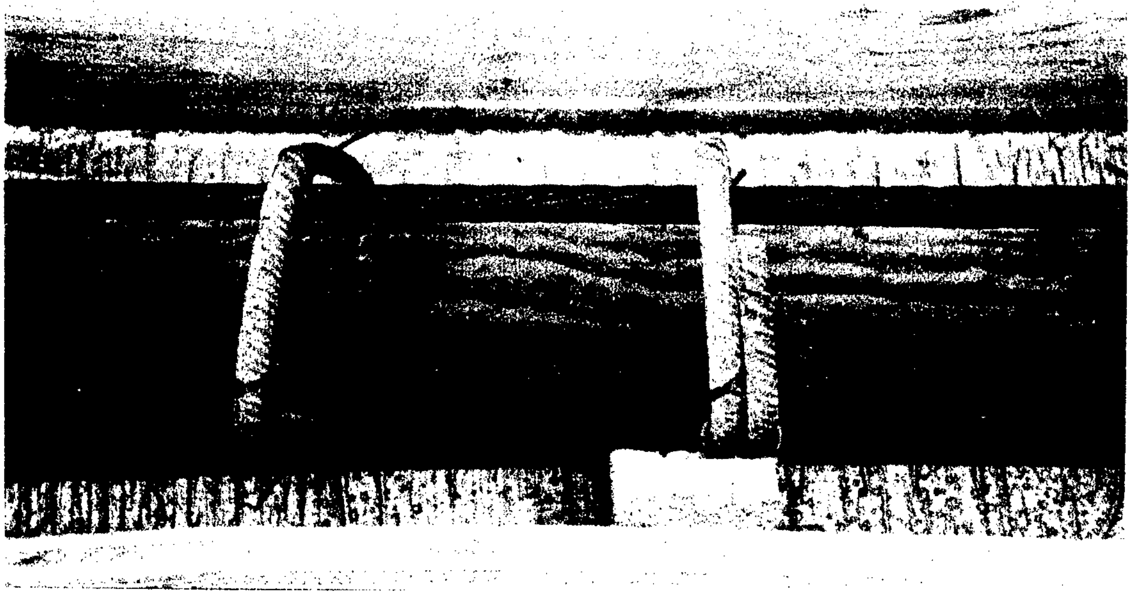

Fig. 5.2 Details of reinforcement at the mid-portion of the columns

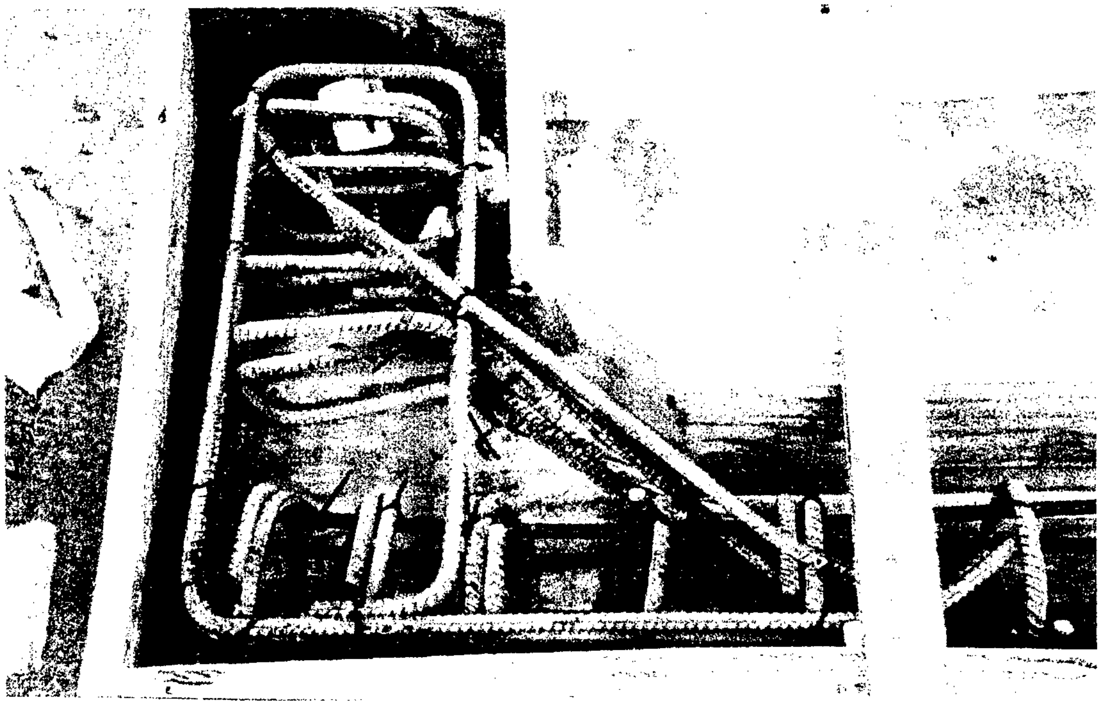

Fig. 5.3 Details of reinforcement at the enlarged ends of the columns

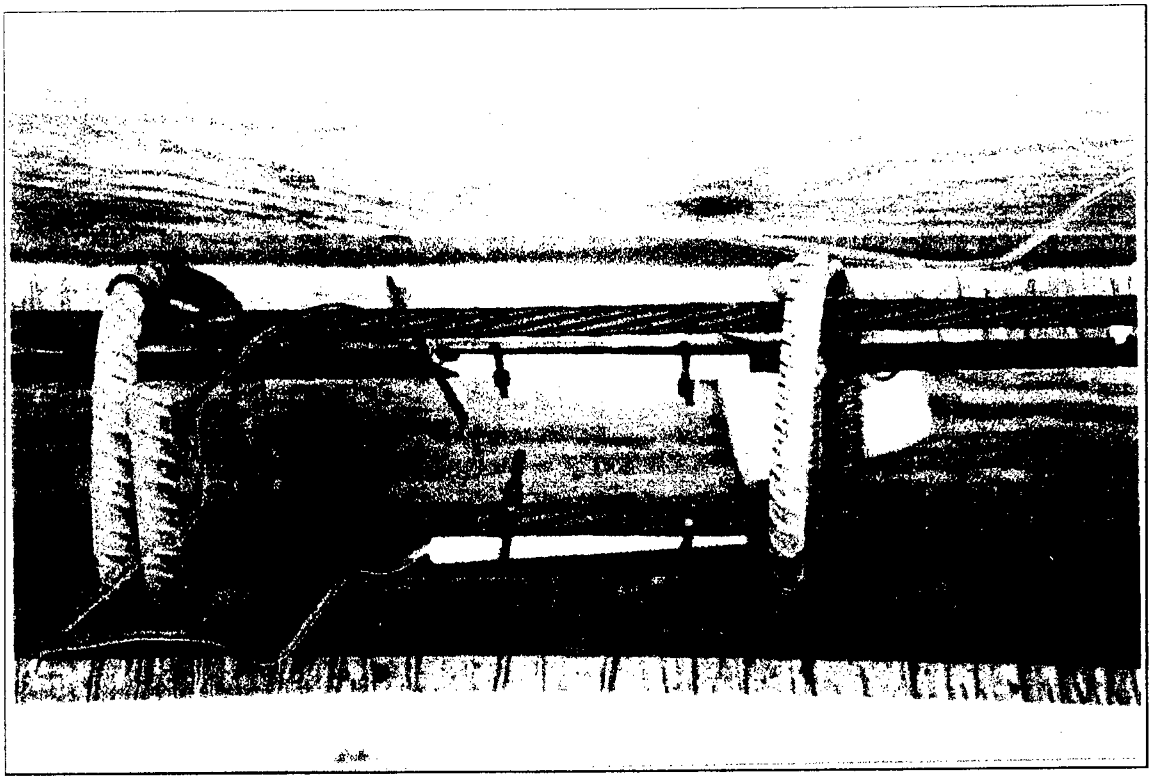

Fig. 5.4 Strain gages embedded along the top and bottom of the CFRP reinforcement

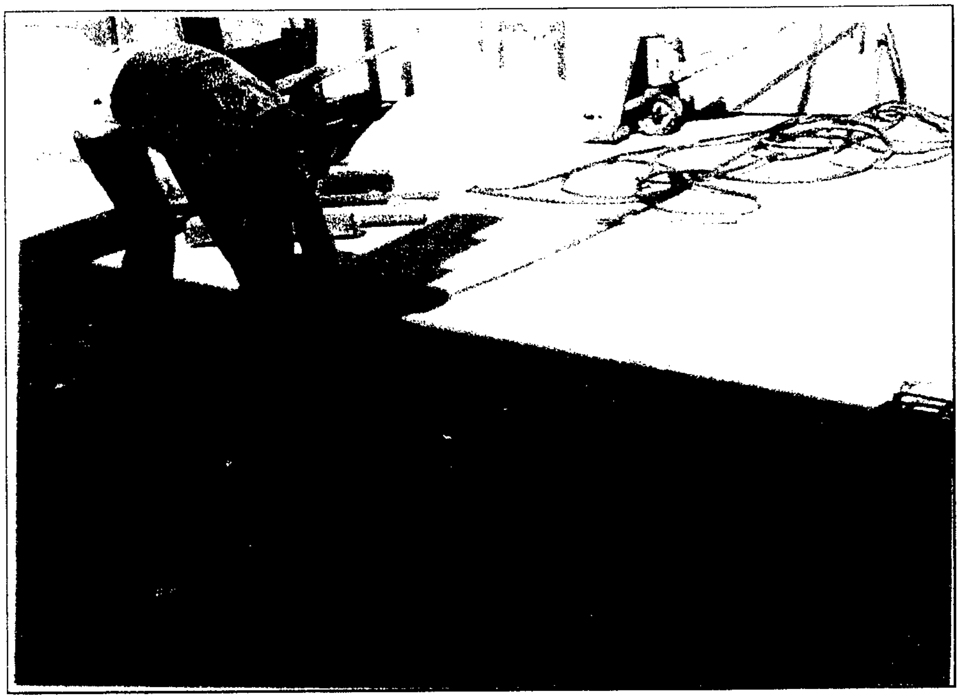

Fig. 5.5 Reinforcement details

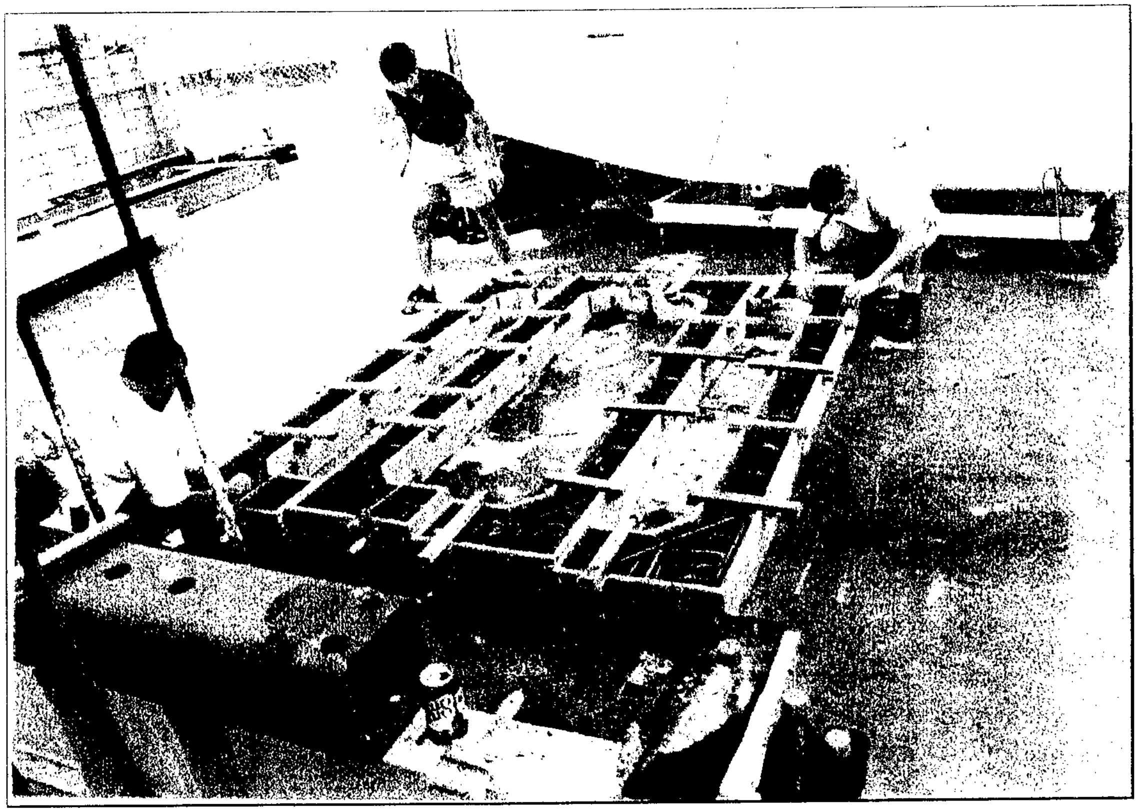

Fig. 5.6 Preparing the formwork and reinforcement

Fig. 5.7 Concrete casting of the columns

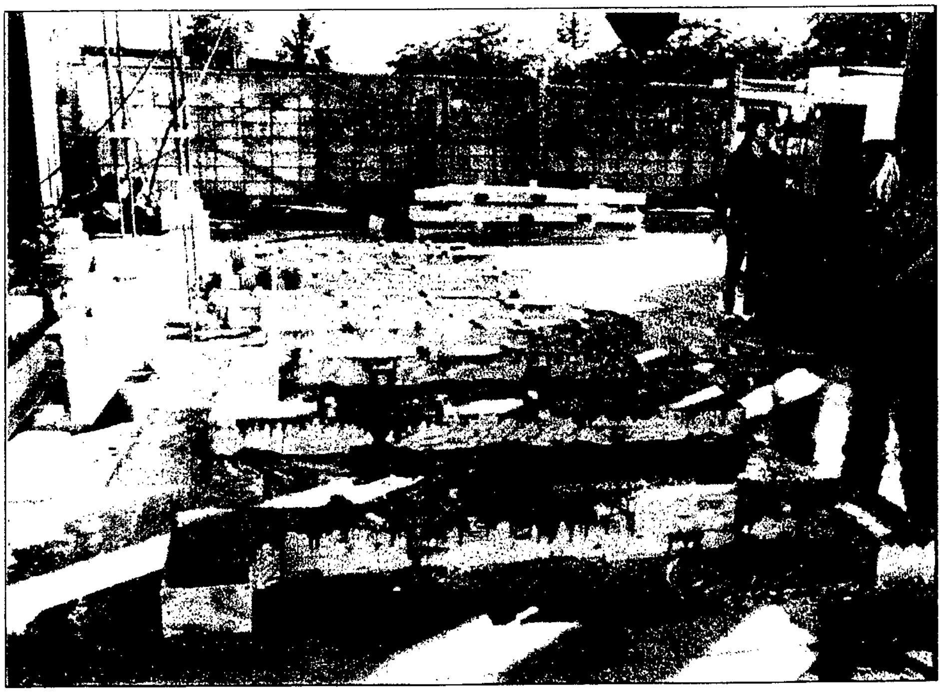

Fig. 5.8 Columns in formwork after casting

5.3 COLUMN INSTRUMENTATION AND TEST SETUP

Columns were instrumented with surface and embedment strain gages and digital micrometer gages to monitor the strain changes during the test (Fig. 5.9). At the compression zone, one surface strain gage was attached at the quarter span of the columns. Three surface strain gages were mounted at the mid-span about 25 mm and 51 mm from the compression face (Fig. 5.10). One micrometer gage was set at the quarter span of the columns in the tension zone. Three micrometer gages were installed at the mid-span about 25 mm and 51 mm from the tension face. Deflectometer was positioned at the mid-span of the column to measure the lateral deflection during the test (Fig. 5.11). The load cell was positioned between the hydraulic jack and the end of the column to measure the axial loads (Fig. 5.12).The readings from the load cell were compared with those form the pressure gage. The embedded strain gages, surface strain gages and the load cell were connected to data acquisition System 4000 to record the data (Fig. 5.13).

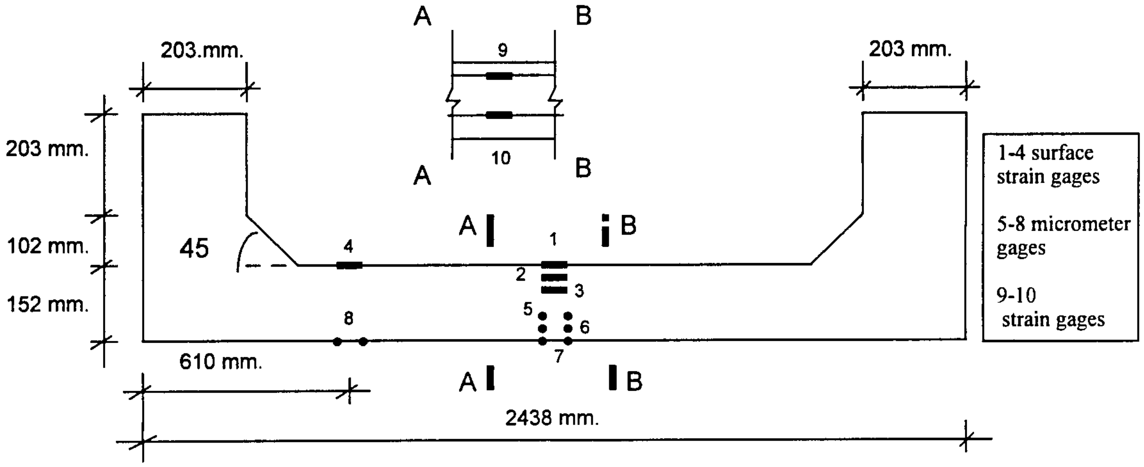

Fig. 5.9 Typical arrangement of strain gages in the column

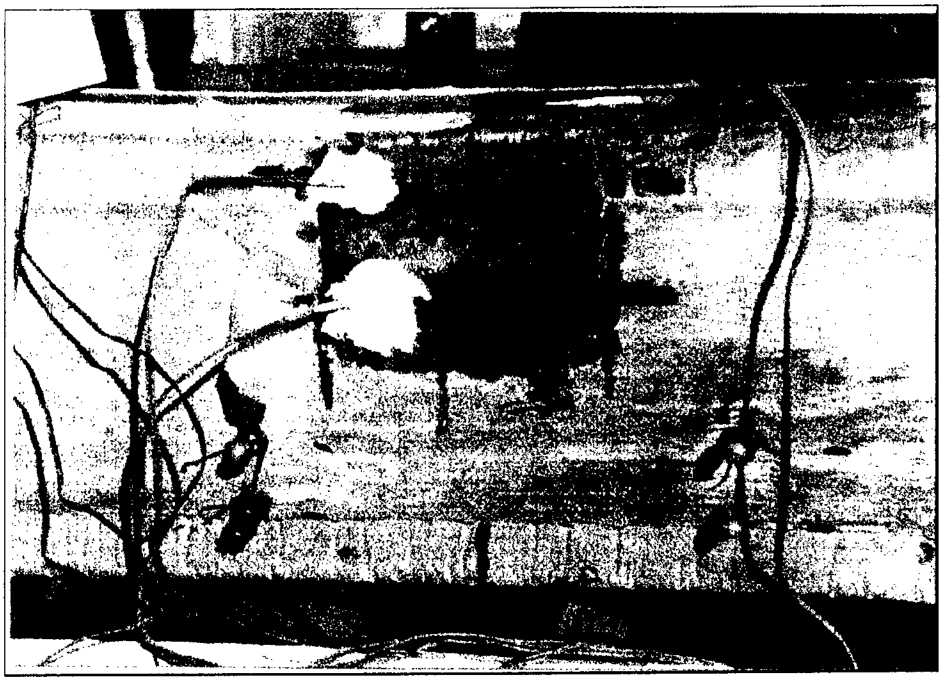

Fig. 5.10 Surface strain gages / micrometer gages mounted on the column

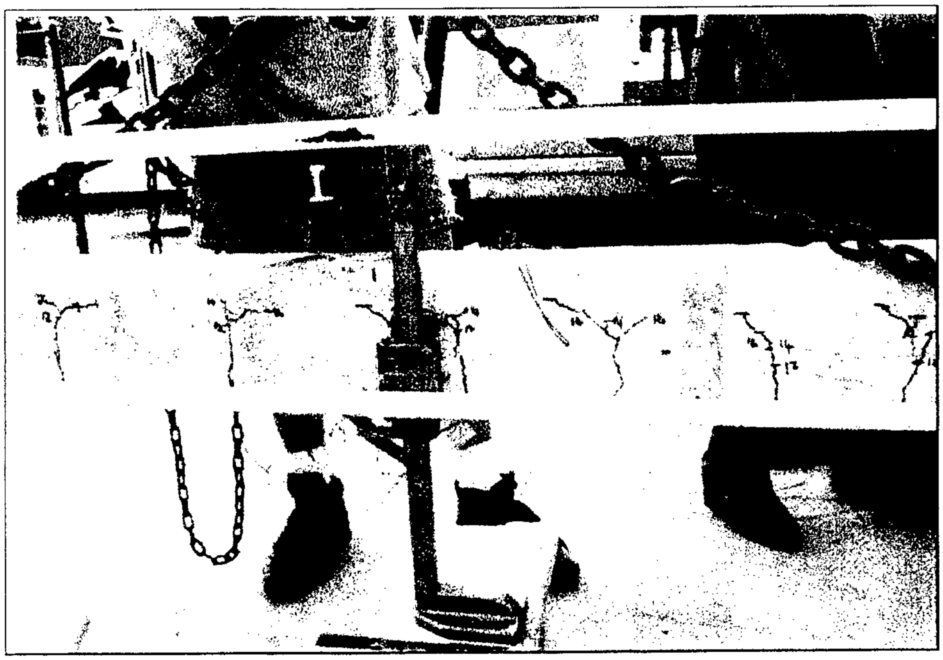

Fig. 5.11 Deflectometer at the mid-span of column

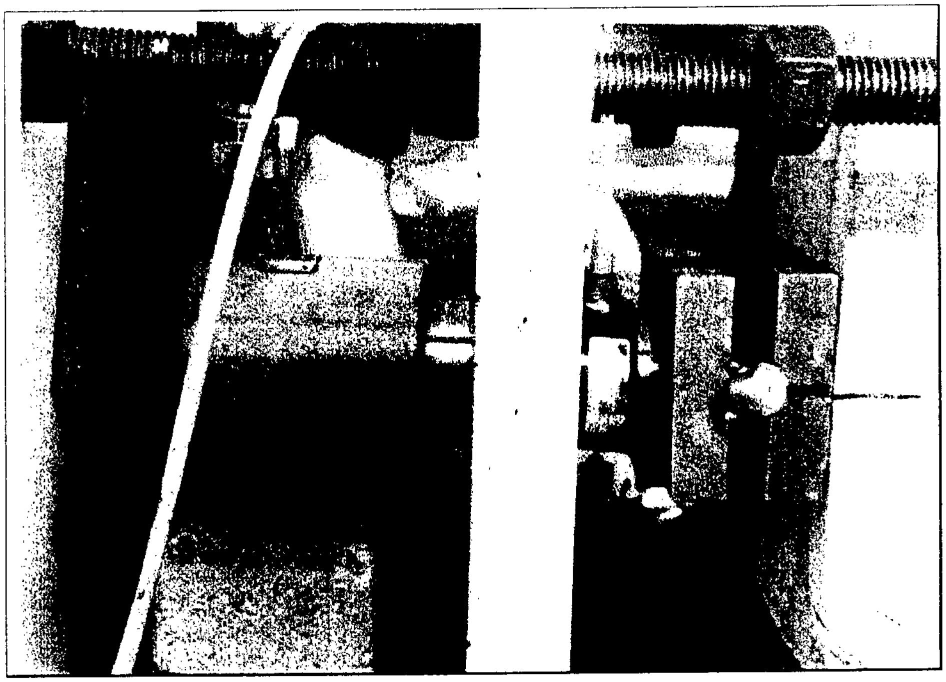

Fig. 5.12 Load cell mounted at the end of column

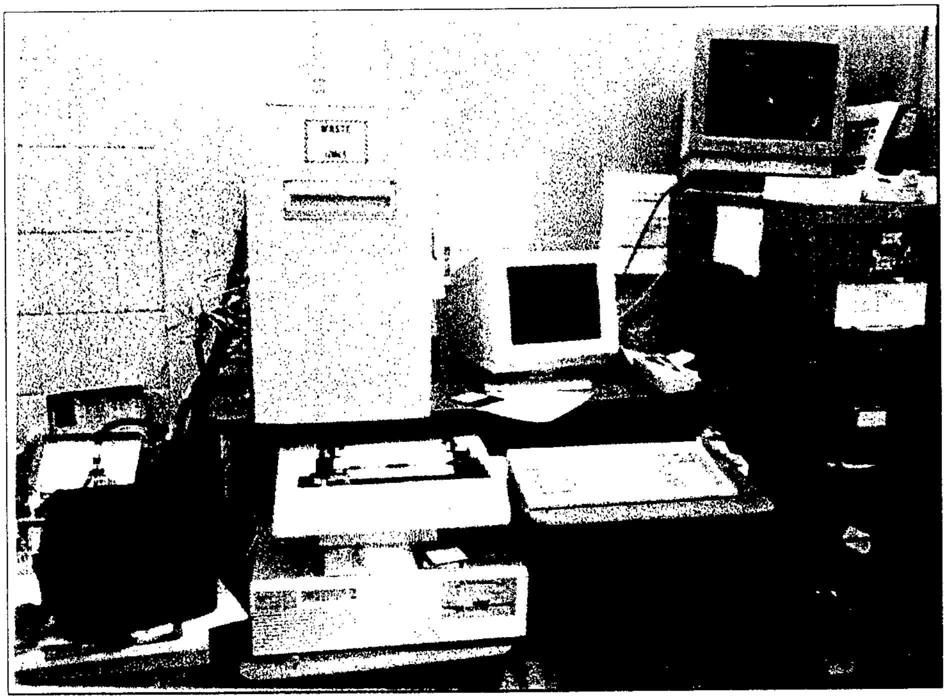

Fig. 5.13 System 4000 for data acquisition

A steel reaction frame was fabricated using three thick steel plates connected by four steel rods as shown in Fig. 5.14. The columns were tested horizontally in the steel reaction frame (Fig. 5.15). The ends of the column were provided with steel pinned supports to allow free rotation (Fig 5.16).

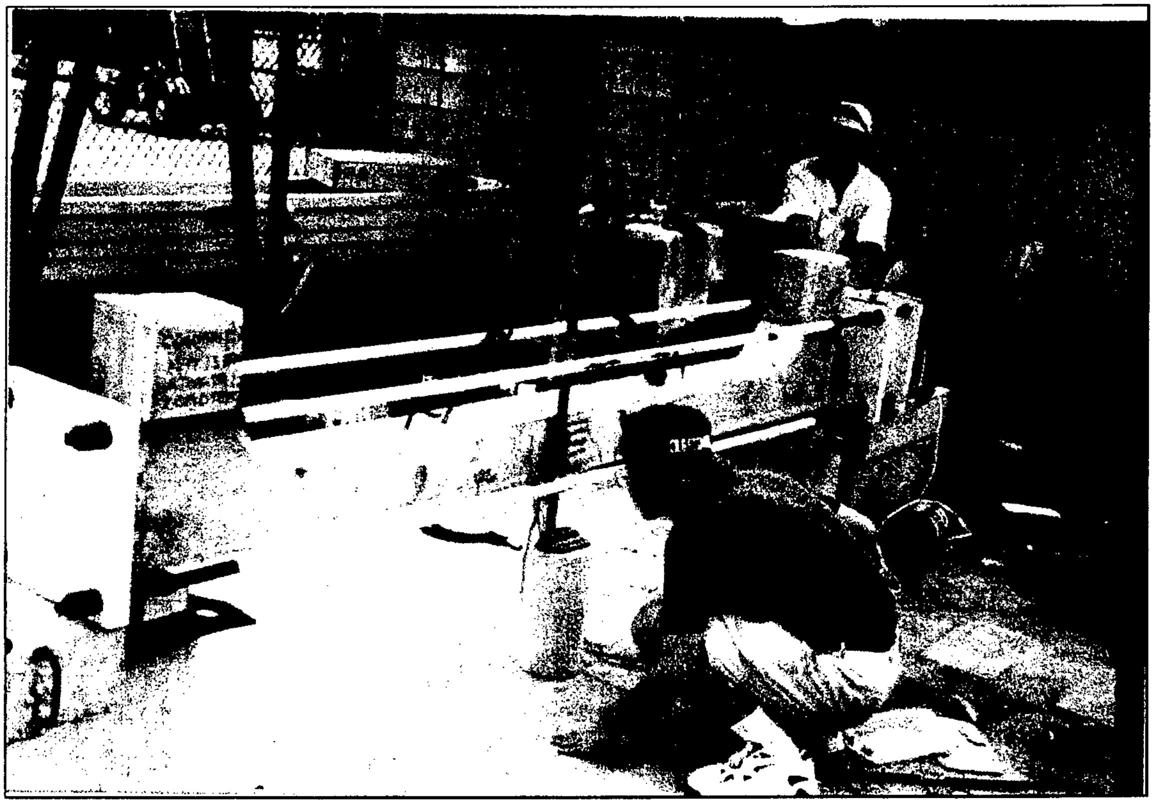

Fig. 5.14 Overview of the steel reaction frame

Fig. 5.15 Positioning the column

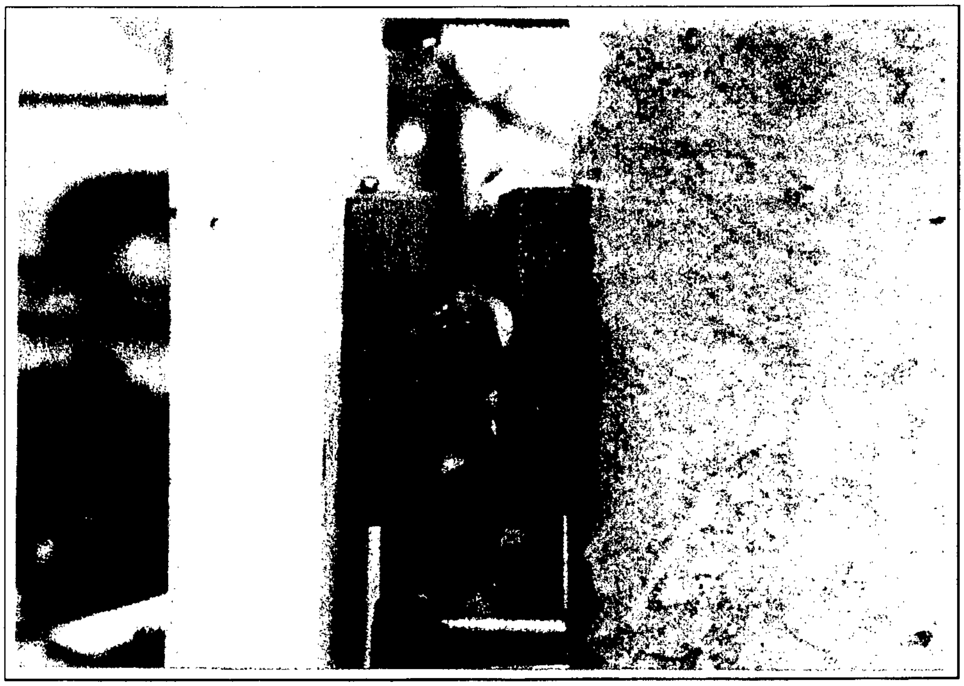

Fig. 5.16 Pin supports at the column ends

5.4 TEST PROCEDURE

For the first set of columns, the loads were applied with varying eccentricities of 305 mm, 127 mm, 66 mm and 33 mm (Table 5.1b). The loads were applied in increments ranging from 2.22 to 8.90 kN until failure. The strains, deflections and loads were recorded for each load increment (Fig. 5.17). Throughout the tests, the cracks on the columns were carefully monitored and marked until failure (Fig. 5.18).

For the second set of columns, the test setup was modified to enhance the accuracy of measurements. Simple supports were provided at the column ends to support the selfweight of the column. The loads were applied with varying eccentricities of 305 mm, 124.5 mm, 63.5 mm and 38.1 mm (Table 5.1b).

5.5 EXPERIMENTAL RESULTS AND DISCUSSIONS

5.5.1 Strain variations along the column depth

The concrete strains were obtained from the micrometer gages, surface strain gages and embedded gages mounted on the CFRP reinforcement. The concrete strains at different load levels for the eight columns are shown in Figs. 5.19-5.26. The strain variations across the column depth were essentially linear. The compressive strains recorded by the strain gages attached to the CFRP reinforcement were comparable to those from the surface gages in the concrete at the level of the reinforcement. However, the tensile strains from the embedded and micrometer gages were less reliable after the first crack.

Fig. 5.17 Recording of micrometer gage readings

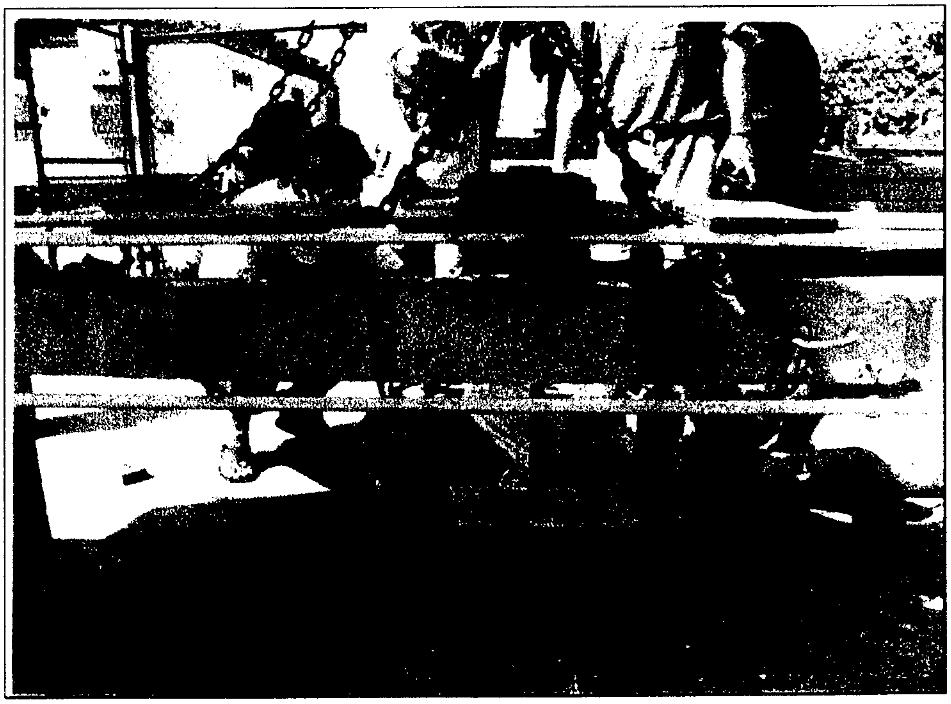

Fig. 5.18 Marking the cracks on the column

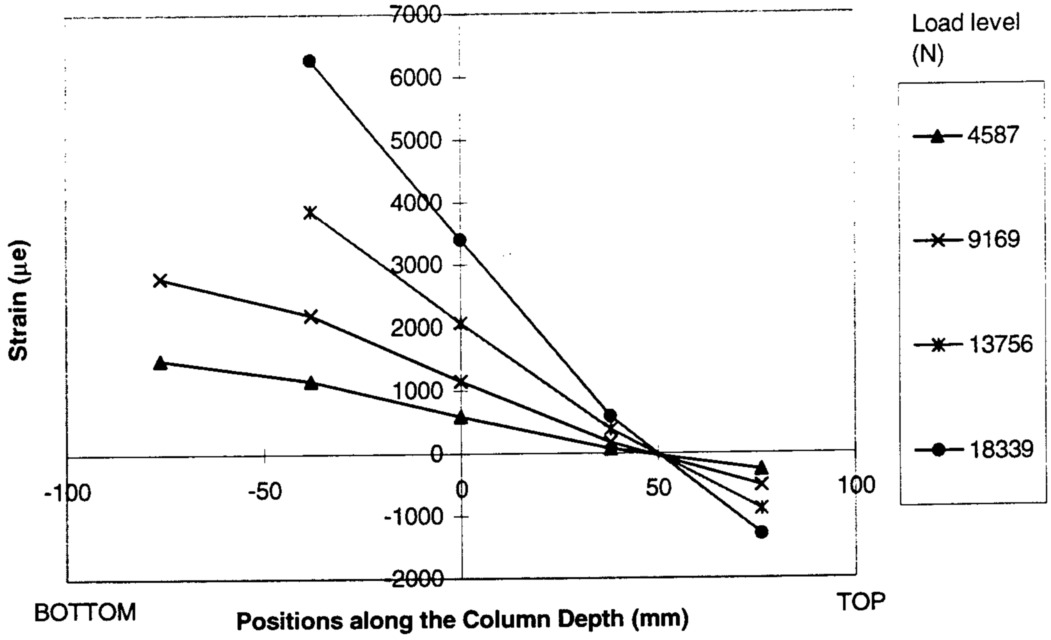

Fig. 5.19 Strain variation along the column depth for column #1 (e=305 mm)

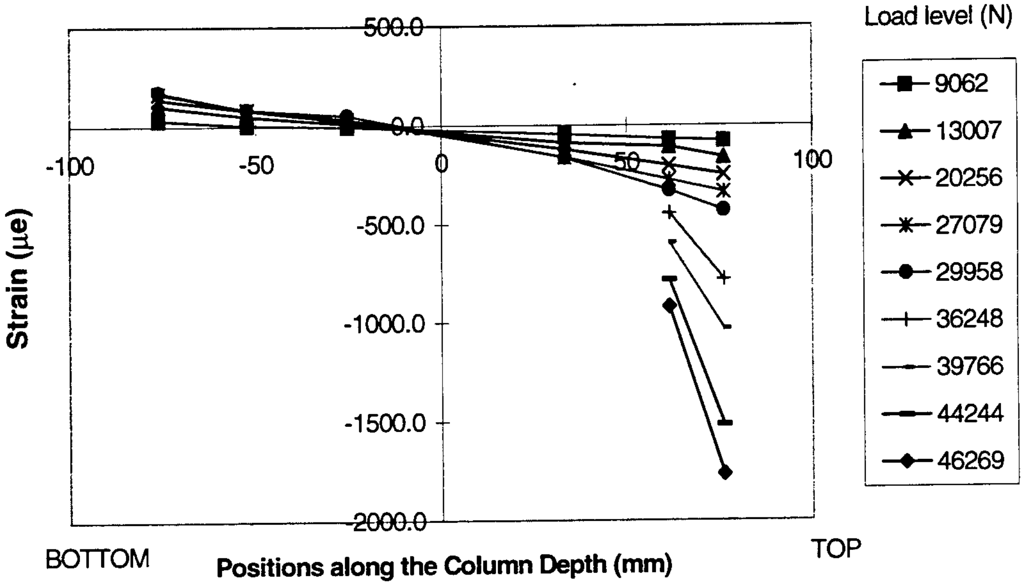

Fig. 5.20 Strain variation along the column depth for column #2 (e=127 mm)

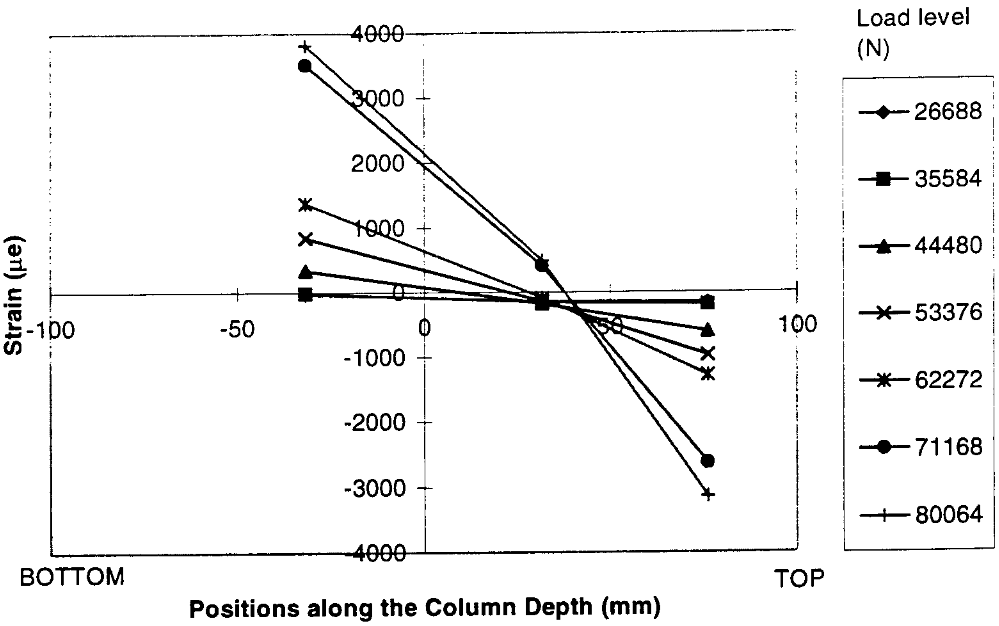

Fig. 5.21 Strain variation along the column depth for column #3 (e=66 mm)

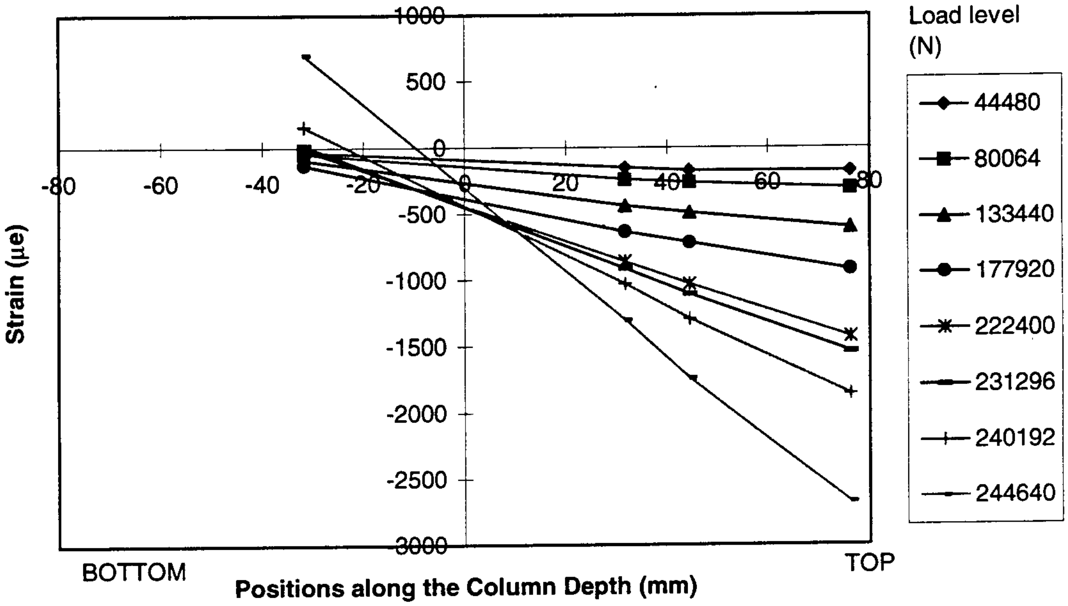

Fig. 5.22 Strain variation along the column depth for column #4 (e=33 mm)

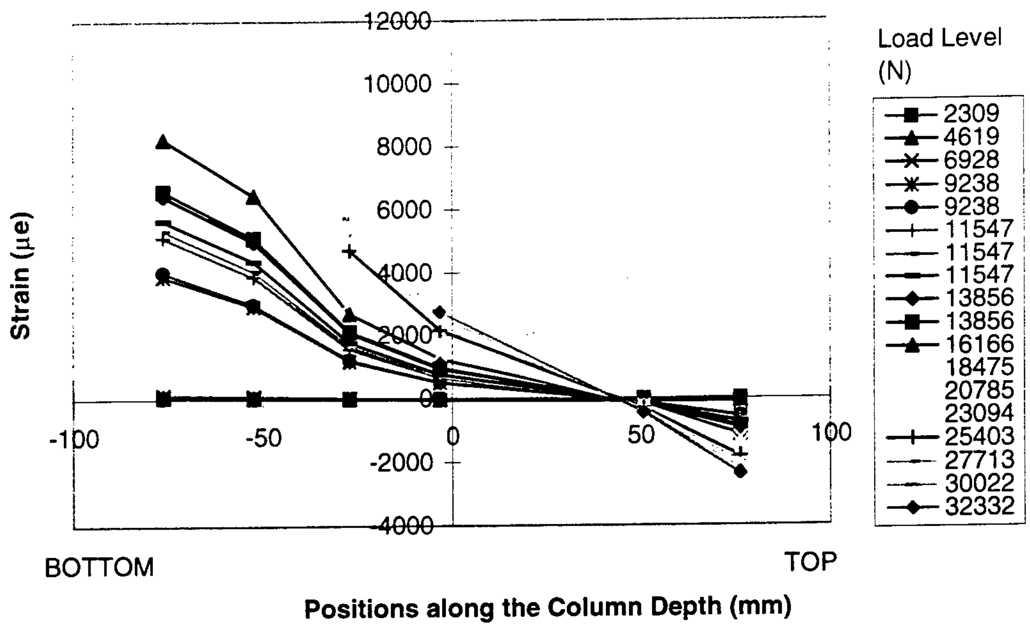

Fig. 5.23 Strain variation along the column depth for column #5 (e=305 mm)

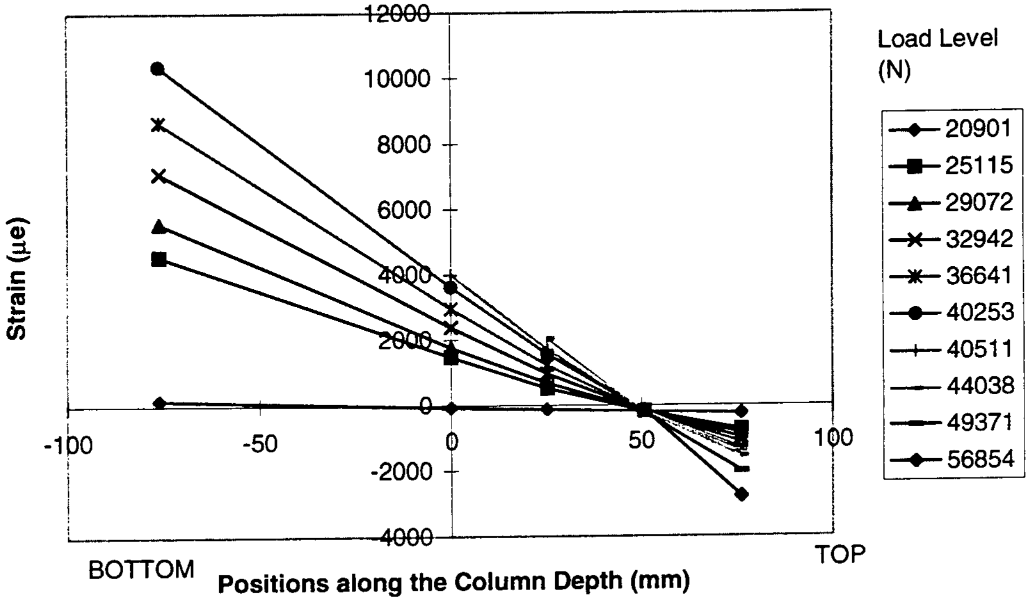

Fig. 5.24 Strain variation along the column depth for column #6 (e=124.5 mm)

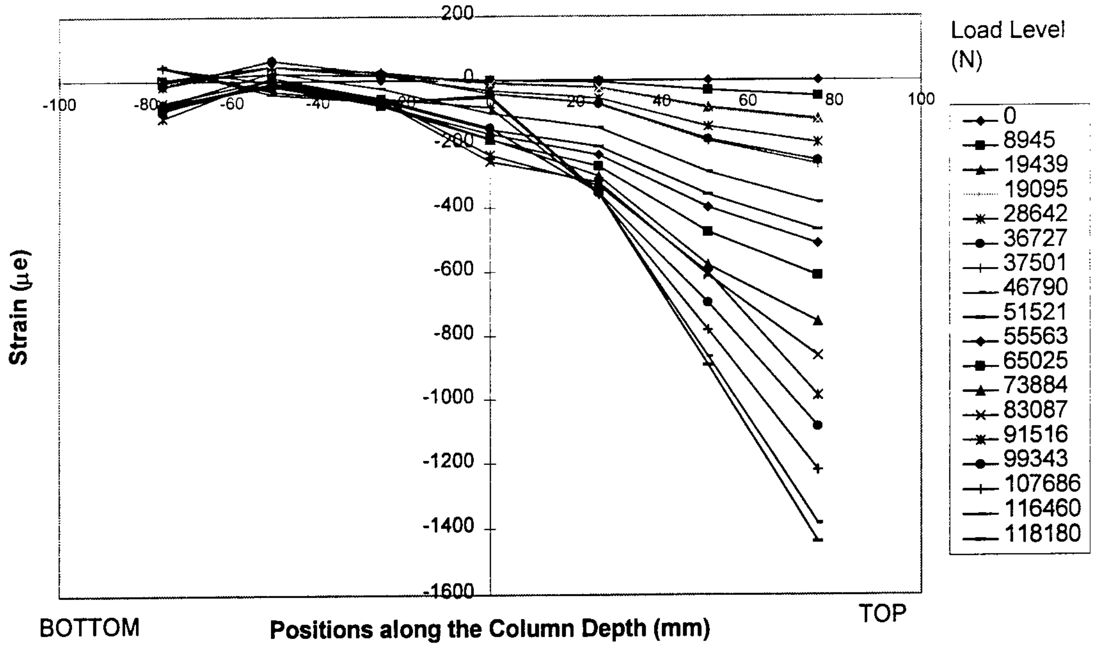

Fig. 5.25 Strain variation along the column depth for column #7 (e=63.5 mm)

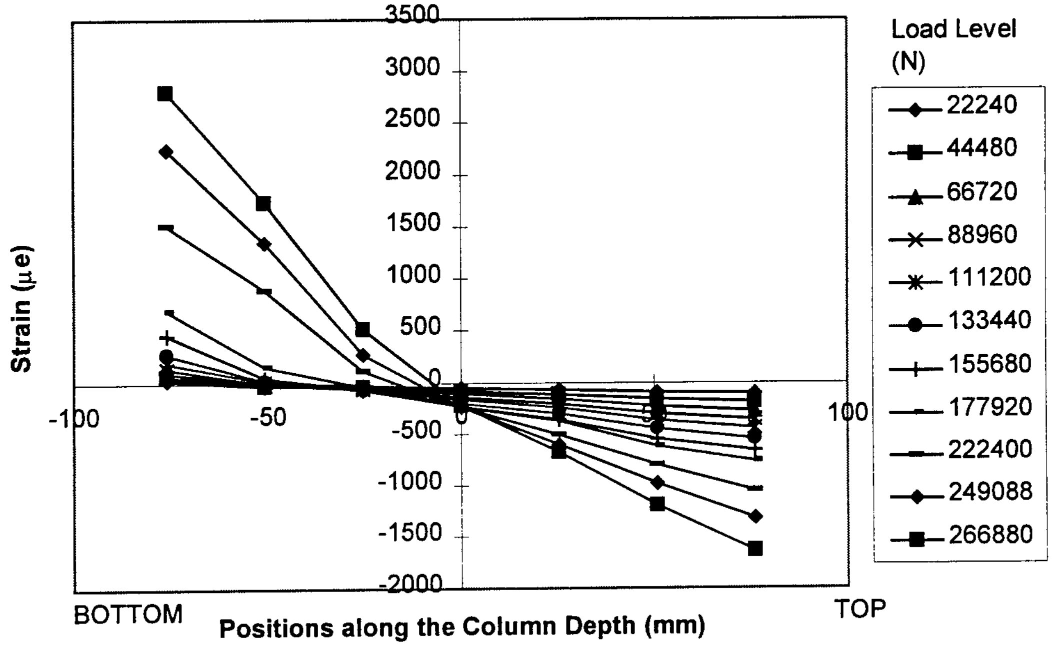

Fig. 5.26 Strain variation along the column depth for column #8 (e=38.1 mm)

5.5.2 Applied load vs. concrete compressive strains

The compressive strains at the top concrete surface increase with increasing applied loads (Figs. 5.29 - 5.36). The compressive strain variation with respect to applied load was linear at the initial stages followed by non-linear behavior with higher loads. The maximum measured concrete strains due to the applied loads is about 3150 micro-strains. But in some cases, the strain recording was stopped before the final failure because of safety considerations. Generally, the maximum measured compressive strains were smaller than the theoretical values. This may be due to the following:

i) The initial deformations due to the self weight of the column were not included in the measured strains.

ii) The applied loads at the column ends were assumed to be symmetric in the theoretical analysis, whereas the crack patterns in the columns #2 and #5 were observed to be unsymmetric.

iii) The columns in the first set (columns #1 to #4) were initially held in position by a pair of ropes until sufficient axial load is applied at column ends to maintain equilibrium (Fig. 5.27). The actual measured deformations in the initial stage were small due to the tension in the rope. It could be observed from Figs. 5.29-5.32 that the slopes of the load compressive strain relationship are relatively larger at initial loads than those observed for subsequent applied loads.

For the second set of columns, pinned supports were used instead of the ropes, which allowed free rotation at the column ends (Fig. 5.28). These supports provided ideal boundary conditions and the measured deformations show better correlation with the theoretical values (Figs. 5.33 - 5.36).

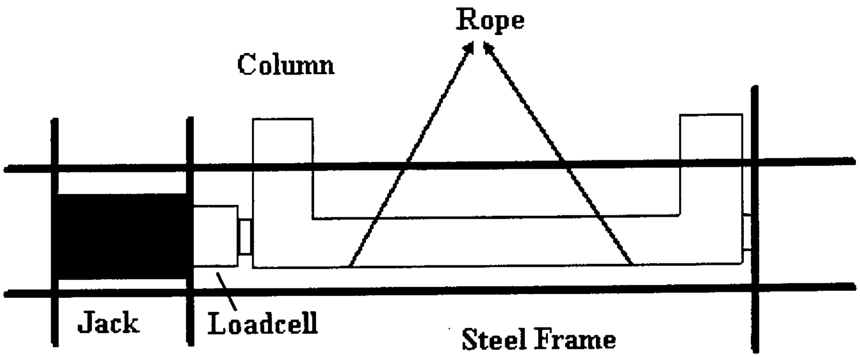

Fig. 5.27 Test setup of column set I

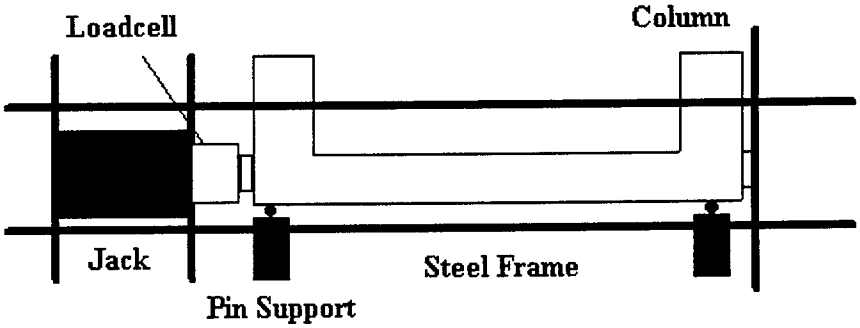

Fig. 5.28 Test setup of column set II

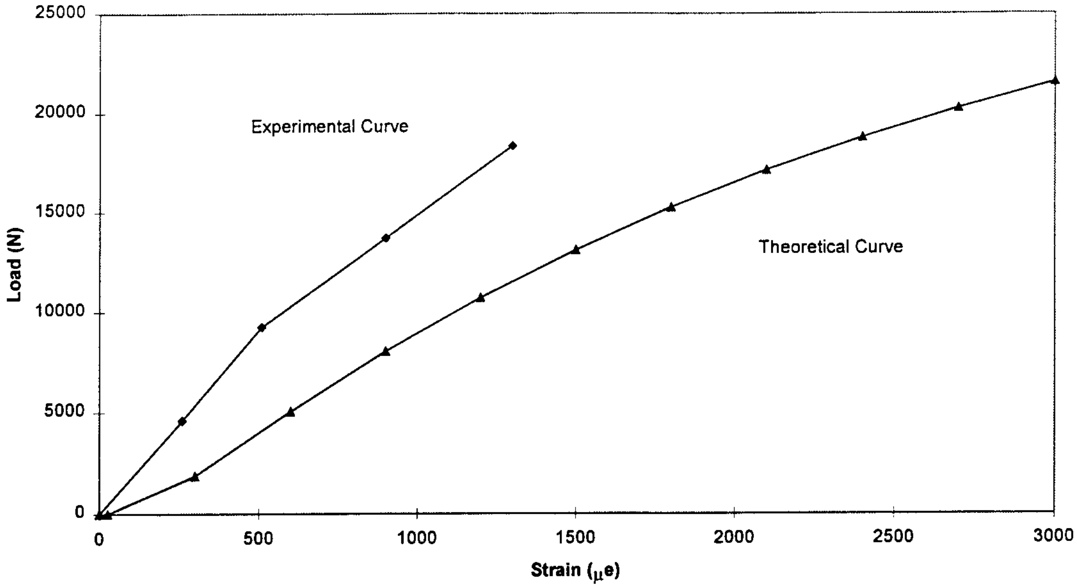

Fig. 5.29 Compressive strains on top surface versus applied loads for column #1 (e = 305 mm)

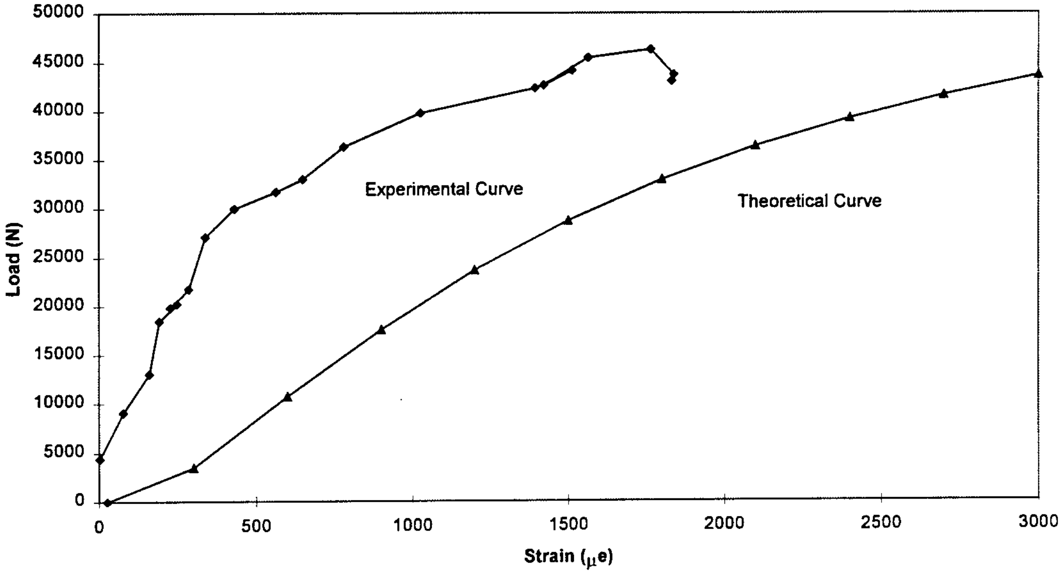

Fig. 5.30 Compressive strains on top surface versus applied loads for column #2 (e = 127 mm)

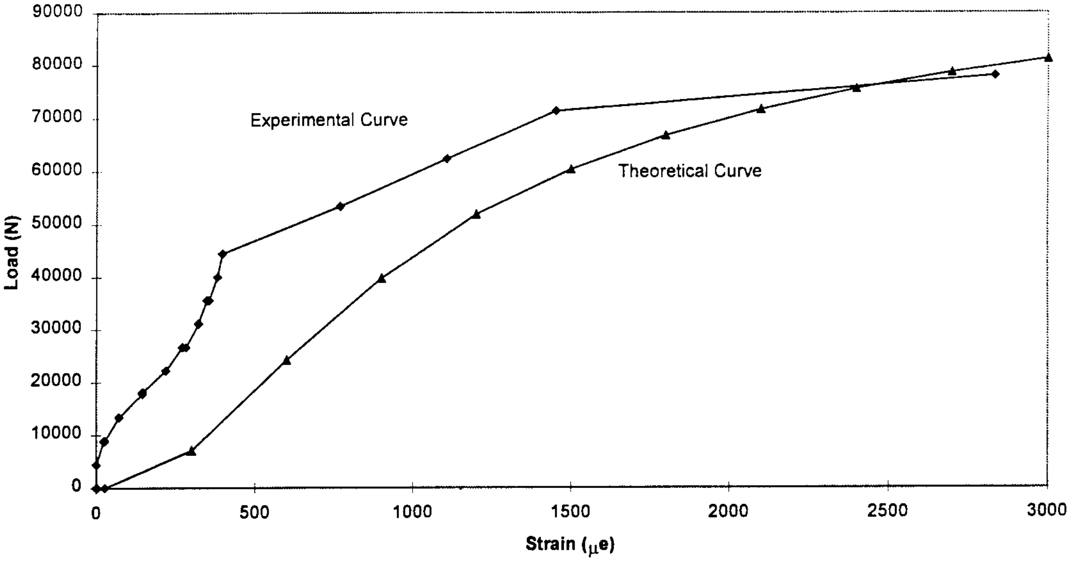

Fig. 5.31 Compressive strains on top surface versus applied loads for column #3 (e=66 mm)

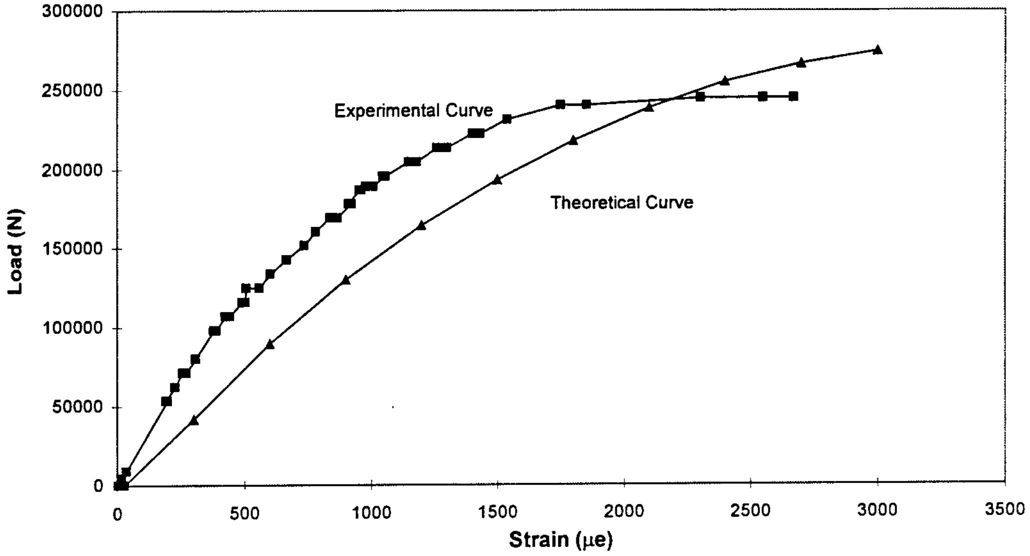

Fig. 5.32 Compressive strains on top surface versus applied loads for column #4 (e = 33 mm)

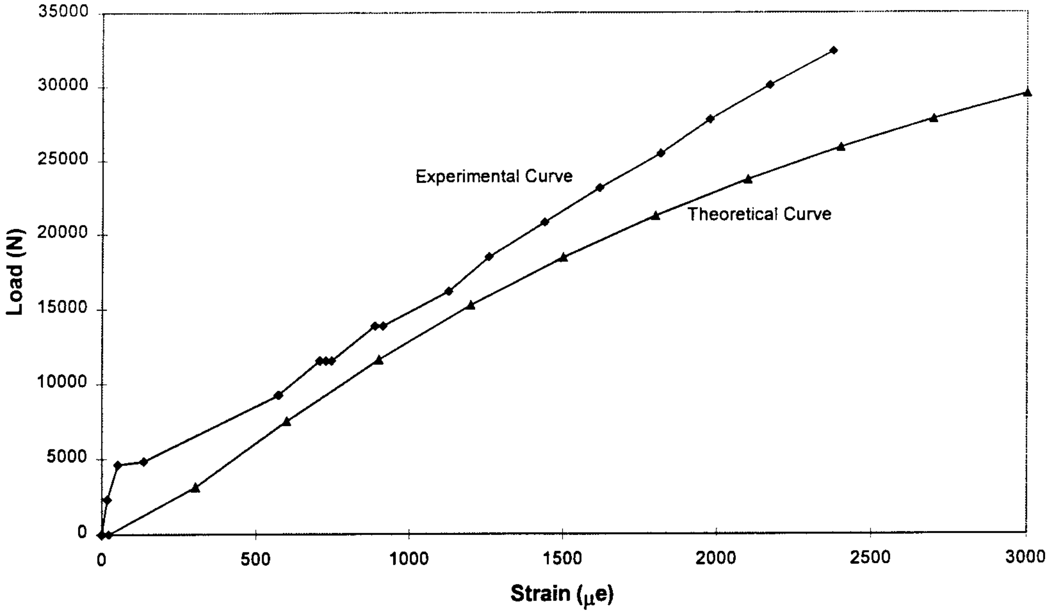

Fig. 5.33 Compressive strains on top surface versus applied loads for column #5 (e = 305 mm)

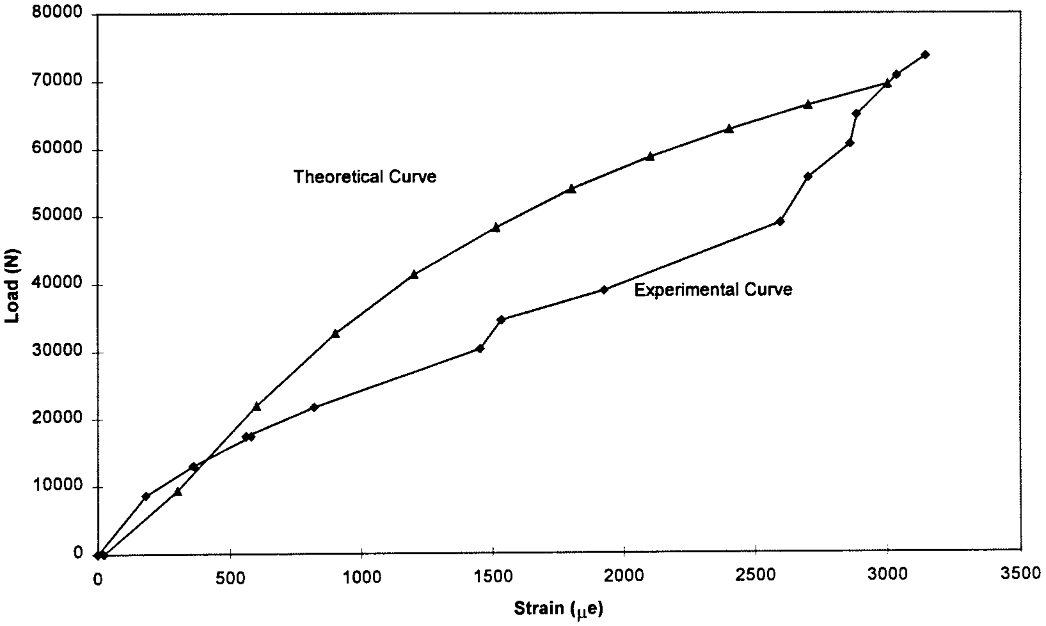

Fig. 5.34 Compressive strains on top surface versus applied loads for column #6 (e = 124.5 mm)

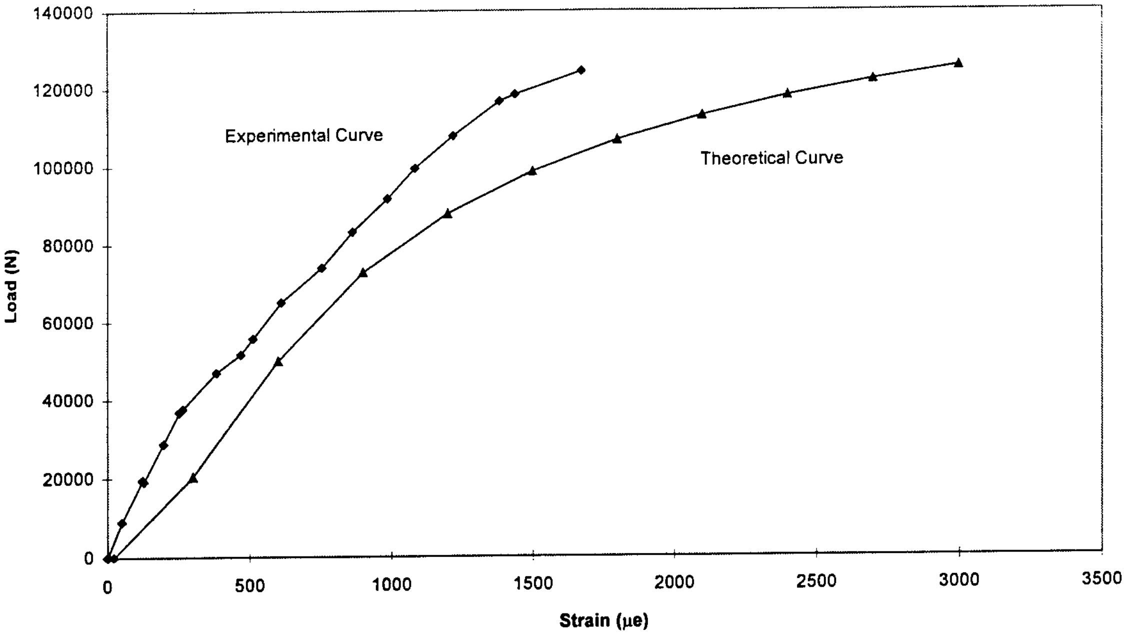

Fig. 5.35 Compressive strains on top surface versus applied loads for column #7 (e = 63.5 mm)

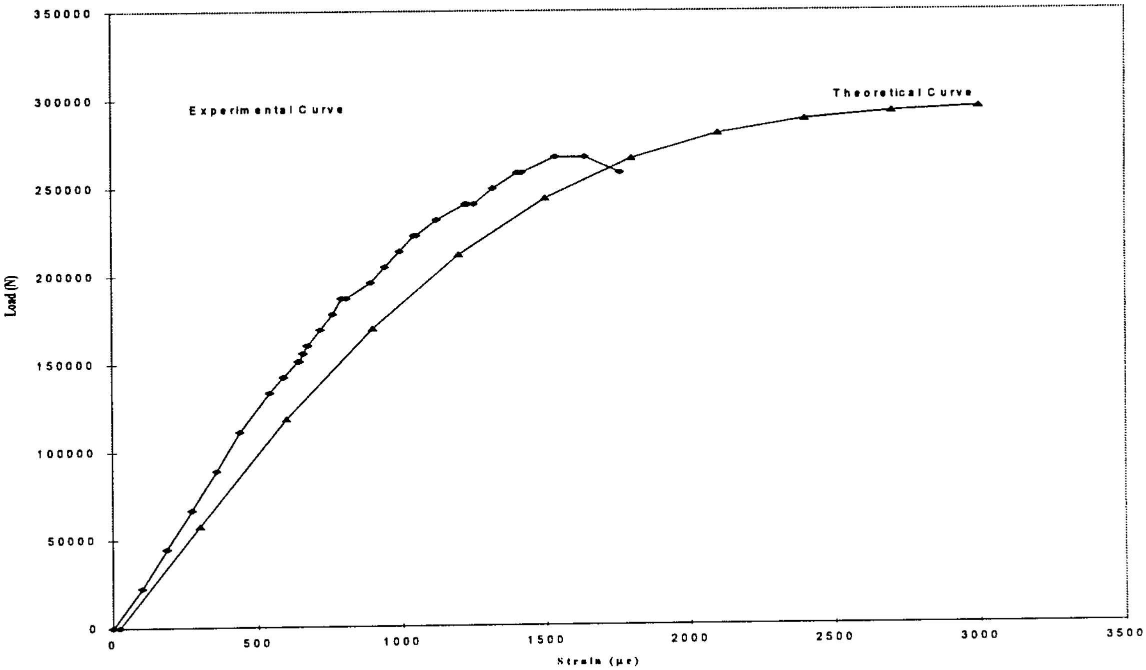

Fig. 5.36 Compressive strains on top surface versus applied loads for column #8 (e = 38.1 mm)

It can be observed from Figs. 5.37 and 5.38 that the slopes of the curves increase as the eccentricity decreases. The relationship of the maximum compressive strain vs. axial load becomes non-linear at relatively large loads for small eccentricities. The slope of load vs. compressive strain for columns having a higher concrete strength (f_c' = 42.76 MPa) is higher than that of columns with a lower concrete strength (f_c' = 30.23 MPa) (Figs. 5.37 and 5.38).

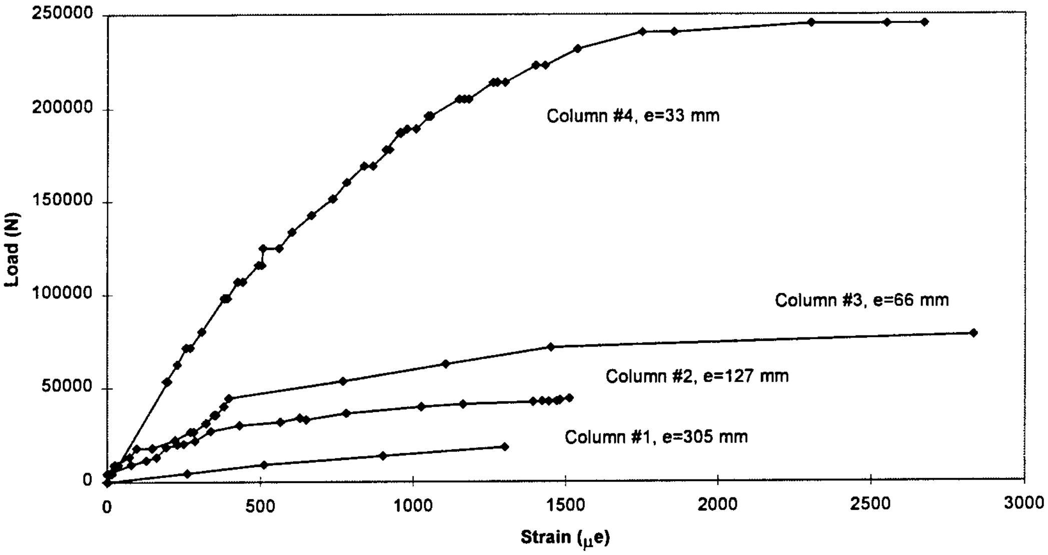

Fig. 5.37 Comparison of maximum compressive strains for different eccentricities for column set I (f_c' = 30.23 MPa)

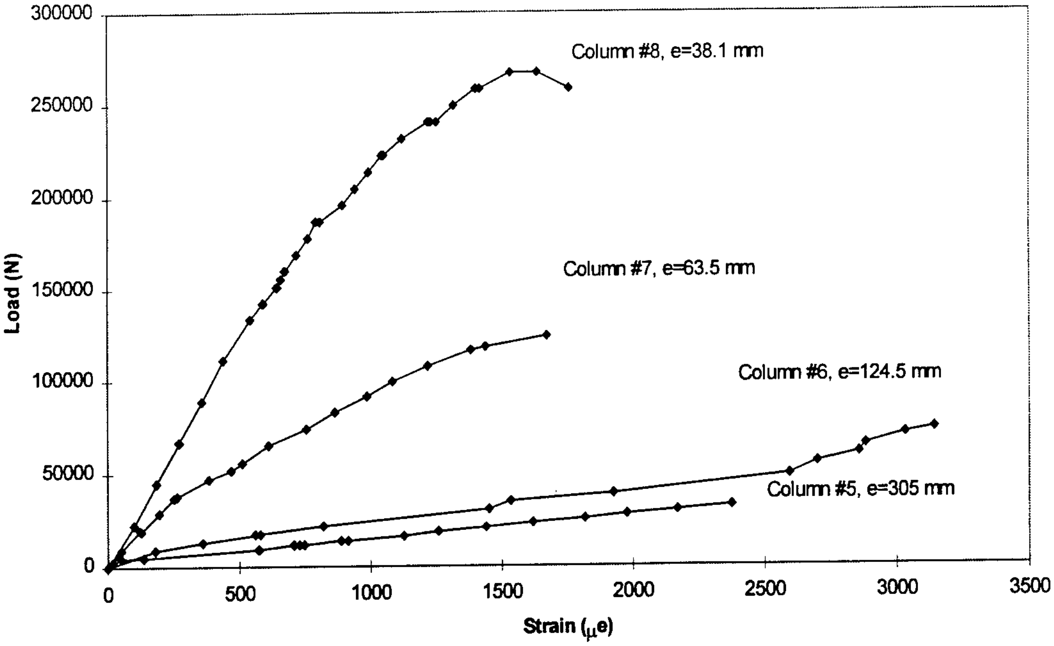

Fig. 5.38 Comparison of maximum compressive strains for different eccentricities for column set II (f_c' =42.76 MPa)

5.5.3 Load - midspan deflection characteristics

Figs. 5.39-5.46 show the load-midspan deflection relationships of the CFRP reinforced concrete columns under eccentric loads. At the first load stage, the load deflection relationship is linear up to the first crack. After the first crack, the columns exhibited larger deformation with smaller slope due to the change in the moment of inertia of the cracked section. The columns exhibited reduced stiffness in each successive load due to the cracks formed in the previous load stage, which contribute to loss of stiffness and the resulting larger deflection. At the post cracking stage, the deflection increased rapidly with very little change in load. Generally, the measured deflections compare reasonably with the analytical values for the second set of columns. For most cases, recording of deflections was stopped before the final column failure due to safety considerations and hence the final deflections at failure are not shown in the graphs.

For the first set of columns, the slopes of the load deflection relationships were steeper in the initial stage prior to releasing the tensions in the supporting rope (Fig. 5.27). The observed deflections are generally larger than theoretical values for the first set of columns. This could be attributed to the use of micrometer deflection gage that required frequent adjustment during the test. However, the observed deflections compare reasonably with the theoretical values for the second set of columns, where deflectometer was used for deflection measurements.

Figs 5.47 and 5.48 show the variation of deflection with load for different eccentricities. The load vs. midspan deflection relationships are very similar to those shown in Figs. 5.37 and 5.38.

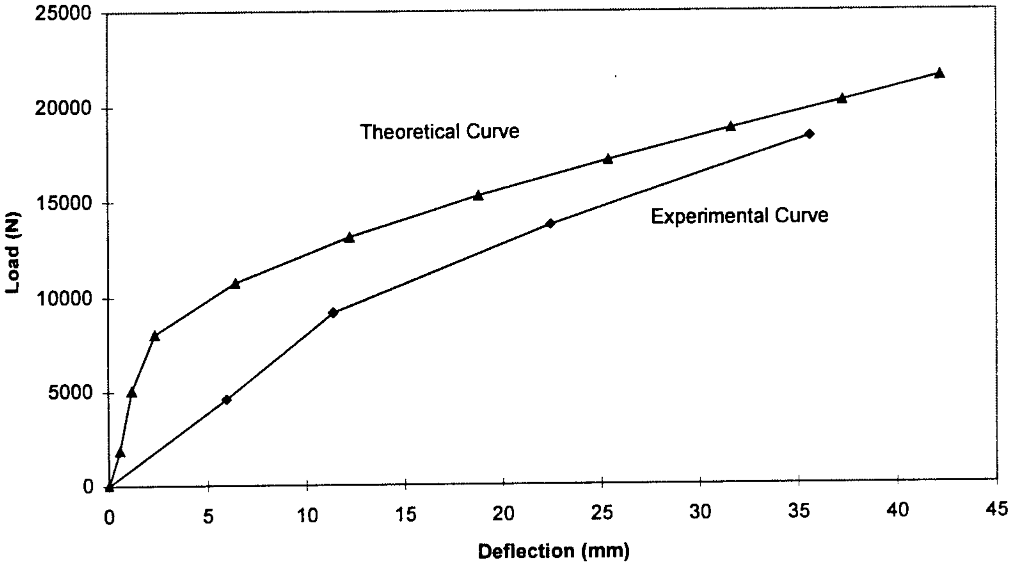

Fig 5.39 Load-midspan deflection relationship for column #1 (e = 305 mm, Set I)

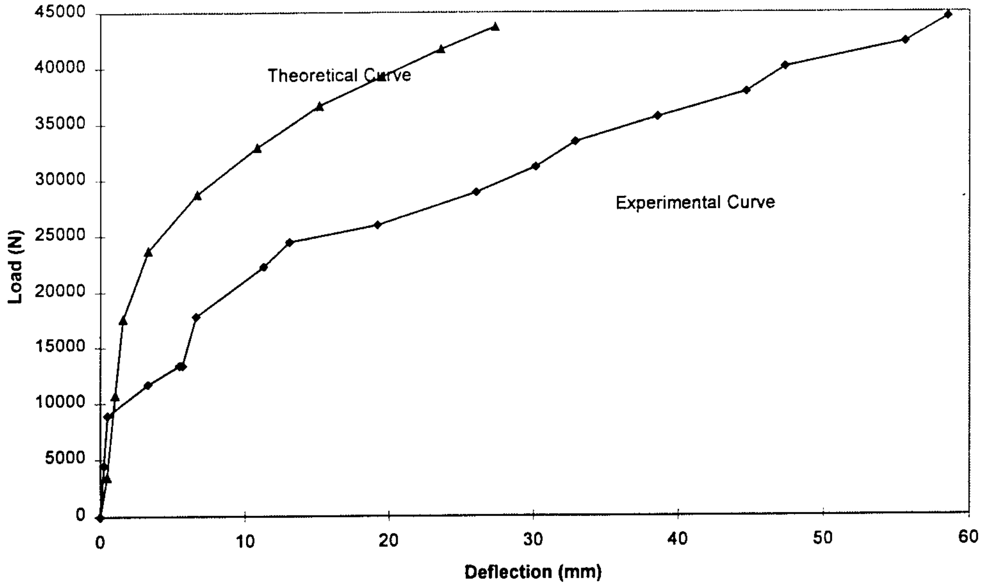

Fig 5.40 Load-midspan deflection relationship for column #2 (e = 127 mm, Set I)

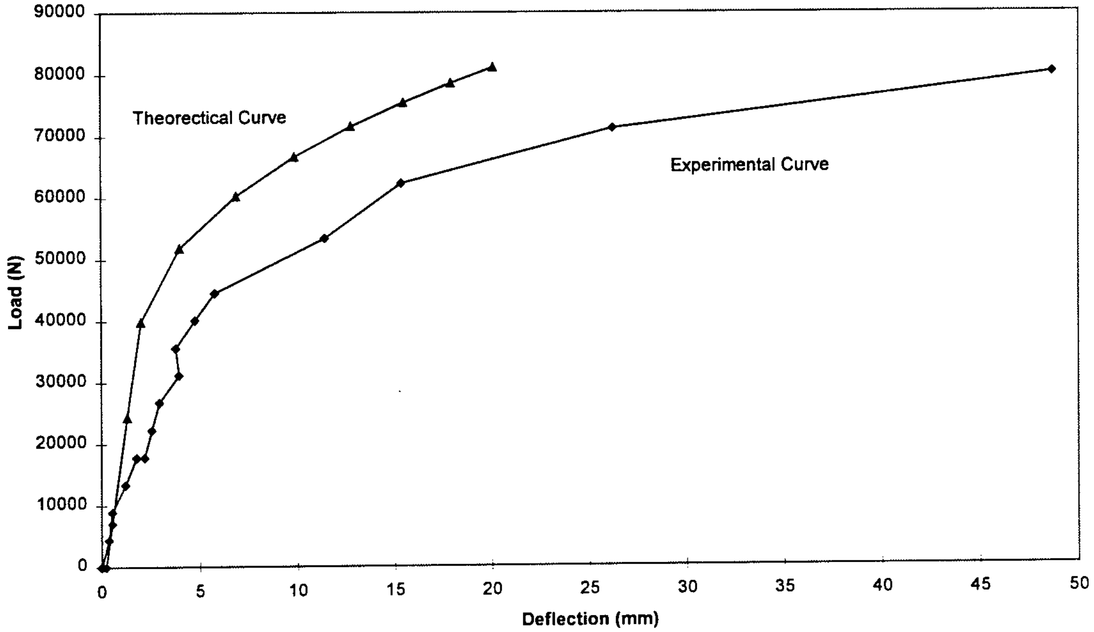

Fig 5.41 Load-midspan deflection relationship for column #3 (e = 66 mm, Set I)

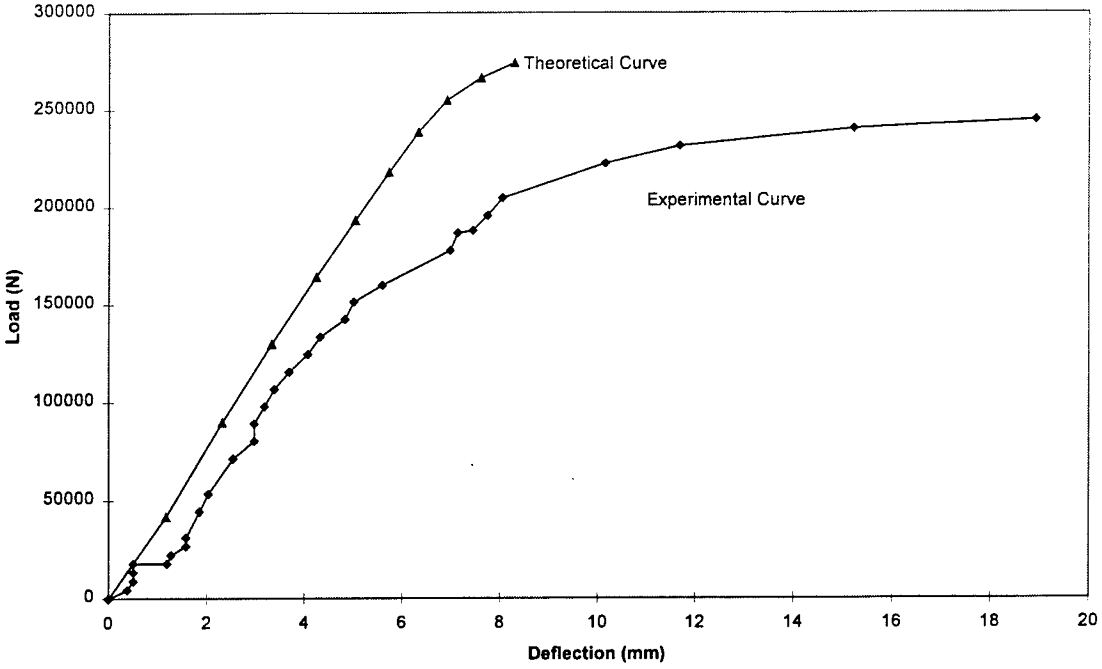

Fig 5.42 Load-midspan deflection relationship for column #4 (e =33 mm, Set I)

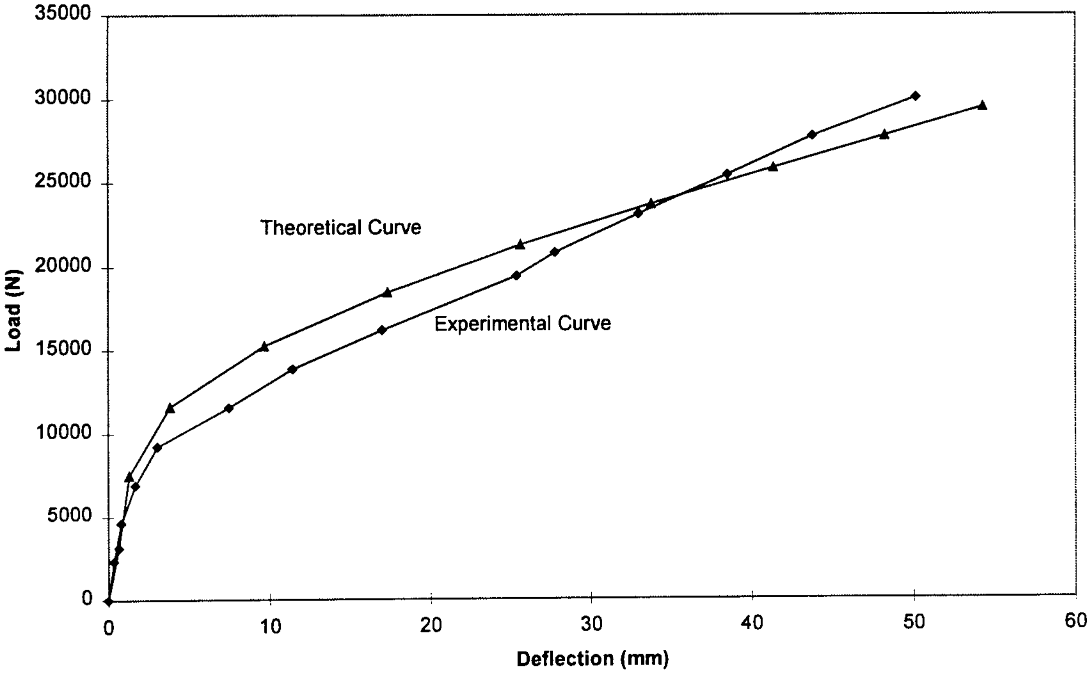

Fig 5.43 Load-midspan deflection relationship for column #5 (e = 305 mm, Set II)

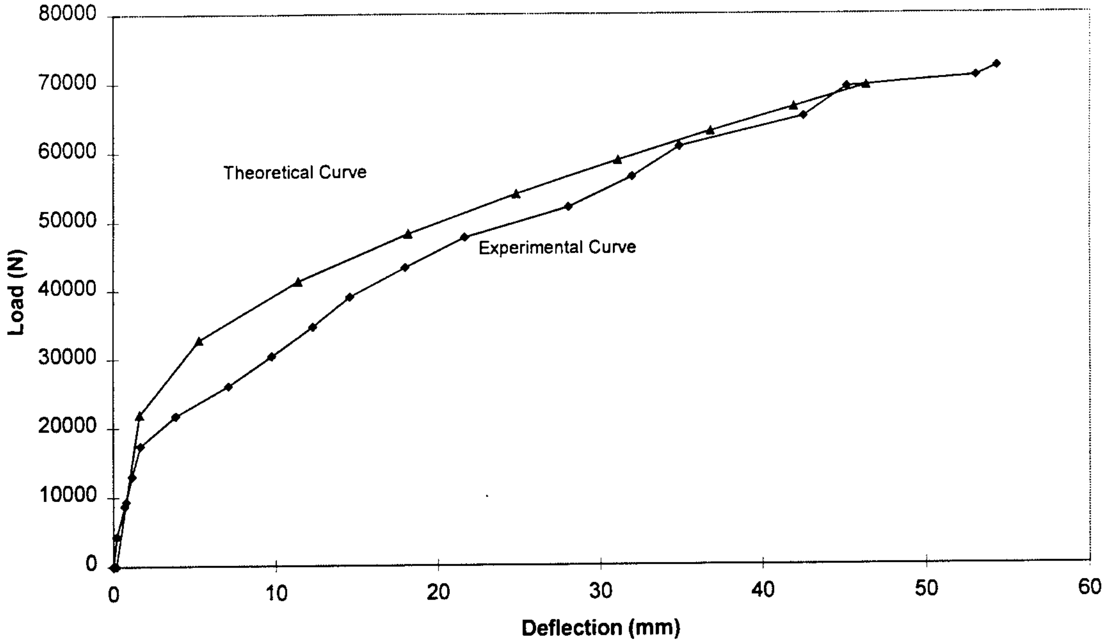

Fig 5.44 Load-midspan deflection relationship for column #6 (e = 124.5 mm, Set II)

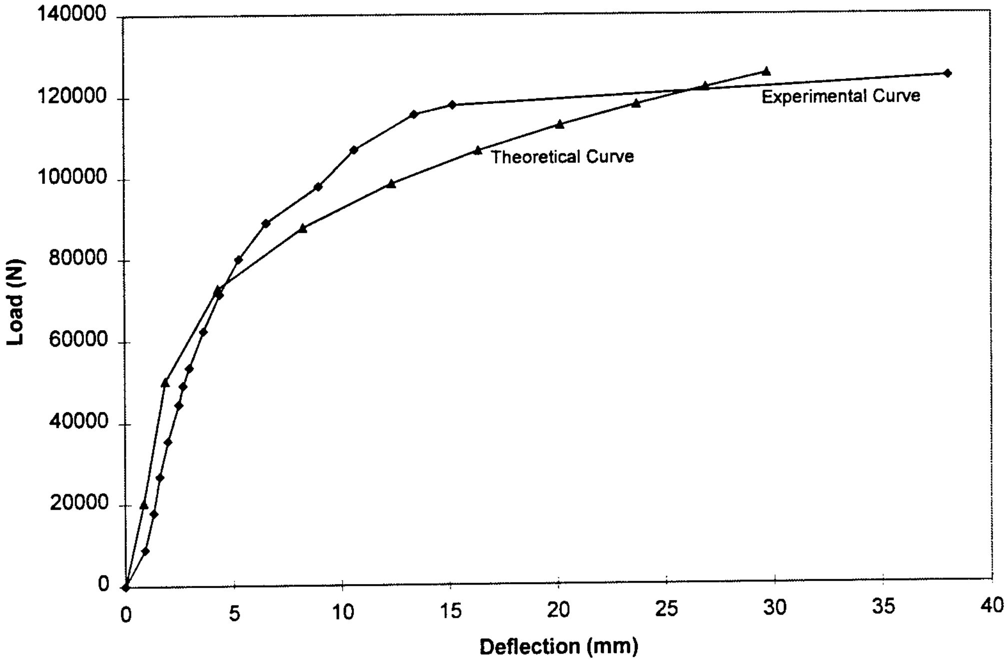

Fig 5.45 Load-midspan deflection relationship for column #7 (e = 63.5 mm, Set II)

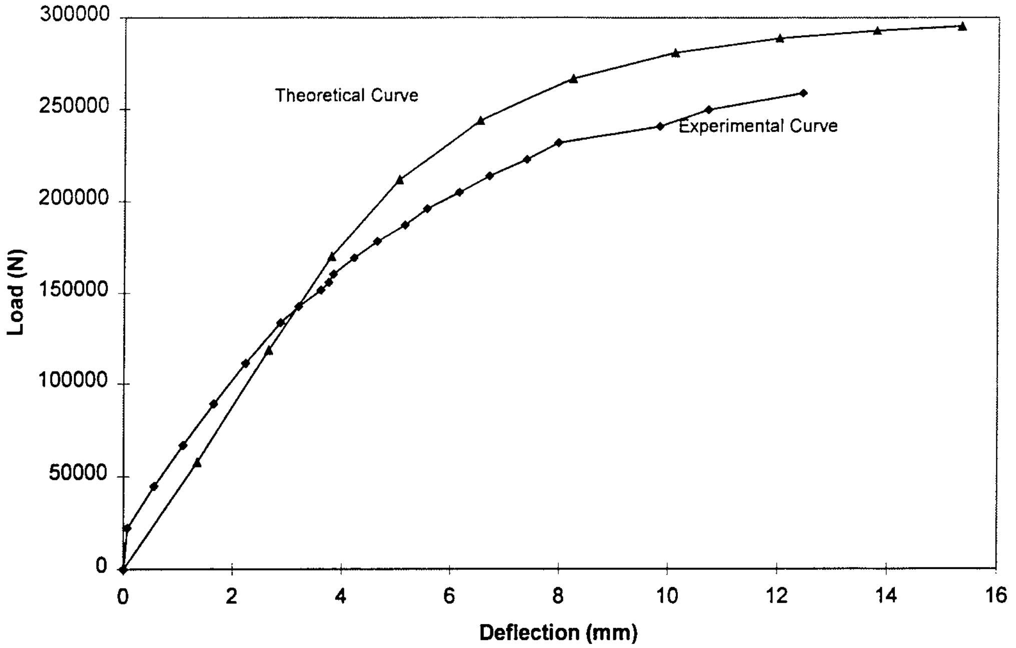

Fig 5.46 Load-midspan deflection relationship for column #8 (e=38.1 mm, Set II)

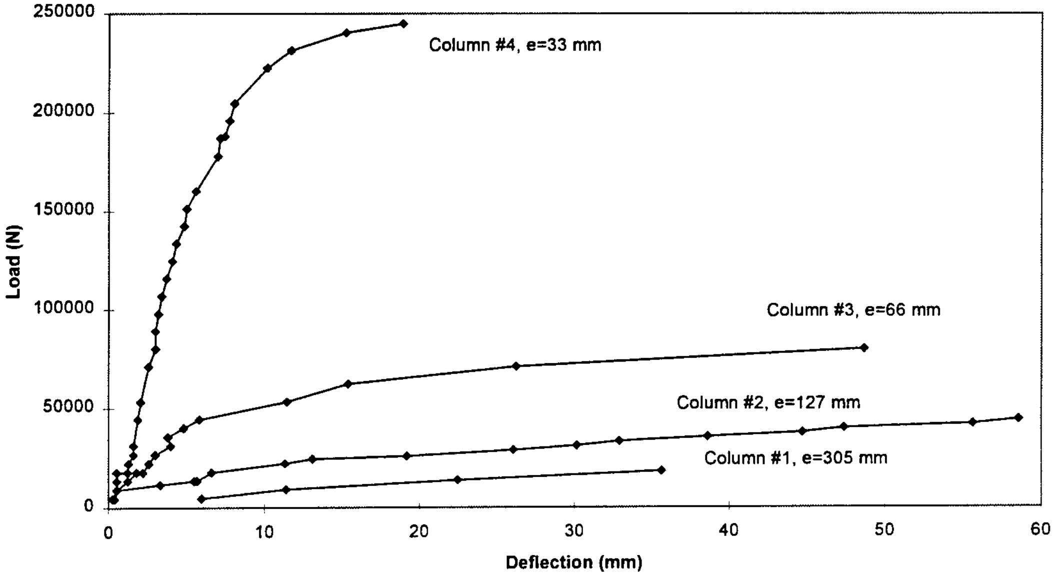

Fig. 5.47 Load-midspan deflection relationship for column set I (f_c' = 30.23 MPa)

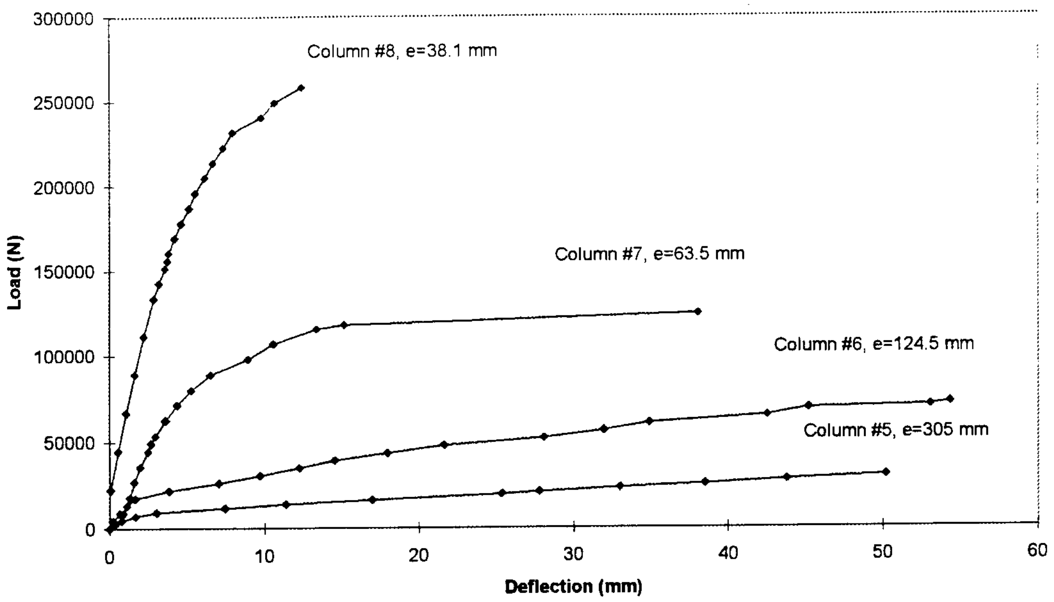

Fig. 5.48 Load-midspan deflection relationship for column set II (f_c' = 42.76 MPa)

5.5.4 Moment - Curvature characteristics

Figs. 5.49-5.56 show the moment – midspan curvature relationships of the CFRP reinforced concrete columns under the eccentric load based on the experimental and theoretical results. It is observed that the experimental and theoretical moment-curvature relationships of columns subjected to axial load with an eccentricity of 305 mm are predominantly linear during the entire loading stage. With decrease in eccentricity, the moment-curvature relationships become non-linear after early stages of loading. At the first load stage, the moment - curvature relationship is linear up to the first crack load. After the section is cracked, the curvatures tend to increase due to the reduced moment of inertia of the cracked column. At the post cracking stage, the curvatures increased rapidly with very little change in applied load.

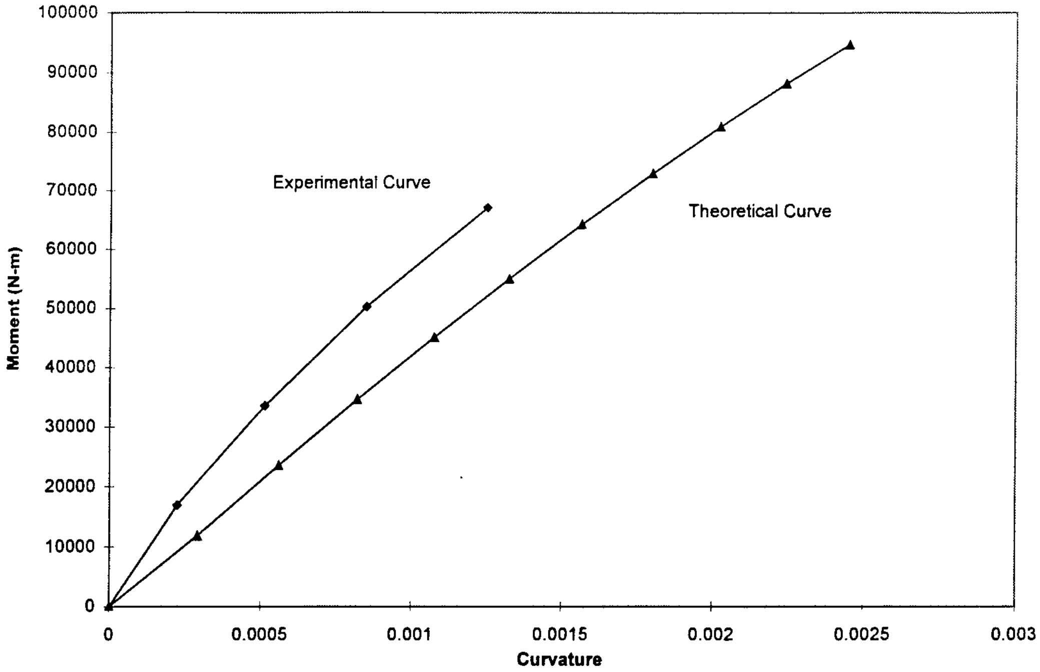

Fig 5.49 Moment – midspan curvature relationship for column #1

(e = 305 mm, Set I)

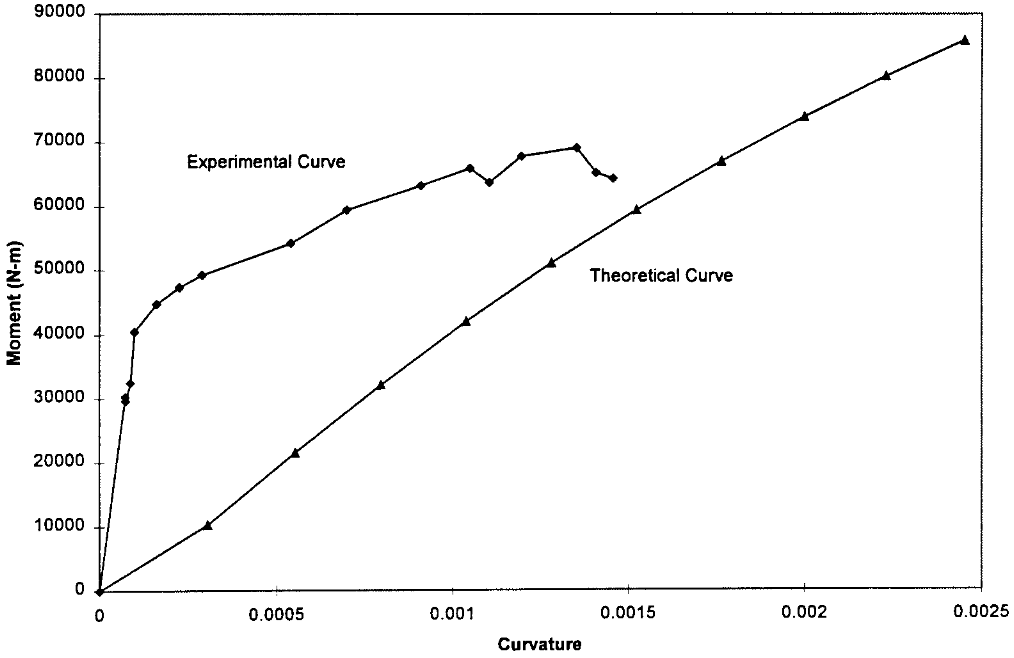

Fig 5.50 Moment – midspan curvature relationship for column #2

(e = 127 mm, Set I)

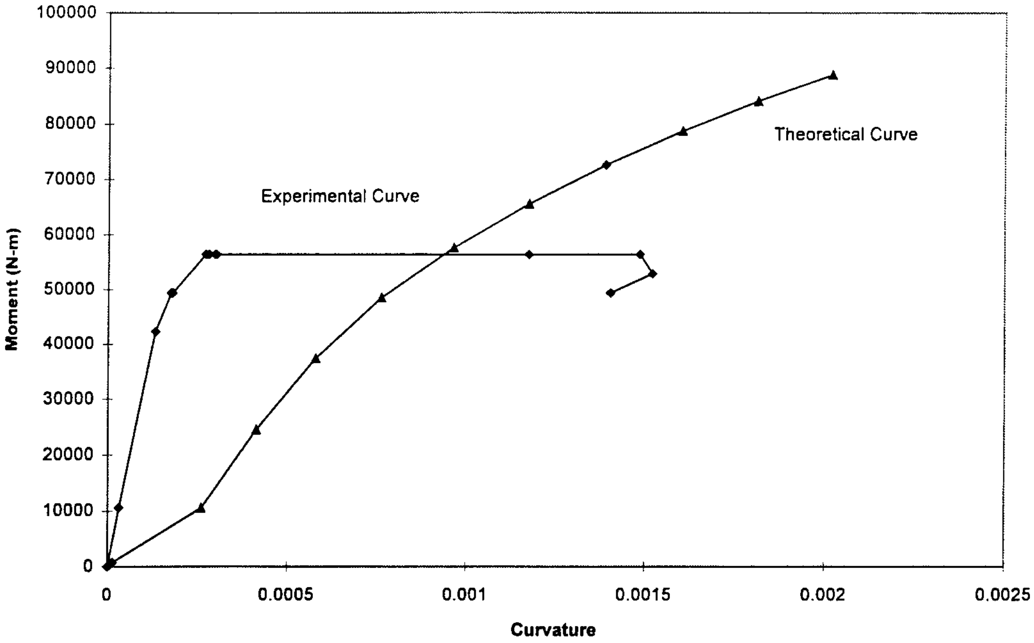

Fig 5.51 Moment – midspan curvature relationship for column #3 (e = 66 mm, Set I)

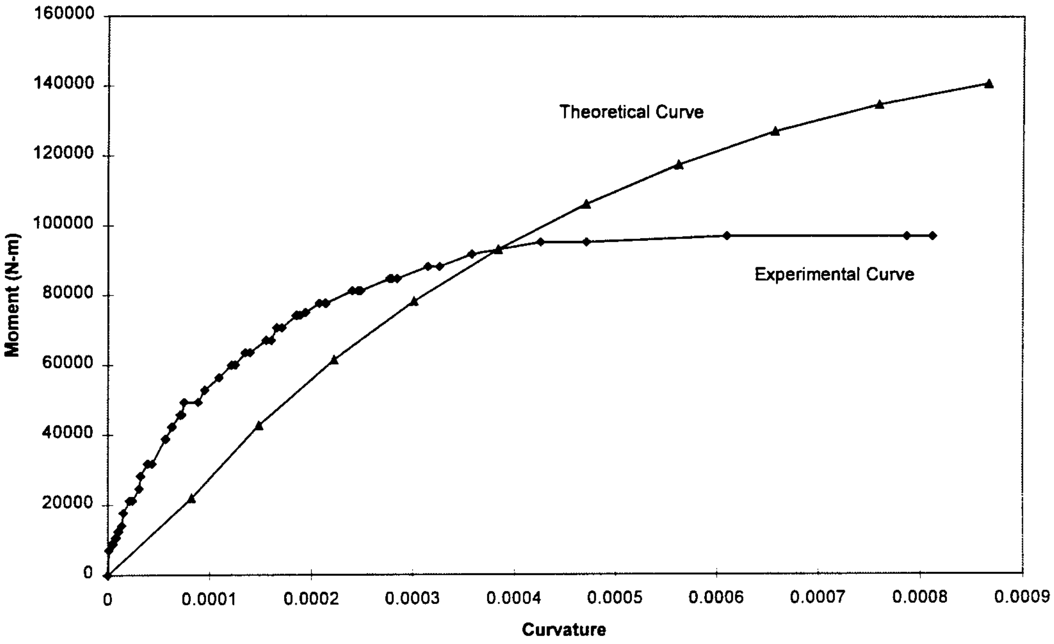

Fig 5.52 Moment – midspan curvature relationship for column #4 (e = 33 mm, Set I)

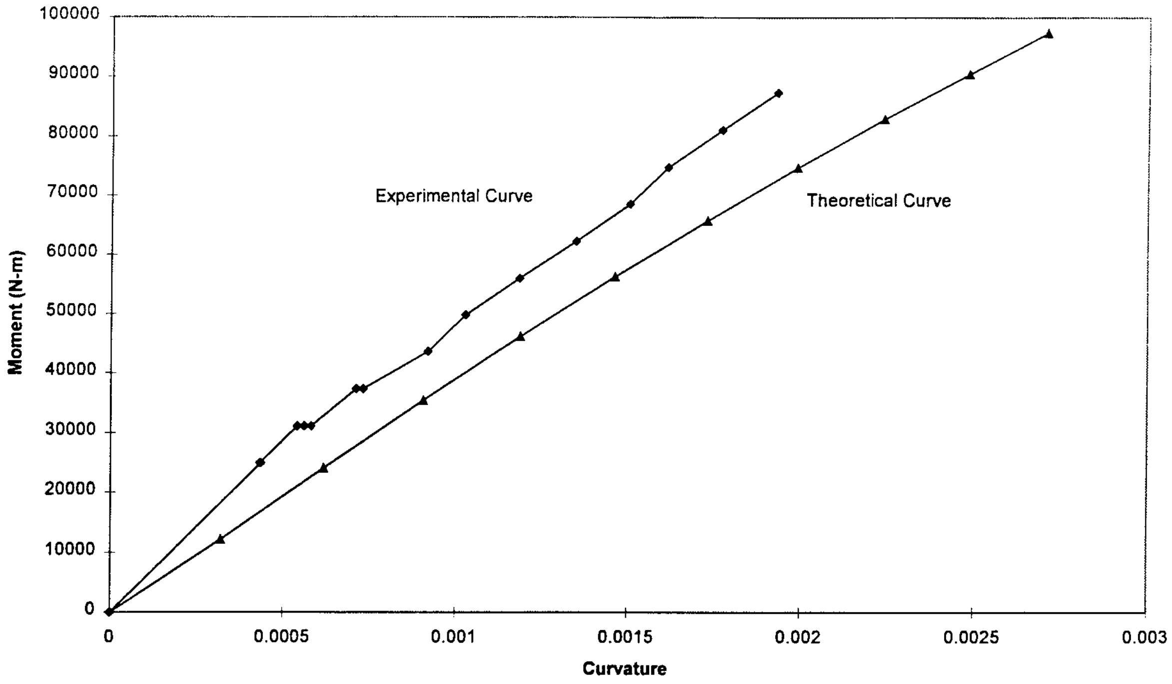

Fig 5.53 Moment - midspan curvature relationship for column #5
(e = 305 mm, Set II)

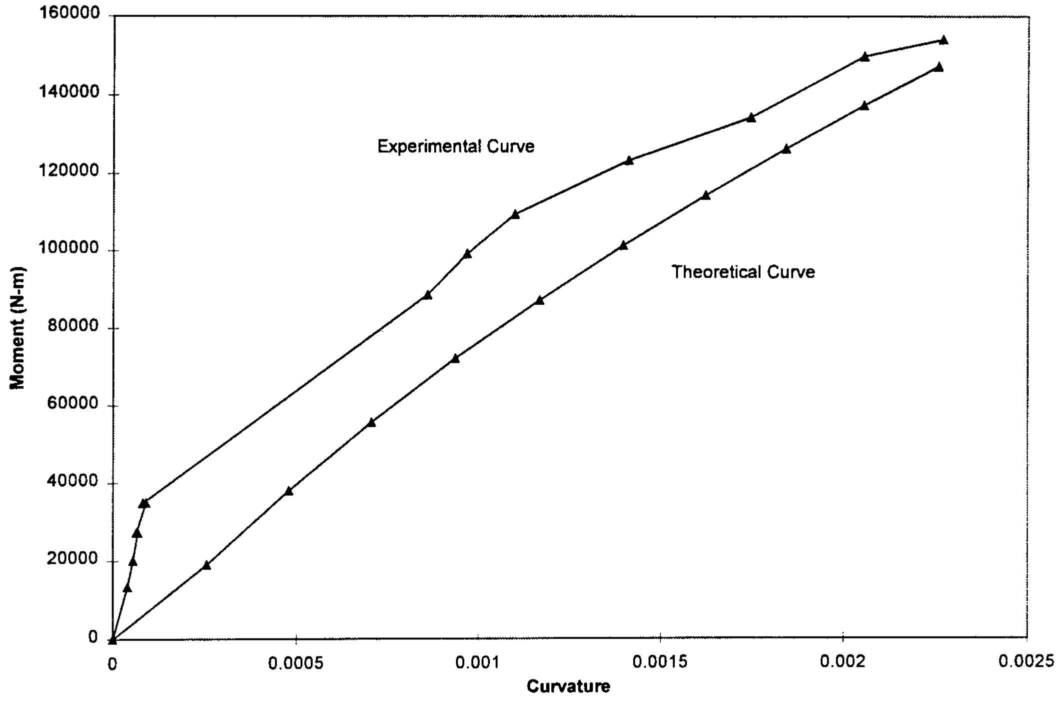

Fig 5.54 Moment – midspan curvature relationship for column #6
(e = 124.5 mm, Set II)

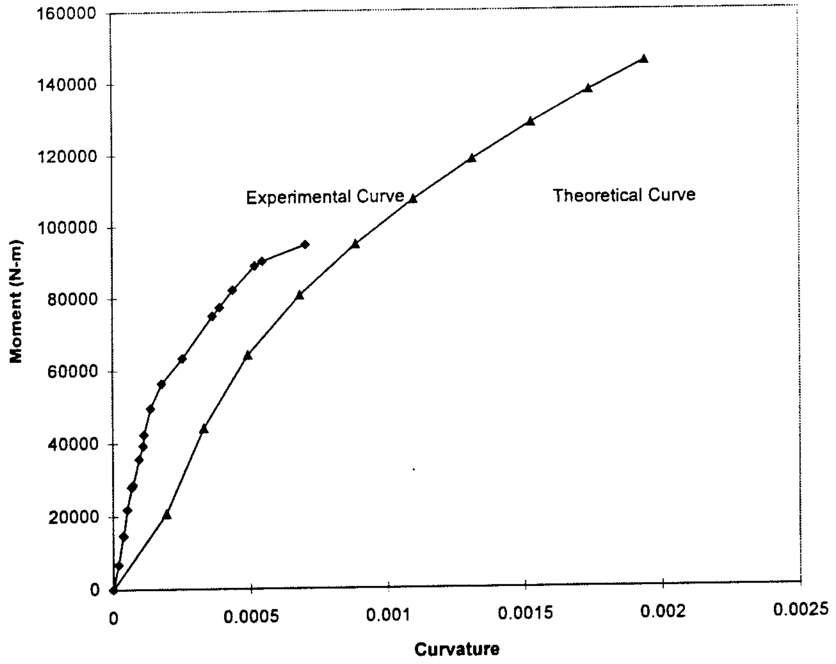

Fig 5.55 Moment – midspan curvature relationship for column #7 (e = 63.5 mm, Set II)

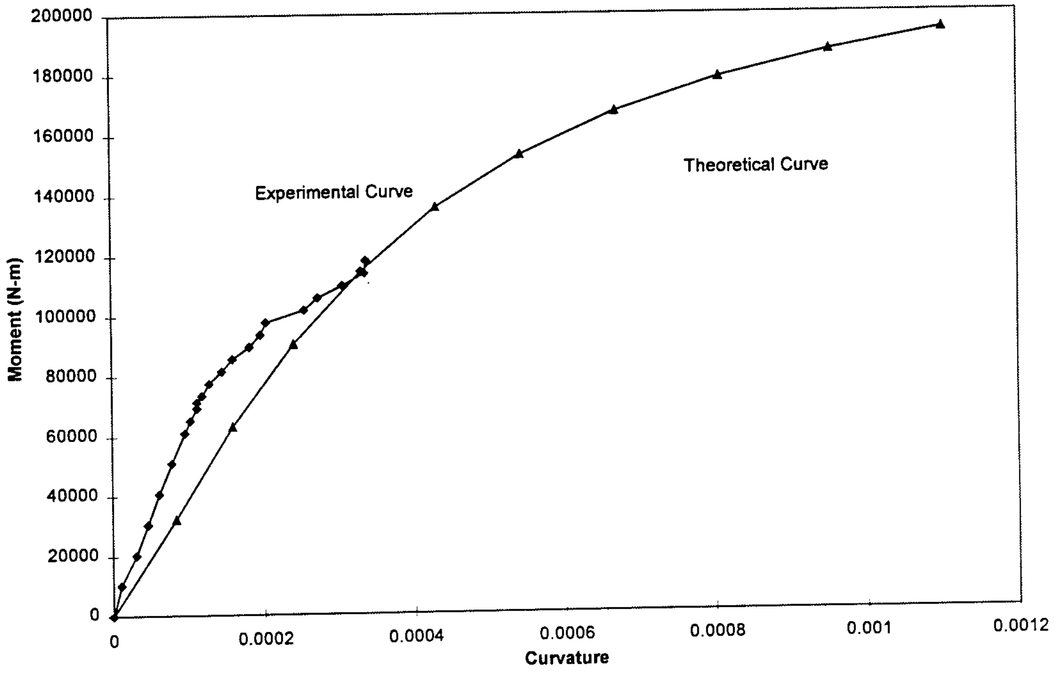

Fig 5.56 Moment – midspan curvature relationship for column #8 (e = 38.1 mm, Set II)

Figs 5.57 and 5.58 show that the slopes of moment-curvature relationships increase with decrease in eccentricity. For a given moment, the curvatures are larger with loads applied with higher eccentricities.

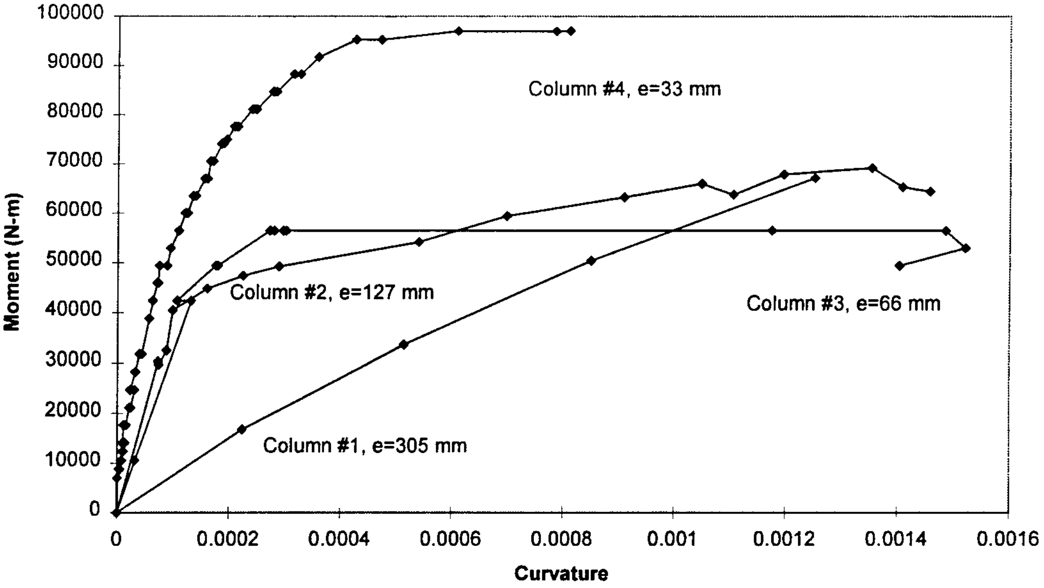

Fig 5.57 Moment – midspan curvature relationship for column set I (f_c' = 30.23 MPa)

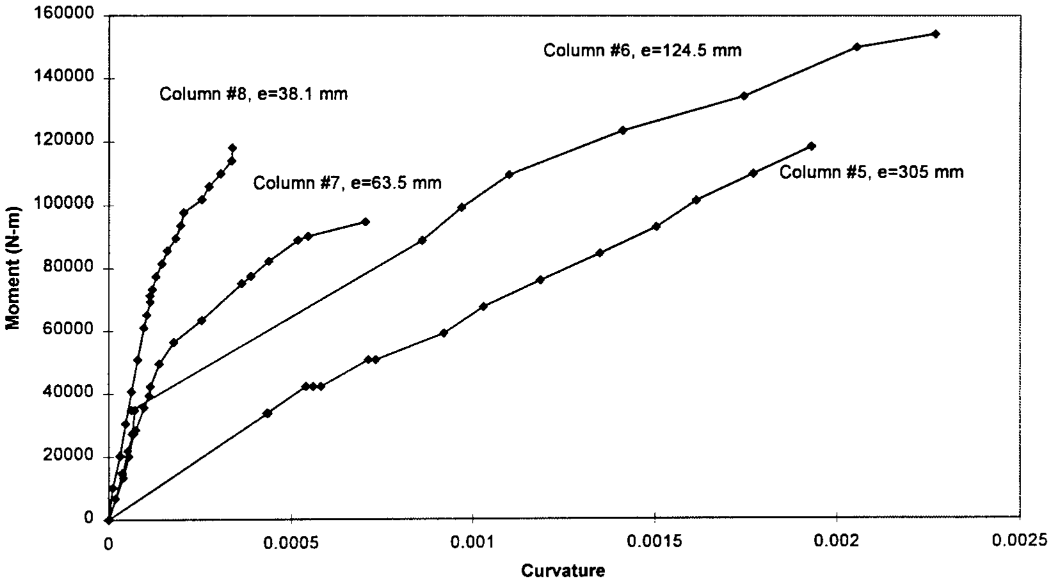

Fig 5.58 Moment – midspan curvature relationship for column set II (f_c' = 42.76 MPa)

5.5.5 Crack patterns

The crack patterns of the eight columns after failure are shown in Figs. 5.60-5.67. Flexural cracks symmetric about the mid-span were generally observed in the columns (Fig. 5.59a). With increase in the applied load, the cracks propagated with increase in crack width and length. The new flexural cracks formed symmetrically along the height of columns, sometimes accompanied with sudden loud noise due to the loss of the bond between the concrete and the CFRP reinforcement. At the same time, the flexural cracks slowly deviated from the vertical toward the top compressive zone at the mid-span (except columns #2 and #5 - Fig. 5.59b). When the axial loads approached the failure loads, the flexural cracks propagated rapidly towards the top compressive zone at the mid-span of the columns (Fig. 5. 59c).

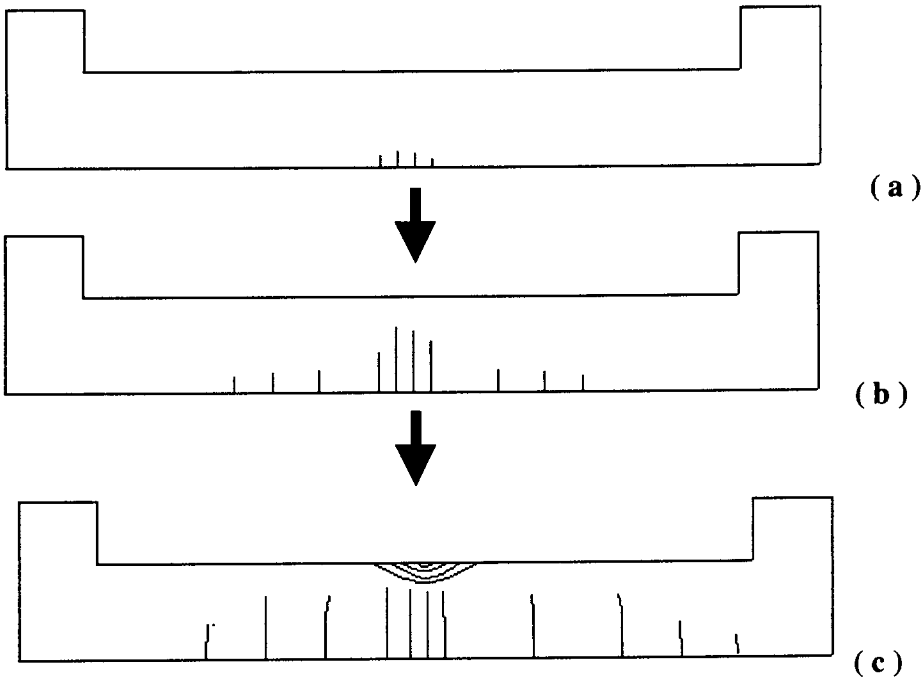

Fig. 5.59 Sketch of column crack pattern

Column #1
(fc'=30.23 MPa)
b=152 mm
h=152 mm
d=109 mm
d1=44 mm
e=305 mm

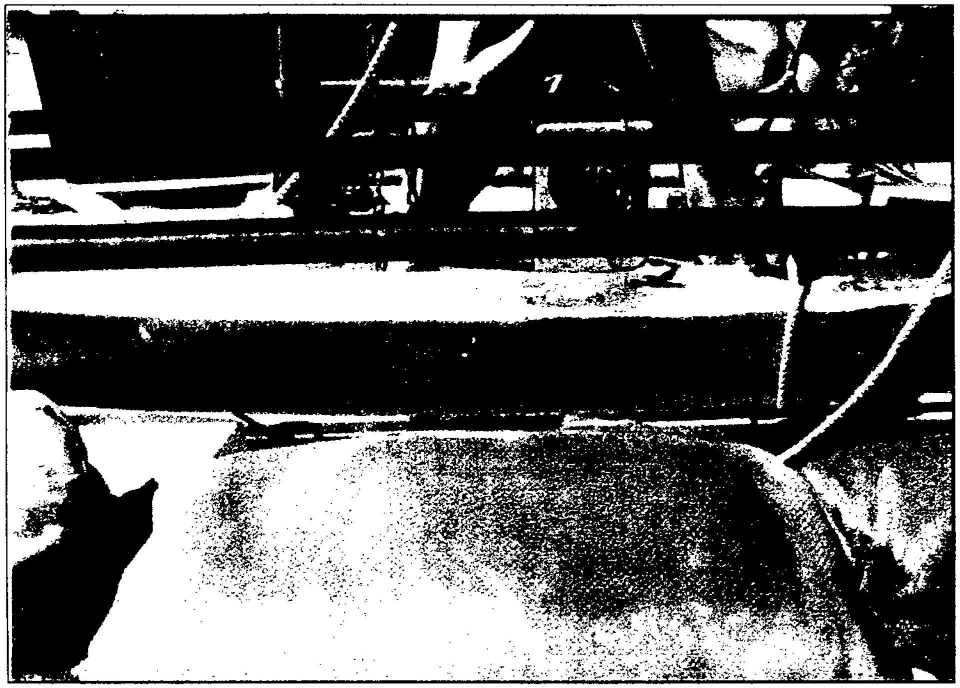

Fig. 5.60 Crack pattern of column #1 (e = 305 mm Set I)

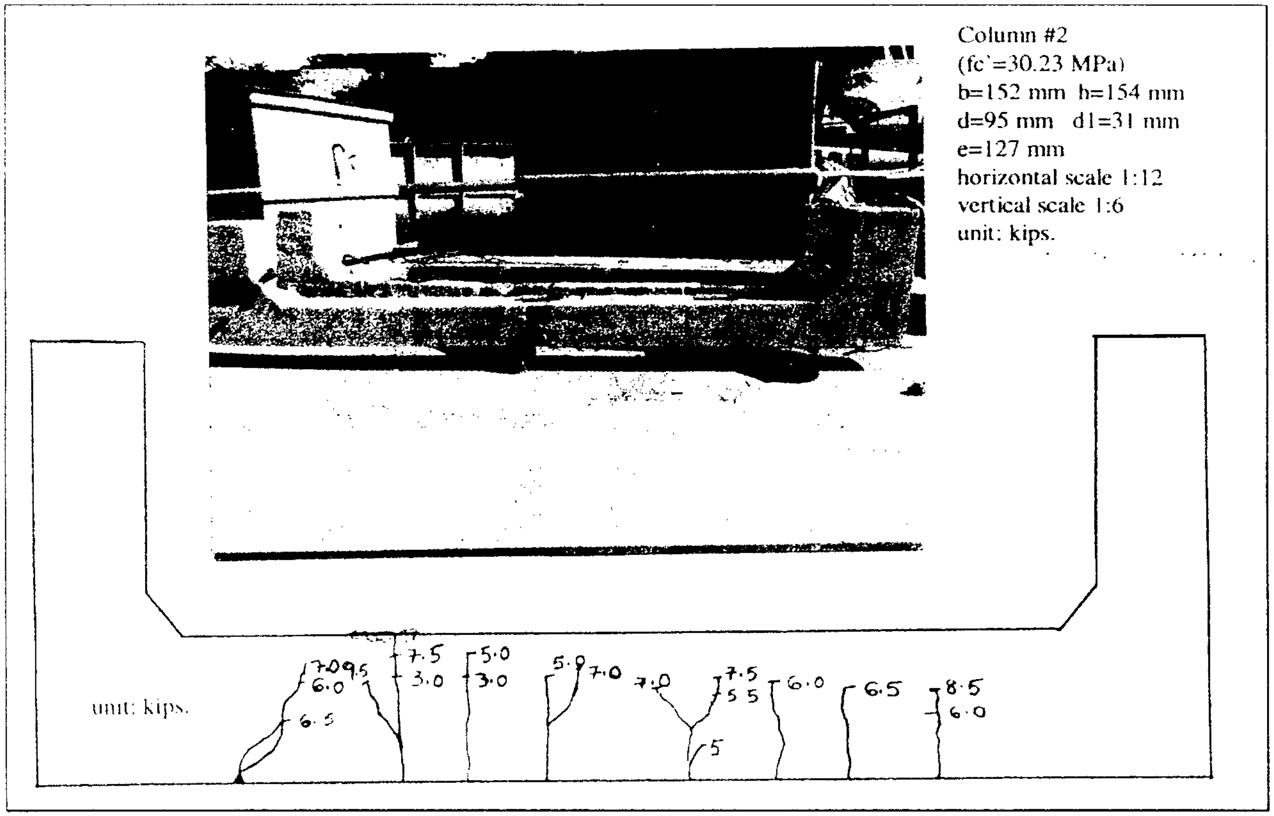

Fig. 5.61 Crack pattern of column #2 (e = 127 mm Set I)

Column #3
(fc'=30.23 MPa)
b=152 mm h=149 mm
d=87 mm   d1=40 mm
e=66 mm
horizontal scale 1:12
vertical scale 1:6
unit: kips.

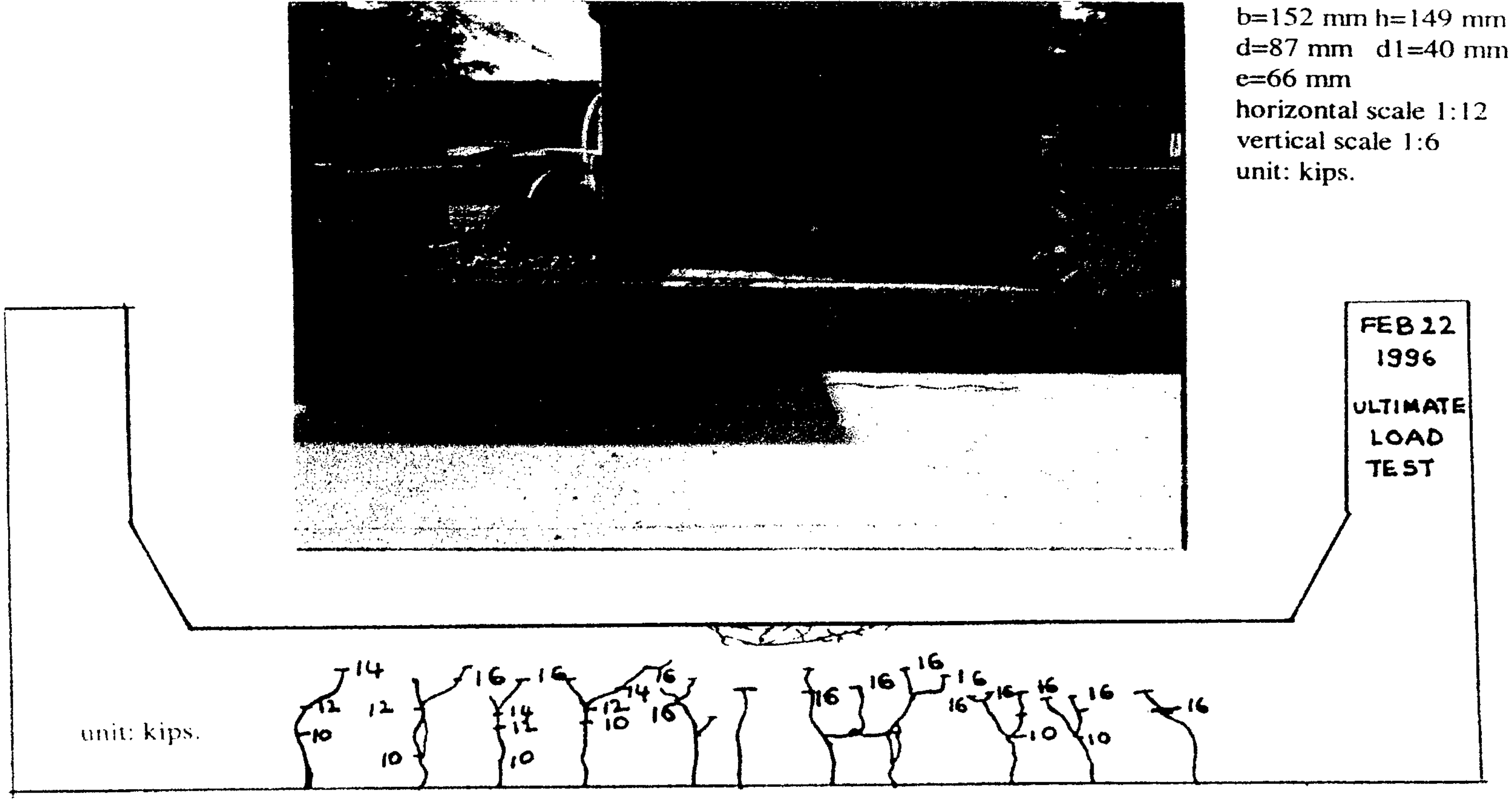

Fig. 5.62 Crack pattern of column #3 (e = 66 mm Set I)

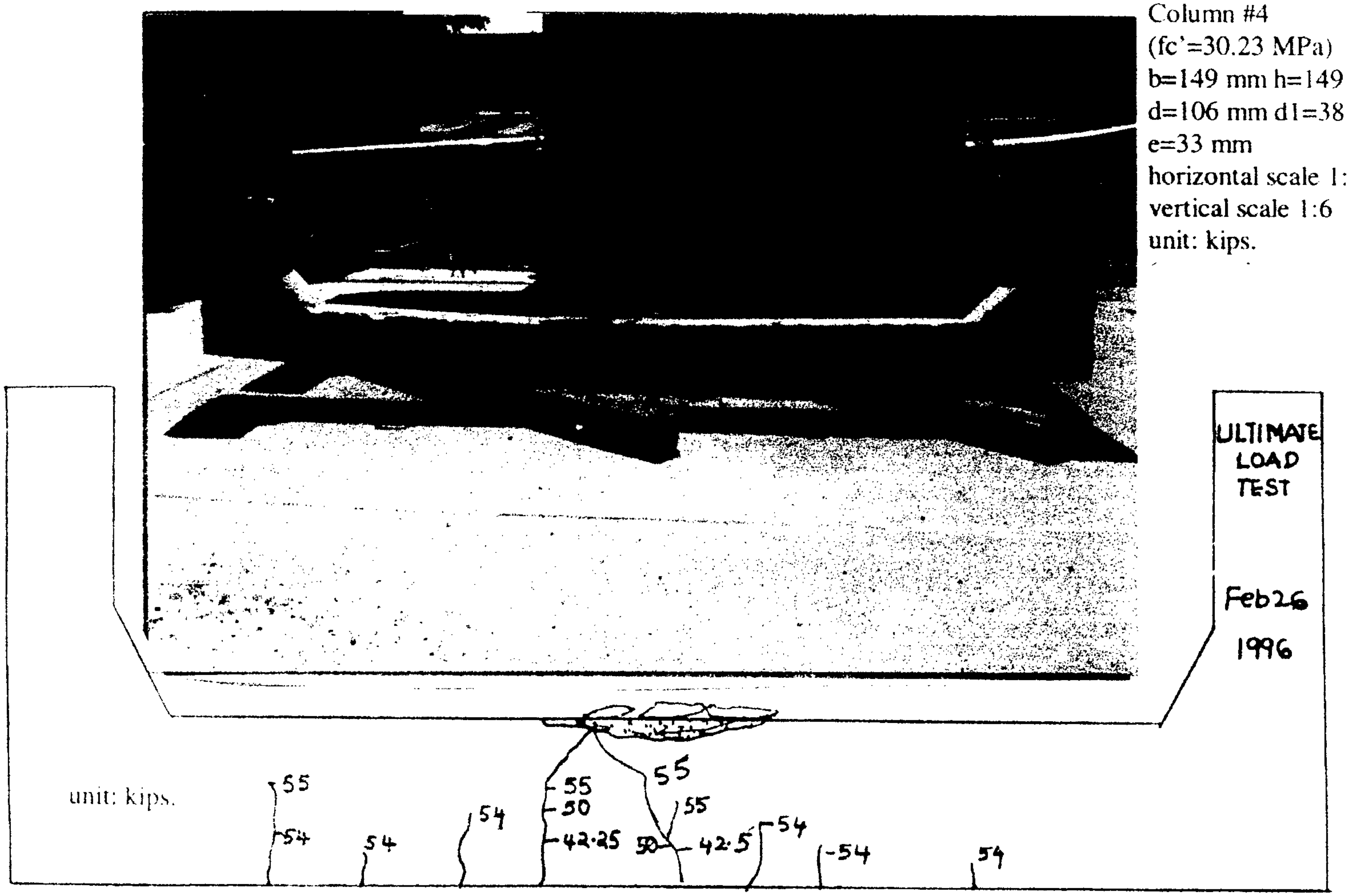

Column #4
(fc'=30.23 MPa)
b=149 mm h=149 mn
d=106 mm d1=38 mr
e=33 mm
horizontal scale 1:12
vertical scale 1:6
unit: kips.

Fig. 5.63 Crack pattern of column #4 (e = 33 mm Set I)

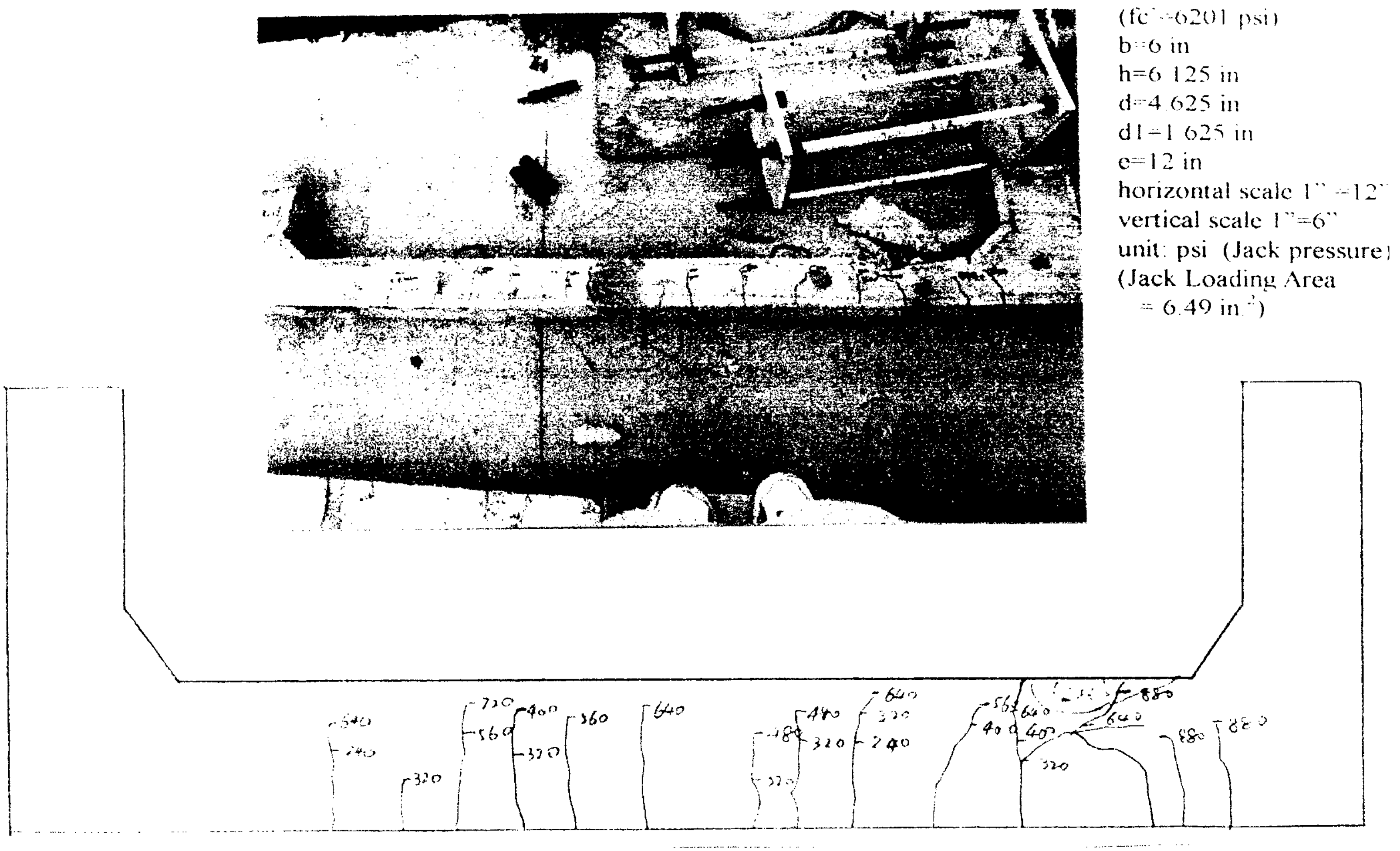

Column #5
(fc'=6201 psi)
b=6 in
h=6.125 in
d=4.625 in
d1=1.625 in
e=12 in
horizontal scale 1"=12"
vertical scale 1"=6"
unit: psi (Jack pressure)
(Jack Loading Area
= 6.49 in.^{2})

Fig. 5.64 Crack pattern of column #5 (e = 305 mm Set II)

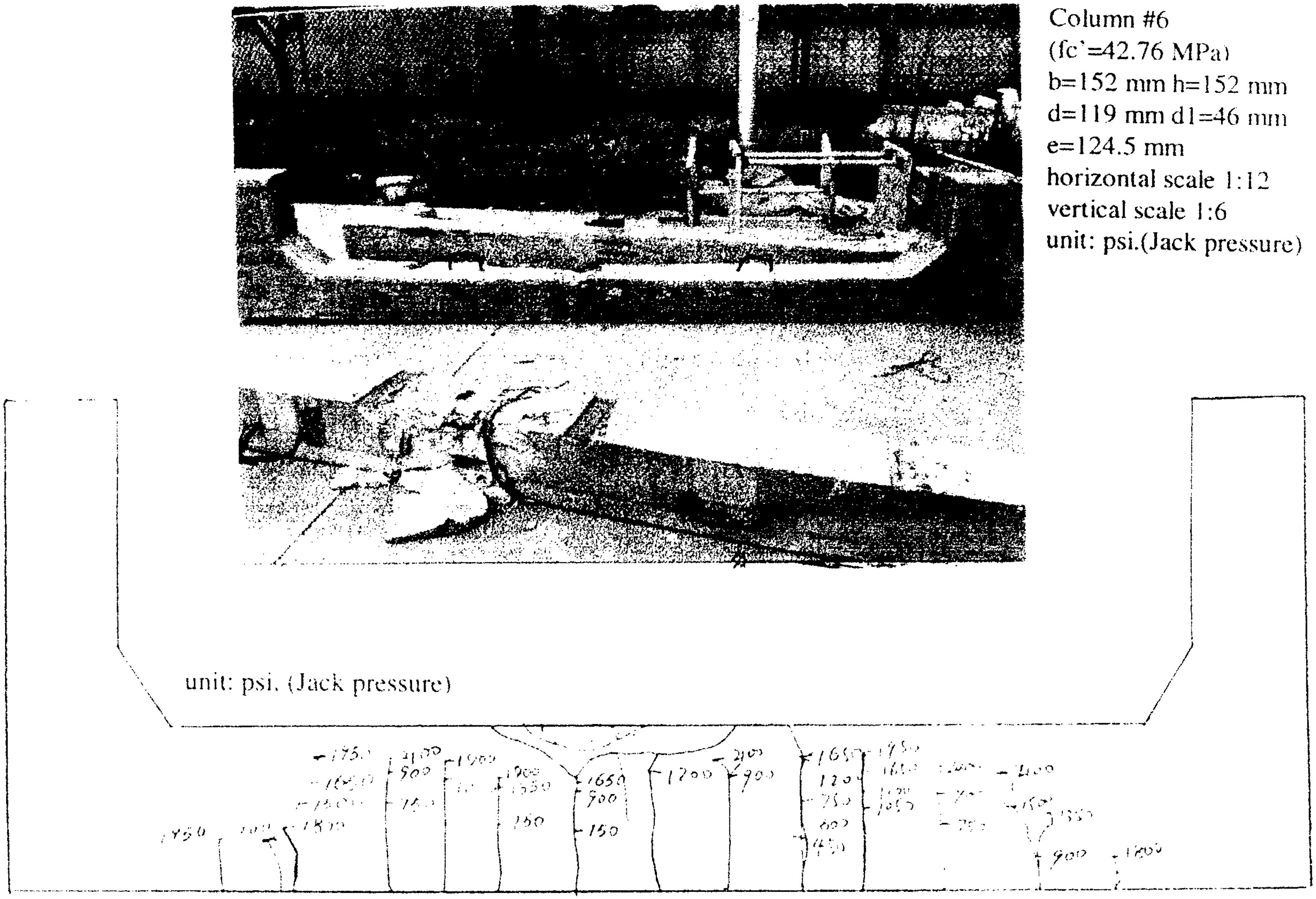

Column #6
(fc'=42.76 MPa)
b=152 mm h=152 mm
d=119 mm d1=46 mm
e=124.5 mm
horizontal scale 1:12
vertical scale 1:6
unit: psi.(Jack pressure)

Fig. 5.65 Crack pattern of column #6 (e = 124.5 mm Set II)

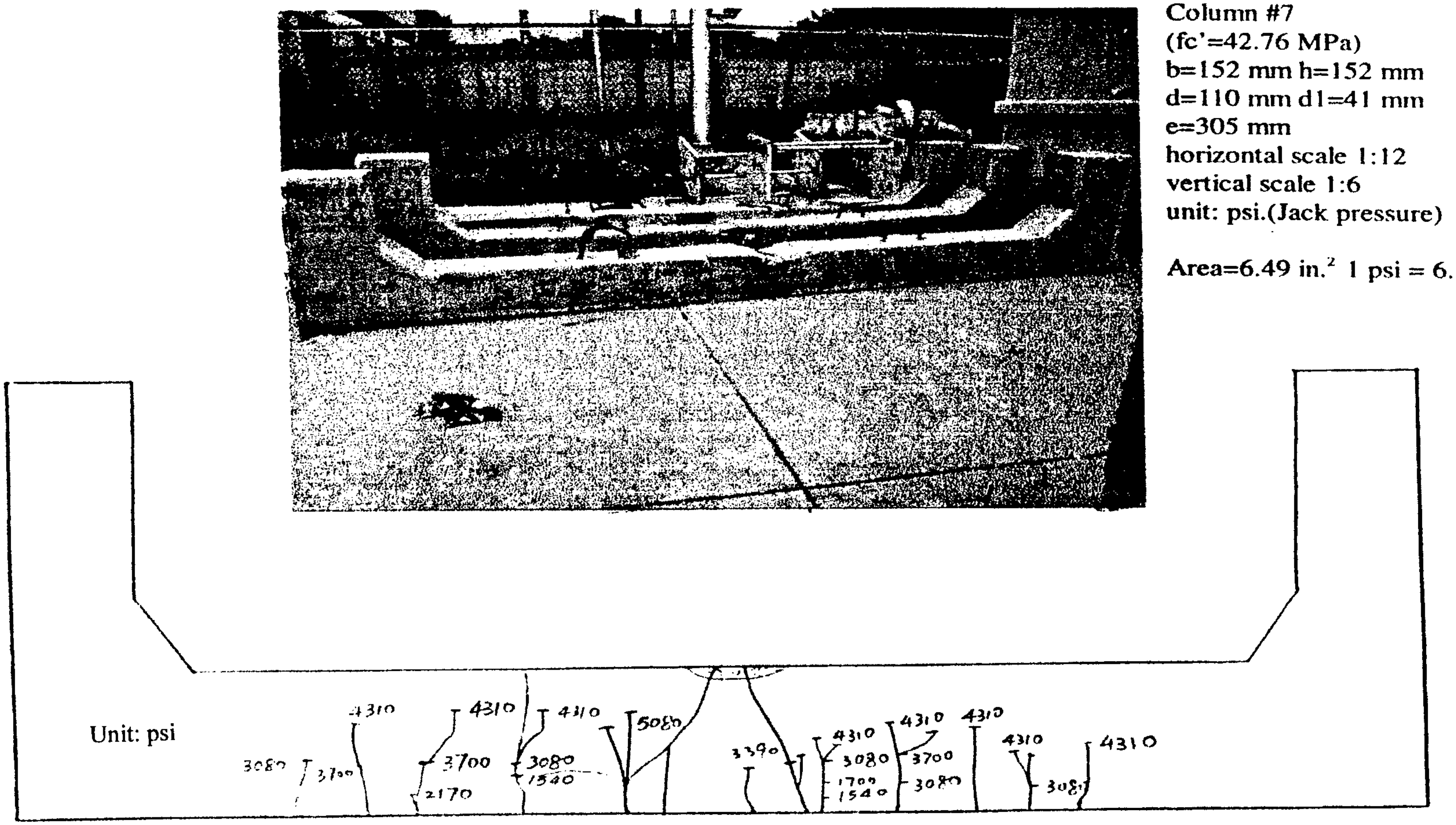
Column #7
(fc'=42.76 MPa)
b=152 mm h=152 mm
d=110 mm d1=41 mm
e=305 mm
horizontal scale 1:12
vertical scale 1:6
unit: psi.(Jack pressure)

Area=6.49 in.^{2} 1 psi = 6.

Fig. 5.66 Crack pattern of column #7 (e = 63.5 mm Set II)

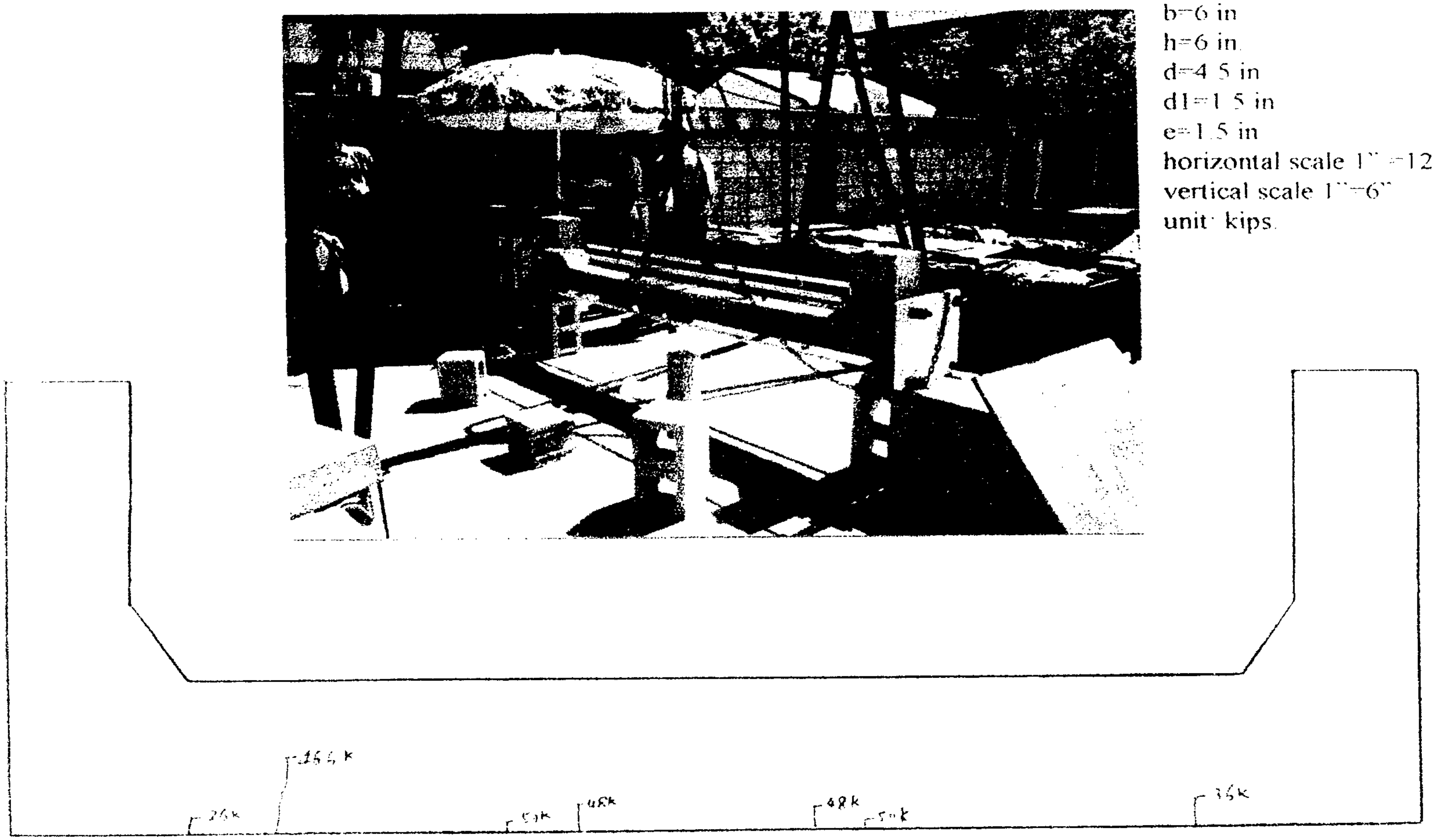

Column #8
(fc'=6201 psi)
b=6 in
h=6 in
d=4.5 in
d1=1.5 in
e=1.5 in
horizontal scale 1"=12"
vertical scale 1"=6"
unit: kips.

Fig. 5.67 Crack pattern of column #8 (e = 38.1 mm Set II)

5.5.6 Comparison of the experimental and theoretical ultimate loads

The results from the analytical method presented in Chapter 4 are compared with the experimental results. The eight columns were divided into two groups of four columns in each group, with two different concrete strengths. The actual concrete cover to the CFRP reinforcement was used in the analytical computations. The cover to the CFRP reinforcement in each column is summarized in Table 5.1b. The experimental results and the theoretical values are compared in Table 5.2 and 5.3. Due to the safety considerations, deflections, strains and loads were recorded in column #1 up to a load of 18.68 kN, while the failure load was 23.93 kN. Column #8 was loaded only up to 267.0 kN, which is very close to the design load capacity of the test frame.

The observed first crack loads and the theoretical values are compared in Table 5.2. The experimental first crack loads are very close to the theoretical values. Generally, the experimental results are larger than those from the theoretical analysis. The first cracks may develop at loads earlier than the instant they are observed during the test.

The observed ultimate loads and the theoretical values are compared in Table 5.3. The experimental ultimate loads agree reasonably well with theoretical values. Figs. 5.68 and 5.69 show the CFRP reinforced concrete column interaction diagrams for columns in Set I and II. The moments for columns in Figs. 5.68 and 5.69 are based on the eccentricity of the applied end loads and the maximum measured deflection during the ultimate load stage. The deflection measurements for columns 1 and 2 in Set I were taken only up to the instant during the test when it was safe to record the readings. The ultimate moments for the columns were, therefore, somewhat smaller than the actual values, and hence the plotted points lie inside the interaction diagram.

Table 5.2 Comparison of the experimental and theoretical first crack loads (kN)

column #	e (mm)	P (first crack)		
		Experimental	Theoretical	$(P_{test}-P_{theoretical}) / P_{theoretical}$
1	305	*	5.86	*
2	127	15.57	16.63	-6.4%
3	66	40.03	37.90	+5.6%
4	33	180.37	199.21	-9.5%
5	305	7.43	7.62	-2.5%
6	124.5	19.43	20.61	-5.7%
7	63.5	51.52	53.75	-4.1%
8	38.1	158.86	165.60	-4.1%

Note: * The first crack load of column #1 was missed during measurements

Table 5.3 Comparison of the experimental and theoretical ultimate loads (kN)

column #	e (mm)	Pn. (ultimate)		
		Experimental	Theoretical	$(P_{ntest}-P_{ntheoretical}) / P_{ntheoretical}$
1	305	23.93	22.03	+8.6%
2	127	46.26	45.81	+1.0%
3	66	80.07	82.42	-2.9%
4	33	244.64	249.17	-1.8%
5	305	32.33	29.02	+11.4%
6	124.5	76.50	70.35	+8.7%
7	63.5	124.18	128.16	-3.1%
8	38.1	>267.00**	283.69	**

Note: ** Column #8 was loaded up to 267.0 kN.

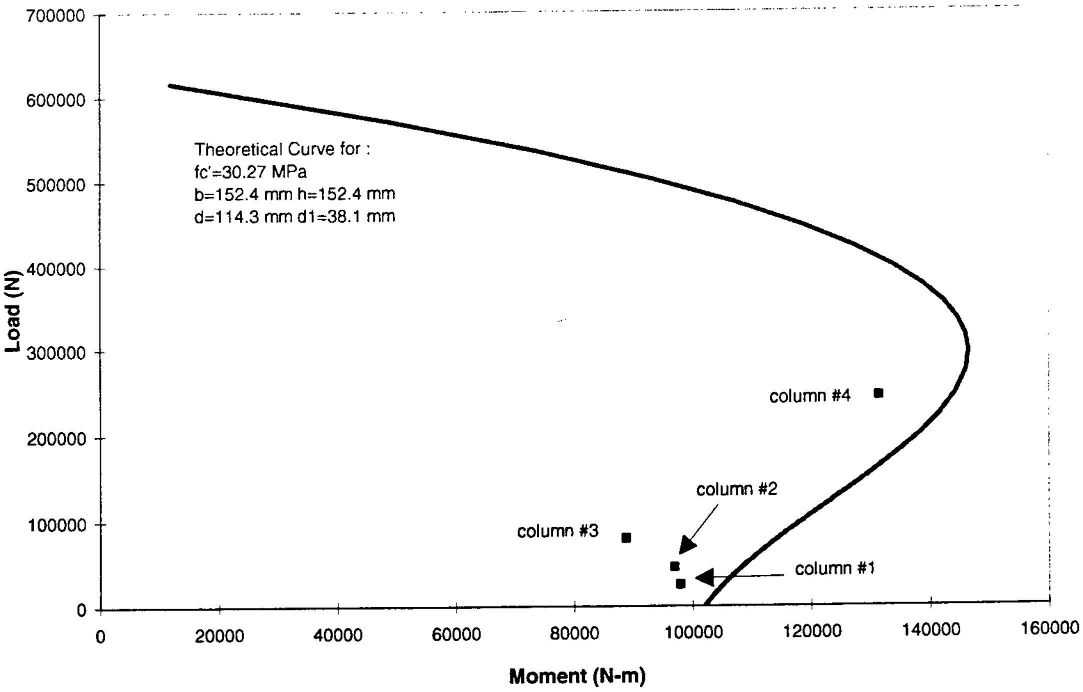

Fig. 5.68 CFRP-reinforced concrete column interaction diagram for set I

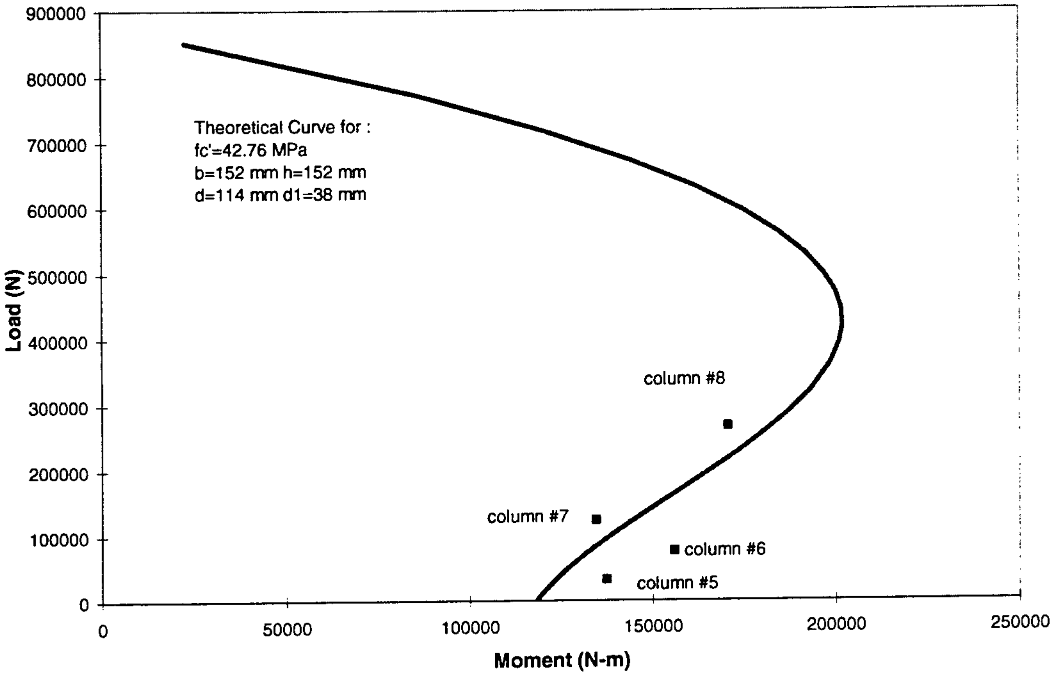

Fig. 5.69 CFRP-reinforced concrete column interaction diagram for set II

CHAPTER 6

EXPERIMENTAL PROGRAM FOR TIME DEPENDENT DEFORMATIONS OF CFRP REINFORCED CONCRETE BEAMS AND COLUMNS

6.1 INTRODUCTION

Four concrete beams and four columns reinforced with CFRP bars were cast to study the long term behavior under sustained loading. The beams were setup over simple supports and subjected to uniform sustained flexural loading. The columns were arranged in a framework and subjected to sustained uniform axial compressive force. The deflections and strains at the mid-span were recorded periodically for the concrete beams using deflectometer and strain gages respectively. The strains at different locations were recorded for the concrete columns using strain gages. The beams and columns were subjected to a loading period of about two years. The test setups were arranged in an open-air facility at the Center for Infrastructure and Constructed Facilities, Florida Atlantic University.

6.2 MATERIALS

6.2.1 Concrete

The properties of the concrete mix used for test beams and columns are shown in Table 6.1.

Table 6.1 Properties of concrete

Items	Beam Set I :	Beam Set II and Columns:
Cement : sand : aggregate	1: 1.88 : 2.68	1: 1.31 : 2.14
Cylinder compressive strength after 28 days	32.1 MPa (4657 psi)	42.8 MPa (6200 psi)
Modulus of elasticity of concrete	26.80 GPa (3887 ksi)	30.92 GPa (4484 ksi)

6.2.2 Carbon FRP

Materials used for manufacturing carbon FRP are carbon fiber of the PAN base system and matrix resins. The properties of carbon, matrix resin and carbon FRP are presented in Table 5.1c.

6.3 CFRP REINFORCED CONCRETE BEAMS

6.3.1 Beam casting

Four rectangular beams reinforced with CFRP bars were cast in two sets on July and November 1995. The first set of beams (B1 and B2) and the second set of beams (B3 and B4) were of size 152 mm x 203 mm x 2438 mm (6 in. x 8 in. x 8 ft.) and 152 mm x 152 mm x 2438 mm (6 in. x 6 in. x 8 ft.) respectively. Each beam is reinforced with two 7.5 mm CFRP bars in the top and bottom (Figs. 6.1 and 6.2). The spacing of the #3 steel stirrups is 76.2 mm (3 in.) at both ends and the spacing gradually increases to 152 mm (6 in.) at the mid-span. Fig. 6.3 shows the compaction of fresh concrete using a mechanical vibrator. Concrete blocks of size 305 mm x 305 mm x 610 mm (1 ft. x 1 ft. x 2 ft.) and 305 mm x 152 mm x 610 mm (1 ft. x 6 in. x 2 ft.) were cast at the same time, which were used to simulate the sustained distributed load (Fig. 6.4).

6.3.2 Instrumentation

Strains were measured using five electrical resistance surface strain gages at the mid-span of beams B1 and B2 (Fig 6.5) Three electrical resistance surface strain gages were attached to beams B3 and B4 (Fig. 6.6). These gages were epoxy coated to prevent moisture intrusion, which affects the strain gage functioning over the long time period. Embedded strain gages were attached to the CFRP bars. The electrical resistance strain gages were attached to the concrete surface at different levels across the depth and strains monitored by the strain indicator (beams B1 and B2) / data acquisition system 4000 (beams B3 and B4). The deflections at the mid-span of the beams were recorded using a deflectometer (Fig. 6.7).

6.3.3 Test setup

After the beams were cured, they were positioned on simple supports (Fig. 6.8) and subjected to sustained distributed loads (Fig. 6.9) simulated by using concrete blocks. Beams B1, B2, B3 and B4 were subjected to the loading shown in Fig. 6.11. Beam B1 was subjected to 77% of the first cracking moment. Beams B2, B3 and B4 were subjected to 120%, 110% and 123% of their respective cracking moments (Table 6.2). The effect of cracks is considered in the study of the long-term behavior of CFRP reinforced concrete beams.

Table 6.2 Beams for the creep test

Beam	Cross-section (mm x mm)	Applied moment to cracking moment (%)	Remarks on beam condition
B1	152 x 203	77	Uncracked
B2	152 x 203	120	Cracked
B3	152 x152	110	Cracked
B4	152 x152	123	Cracked

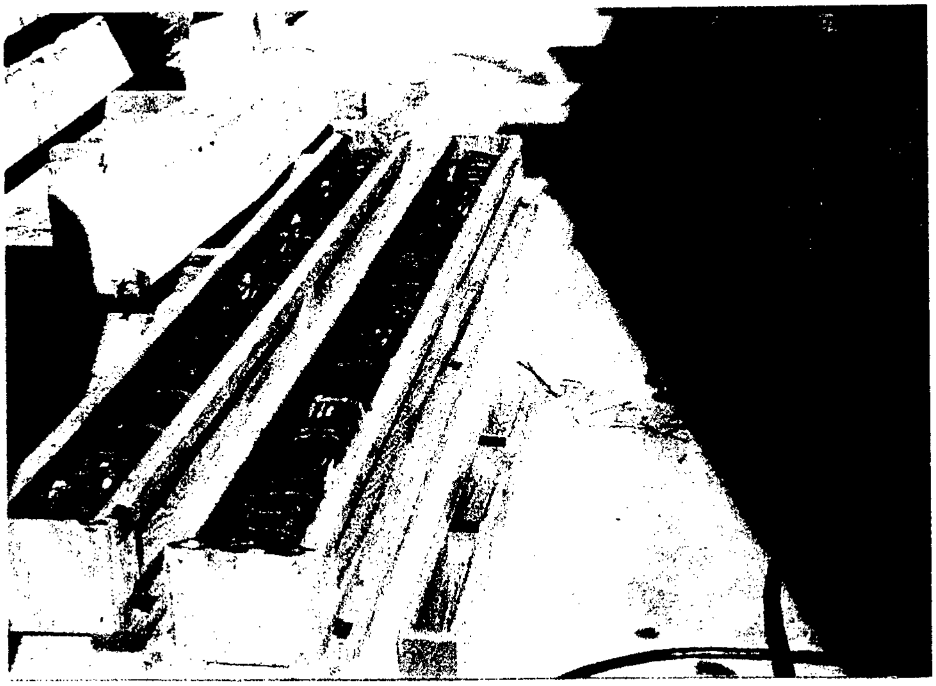

Fig. 6.1 Formwork and the reinforcement arrangement details

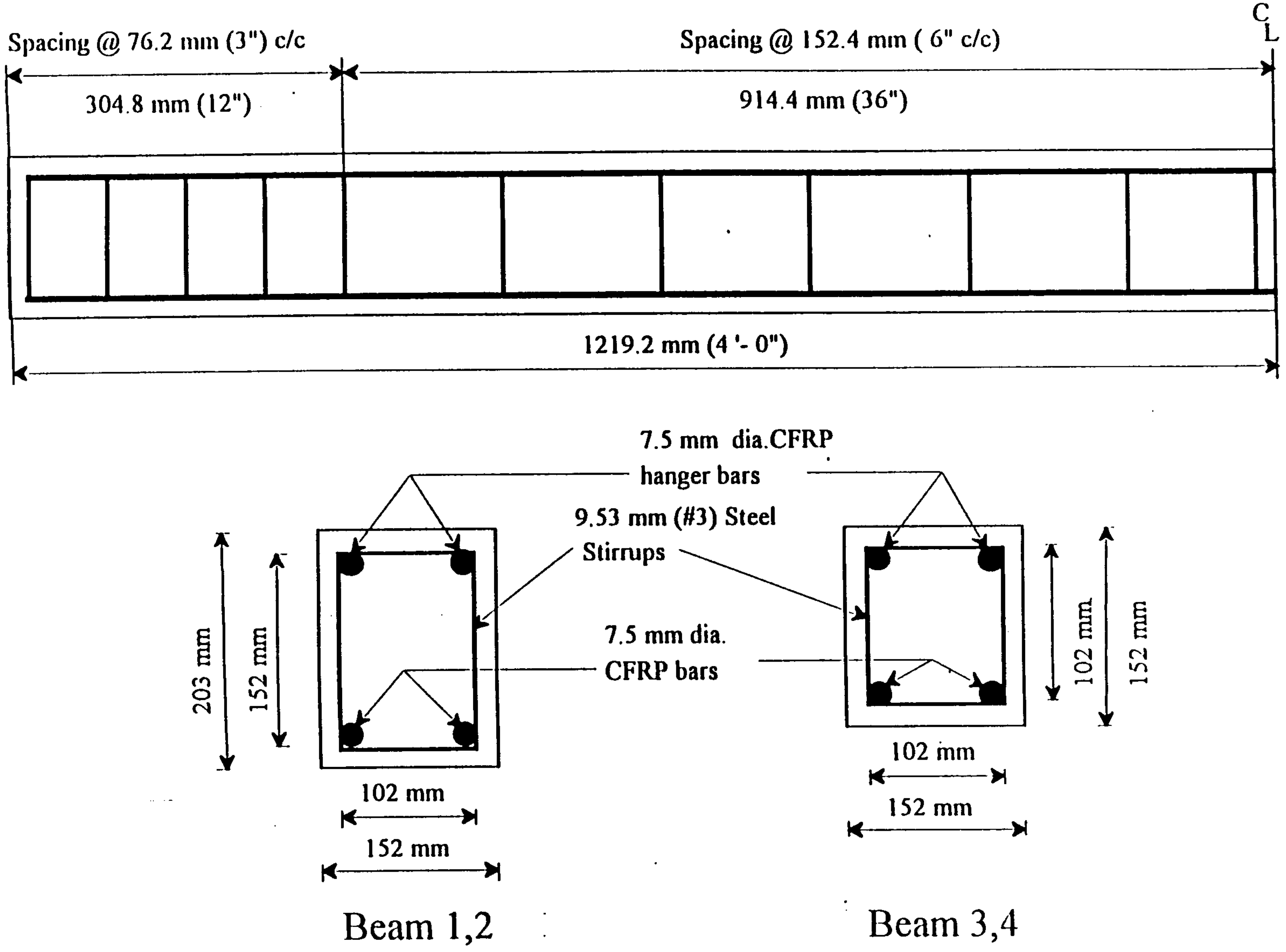

Figure 6.2 Reinforcement details of concrete beam

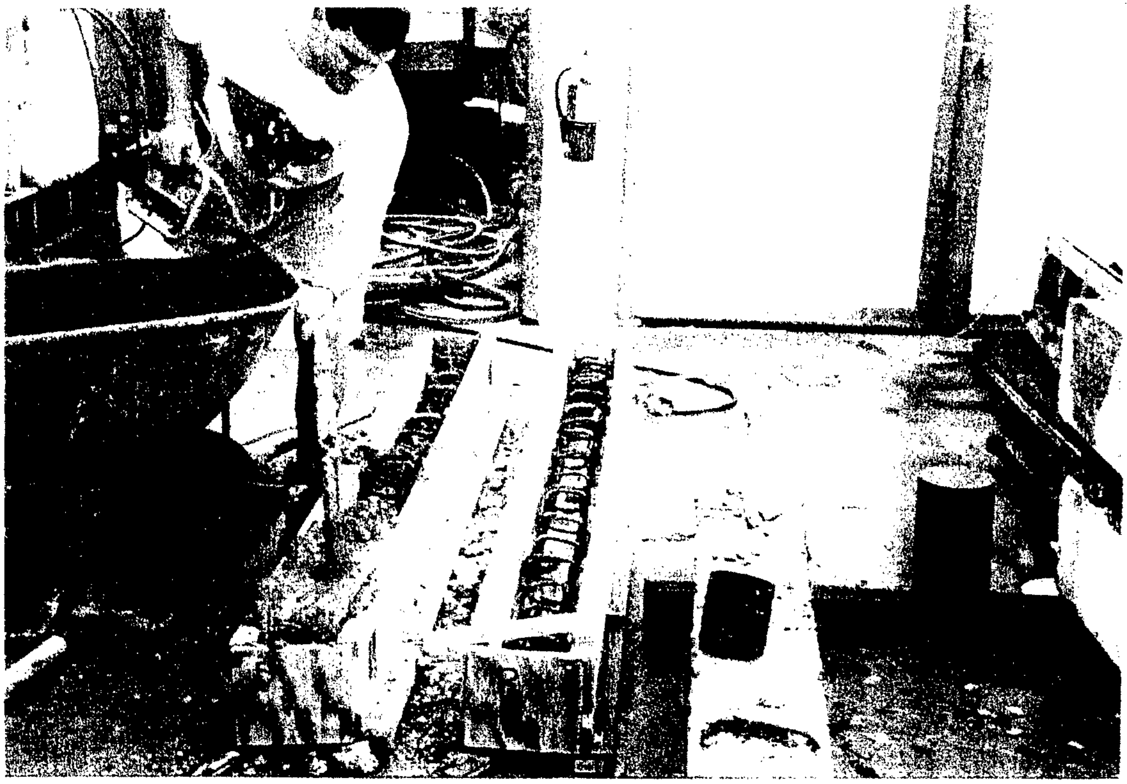

Fig. 6.3 Concrete casting in progress

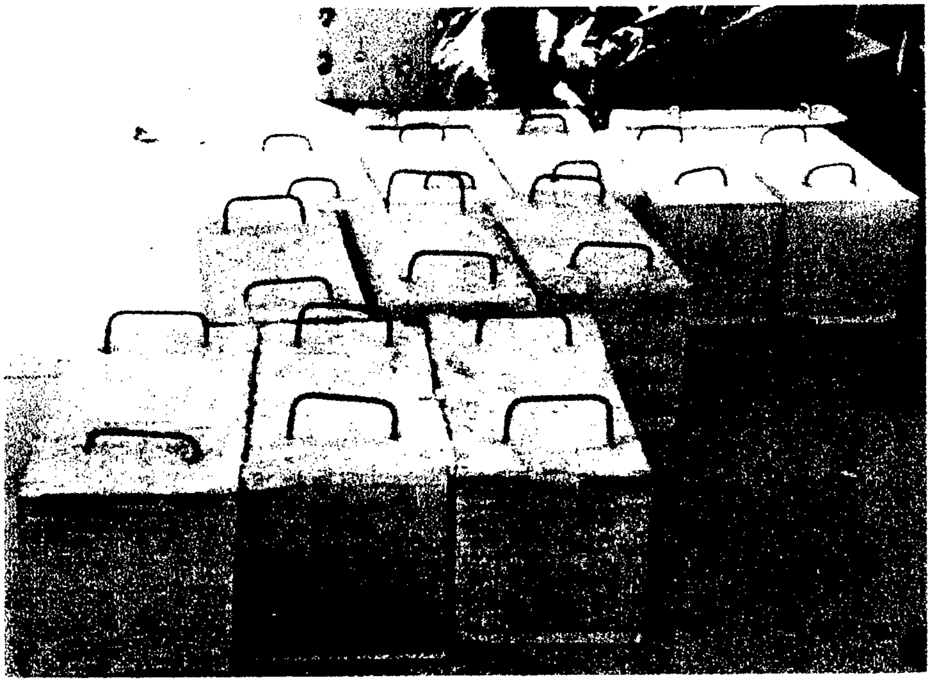

Fig. 6.4 Concrete blocks for simulation of sustained distributed loading

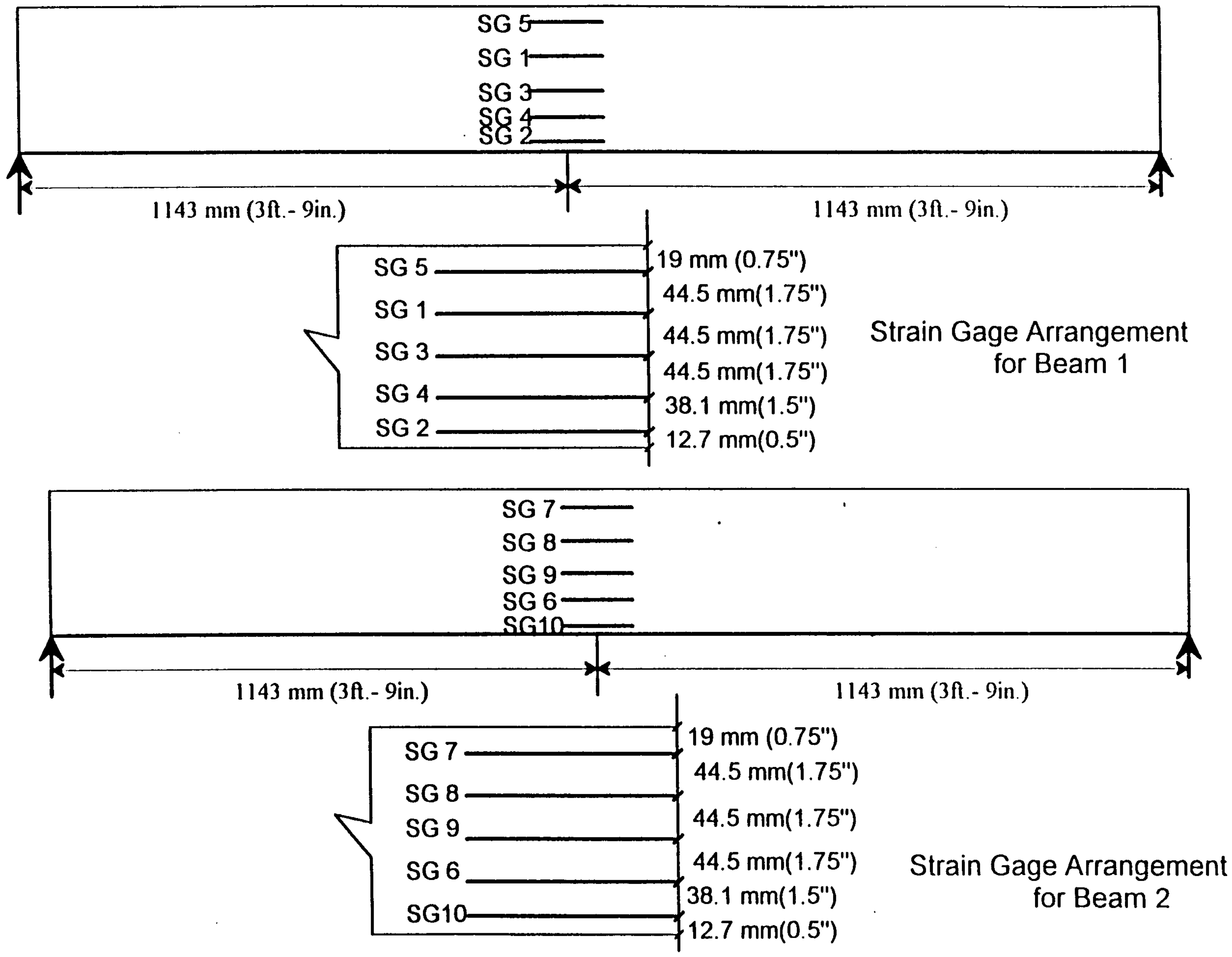

Figure 6.5 Strain gage arrangement for beams B1 and B2

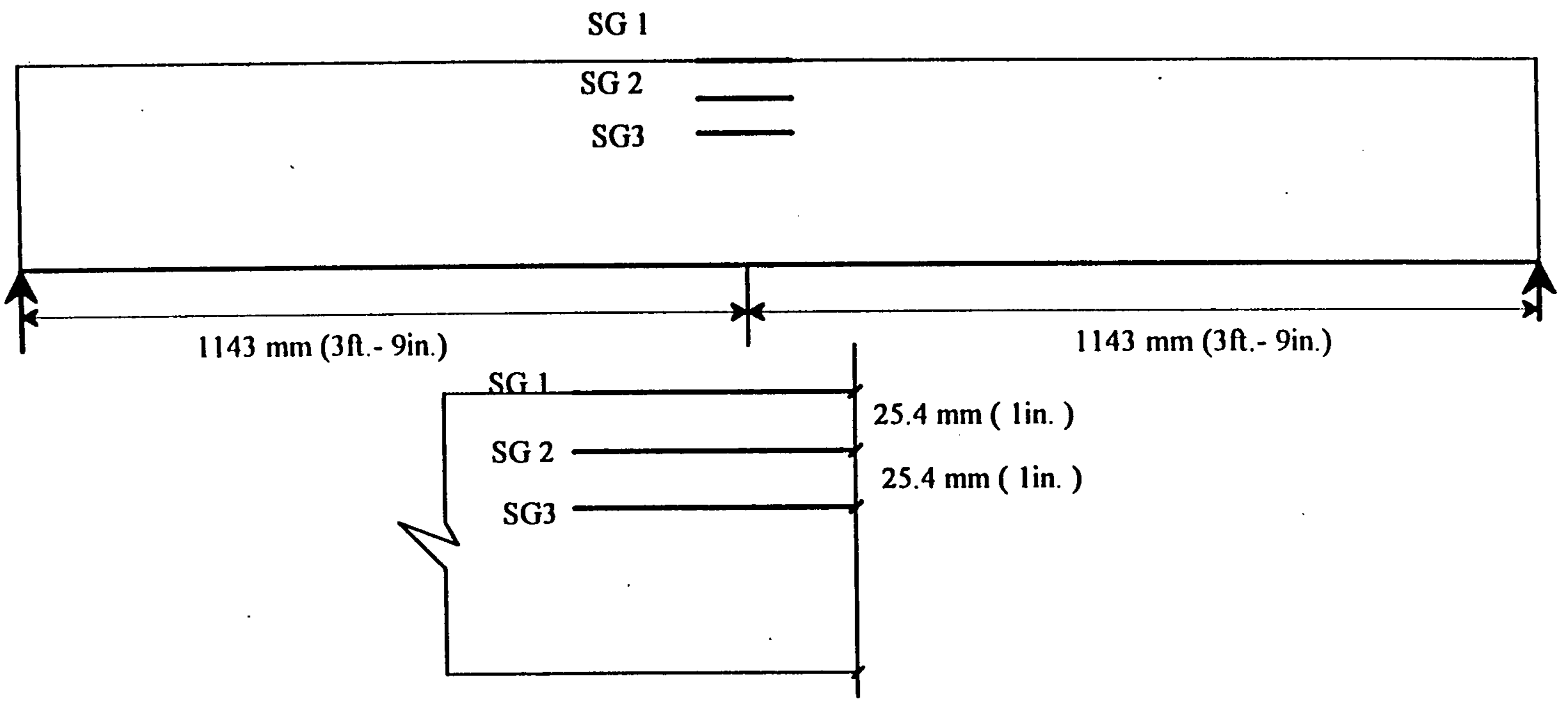

Figure 6.6 Strain gage arrangement for beams B3 and B4

Fig. 6.7 Instrumentation at the midspan

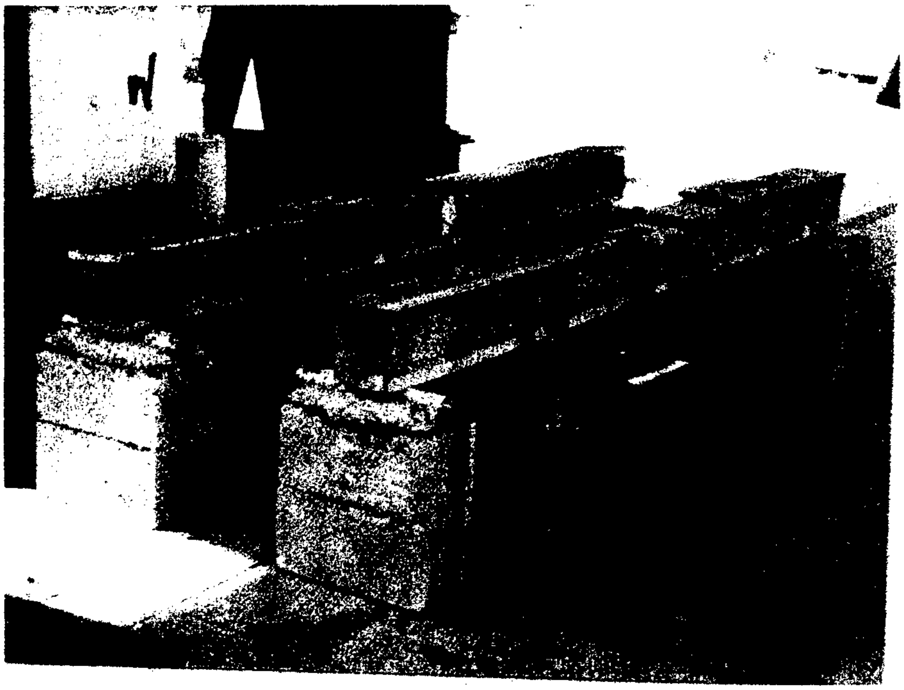

Fig. 6.8 Beam over the simple supports

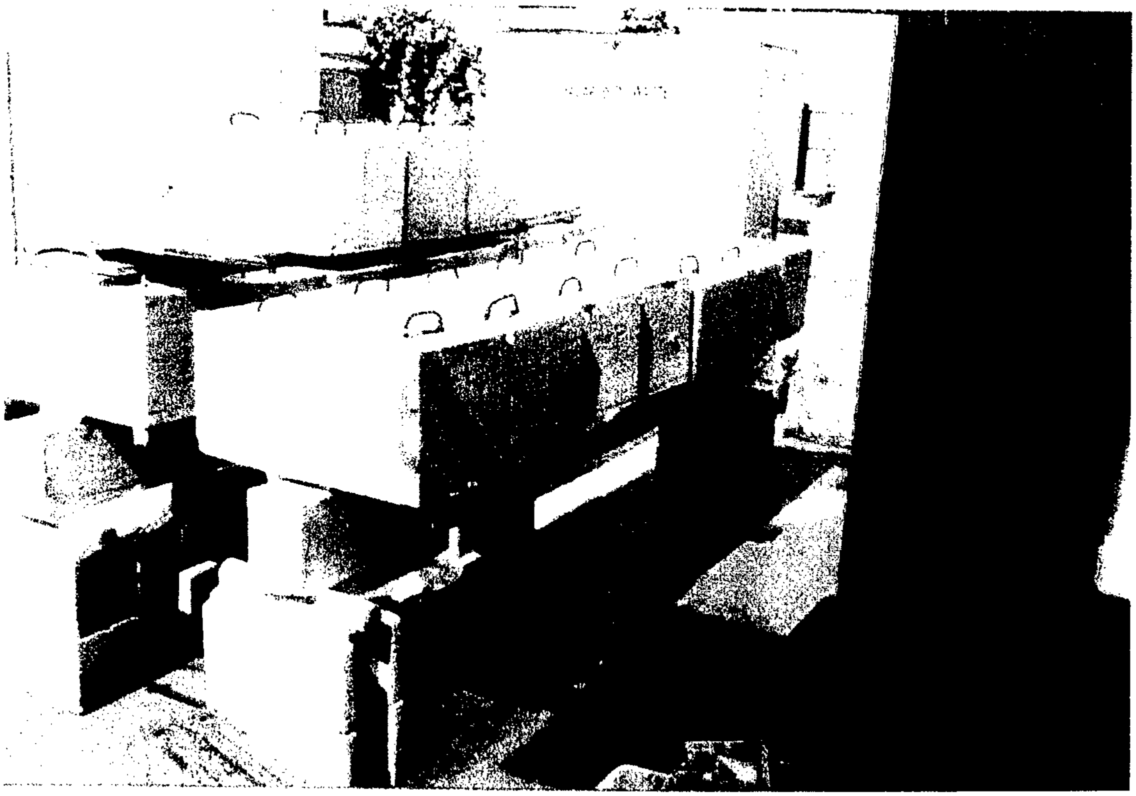

Fig. 6.9 Concrete blocks simulating the sustained distributed load

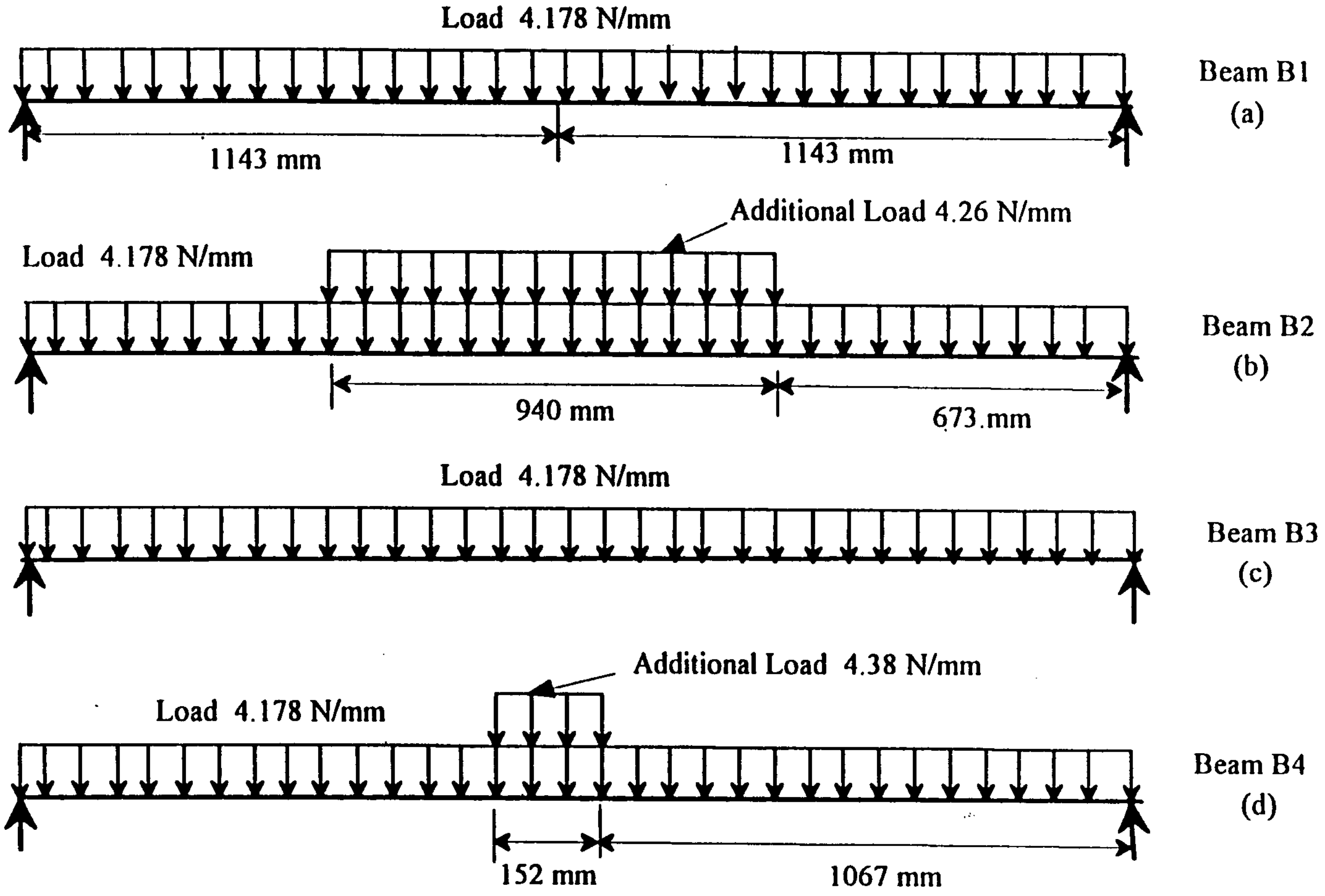

Figure 6.10 Sustained loading on beams

6.3.4 Observations

For the first three weeks, the strains and deflections at the mid-span of the beams were recorded twice a day and thereafter once a day for a three months period. As the recorded data indicated a steady trend, the time interval between successive observations was increased to once a week. It was noticed that new cracks developed during the first couple of weeks in the precracked beams B2, B3, and B4 due to higher load intensity. The measured results are discussed in Chapter 8.

6.4 CFRP REINFORCED CONCRETE COLUMNS

6.4.1 Column casting

Four concrete columns of size 152 mm x 152 mm x 2348 mm (6 in. x 6 in x 8 ft.) were cast and subjected to uniform sustained axial load to study the time dependent behavior (Table 6.3). Each column is reinforced with four 7.5 mm diameter CFRP bars and provided with steel stirrups of 9.53 mm (#3) bars. The stirrup spacing is 152 mm (6 in.) in the middle and 76 mm (3 in.) towards the column ends (Fig. 6.11). The compressive strength of the concrete (f'_c) and modulus of elasticity of the CFRP (E_{CFRP}) are 42.8 MPa and 137 GPa respectively.

Table 6.3 Columns for the creep test

Column	Load applied kN (kips)	Groups
C1	195 (44)	Group I
C2	195 (44)	
C3	293 (66)	Group II
C4	293 (66)	

6.4.2 Instrumentation and test setup

Electrical resistance strain gages were attached to the concrete surface (Fig. 6.12) and embedded inside the columns to measure the strain. The gages were epoxy coated to prevent moisture intrusion that would affect the strain gage functioning over the long time period. A schematic representation of the loading of the columns is shown in the Fig. 6.13. The columns were assembled in two frameworks as shown in Fig. 6.14. Steel end plates were used to ensure a uniform stress distribution . In each framework, two columns were placed horizontally and loaded using a hydraulic jack.

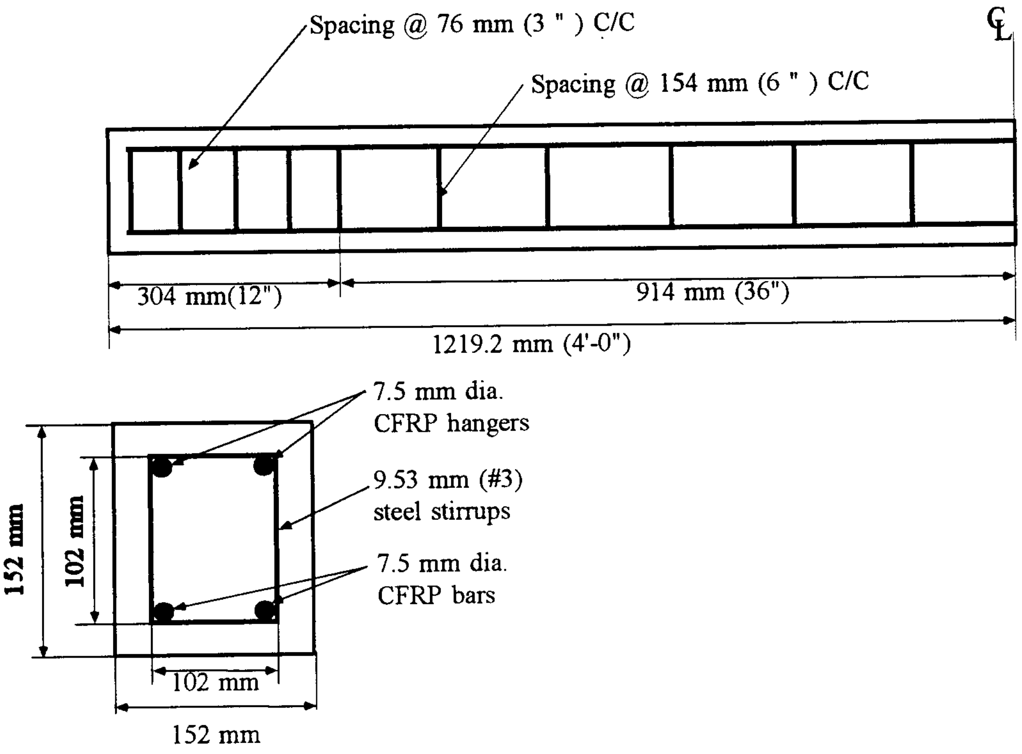

Fig. 6.11 Reinforcement details of concrete columns reinforced with CFRP

Fig. 6.12 Strain gage attached to column surface

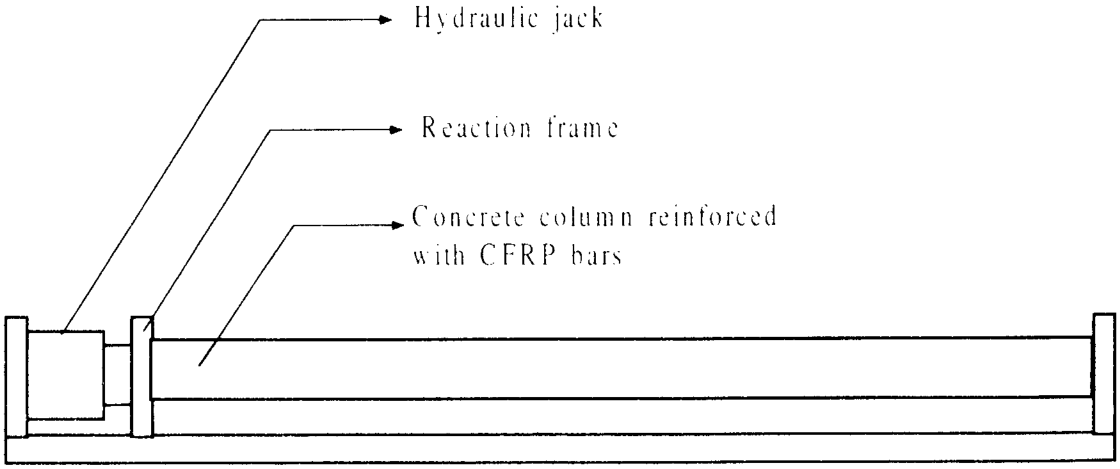

Fig. 6.13 Column test setup

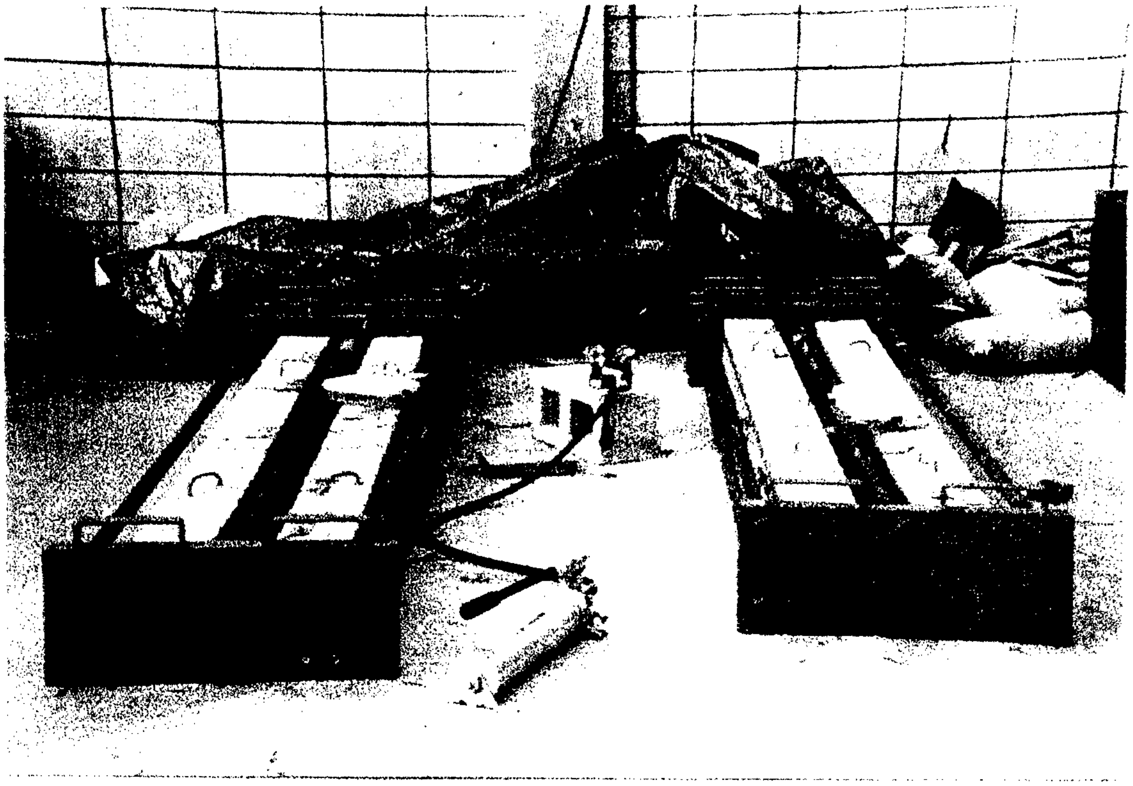

Fig. 6.14 Framework and testing arrangement

6.4.3 Observations

Columns in group I were axially loaded after 22 days of casting and 28 days after those in Group II. The axial sustained loads were 196 kN (44 kips) and 294 kN (66 kips) for groups I and II respectively. These loads correspond to applied stresses of 0.2 f'_c and 0.3 f'_c respectively. Following the application of the loads, readings were taken twice a day for the first two weeks and then once a day. As the recorded data indicated a steady trend, the time interval between successive observations was increased to once a week. The applied sustained loads were checked before measuring time dependent deformations.

CHAPTER 7

ANALYSIS OF TIME DEPENDENT DEFORMATIONS OF CFRP REINFORCED CONCRETE BEAMS AND COLUMNS

7.1 INTRODUCTION

The total deformation at any time is the sum of the instantaneous and time-dependent deformations. The instantaneous deformation due to applied loads can be determined from elastic analysis, whereas the time dependent deformations induced by creep and shrinkage are calculated based on the age-adjusted elastic modulus method [Bazant, 1982].

The concrete beams and columns are reinforced with CFRP bars forming a heterogeneous section. In the analysis, the heterogeneous section is converted into a homogenous section by transforming the properties of the CFRP into equivalent concrete. Transformed area of the reinforced concrete section is the area of the concrete plus m times the area of the CFRP reinforcement

$$A = A_c + m\, A_{CFRP} \tag{7.1}$$

where $m = \frac{E_{CFRP}}{E_c}$, A_c and E_c are the area and the modulus of elasticity of the concrete respectively, A_{CFRP} and E_{CFRP} are respectively the area and the modulus of elasticity of the CFRP.

7.2 ANALYTICAL PREDICTION OF THE LONG TERM DEFORMATION OF THE CONCRETE BEAMS REINFORCED WITH CARBON FRP

The curvature, stresses and deflections are determined immediately after the application of the lateral loads and after a period of time in which creep and shrinkage occur.

7.2.1 Instantaneous deformation

The instantaneous curvature of bending of the section is given by

$$\psi = \frac{M}{E_c(t_0)I} \tag{7.2}$$

where

M = bending moment

$E_c(t_0)$ = modulus of elasticity of concrete at the time of load application

I = moment of inertia of the transformed section

A reinforced concrete member subjected to bending would be free from cracks, when the applied moment is less than the first cracking moment of the section given by,

$$M_r = S\, f_r \tag{7.3}$$

where

S = section modulus of the uncracked section

f_r = modulus of rupture.

After cracking, the internal forces at the cracked section must be resisted by the reinforcement and uncracked part of the concrete section mainly in compression zone and partially in tension. The stiffness of the member at the cracked section is reduced substantially. The weakest section in a cracked member is the section at which a crack is formed. At sections away from the cracks, the entire section contributes in resisting the internal forces and hence to the stiffness of the member. The actual deformation of a cracked member depends on the magnitude of the applied load. The deformations are calculated by interpolation between two extreme cases: i) uncracked section, whereas the full area of concrete is considered effective and ii) fully cracked section, where concrete in tension is completely ignored.

Mean curvature at time of loading t_0 is given by

$$\psi(t_0) = (1-\zeta 1).\psi 1 + \zeta 1.\psi 2 \tag{7.4}$$

where

$\psi 1$ = the instantaneous curvature for an uncracked section

$\psi 2$ = the instantaneous curvature for a cracked section

$\zeta 1$ = the coefficient for instantaneous curvature

$$\zeta 1 = \begin{cases} 1 - \left(\dfrac{M_{\text{cracked}}}{M_{\text{applied}}}\right)^2 & \text{for a cracked section} \\ 0 & \text{for an uncracked section} \end{cases} \tag{7.5}$$

Deflection is calculated assuming parabolic variation of curvature along the member axis, with zero deflection at the ends and maximum at the center. Instantaneous deflection at the center is given by

$$\Delta_i = \frac{\psi(t_0).L^2}{9.6} \qquad (7.6)$$

where

L = span length of the beam

The strain at any fiber is given by

$$\varepsilon(t_0) = \varepsilon_0 + y\psi(t_0) \qquad (7.7)$$

where

ε_0 = instantaneous strain at the centroid of the transformed section

y = distance to the fiber from the reference point O (Fig. 7.1a)

Figure 7.1(b) shows the instantaneous strain distribution due to loading at time t_0 whereas the change in strain distribution for the period $(t-t_0)$ and the total strain variation at time t are shown in Fig. 7.1(c) and 7.1(d) respectively.

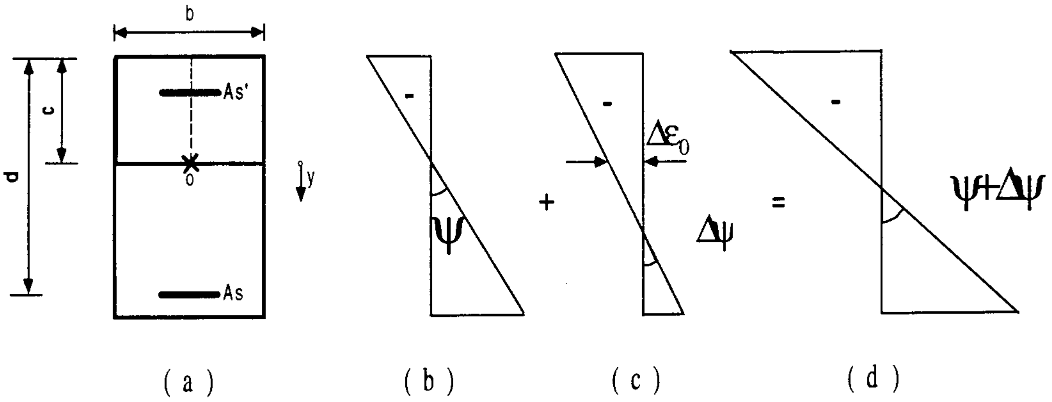

Fig. 7.1 Strain distribution in a cross section

7.2.2 Total deformation including time dependent effects

The mean curvature at time t is given by

$$\psi(t) = (1-\zeta 2).(\psi 1+\Delta\psi 1) + \zeta 2.(\psi 2+\Delta\psi 2) \tag{7.8}$$

where

$\Delta\psi 1$ = the change in curvature of the uncracked section

$\Delta\psi 2$ = the change in curvature of the cracked section

$\zeta 2$ = the coefficient for long-term curvature

$$\zeta 2=\begin{cases} 1-0.5\left(\dfrac{M_{\text{cracked}}}{M_{\text{applied}}}\right)^2 & \text{for a cracked section} \\ 0 & \text{for an uncracked section} \end{cases} \tag{7.9}$$

The change in the deflection at the mid-span from time t_0 to t is given by

$$\Delta_L = \frac{\psi(t).L^2}{9.6} \tag{7.10}$$

The time dependent change in strain at the centroid of the section and curvature due to creep and shrinkage strains are given by

$$\Delta\varepsilon_0 = \eta\ [\ \phi(t, t_0)(\varepsilon_0 + \psi\, y_c) + \varepsilon_{cs}(t, t_0)\ ] \tag{7.11}$$

$$\Delta\psi = \kappa\ [\phi(t, t_0)(\psi + \varepsilon_0 \frac{y_c}{r_c^2}) + \varepsilon_{cs}(t, t_0)\ \frac{y_c}{r_c^2}] \tag{7.12}$$

where

$$r_c^2 = \frac{I_c}{A_c}$$

η = axial strain reduction factor = $\frac{A_c}{A'}$

κ = curvature reduction factor = $\frac{I_c}{I'}$

$\phi(t, t_0)$ = creep coefficient from time t_0 to t

$\varepsilon_{cs}(t, t_0)$ = shrinkage strain from time t_0 to t

y_c = distance between centroids of the effective concrete area and the age adjusted transformed area

A_c = area of concrete

A' = area of the age adjusted transformed section

I_c = moment of inertia of concrete about the centroid after age adjustment

I' = moment of inertia of age adjusted transformed section using modular ratio $m'(t,t_0)$, given by

$$m'(t,t_0) = \frac{E_{CFRP}}{E'_c(t,t_0)} \tag{7.13}$$

where $E'_c(t, t_0)$ = age-adjusted modulus of elasticity of concrete

The strain at any fiber in the transformed section at time t is computed as the algebraic sum of the instantaneous strain and change in strain from time t_0 to t due to creep and shrinkage at the fiber under consideration (Fig. 7.1d). A flowchart for the calculation of the time dependent deformations of the CFRP reinforced concrete beams is shown in Fig. 7.2.

7.3 ANALYTICAL PREDICTION OF THE TIME DEPENDENT STRAINS OF THE CONCRETE COLUMNS REINFORCED WITH CARBON FRP

The strains are determined immediately after the application of the axial loads and after a period of time in which creep and shrinkage occur.

7.3.1 Instantaneous strain

For an axially loaded column, the instantaneous stress is due to the applied load and given by

$$\sigma_c(t_0) = \frac{P}{A_c + mA_{CFRP}} \tag{7.14}$$

The instantaneous or elastic strain at the section is given by

$$\varepsilon_c(t_0) = \frac{\sigma_c(t_0)}{E_c(t_0)} \tag{7.15}$$

where

$E_c(t_0)$ = modulus of elasticity of concrete at the time of application of the load.

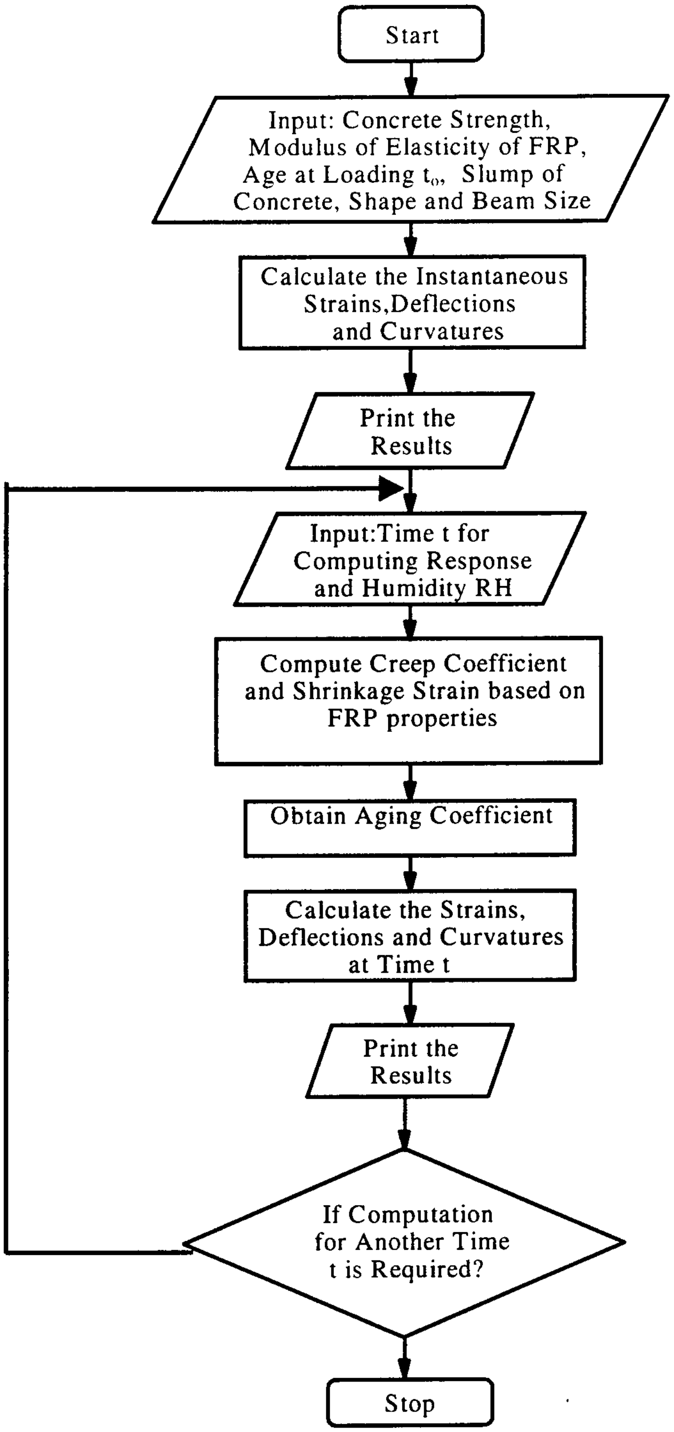

Fig. 7.2 Flowchart for calculation of deformations for CFRP reinforced concrete beams

7.3.2 Time-dependent effects on stress

For a uniformly loaded column member, strain compatibility requires that the strains experienced by concrete and CFRP would be same at any time t;

$$\varepsilon_c(t) = \varepsilon_{CFRP}(t) \tag{7.16}$$

Force equilibrium condition requires that the total load is shared by the concrete and CFRP reinforcement

$$\sigma_c(t)A_c + \sigma_{CFRP}(t)A_{CFRP} = P \tag{7.17}$$

The instantaneous concrete stress is given by

$$\sigma_c(t_0) = \frac{P}{(A_c + mA_{CFRP})} \tag{7.18}$$

From inelastic stress-strain relationship for the concrete

$$\varepsilon_c(t) = \frac{\sigma_c(t_0)}{E_c}(1-\lambda)\varphi(t,t_0) + \frac{\sigma_c(t)}{E_c}(1+\lambda)\varphi(t,t_0) \tag{7.19}$$

Elastic stress-strain relationship for CFRP

$$\varepsilon_{CFRP} = \frac{\sigma_{CFRP}(t)}{E_{CFRP}} \tag{7.20}$$

Solving the equations (7.16-7.20),

$$\sigma_c(t_0).(A_c + mA_{CFRP}) = \sigma_c(t).A_c + mA_{CFRP}[\sigma_c(t_0)(1-\lambda)\varphi(t,t_0) + \sigma_c(t)(1+\lambda\varphi(t,t_0))] \tag{7.21}$$

$$\sigma_c(t) = \frac{\sigma_c(t_0).(A_c + mA_{CFRP} - mA_{CFRP}(1-\lambda).\varphi(t,t_0))}{A_c + mA_{CFRP}(1+\lambda.\varphi(t,t_0))} \tag{7.22}$$

Under uniform sustained stress, the total strain is the sum of the instantaneous creep and shrinkage strains. The magnitude of the applied stress in the concrete member changes with time due to creep and shrinkage. The total strain at any time, t is the sum of the instantaneous strain and strains due to creep and shrinkage and given by

$$\varepsilon_c(t) = \underset{\text{Elastic strain}}{\varepsilon_c(t_0)} + \underset{\text{Creep strain}}{\varepsilon_C(t,t_0)} + \underset{\text{Shrinkage strain}}{\varepsilon_{cs}(t,t_0)} \tag{7.23}$$

$$\varepsilon_c(t) = \frac{\sigma_c(t_0)}{E_c(t_o)}[1+\varphi(t,t_0)] + \int \frac{1+\varphi(t,\tau)}{E_c(\tau)} d\sigma_c(\tau) + \varepsilon_{cs}(t,t_0) \tag{7.24}$$

where

$$\int \frac{1+\varphi(t,\tau)}{E_c(\tau)} d\sigma_c(\tau) = \frac{\Delta\sigma_c(t)}{E_c(t_o)}[1+\lambda\varphi(t,t_0)] \tag{7.25}$$

$$\varepsilon_{ct} = \frac{\sigma_c(t_0)}{E_c(t_o)}[1+\varphi(t,t_0)] + \frac{\Delta\sigma_c(t)}{E_c(t_o)}[1+\lambda\varphi(t,t_0)] + \varepsilon_{cs}(t,t_0) \tag{7.26}$$

where

$E_c(\tau)$ = Modulus of elasticity of concrete at age τ

P = Load applied at column ends

τ = Intermediate age between t_0 and t

$\sigma_c(t_0)$ = Initial stress applied at age t_0

$\sigma_c(t)$ = Stress at age t

$\Delta\sigma_c(t)$ = Change in stress level from time t_0 to t

$d\sigma_c(\tau)$ = Elemental stress applied at age τ

$\varepsilon_c(t)$ = Total strain in concrete at time t

$\varepsilon_{CFRP}(t)$= Total strain in carbon FRP bars at time t

$\phi(t,\tau)$ = Coefficient of creep for loading at age τ

λ = Aging coefficient from Bazant's Table (Appendix A)

The creep coefficient and free shrinkage strain are calculated based on the ACI model and CEB-FIP model (Appendix A) for the prediction of creep and shrinkage effects. The flow chart for the calculation of the time dependent deformations of the CFRP reinforced concrete columns is shown in Fig. 7.3.

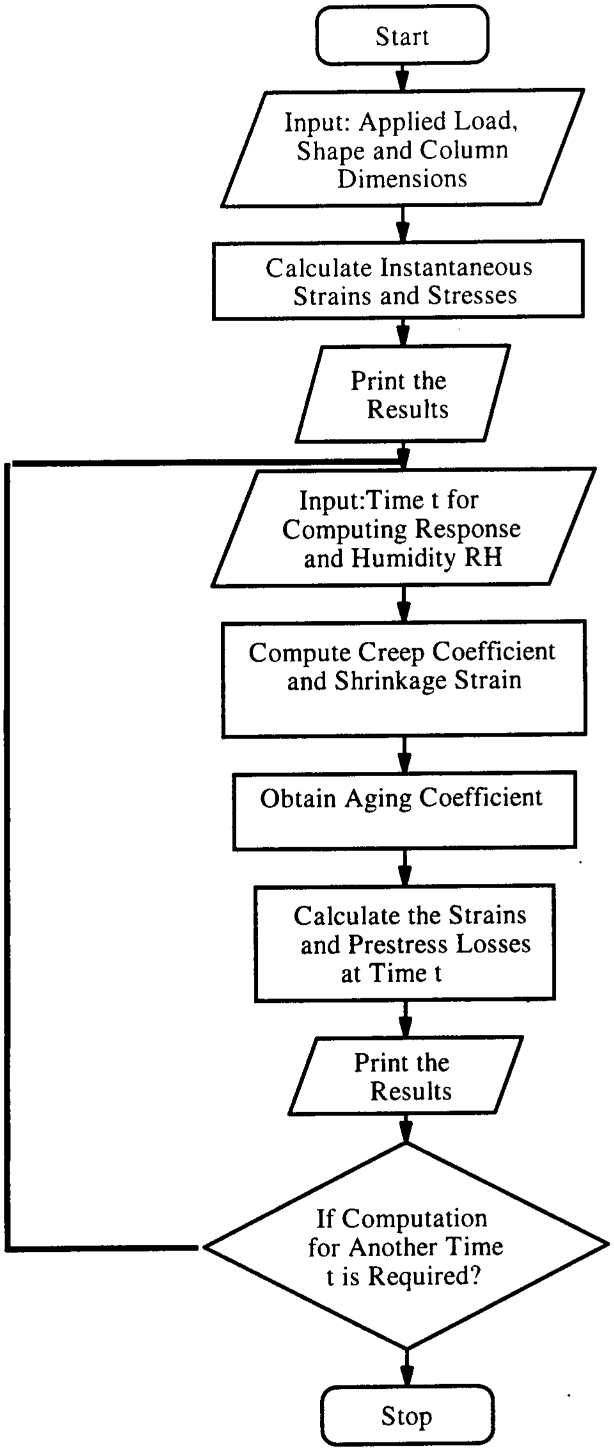

Fig. 7.3 Flowchart for calculation of deformations for CFRP reinforced concrete columns

CHAPTER 8

COMPARISON OF ANALYTICAL AND EXPERIMENTAL TIME DEPENDENT DEFORMATIONS

8.1 INTRODUCTION

The measured time dependent deformations of the beams and columns reinforced with CFRP are compared with the theoretical values. The age-adjusted elastic modulus method is used for the calculation of the deformations. The creep coefficient and the shrinkage strain are based on the ACI and CEB models. The creep and shrinkage of concrete is influenced by various factors, which depend on the environment and concrete mix. Table 8.1 shows the influence of several factors on the long-term deformations.

The test setup for both the beams and columns are arranged in an open-air test facility in tropical weather conditions. The predicted deformations take into account the change in the relative humidity of the atmosphere, CFRP material characteristics, member size, concrete strength, sustained load intensity and duration of loading. The analytical results are calculated based on the creep and shrinkage coefficients considering the recorded daily maximum and minimum relative humidities.

Table 8.1 Factors affecting the long-term deformations

Factors	Long – term deformations	
	Decrease	Increase
Concrete mix		
Cement content of concrete	Decrease of cement content	Increase of cement content
Water-cement ratio	Lower w/c ratio	Higher w/c ratio
Sand-gravel ratio	Concrete mix with relatively high percentage of gravel	Concrete mix with relatively high percentage of sand
Environment		
Relative humidity	High relative humidity	Low relative humidity
E_c- Modulus of concrete (only for creep strain)	High modulus of elasticity	Low modulus of elasticity
Curing of concrete	Cooling of concrete after pouring	No cooling

8.2 BEAMS REINFORCED WITH CFRP BARS

The observed deformations are compared with the analytical results based on ACI and CEB coefficients. Comparisons of the deformations are also made for the members at different stress levels. The deflections, strains and curvatures at the mid-span of the beams reinforced with CFRP are compared with the theoretical values.

8.2.1 Deflections

Fig. 8.1 shows the time dependent deflections at the mid-span for the beams B1, B2, B3 and B4. The deflections at the mid-span increase with time. The load intensity in beam B3 is smaller than that in beam B4 and hence beam B3 exhibits smaller long-term deflections than those of beam B4. Beam B1 remained uncracked and exhibited a very small increase in long term-deflection. The increase in deflections over the instantaneous values for a period of 540 days is 15%, 115%, 65% and 71 % for beams B1, B2, B3 and B4 respectively. Beams B1 and B2 showed an increase in deflections of 28%, and 125 % after a period of 690 days.

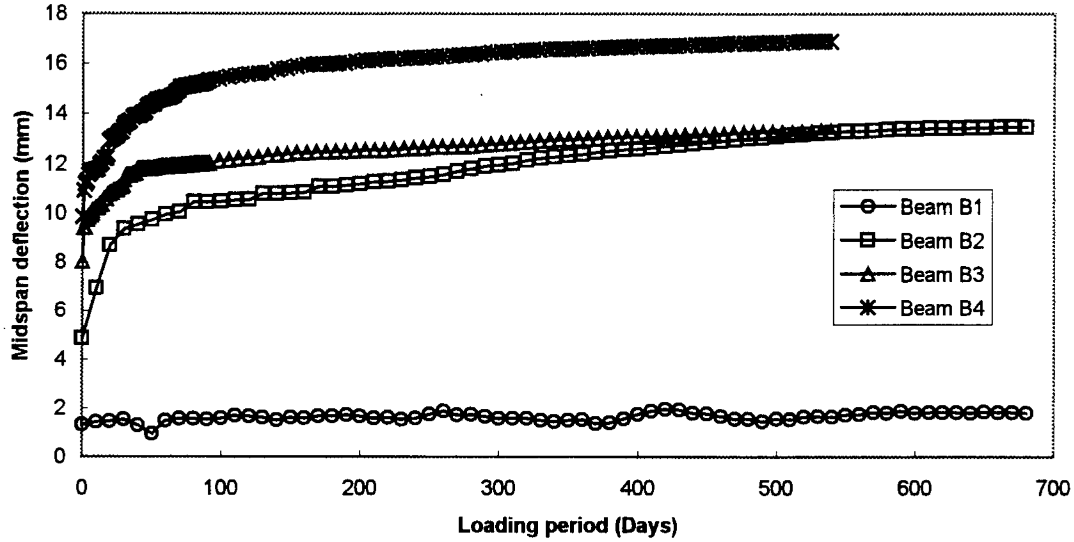

Fig. 8.1 Measured long term deflection variations with time

The deflections at the midspan for the beam B1 are compared with the theoretical results based on ACI and CEB coefficients (Figs. 8.2a and 8.2b) . The comparisons for the beams B2, B3 and B4 based on ACI and CEB coefficients are shown in Figs. 8.3-8.5. The mid-span deflections compared well with the theoretical values. A larger difference between the experimental and theoretical deflections was observed at the initial period and the deflections tend to remain constant with time.

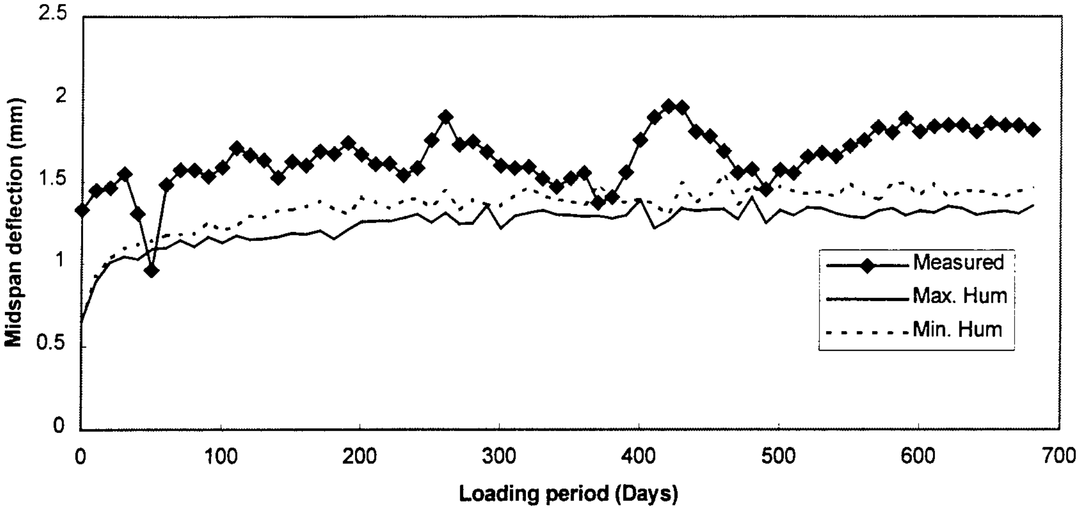

Fig. 8.2a Comparison of midspan deflection with the analytical predictions based on ACI coefficients for beam B1

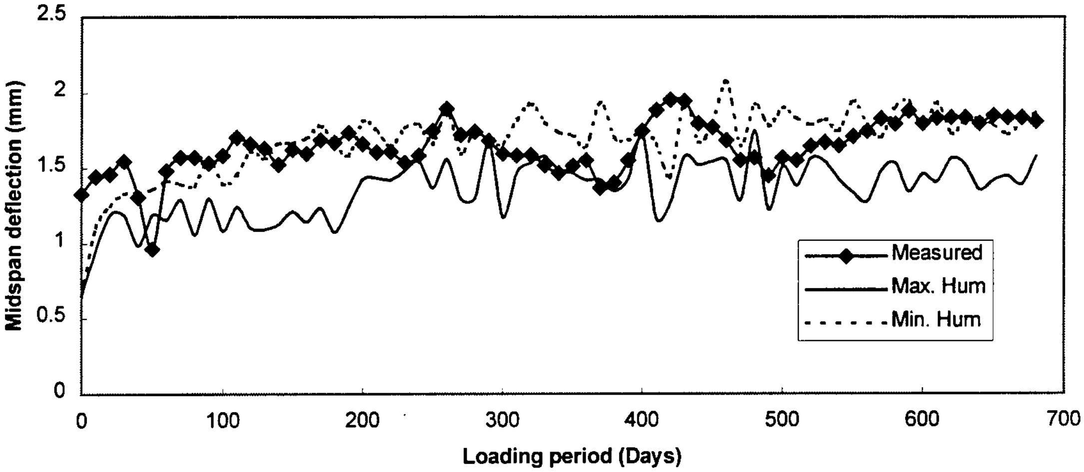

Fig. 8.2b Comparison of midspan deflection with the analytical predictions based on CEB coefficients for beam B1

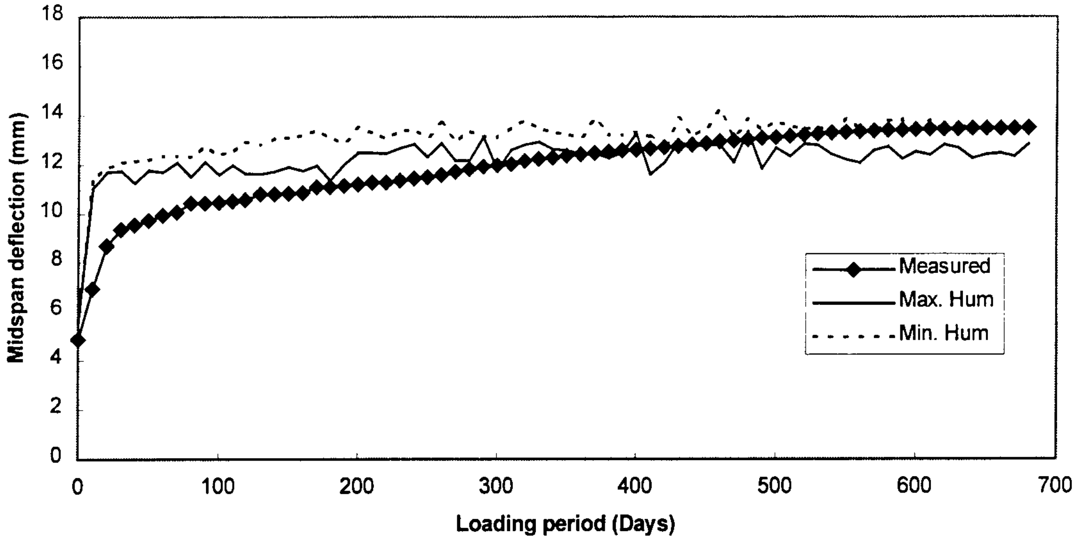

Fig. 8.3a Comparison of mid span deflection with the analytical predictions based on ACI coefficients for beam B2

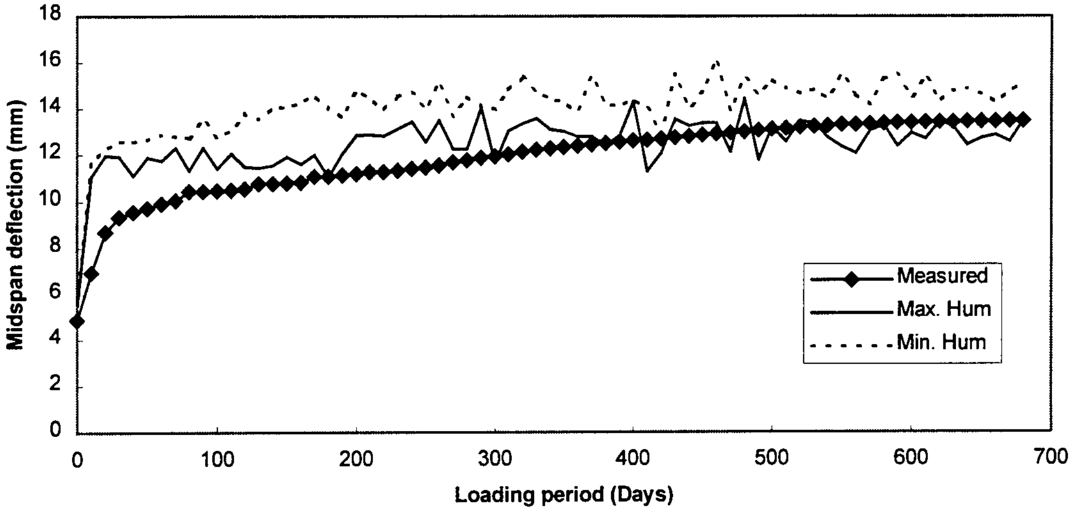

Fig. 8.3b Comparison of midspan deflection with the analytical predictions based on CEB coefficients for beam B2

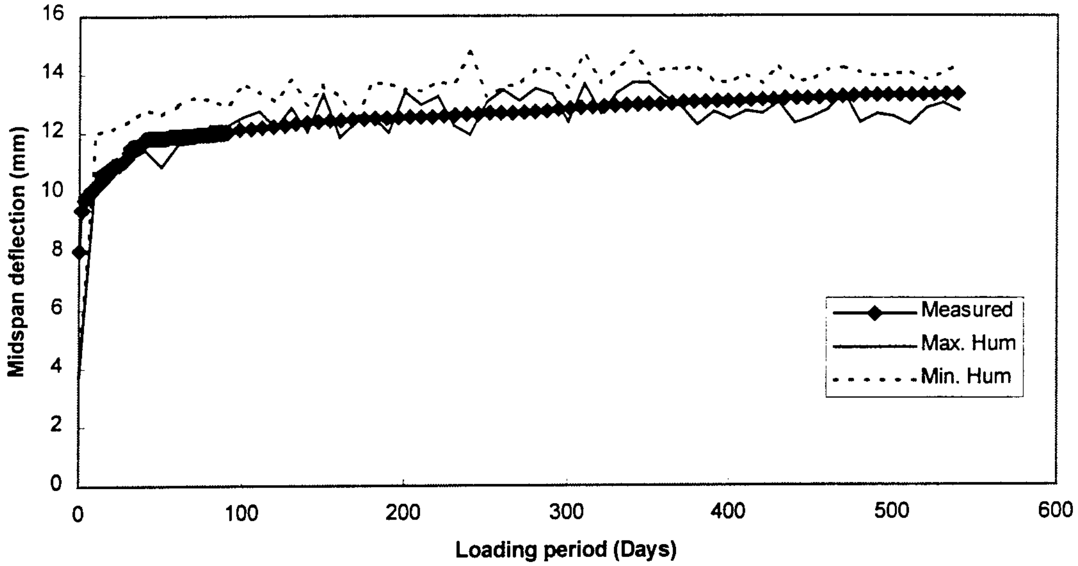

Fig. 8.4a Comparison of midspan deflection with the analytical predictions based on ACI coefficients for beam B3

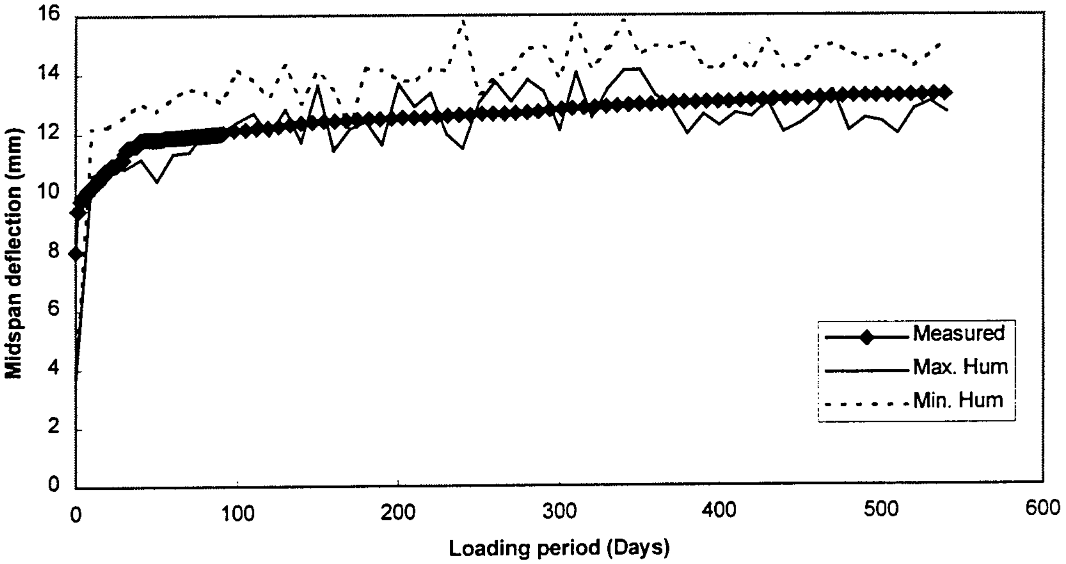

Fig. 8.4b Comparison of midspan deflection with the analytical predictions based on CEB coefficients for beam B3

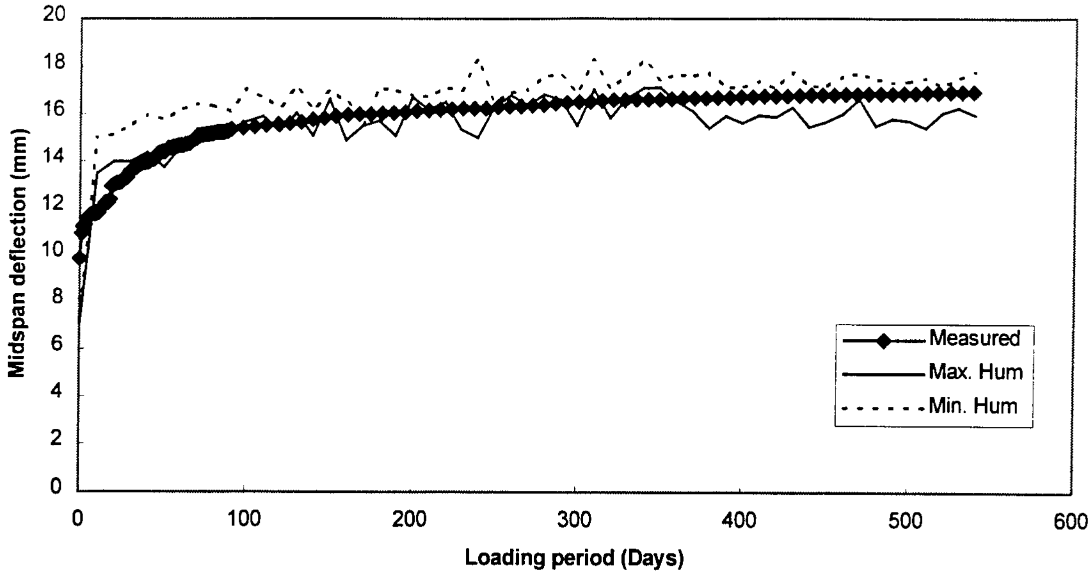

Fig. 8.5a Comparison of midspan deflection with the analytical predictions based on ACI coefficients for beam B4

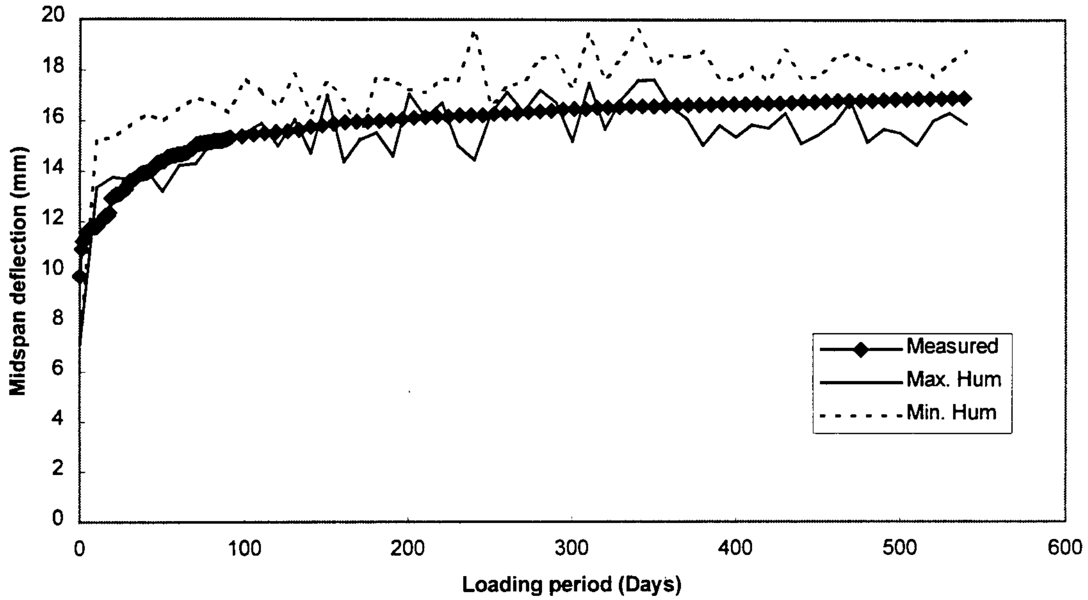

Fig. 8.5b Comparison of midspan deflection with the analytical predictions based on CEB coefficients for beam B4

8.2.2 Concrete strains

Fig. 8.6 shows the total time dependent compressive strains observed at the top concrete surface for beams B1, B2, B3 and B4. Beam B1 was subjected to a load intensity less than beam B2 and was uncracked and hence it exhibited smaller compressive strain. The compressive strain at the top surface of the beam B4 is only marginally larger than that in beam B3, since the load intensity in beam B4 is more than that in beam B3. The increase in the strain over the instantaneous value for a period of 540 days is 101%, 151 %, 209 % and 245 % for beams B1, B2, B3 and B4 respectively. The strains observed at different levels for the beams B1, B2, B3, and B4 are given in Figs. 8.7-8.10.

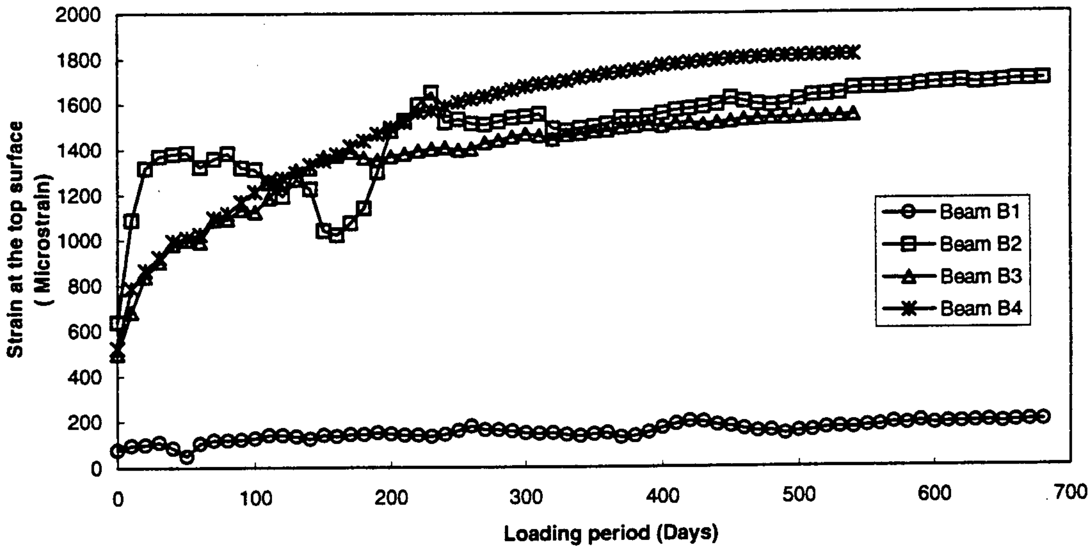

Fig. 8.6 Compressive strain observed at the top surface of the beams

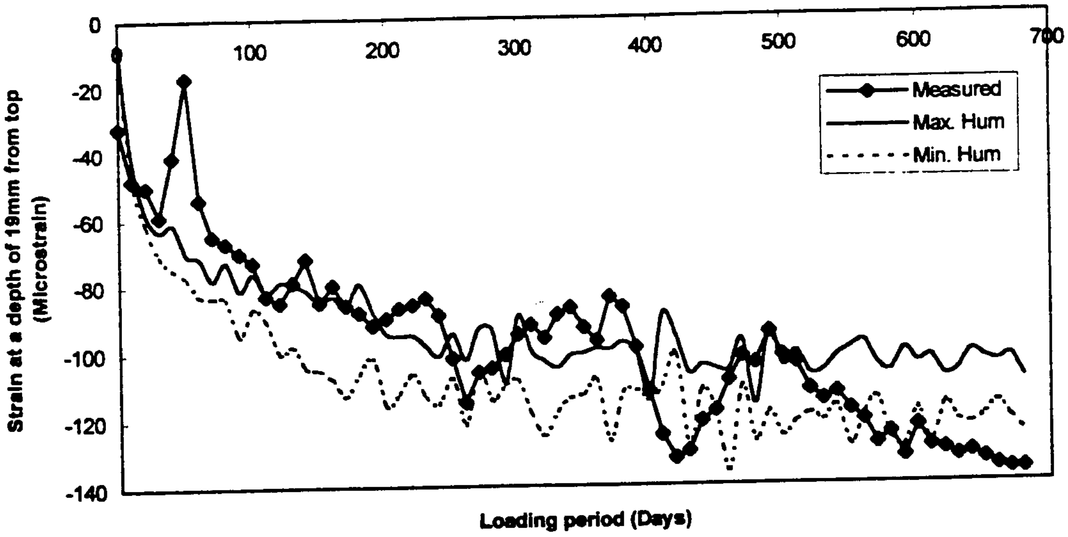

Fig. 8.7a Comparison of strain at a depth of 19 mm from top with the analytical predictions based on ACI coefficients for beam B1

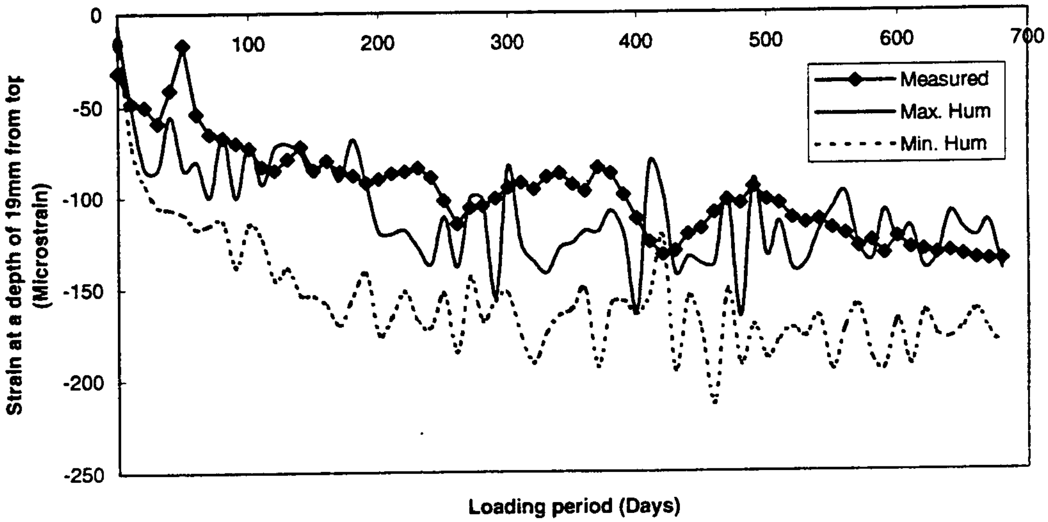

Fig. 8.7b Comparison of strain at a depth of 19 mm from top with the analytical predictions based on CEB coefficients for beam B1

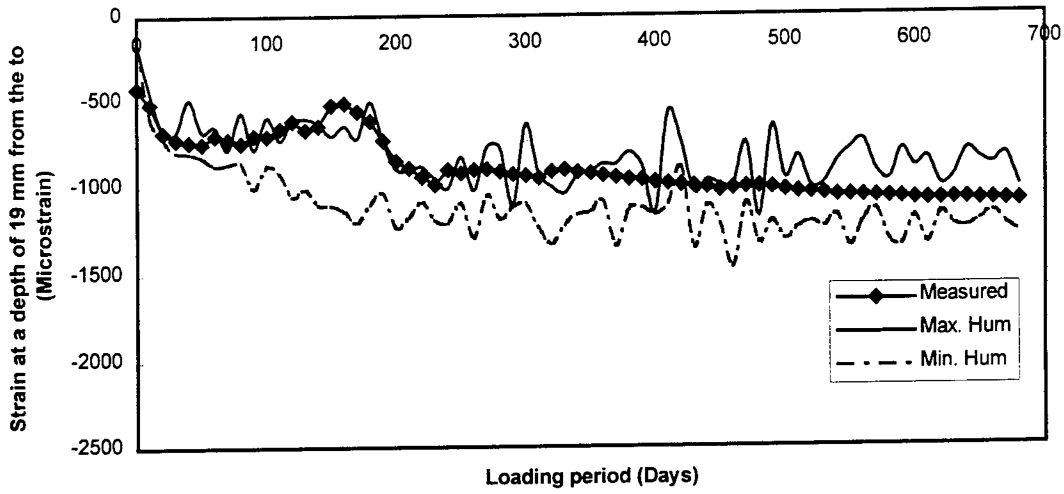

Fig. 8.8a Comparison of strain at a depth of 19 mm from top with the analytical predictions based on ACI coefficients for beam B2

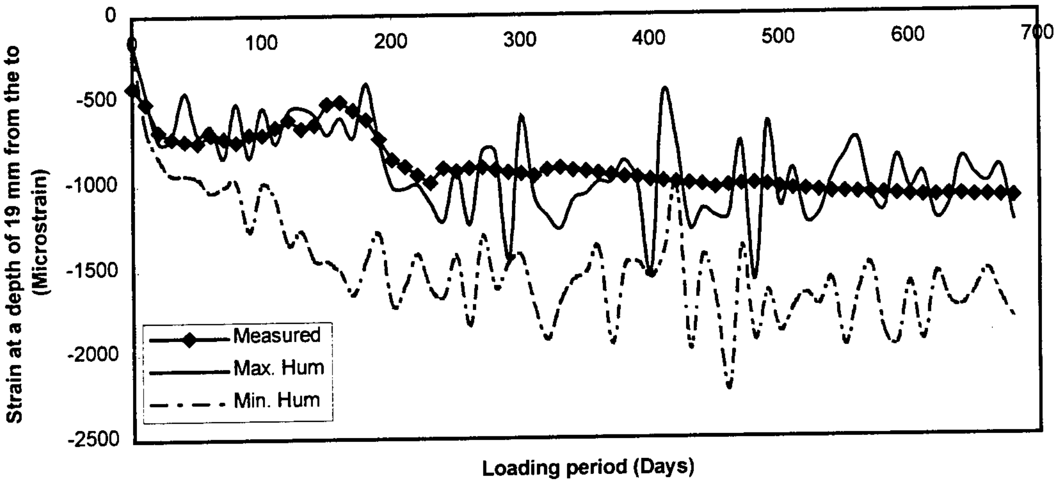

Fig. 8.8b Comparison of strain at a depth of 19 mm from top with the analytical predictions based on CEB coefficients for beam B2

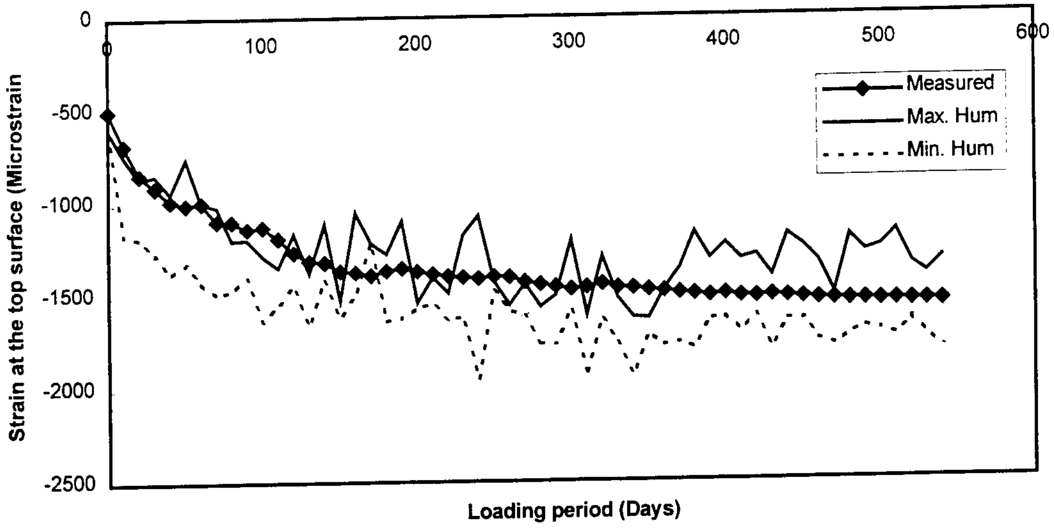

Fig. 8.9a Comparison of strain at top surface with the analytical predictions based on ACI coefficients for beam B3

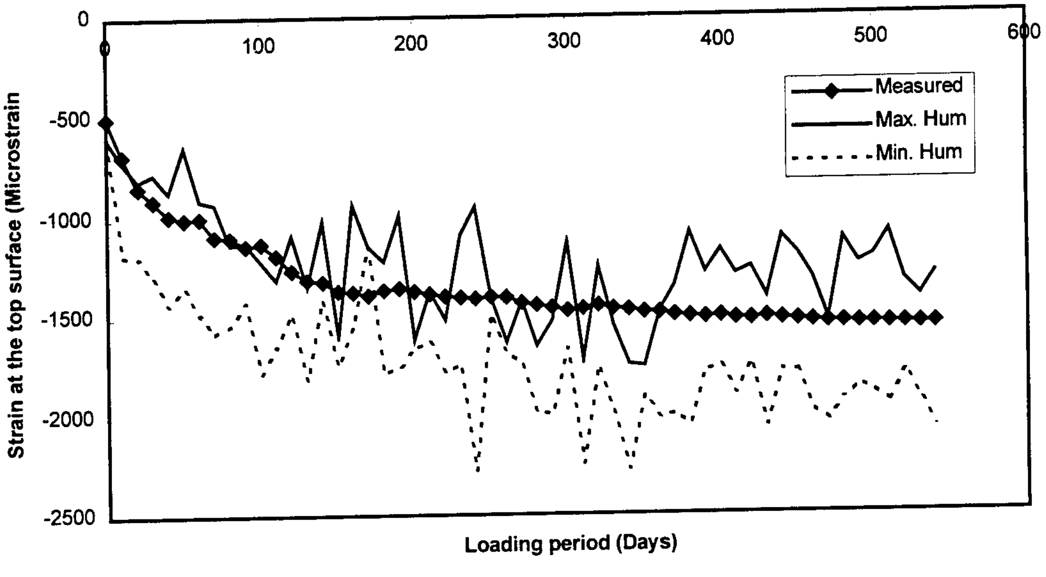

Fig. 8.9b Comparison of strain at top surface with the analytical predictions based on CEB coefficients for beam B3

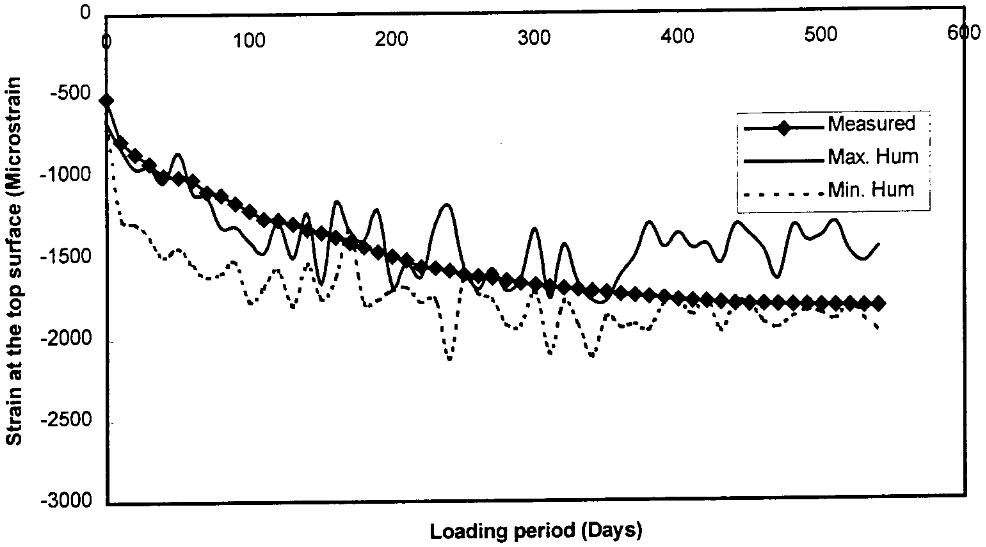

Fig. 8.10a Comparison of strain at top surface with the analytical predictions based on ACI coefficients for beam B4

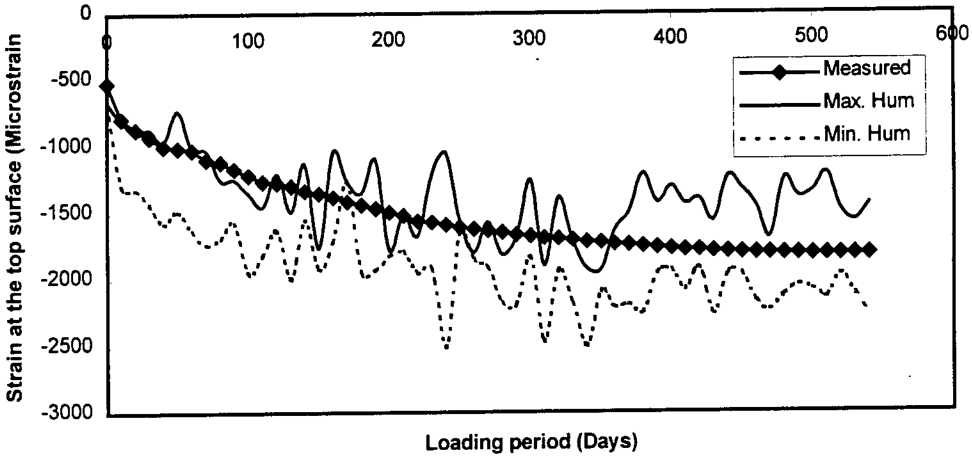

Fig. 8.10b Comparison of strain at top surface with the analytical predictions based on CEB coefficients for beam B4

8.2.3 Curvature

Figure 8.11 shows the variation of the curvature observed at the mid-span of the beams B2, B3, and B4. The beam B2 with a larger depth than B3 and B4 shows a smaller curvature. The load intensity in beam B3 is smaller than that in beam B4 and hence it exhibited curvatures smaller than those of B4.

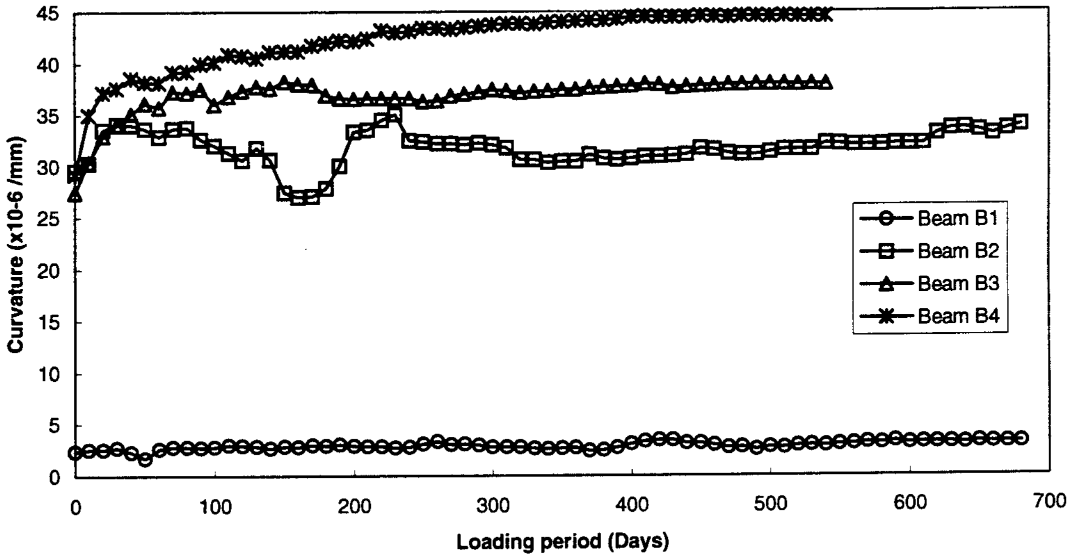

Fig. 8.11 Variation of curvature with time

The curvatures at the mid-span calculated based on the strains observed at different depths are compared with the theoretical values and presented in Figs. 8.12-8.15 for beams B1, B2, B3 and B4 respectively.

The curvatures at the mid-span calculated based on the strains observed at different depths are compared with the theoretical values and presented in Figs. 8.12-8.15 for beams B1, B2, B3 and B4 respectively.

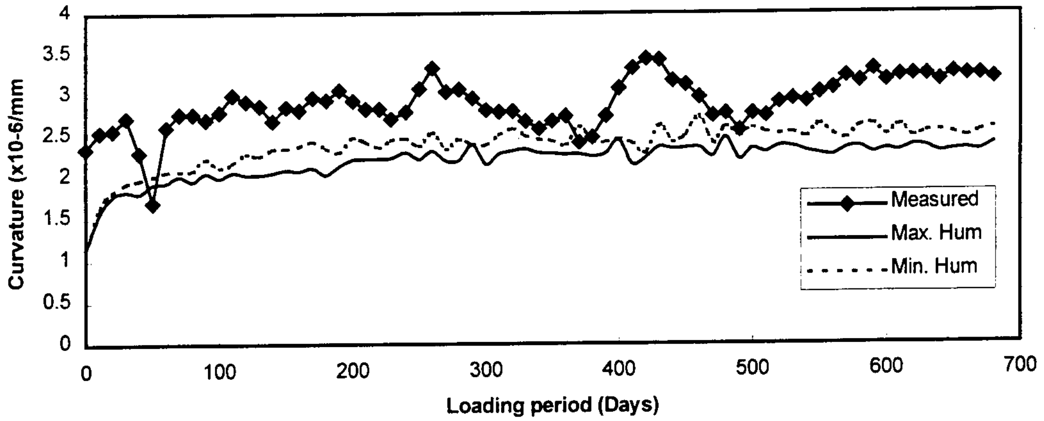

Fig. 8.12a Comparison of curvature at mid-span with the analytical predictions based on ACI coefficients for beam B1

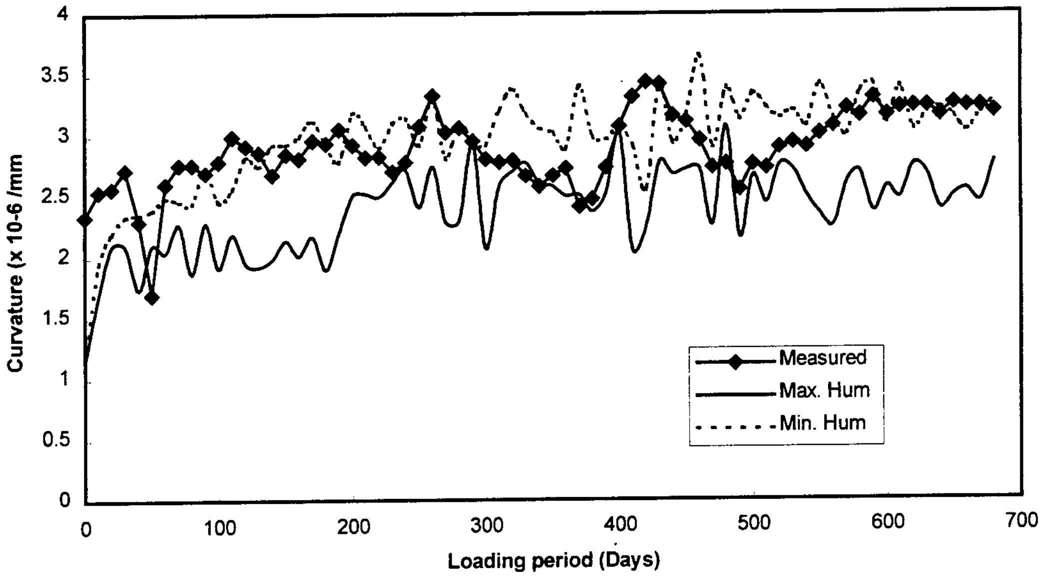

Fig. 8.12b Comparison of curvature at midspan with the analytical predictions based on CEB coefficients for beam B1

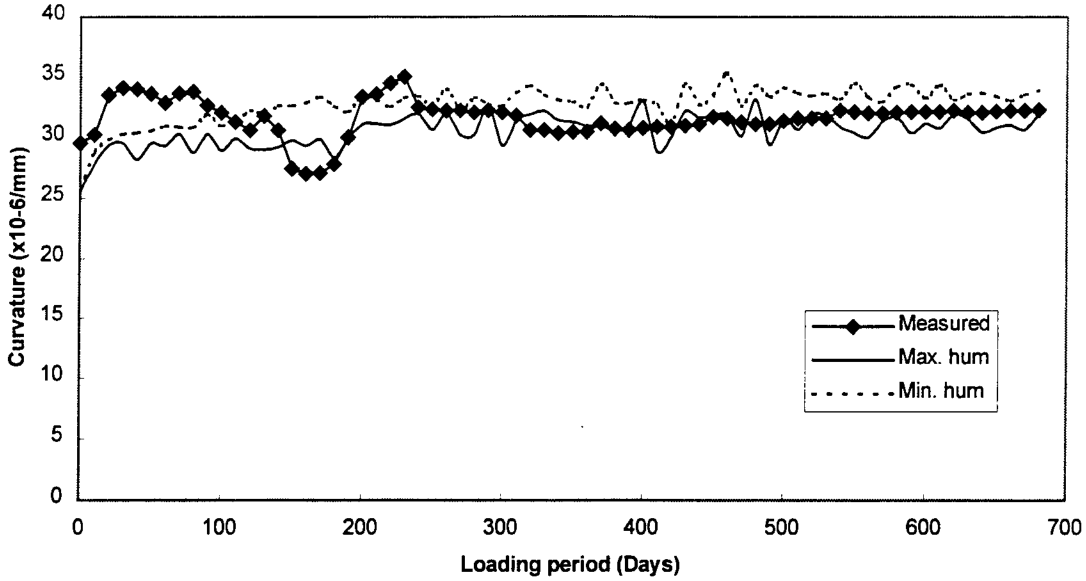

Fig. 8.13a Comparison of curvature at midspan with the analytical predictions based on ACI coefficients for beam B2

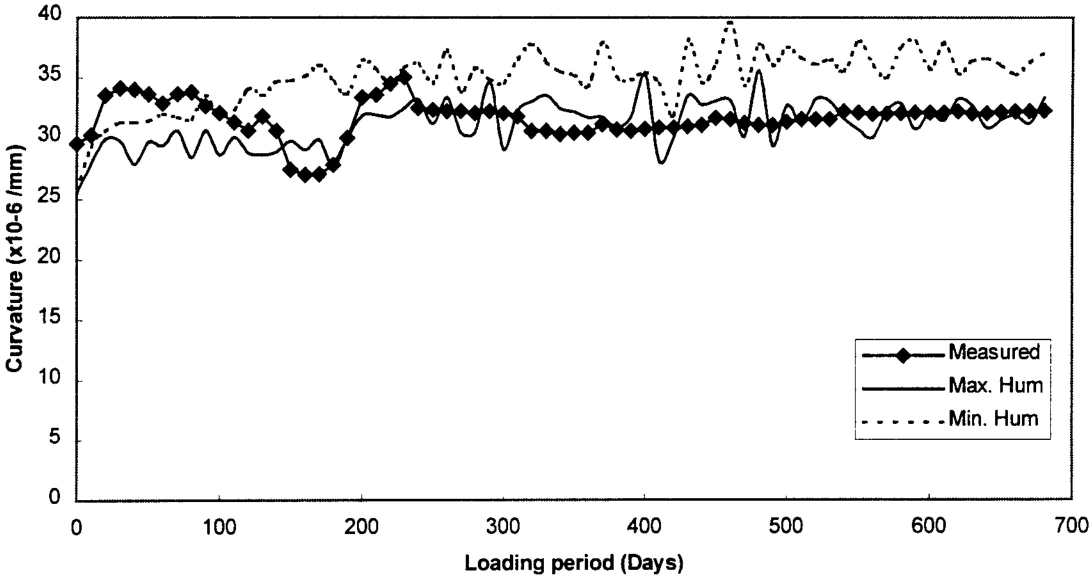

8.13b Comparison of curvature at midspan with the analytical predictions based on CEB coefficients for beam B2 Fig.

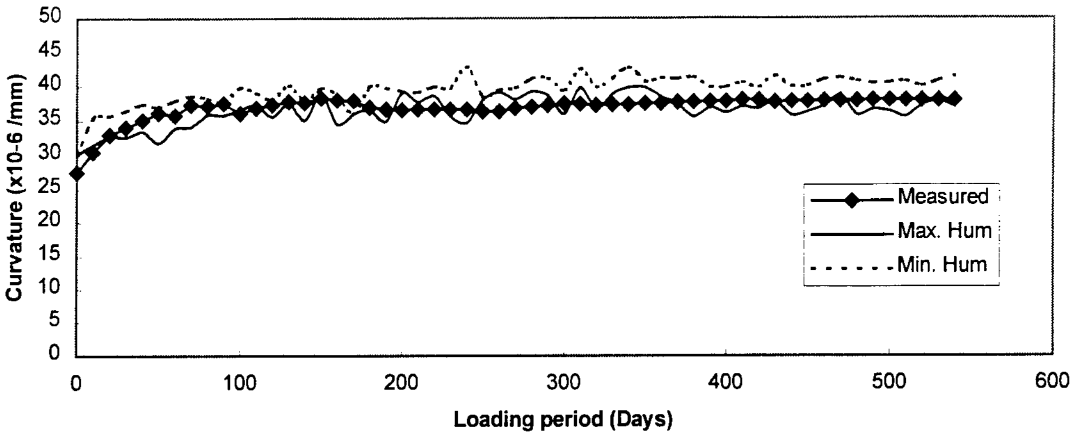

Fig. 8.14a Comparison of curvature at midspan with the analytical predictions based on ACI coefficients for beam B3

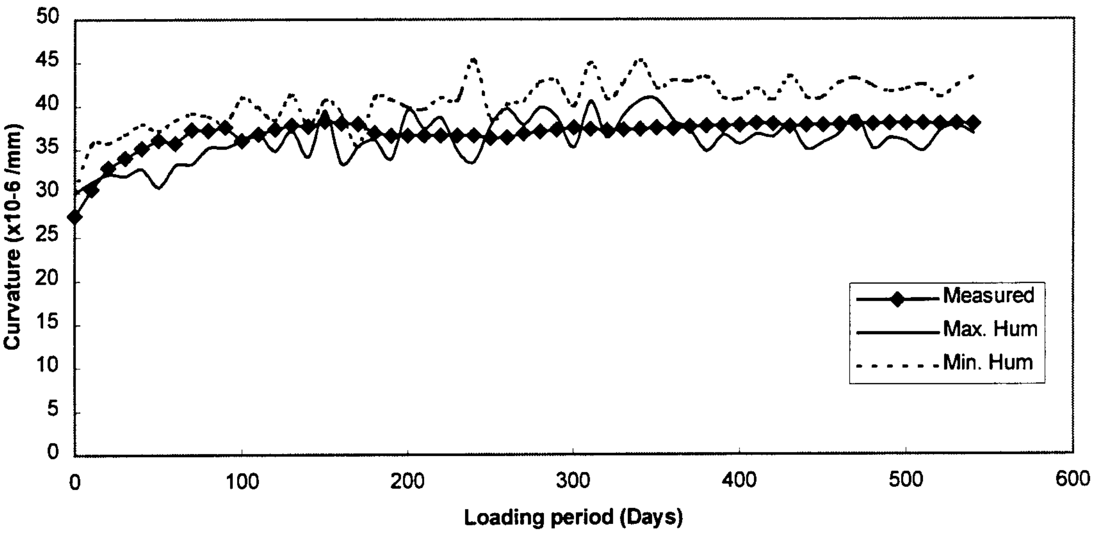

Fig. 8.14b Comparison of curvature at midspan with the analytical predictions based on CEB coefficients for beam B3

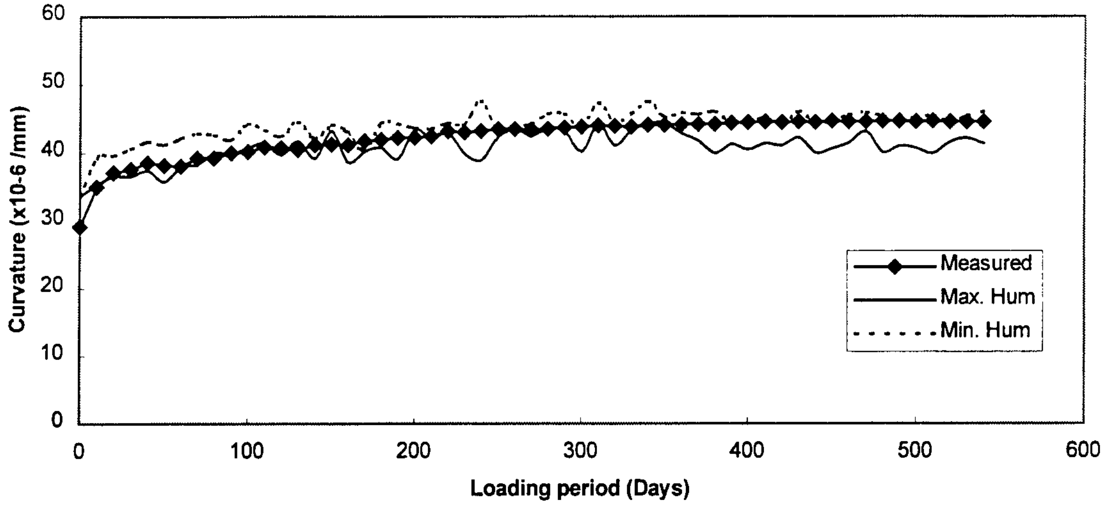

Fig. 8.15a Comparison of curvature at midspan with the analytical predictions based on ACI coefficients for beam B4

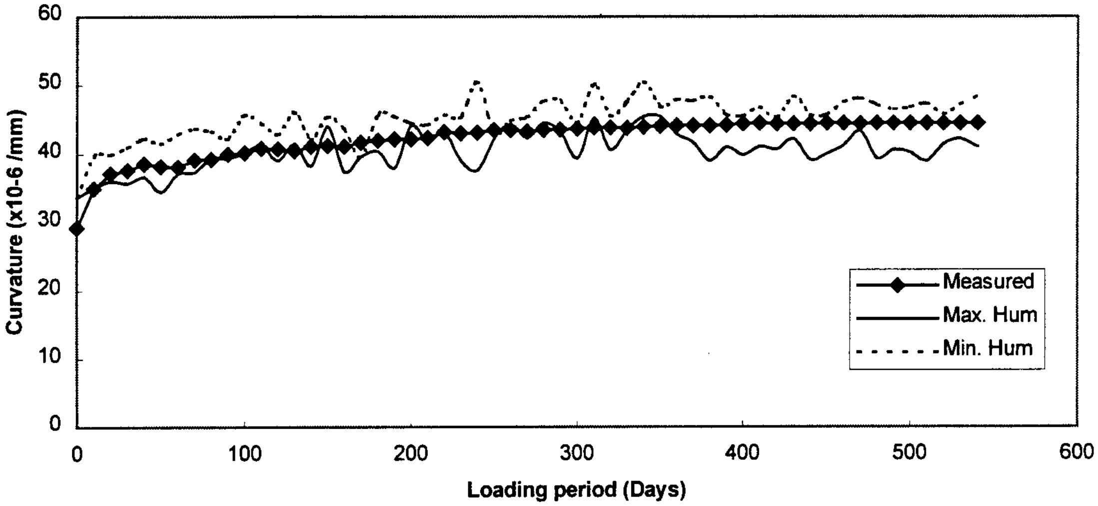

Fig. 8.15b Comparison of curvature at midspan with the analytical predictions based on CEB coefficients for beam B4

8.2.4 Proposed Equation for long-term Deflection

The calculation of long-term deflection at any time t is a tedious and complex process. The ACI 318-95 code recommends that the additional long-term deflection resulting from creep and shrinkage of steel reinforced concrete beams can be obtained by multiplying the instantaneous deflection by a factor. The additional long-term deflection for beams reinforced with CFRP bars can be determined in a similar manner by multiplying the instantaneous deflection by a modified factor. The following equation for the modified factor is proposed based on the experimental data and given by

$$\lambda = \frac{x}{1+50m\rho'} \tag{8.1}$$

where m = modular ratio of the reinforcement = $\frac{E_{CFRP}}{E_{Steel}}$, ρ' = compression reinforcement ratio of CFRP bars and x = time dependent factor for sustained load. Fig. 8.16 shows the variation of time-dependent factor x for beams reinforced with CFRP and ACI specified values for the steel reinforced concrete beams. Recommended values of time-dependent factor x for the beams reinforced with CFRP are shown in Fig. 8.16 and Table 8.2.

Table 8.2 Recommended time-dependent factor x

Loading period	ACI 318-95 for steel reinforced concrete beams	Proposed values based on experiments for CFRP reinforced concrete beams
3 months	1.0	0.7
6 months	1.2	0.85
12 months	1.4	1.15
5 or more years	2.0	1.4*

* This value is based on data obtained for 2 year period.

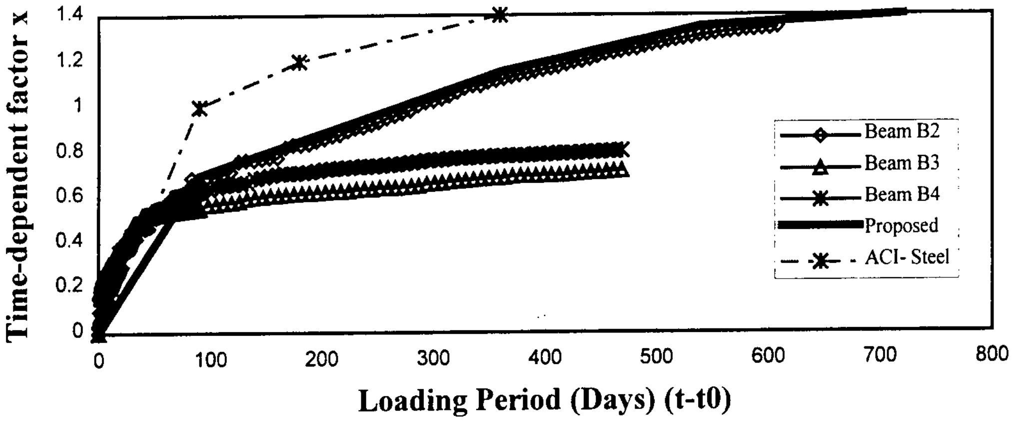

Fig. 8.16 Variation of time-dependent factor x

8.3 COLUMNS REINFORCED WITH CFRP

8.3.1 Comparison of strains

Fig. 8.17 shows the variation of the strain with time for the concrete columns reinforced with CFRP under different stress levels. The strains increase with the increase in stress level and under the sustained loading condition. Fig. 8.18 and 8.19 shows the comparison of the experimental and analytical results for columns in groups I and II. The analytical predications are based on the method outlined in Chapter 7 using the ACI and CEB coefficients for creep and shrinkage. The maximum and minimum relative humidities recorded on the days of measurements are used in the strain predictions. The measured compressive strains agree reasonably with the analytical values.

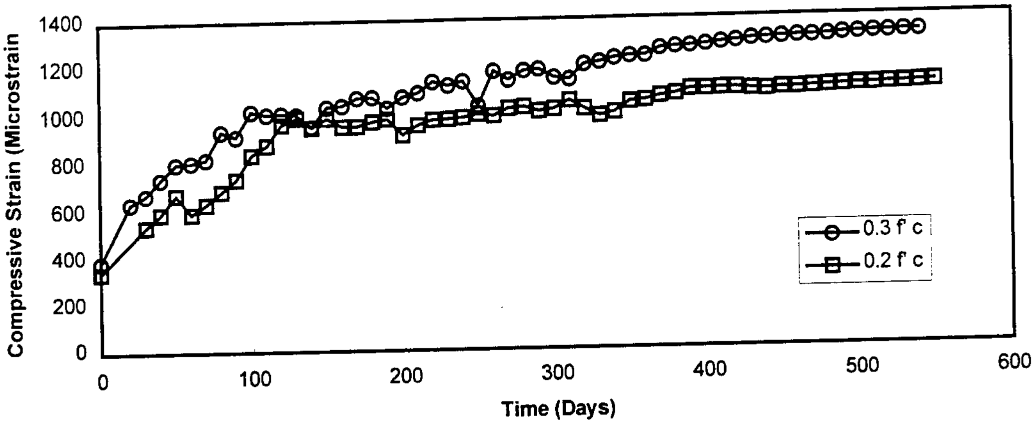

Fig. 8.17 Variation of compressive strain with time at different stress level

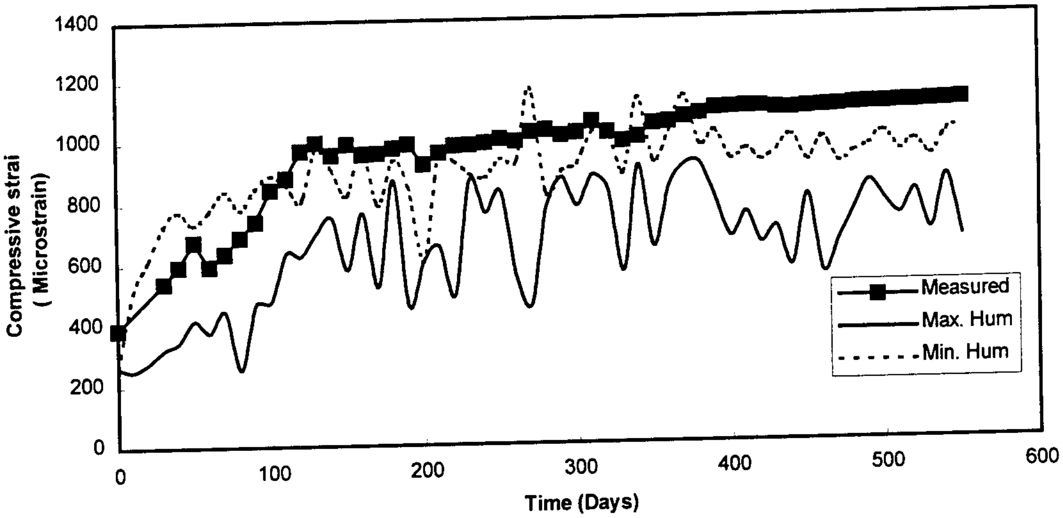

Fig. 8.18a Comparison of strain with the analytical predictions based on ACI coefficients for column group I

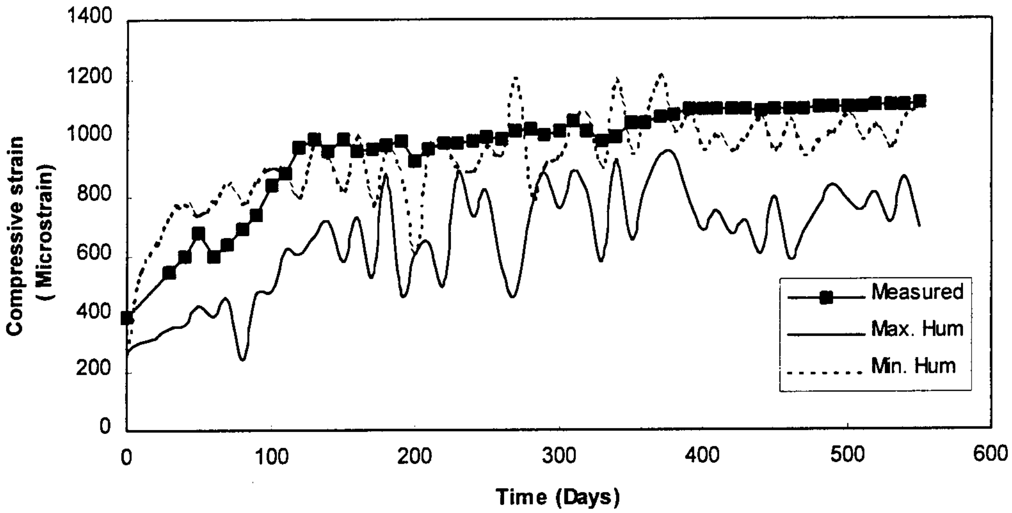

Fig. 8.18b Comparison of strain with the analytical predictions based on CEB coefficients for column group I

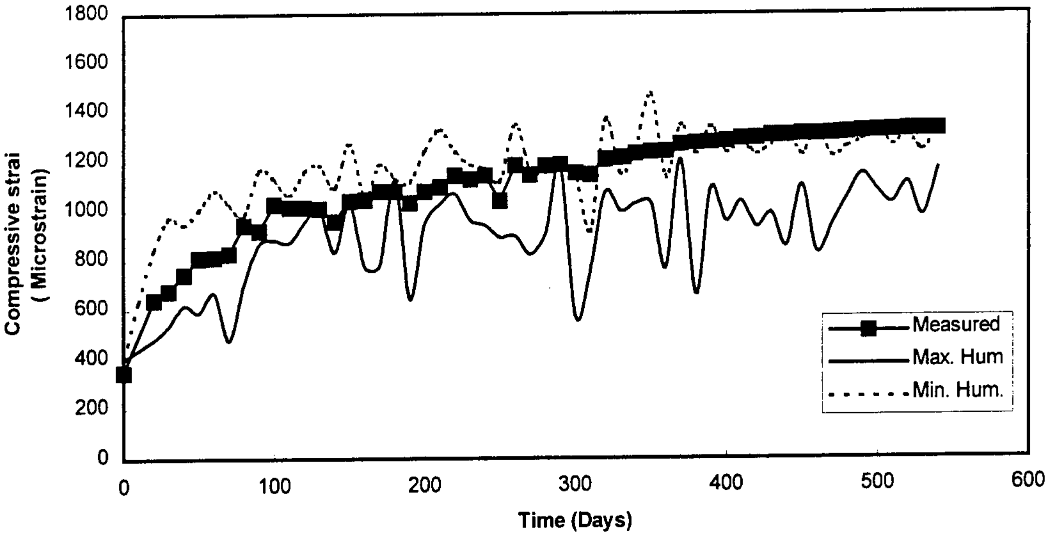

Fig. 8.19a Comparison of strain with the analytical predictions based on ACI coefficients for column group II

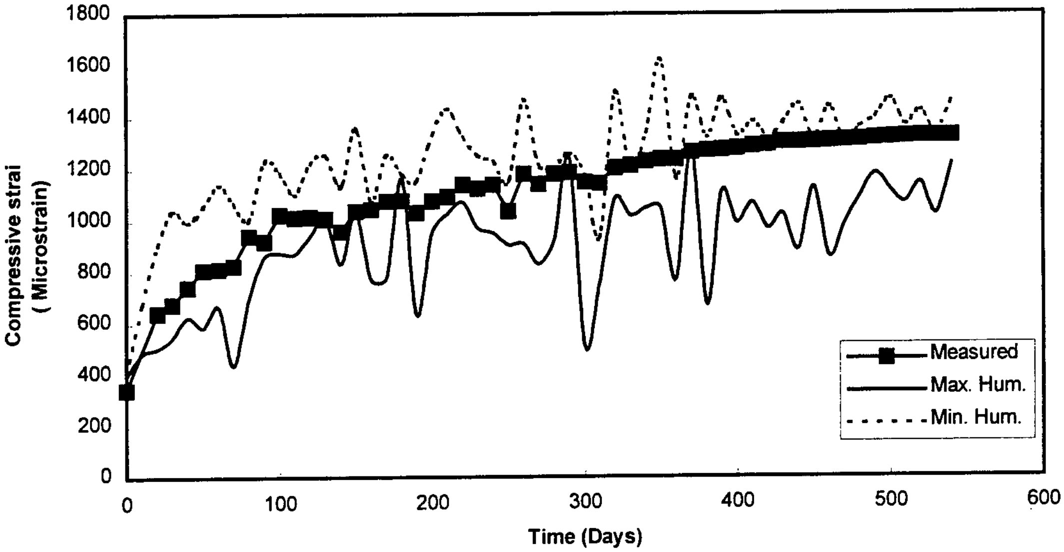

Fig. 8.19b Comparison of strain with the analytical predictions based on CEB coefficients for columns in group II

CHAPTER 9

PRE-DRIVING STUDIES ON CFRP PRETENSIONED CONCRETE PILES

9.1 OVERVIEW OF STUDIES

Concrete piles pretensioned with steel are prone to corrosion in marine environment. The extent of steel corrosion and the resulting concrete degradation reduce the useful service life of the structures. Continuing use of concrete piles prestressed with steel is very costly in initial costs resulting from the over design and subsequent maintenance. The development of FRP composites with improved physical properties provides new opportunities for innovative solution to overcome the concrete deterioration problems in marine structures. The high tensile strength and excellent corrosion resistance of carbon fiber reinforced plastics (CFRP) make them suitable for prestressing the concrete piles for use in marine environment.

The main objective of the studies is to investigate the feasibility of pretensioned concrete piles with CFRP tendons. The design, instrumentation and fabrication of pretensioned concrete piles with CFRP tendons are presented in Chapter 10. Prior to driving the test piles, it was necessary to make an investigation of the site and equipment in order to determine the pile driving stresses using the wave equation analysis based on wave propagation theory. The pile driving test results of the CFRP pretensioned concrete piles are discussed and presented in Chapter 11.

9.2 WAVE EQUATION ANALYSIS

Wave equation analysis is a mathematical tool to model the soil-pile-driving-system. This section discusses the wave equation analysis, its development with discussions on the input and output parameters, the modeling of the hammer and the parameters used for pile driving test.The concept of wave equation was applied to pile driving by Smith (1951, 1960), in which the discrete method was used for modeling the hammer-pile-soil system. WEAP (Wave Equation Analysis of Piles) is a typical software program for predicting pile capacity and optimum hammer driving system.

9.2.1 Soil-pile system

The basic pile system for the wave equation analysis of piles is represented by a series of masses and springs as shown in Fig. 9.1. The size of each mass and the stiffness of the springs reflect the mass and stiffness of the various parts of the real soil – pile system. The pile length may be divided into 5 to 10 feet short sections. It is very essential to use an appropriate time interval to depict the movement accurately. The lumped mass model of the pile is only stable, if the time increments are chosen shorter than the corresponding wave travel time through the segment. The wave speed depends on the modulus of elasticity of the pile material. On the other hand, if the time interval is very short, it takes more computational time with a small increase in accuracy of the results.

The ram, anvil, cap block, helmet and cushion are represented by internal springs and shown in Fig. 9.1. The load-deformation behavior of these elements is assumed to be linear. For the components such as the cap block and the cushion, internal damping also may be considered in the model. The soil is modeled by a spring and a dash pot attached

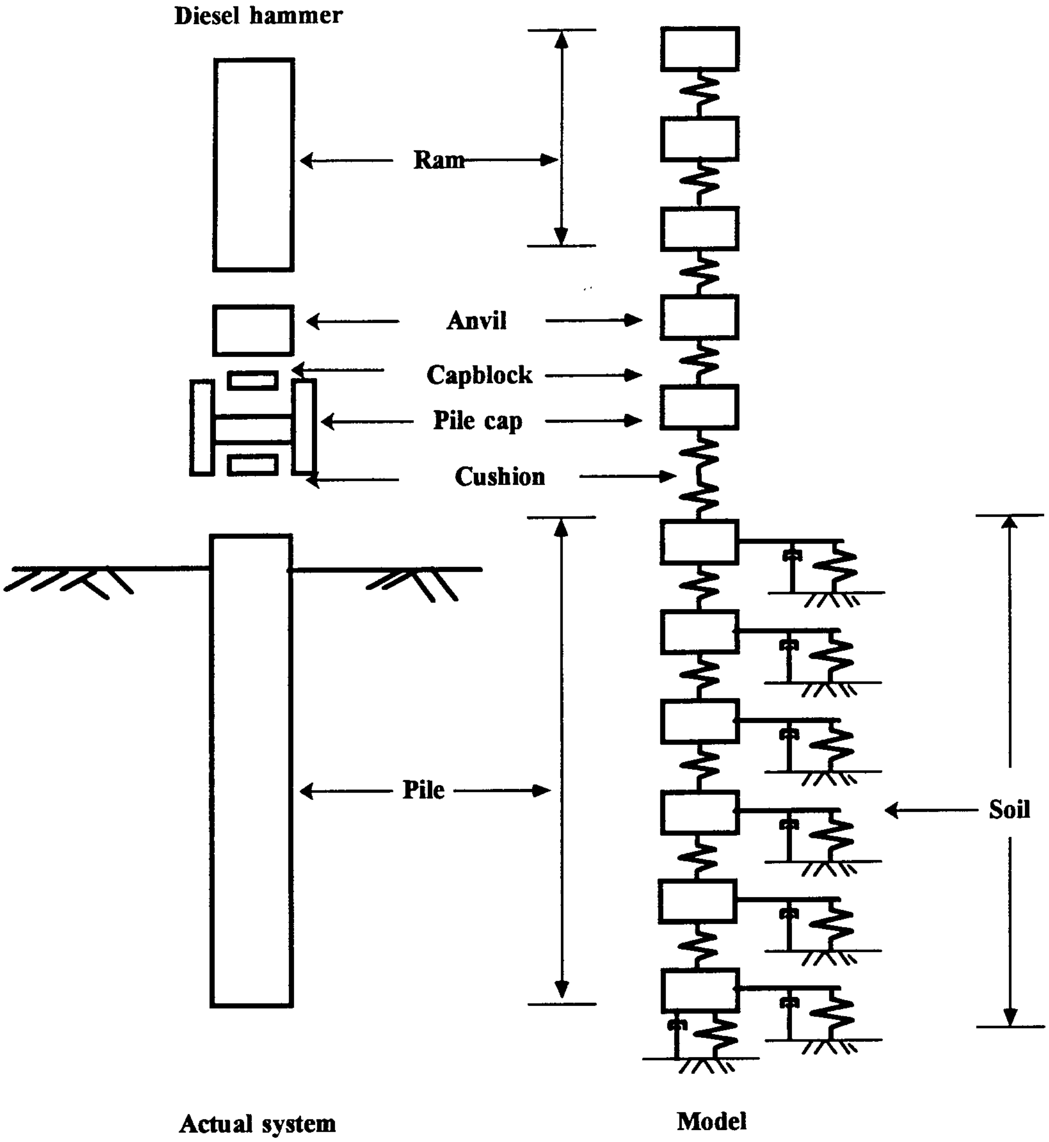

Figure 9.1 Hammer-pile-soil model for wave equation analysis

to each mass. The static and dynamic soil resistances are shown in Fig. 9.2. The force in spring is linear elasto-plastic where the maximum force, R_u is reached at a displacement q, called the quake. The dynamic resistance is linearly proportional to the element velocity for the dash pot.

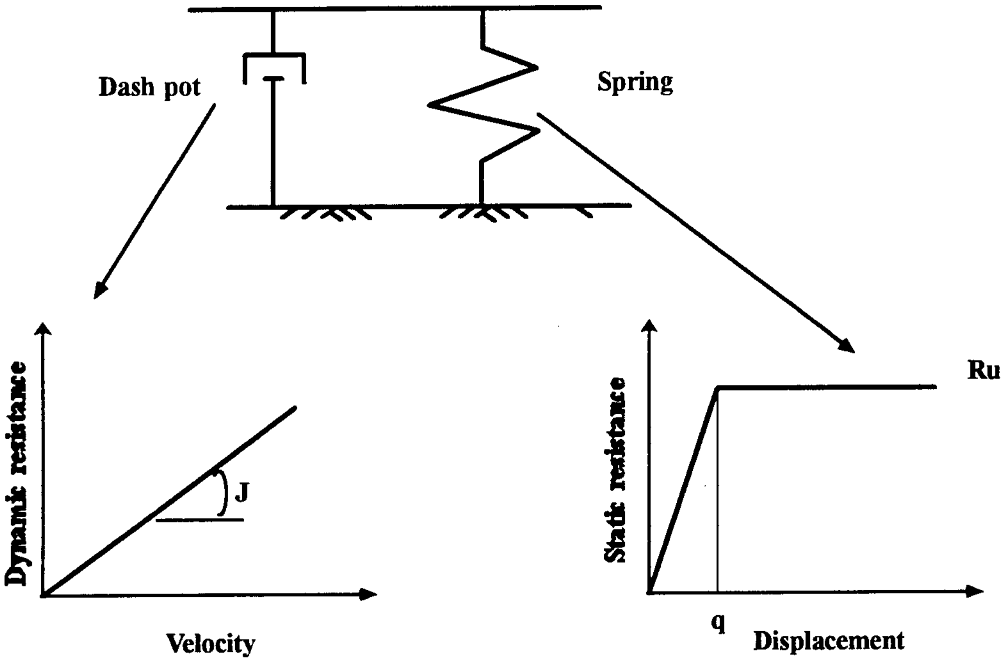

Figure 9.2 Soil model

The response of the soil to the static loading is illustrated in Fig. 9.3a. The instantaneous resistance of the soil increased by the dynamic loading (Fig. 9.3b). To characterize this dynamic behavior, a parameter J (damping constant) was introduced, which is estimated by the dash pot (Fig. 9.3c). This additional resistance is assumed proportional to the damping factor and the velocity of the element, and the static resistance. Therefore,

$$R_{udynamic} = R_{ustatic}(1+J*V) \qquad (9.1)$$

where

$R_{udynamic}$ = ultimate dynamic soil resistance
$R_{ustatic}$ = ultimate static soil resistance
J = damping constant
V = velocity of element

The damping constant, J consists of side damping constant, J_s and point damping constant, J_p. Normally, an average side damping factor (J_s) is introduced for friction and weighted according to the resistance in each layer based on the following relationship:

$$J_s = \frac{\sum (J_{si} R_{usi})}{\sum R_{usi}} \tag{9.2}$$

where:

J_s = average side damping factor

J_{si} = estimated damping factor for the layer i

R_{usi} = estimated friction for layer i

A value of point damping (J_p) is used to represent the soil at the pile tip. Soil damping factors determined in the laboratory and field show that there is a wide variation in damping for various soil types, especially cohesive soils. Selection of these soil variables often becomes the most difficult part of a successful application of wave equation. Goble and Rausche (1976) recommended the damping values shown in Table 9.1 for use with the wave equation pile analysis program (WEAP). For a given hammer-pile system, the maximum tensile stress and pile penetration resistance always depend on the assigned soil variables. A reasonable estimate of the proportions of shaft and end bearing resistance can be made by calculating the frictional resistance and end bearing for known soil properties. The value of quake (q) generally varies between 0.10 to 0.20.

Table 9.1 Damping values for various soil types

Soil type	Side damping factor J_s, sec/m (sec/ft)	Point damping factor J_p, sec/m (sec/ft)
Gravel	0.16 (0.05)	0.16(0.05)
Sand	0.16 (0.05)	0.33-0.66(0.10 - 0.20)
Silt	0.33-0.49 (0.10 – 0.15)	0.33-1.64(0.10 - 0.50)
Clay	0.66 (0.20)	0.03-3.33(0.01 - 1.0)

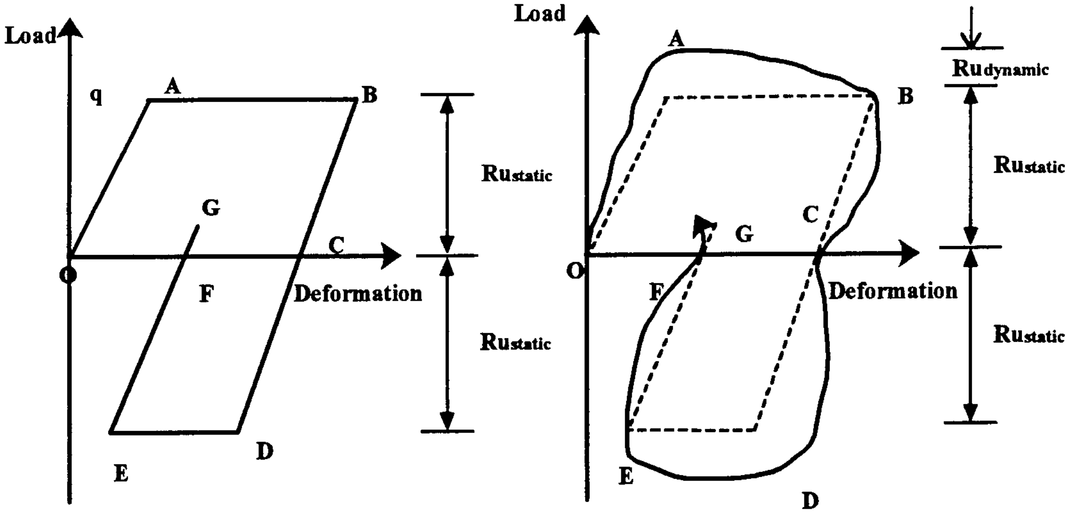

a) Static loading

b) Dynamic loading

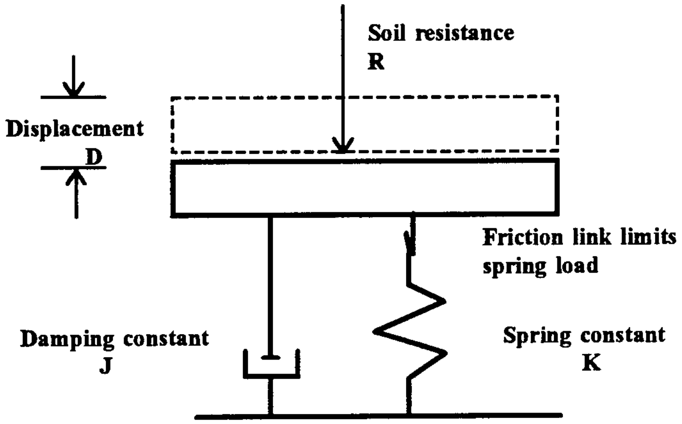

c) Equivalent rheological model of soil

Figure 9.3 Response of soil to static and dynamic loadings

9.2.2 Hammer model

The hammer is modeled using masses and springs as the main components. Fig. 9.4 illustrates the internal combustion hammer that was utilized for driving the CFRP concrete piles in this study. The internal combustion hammers have long and slender rams, which are modeled typically as three-spring mass segments. Generally, the impact block (cushion and ram) of the diesel hammer is modeled as single mass and the stroke is computed as a function of soil resistance.

The driving system consists of hammer cushion, the helmet and the pile cushion used for concrete piles. The helmet is a heavy steel box that contains certain inserts to adapt to various pile sizes and types. This is modeled as a rigid mass with the total weight of the driving system. The cushions are modeled as springs with stiffness k, given by the following equation:

$$k = \frac{EA}{t} \tag{9.3}$$

where

k = stiffness of the spring
E = modulus of elasticity of the material
A = area of cushion
t = thickness of the cushion

In order to model the energy dissipation characteristics, a coefficient of restitution is assigned to all the cushions. Since the pile cushions may be crushed by the forces during the driving, the elastic modulus and thickness of the cushion could vary considerably during the driving of the pile.

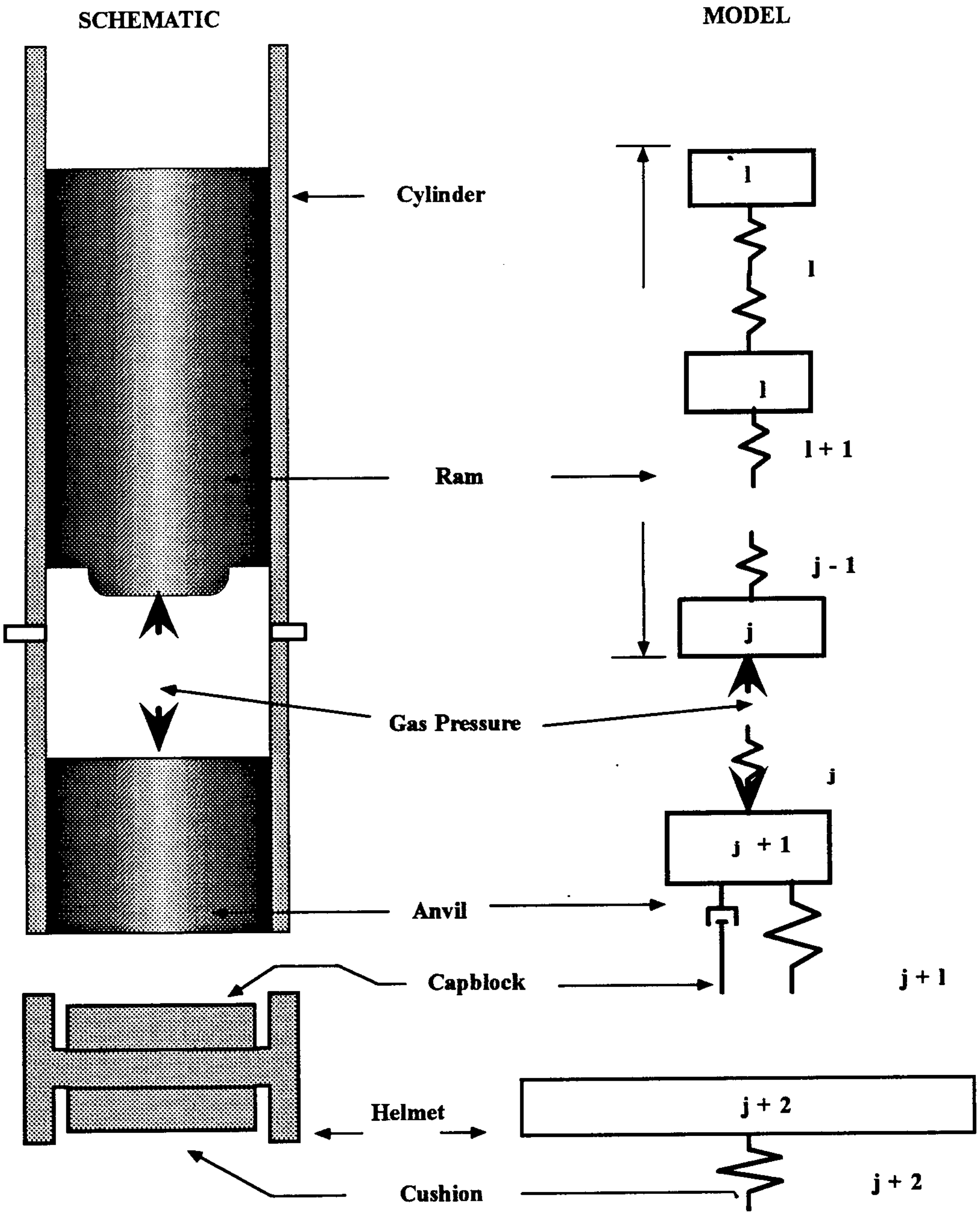

Figure 9.4 Internal combustion hammer model

9.2.3 Wave propagation

The one-dimensional wave equation was derived using the Newton's Second Law applied to an infinitesimal length of rod element. It is expressed by the following partial differential equation.

$$\frac{\partial^2 u}{\partial t^2} = c^2 \frac{\partial^2 u}{\partial x^2} \tag{9.4}$$

where

u = displacement

t = time

$c = \sqrt{\frac{E}{\rho}}$ = longitudinal wave propagation velocity

$\rho = {}^{\gamma}\!/_{g}$ = mass density

γ = unit weight

g = acceleration due to gravity

x = distance along rod

Eqn. 9.4 is modified to include the resistance of the soil surrounding the pile and the resulting equation given by

$$\frac{\partial^2 u}{\partial t^2} = c^2 \frac{\partial^2 u}{\partial x^2} \pm R \tag{9.5}$$

where

R = soil resistance.

The wave equation is based on the longitudinal vibrations of homogeneous, isotropic, elastic rod, which neglects the lateral inertial forces. The solution of the wave equation has the general form

$$u = f(ct + x) + h(ct - x) \quad \text{.........} \quad (9.6)$$

where f and h are arbitrary functions. The term h(ct - x) represents a wave traveling in the positive x direction with velocity 'c', while f(ct + x) represents a wave traveling in the negative x direction with velocity 'c'.

The partial derivative of the displacement with respect to time equals the particle velocity (V_p) in the elastic rod, whereas 'c' represents the speed at which a stress wave travels along the rod and its value depends on the material properties of the rod. V_p must always be less than 'c'. The particle velocity V_p depends upon the stress intensity as well as the material properties. The direction of the V_p and 'c' is same in the case of compression waves, and opposite for tensile waves. The particle velocity can be expressed as

$$V_p = \frac{\sigma * c}{E} = \frac{\sigma}{\rho * c} \qquad \text{......... (9.7)}$$

where:

$\rho = {}^{\gamma}\!/_{g}$ = mass density

σ = stress

E = modulus of elasticity

Boundary conditions

The input stress wave is always compressive, if the pile is driven from the top. The soil side resistance and internal damping are negligible for normal weight concrete and the wave shape and magnitude remain the same till it reaches the pile tip. A compressive wave is reflected as a tensile wave, if the end of the pile is free. The particle velocity at a free end of the rod is doubled, and the stress is zero. If the end of the pile is fixed, a compressive wave is reflected as a compressive wave of same shape and magnitude and therefore, the stress is doubled at the fixed end of the rod. The particle velocity at a fixed end is always zero. As long as the stresses are in the elastic range, one may add the effects of any number of waves to determine the net effect.

Therefore, the stress at any point in the pile depends on the boundary conditions at this location. The point stress is generally given by the sum of the incident and the reflected stresses and the theoretical range of point stress is zero to two times the incident stress reaching the pile top. An increase in point damping will increase the point stress. The particle velocity to overcome the point resistance becomes less than that in a friction pile, if friction and damping were to be absent.

9.2.4 Compressive stress in the pile

Theoretically, the maximum compressive stress can occur at any point in the pile along its length. As the pile driving proceeds, the location of the maximum stress in the pile changes continuously. It occurs at the pile head in many cases at the beginning of driving. As resistance builds up at the pile point, the point of maximum stress moves down the pile until it reaches the pile point. The idealized pile with an elastic cushion on top shown in Fig. 9.5 explains the shape of the compression wave, as it travels down the length of the pile, when the ram strikes the cushion and bounces back. A compressive stress wave is produced at the head of the pile when the ram strikes the head of the pile. It travels down the pile at a speed given by

$$c = \sqrt{E/\rho} \qquad \ldots\ldots\ldots \quad (9.8)$$

where c = velocity of the stress wave.

The magnitude of the stress wave is dependent on the ram impact velocity and weight of ram, cushion and pile stiffness. The heavier the ram weight for a given pile system, the higher the maximum pile head stress and the longer the wave length. For a given driving energy, the maximum compressive stress decreases with an increase in ram weight due to the lower impact velocity as the ram weight increases. Generally, the maximum pile head stress would be higher if the pile cushion were to be stiffer.

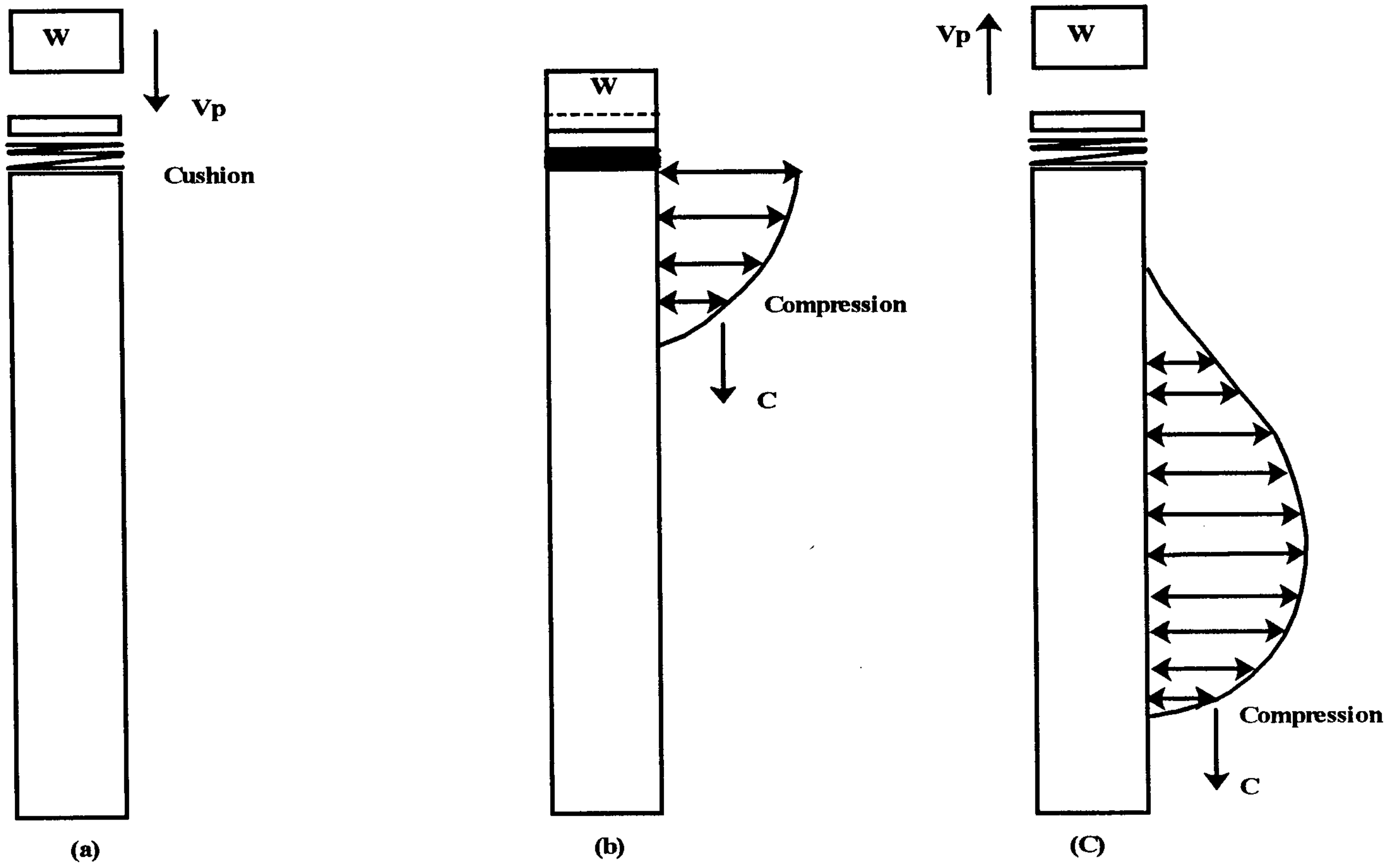

Figure 9.5 Stress wave produced when ram strikes the head of concrete pile

9.2.5 Tensile stress in the pile

The maximum tensile stress in the pile is always due to a reflected wave from either the pile tip or pile head. The tensile stresses are influenced significantly by the boundary conditions and tend to occur in long piles (length > 15.75m (50 ft)) causing cracking at any point along the length of the pile. When the pile is driven in soft soils or in the very hard soils, the tensile stress would increase.

9.3 PRE-DRIVING ANALYSIS

9.3.1 Static pile capacity

The wave equation requires the percentage of skin friction and the approximate distribution of the soil as input parameters. The percent skin friction is a function of the total static bearing capacity of the pile which was determined by using Vesic and Meyerhof methods along with FDOT SPT (94) program in the present study. The output of the program includes the percent skin friction and end bearing capacity. A factor of safety of two is applied to the skin friction and a factor of three to the end bearing capacity, combined these values represent the ultimate bearing capacity. The soil survey at the pile driving site (Florida Department of Transportation Maintenance Facility, Miami) was conducted in order to determine the static pile capacity using the standard penetration test.

9.3.1.1 Standard penetration test (SPT)

The standard penetration test was developed in 1927 and is being used extensively to determine the properties of the soils. This method was standardized as ASTM D 1586 in 1958 and has been periodically revised. A split spoon sampler is driven using a standard drop hammer and the blow count for the last two 150 mm increments are added to determine the N value of the soil. A professional soil survey company, Law Engineering conducted a standard penetration test (SPT) at the pile driving site in Miami.

The Split-spoon sampler was driven by a 63.6 kg hammer falling 0.76 m (Fig.9.6). The split spoon was retrieved after each 0.3 m increment and the soil classified (Fig. 9.7). A boring log produced using this data is shown in Fig. 9.8 .

9.3.2 Results from the WEAP analysis

9.3.2.1 Static bearing capacity

The static bearing capacity of the pile using the SPT values obtained from the field test by different methods is summarized in Table 9.2

Table 9.2 Static bearing capacity of the pile by various methods

Method	SPT boring Location	Skin friction (kN)	End Bearing (kN)	Percentage	
				Skin friction	End bearing
Vesic	Miami	120.16	300.58	28.56	71.44
Meyorhof		206.21	351.36	36.99	63.01
FDOT SPT(94)		57.32	409.17	12.3	87.7

9.3.2.2 WEAP analysis

A program (WEAP) based on the stress wave equation was used for analyzing a pile driven by diesel hammers. The program simulates the hammer-pile-soil interaction during pile driving and does not require any measured quantities. The program allows for preliminary analysis of various pile driving scenarios, including variations in hammer, helmet, cushion, pile and soil parameters. It was observed that the WEAP program is not particularly sensitive to the fluctuations in the input soil parameters. The values of hammer data and pile cushion properties significantly affect the output of the wave equation analysis program. The WEAP program gives a bearing graph (Ultimate resistance vs Blow count), and the maximum compressive and tensile stresses [Bowles, 1974].

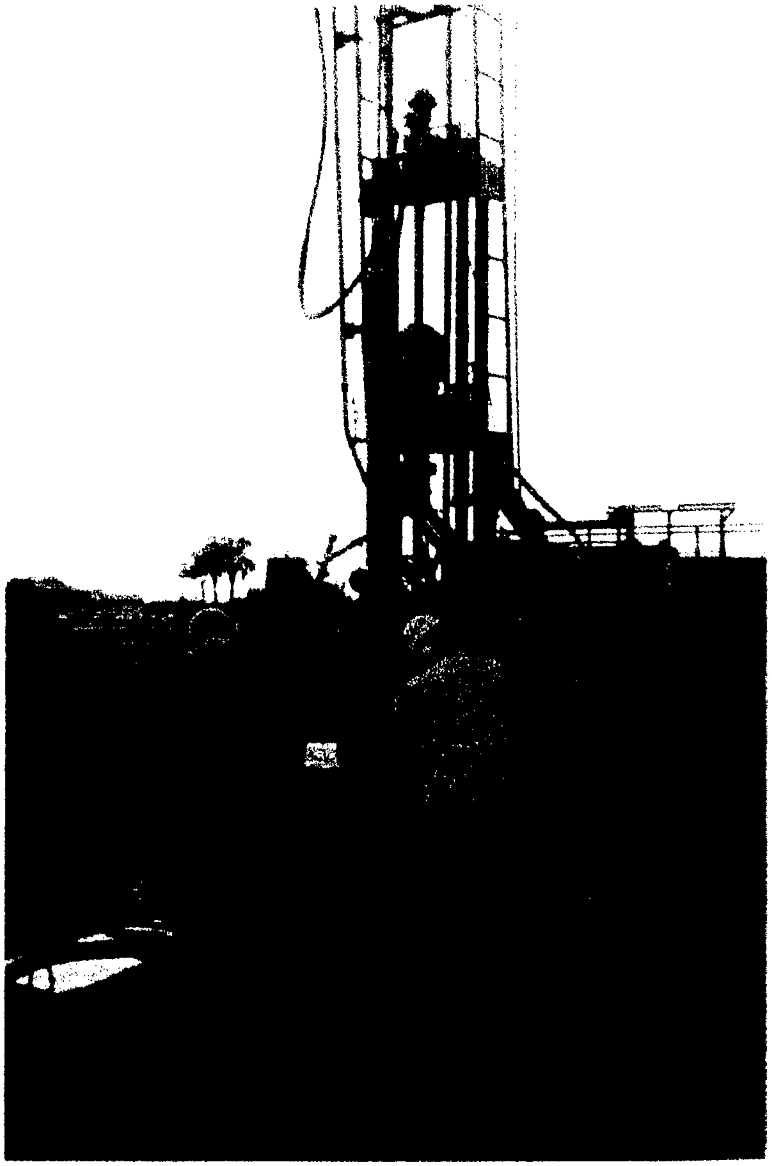

Figure 9.6 SPT equipment

Figure 9.7 Split – Spoon soil sample

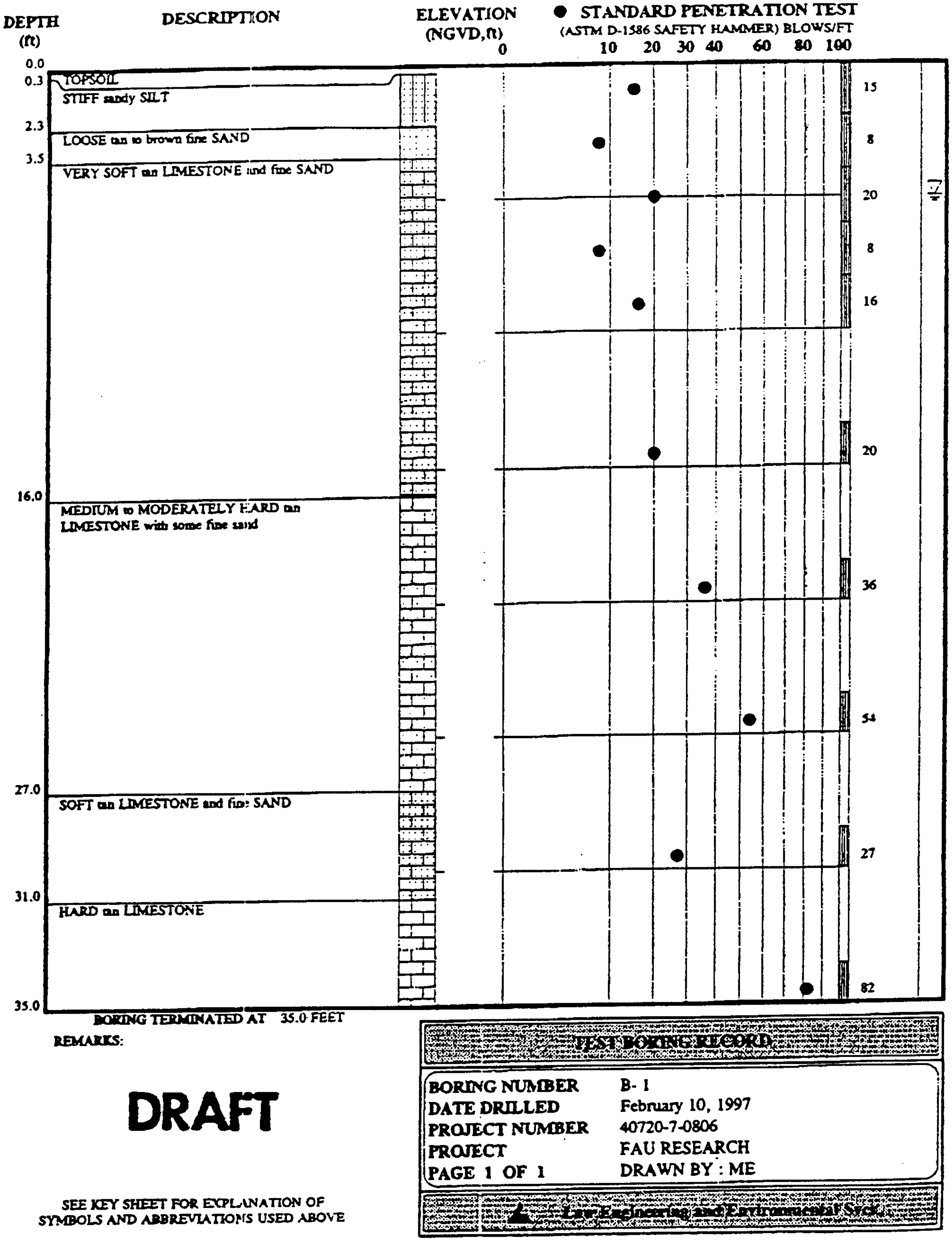

Figure 9.8 Test boring record at FDOT maintenance facility, Miami

Input parameters

Several combinations of the input parameters were used in the program and the optimum combination for the hammer-pile-soil system are given below:

Length of the pile = 7.62 m

Area of cross section = 0.0645 sq. m

Weight of hammer = 12.25 kN

Weight of helmet = 4.45 kN

Hammer efficiency = 0.8

Quake = 0.2

$J_s = 0.16$ s/m, $J_p = 0.5$ s/m

Spring constants: cap block = 21805 kN/m, pile cushion = 13107 kN/m

Results

Table 9.3 shows the results from the program including the given input ultimate loads (R_u), the predicted blow count in blows/m, the predicted tensile stresses (MPa) and the predicted compressive stresses (MPa) and the set (mm). Figure 9.9 shows the maximum stresses for the corresponding blow count, the solid line represent the predicted compressive stress and the dashed line the tensile stress. Figure 9.10 shows the ultimate capacity versus blow count.

Table 9.3 Wave equation analysis program results

R_u (kN)	Blows/ m	Tensile stress (Mpa)	Compressive stress (Mpa)	Set (mm)
178.1	36	-7.17	16.60	27
267.2	56	-3.60	16.67	18
356.3	77	-1.82	16.74	13
445.4	94	-0.30	18.26	11
534.4	111	0.00	19.77	9
623.5	127	0.00	21.08	8
712.6	147	0.00	22.25	7
801.7	170	0.00	23.36	6
890.7	200	0.00	24.32	5

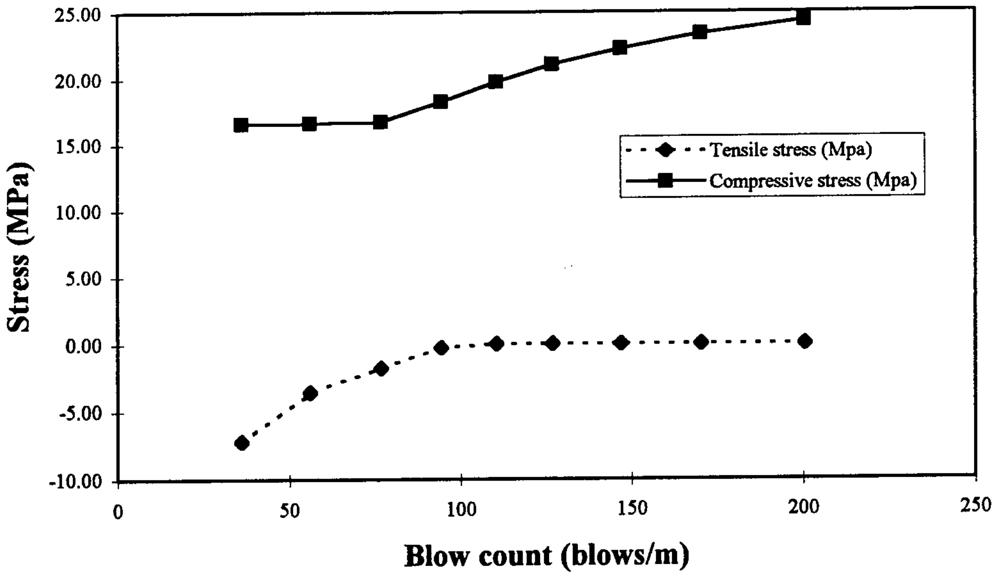

Figure 9.9 Maximum stress versus blow count from WEAP

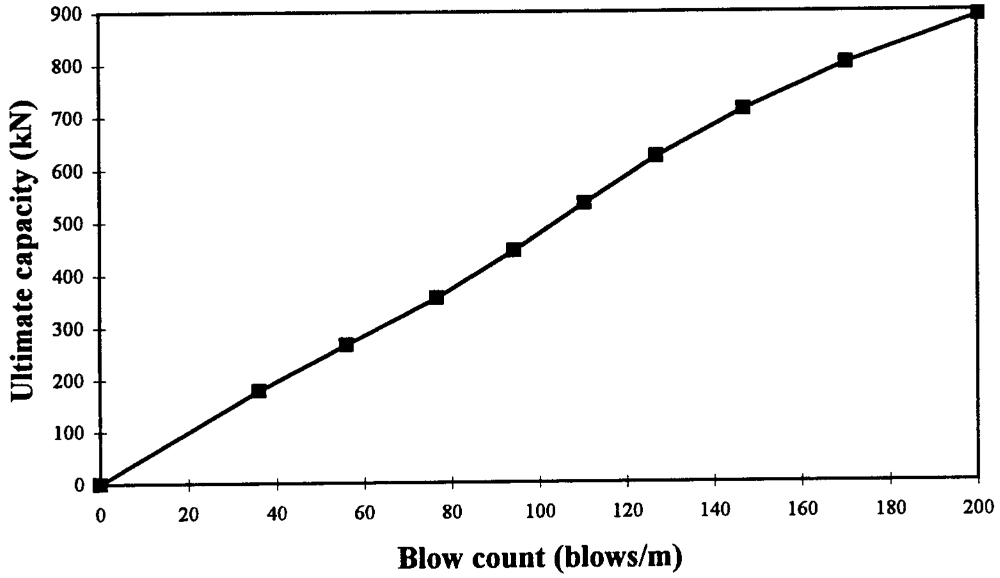

Figure 9.10 Ultimate capacity (R_u) versus blow count from WEAP

CHAPTER 10

DESIGN, INSTRUMENTATION AND FABRICATION OF CFRP PRETENSIONED CONCRETE PILES

10.1 INTRODUCTION

Pretensioned concrete piles are commonly used in the marine and coastal regions to provide an economical foundation for structures. The design and fabrication along with the instrumentation of the CFRP pretensioned concrete piles are discussed in this chapter. The fabrication of the concrete piles pretensioned with CFRP was itself a formidable task in this study. The instrumentation of the piles is basically designed to investigate the feasibility of using the CFRP tendons as a new pretensioning material.

10.2 DESIGN AND FABRICATION

10.2.1 Materials

Carbon Fiber Reinforced Plastics (CFRP) is one type of continuous fiber reinforcing material, which consists of fiber and matrix resin. The CFRP used in this study was developed by Tokyo Rope Mfg. Co., Ltd. and has a commercial name CFCC (Carbon Fiber Composite Cable). The properties of 12.5 mm diameter seven wire CFRP strands used in the study are compared with that of typical seven wire stress relieved steel strands (Grade 270) in Table 10.1.

Table 10.1—Properties of CFRP and steel strands (Grade 270)

Parameter	CFRP	Steel
Strand	12.5 mm. (½ in.) ϕ	12.5 mm.(½ in.) ϕ
Area	76 mm^2	98.7 mm^2
Elastic modulus	137,340 MPa	189,650 MPa
Ultimate tensile strength	2,119 MPa	1,862 MPa
Ultimate tensile strain	1.57 %	5 %

Two types of spirals, CFRP (CFCC 1 x 7, 7.5 mm. ϕ) and steel (5mm. ϕ), were used in pile fabrication. The ultimate strength of the steel spirals was only 1,034 MPa (150 ksi) compared to 2,116 MPa (307 ksi) for CFRP spirals. The compressive strength of the concrete at the time of release of prestress (3 days) was 33.4 MPa (4,850 psi) and the strength at 28 days was 53.2 MPa (7,725 psi).

10.2.2 Pile design

The effective prestress in the concrete piles was chosen so as to match those in the prototype larger steel pretensioned piles normally used in bridges by the Florida Department of Transportation (FDOT). The effective prestress generally ranges from 4.13 to 6.89 MPa (600 to 1000 psi) with typical average values of 6.5 and 4.7 MPa (940 and 680 psi) for the 600 mm (24 in.) and 750 mm (30 in.) square piles respectively.

A pile section of size 254 x 254 mm (10 x 10 in.), prestressed with four CFRP tendons was selected for the study. Each 12.5 mm (½ in.) CFRP tendon was stressed up to a maximum capacity of approximately 88.9 kN (20 kips). The jacking stress equivalent to an average compressive stress in concrete of 5.52 MPa (800 psi), meant that the effective prestress after losses in the CFRP pretensioned piles would be comparable to that in a typical prototype steel pretensioned concrete pile. The pile cross-section and the details of the spacing of the spirals are shown in Fig. 10.1 and Table 10.2.

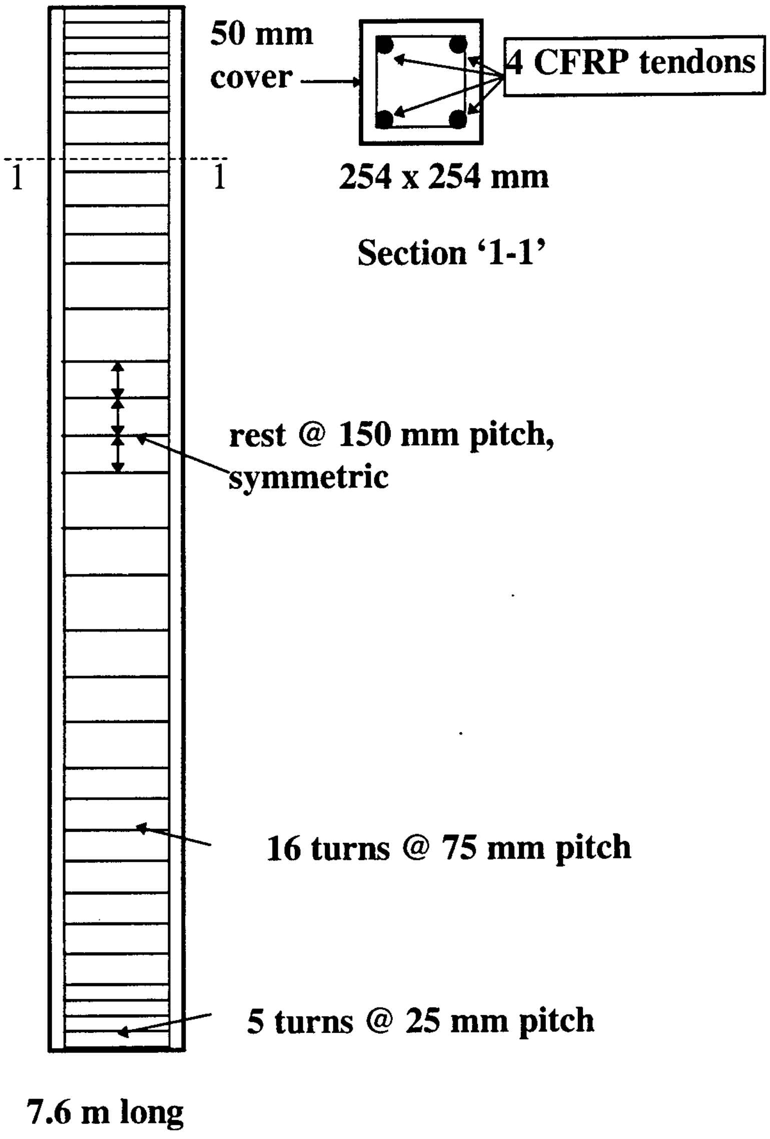

Figure 10.1 Pile cross-section and spiral details

Table 10.2 Details of concrete piles pretensioned with CFRP

Pile	Prestressing tendons	Type of spiral
Pile A	Four CFRP 12.5 mm diameter tendons	CFRP 7.5 mm diameter
Pile B		CFRP 7.5 mm diameter
Pile C		Steel 5.0 mm diameter
Pile D		Steel 5.0 mm diameter

10.3 INSTRUMENTATION OF THE PILES

The pile instrumentation in the present investigation is designed to study the dynamic behavior of the piles while driving. The Pile Driving Analyzer (PDA) is one of the commercially available dynamic testing methods, which was used in this study. The piles were also instrumented with embedded strain gages during fabrication to obtain the dynamic strain data using a data acquisition system (MEGADAC) in addition to PDA.

10.3.1 CFRP strand and pile instrumentation

Instrumentation of the piles included sixteen FLA-10-1L type electrical resistance strain gages installed on the CFRP strands and twenty-four embedded gages tied to the CFRP strands. The readings from the electrical resistance strain gages on the CFRP strands were monitored during stressing and those from the embedded gages during pile driving. The FLA-10-1L type strain gage was of a three wire type compensating for temperature and length effects. The actual length of the gage was 10 mm, which facilitated placement on the surface of the CFRP strands.

A total of six embedded strain gages of the PML-60-1L type were installed in each pile (Table 10.3). The locations of the gages were selected to measure the magnitude and velocity of the critical stress waves produced during driving. Two embedded gages were placed on two opposite CFRP strands at distances of 0.3 m (one foot) from the pile tip, two gages in the middle of the pile and another two gages at 0.3 m (one foot) from the pile toe. The connecting lead wires attached to the strain gages were led through the center of the pile and taken out at the side of the piles within 0.5 m from the pile top.

10.3.2 Pile driving analyzer (PDA)

PDA (PDA, courtesy of Pile Dynamics, Inc. Cleveland, Ohio) is a dynamic testing method, which analyzes the stress wave during driving and restrike. This method involves measuring the strain and acceleration at the top of pile as the pile is being driven. Two strain transducers and accelerometers are attached on opposite sides near the top of the pile as shown in Fig. 10.2. The data are acquired through a connection adaptor in the PDA. Data can be stored in either analog or digital recorders and viewed on an oscilloscope.

Transducer is a device that converts any deformation into a corresponding output signal. The strain transducers have reusable frames, containing four resistance foil gages connected in full bridge. Accelerometers which contain a quartz crystal, are used to measure the pile movement (motion). The pressure on quartz crystal when accelerated produces a voltage linearly proportional to acceleration. These accelerometers are mounted on a special block for electronic and mechanical isolation and also for ease of attachment to the pile.

The maximum tensile and compressive stresses in the pile during driving as well as the static bearing capacity of the pile can be determined by using the PDA method. The force, velocity, displacement, bending stresses and hammer efficiency can also be determined using PDA.

10.4 FABRICATION OF CONCRETE PILES PRETENSIONED WITH CFRP TENDONS

10.4.1 Prestressing bed

The prestressing bed and facilities at Curry Industries, Miami (Fig 10.3) were utilized for the prestressing of the CFRP tendons in the present study. The pretensioning bed with 91.5 m (300 ft.) steel form has two abutments, one at the pulling end and the other at the dead end. Each pile was designed to be 7.63 m (25 ft.) long and the four piles were cast in one casting operation using the pretensioning bed. The prestressing bed consists of steel forms with two abutments designed to sustain 1.3 MN (300 kips). Adjustable steel headers were provided at any desired position along the bed to obtain the predetermined pile length. Prestressing steel strands of 12.7 mm (0.5 in.) diameter and 42.7 m (140 ft.) length were anchored to the dead end of the prestressing bed. The other ends of the prestressing tendons were connected to the CFRP tendons using specially designed steel couplers and then finally to another set of prestressing steel strands, which were tensioned by a hydraulic jack and anchored at the pulling end (Fig 10.4).

10.4.2 Preparations for setup and fabrication

The four piles were cast using eight 21.4 m (70 ft.) CFRP tendons using one 91.5 m (300 ft.)bed. The CFRP tendons were joined with steel tendons by steel couplers utilizing the entire length of the bed. Eighteen steel couplers were designed and fabricated in Pompano Beach, Florida by Consolidated Metal Works Inc. The couplers were 305 mm in length and 76 mm diameter (Fig. 10.5). The wedge system for the CFRP tendons was provided by Tokyo Rope (Fig. 10.6). The strength of the steel couplers was designed to be nearly twice the initial design prestressing force. Headers with holes were positioned in the stressing bed to serve as the spacers at predetermined locations through which the strands were passed. An epoxy coating was applied to the edges of the holes in the headers to ensure a smooth surface for the CFRP cables to ride on (Fig.10.7). Two piles were provided with 152 mm square continuous helicoidal steel

Figure 10.2 Strain transducers attached to the pile

Figure 10.3 Stressing bed

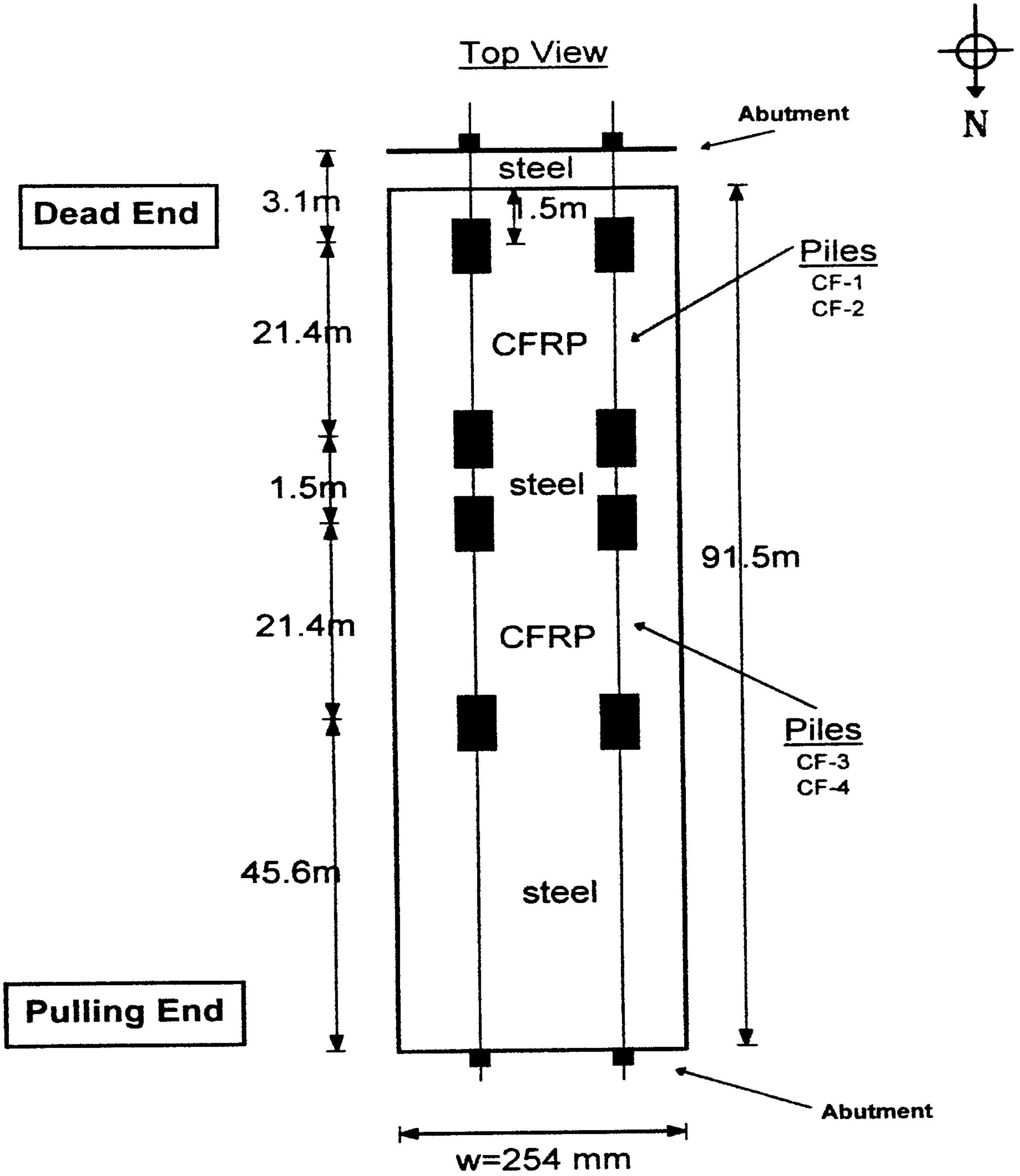

Figure 10.4 Stressing bed layout

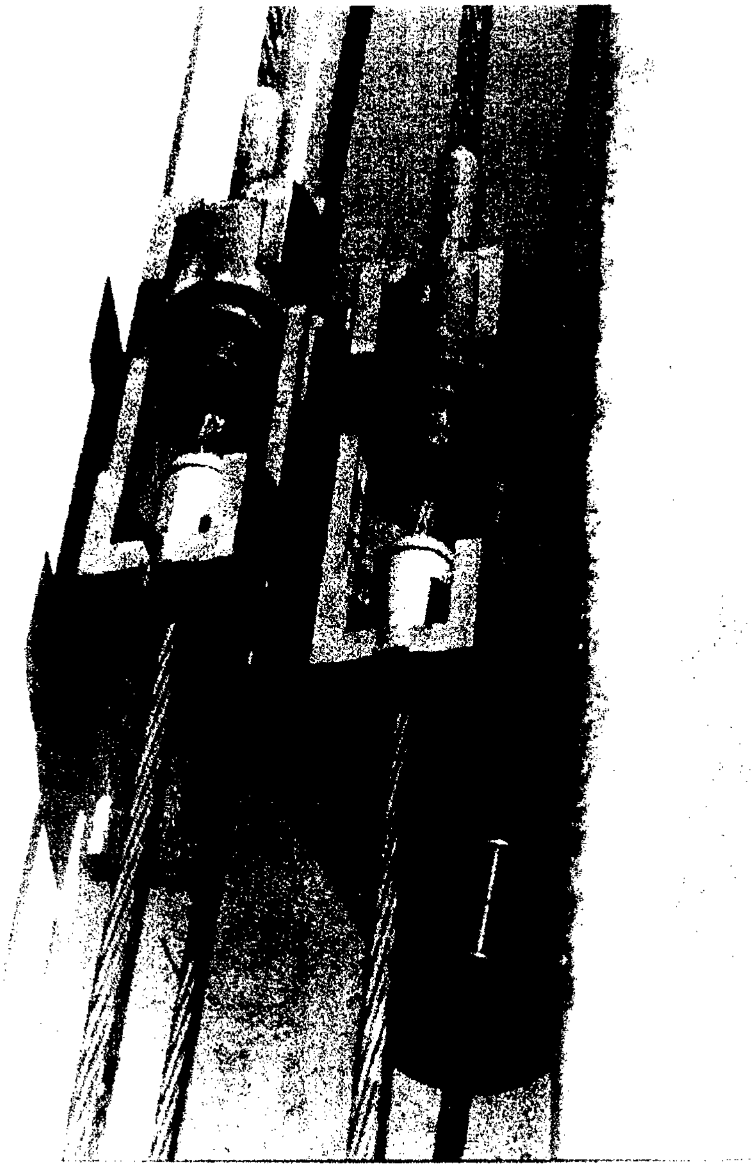

Figure 10.5 CFRP-steel coupler

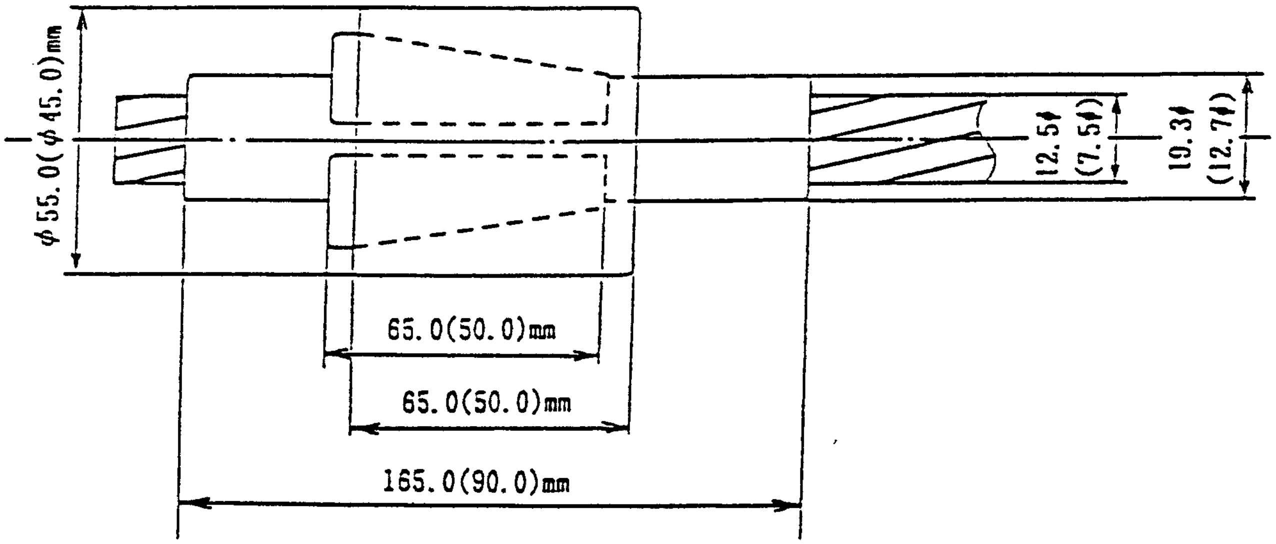

Figure 10.6 Schematic of wedge system

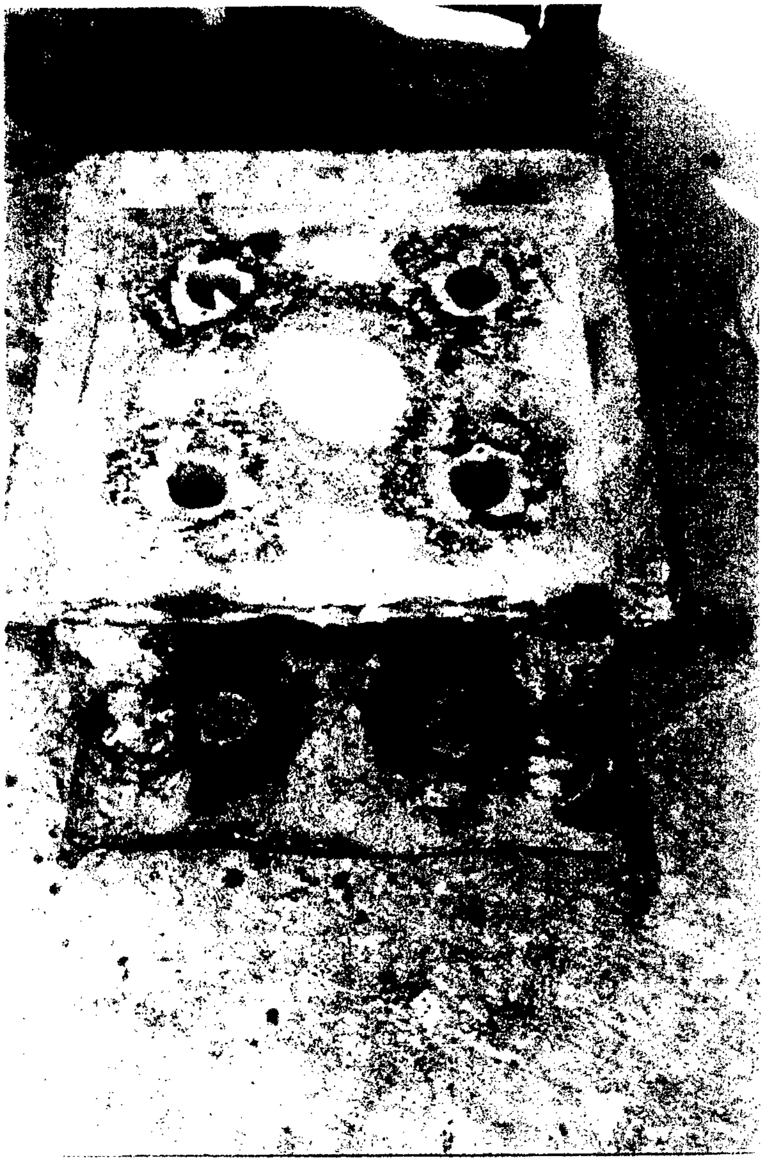

Figure 10.7 Header prepared with epoxy

Table 10.3 Strain gage properties

	PML-60-11-1L	FLA-10	PL-60-1l
Gage length (mm)	1	10	60
Gage width (mm)	1	2.5	1
Nominal resistance (ohms)	120	120	120
Gage factor	2.1	2.1	2.1
Comments	Embedded 3 wire	Surface 3 wire	Concrete Surface

Table 10.4 Load cell values during tensioning and casting

Strand number	**Initial load (kN)**	**Day one tensioned load (kN)**	**Fourth day tensioned load (pour) (kN)**	**Third day after concrete casting (kN)**
1	2.95	81.6	79.5	77.9
2	6.10	101.2	98.1	95.1
3	6.46	81.1	80.0	79.3
4	4.00	80.6	78.4	76.7
Average load	**4.9**	**86.1**	**84.0**	**82.3**

spiral reinforcement. The two remaining piles were reinforced with 152 mm square turns of CFRP transverse reinforcement provided by Tokyo Rope, Japan.

The instrumentation to monitor the initial stresses during prestressing and stresses during pile driving included four load cells, sixteen surface strain gages and twenty four embedded strain gages and a Pile Driving Analyzer. Four load cells were fabricated, calibrated and placed at the dead end abutment. The load cell was fabricated from a steel pipe, 6.4 mm thick, 76 mm long and 32 mm diameter. Two rosette strain gages were attached using epoxy over the smoothed surfaces and along the axis of the pipe at two diametrically opposite sections. Each load cell was calibrated and numbered before installing them in the field. A silicon coating and shrink wrap was then applied at the connections to protect from humidity and moisture effects.

10.4.3 Setup prior to pretensioning

The preparation for pretensioning over two days period was followed by one day for casting preparations and another day for actual casting. It was necessary to inspect the CFRP tendon for any damage resulting from wear and tear on the surface during transportation and storage. Steel anchors were provided at either end of the CFRP strands. Anchors, which had been corroded due to exposure to high humidity were ground to remove corrosion products (Fig. 10.8). Epoxy was applied to the holes in the headers to ensure a smooth surface for the CFRP cables to ride on during threading and prestressing stages.

The headers were placed at the predetermined locations, designating the toes and tips of the piles. The steel and CFRP transverse reinforcements were placed in position in the stressing bed. The CFRP tendons were then laid within the stressing bed and guided through the headers and continuous spiral reinforcement. The steel strands coupling with the CFRP tendons consisted of four 45.75 m. (150 ft.) long and eight 3.05 m. (10 ft.) long tendons.

A uniform coating of two-part epoxy was applied over the CFRP strand to ensure filling up of the grooves between the strands. Immediately after application, a two inch piece of 3M clear tape was wrapped around the epoxy ensuring correct placement and better curing of the epoxy. This process was repeated for all the sixteen surface strain gage locations. The tape was removed from the epoxy locations and the surfaces were sanded to be smooth for placement of strain gages. Using NP-50 epoxy, supplied by Texas Measurements, the gages were installed and the epoxy allowed to cure for 24 hours.

10.4.4 Prestressing of CFRP tendons

The CFRP tendon in the bottom right position was chosen first for stressing. The slack in the CFRP tendons was removed and the load cells placed at the dead end abutment. The prestressing steel strand was passed through the load cell and a 76 mm square steel plate laid between the chuck and the load cell shown in Fig. 10.9. Each coupler was aligned as the slack was removed using the tractor (Fig. 10.10).

The initial strain readings were taken after removal of the slack for all four tendons. A hydraulic jack was positioned at the pulling end of the stressing bed (Fig. 10.11). Strain readings were taken at increments of 22.2 kN (5 kips) up to a maximum of 88.9 kN (20 kips). These strains were compared against the values obtained with load cells and the hydraulic jack pressure reading. The load cell readings were recorded at the beginning and end of the prestressing operation.

Upon completion of the prestressing of the CFRP tendons, the transverse helicoidal reinforcement for each pile was tied in position. The embedded gages were then attached to the CFRP strands at the predetermined locations (Fig. 10.12). The lead wires from the embedded gages were led through the transverse reinforcement to the points located 305 mm from the pile tips. The steel forms were carefully coated with oil by hand using sponges taking care not to expose the CFRP tendons to the oil. It was essential that the surface of the tendons should be free from oil so as to develop a complete bond with the fresh concrete.

10.4.5 Casting of the pretensioned concrete piles

The concrete supplied by CSR Rinker, Miami, was poured into the steel form and vibrated and the surface finished smooth followed by edging (Fig. 10.13). Seven strand cables bent into a V- shape were positioned in the fresh concrete to serve as lifting hooks. Twelve control cylinders, 152 mm x 305 mm size, were also cast during the pour. Within an hour of completing the fresh concrete pour, plastic sheets had been placed over the concrete to minimize plastic shrinkage effects. The piles were kept moist with water for two weeks following the concrete pour. The strain readings from both the load cells and the strains were taken at the completion of the pile casting.

10.4.6 Release of prestress and removal of pretensioned piles from stressing bed

The concrete control cylinders were tested at the end of three days and average concrete strength was found to be 33.40 MPa (4850 psi). Efforts were made to gradually release the prestress in the CFRP tendons to the concrete using the hydraulic jack. The jack was positioned at the pulling end and each strand was tensioned just enough to release the chuck. The hydraulic pressure was then slowly released from the jack. This proceeded smoothly until the release of the tension in the third CFRP tendon. The individual piles did not displace within the prestressing bed as a result of release of tension in the three CFRP tendons. This caused the last CFRP tendon to reach its ultimate strength resulting in a sudden rupture. Flying pieces of the CFRP tendon were observed as it exploded and the tension in all of the CFRP tendons were released at the dead end. Finally, the CFRP tendons between the headers were cut flush to the pile tips and toes using a hand grinder. Two days following the release of prestressing forces, the piles were removed from the stressing bed and carefully transported to a secure area for storage (Fig. 10.14). The piles were kept moist for five days after removal from the bed to insure proper curing.

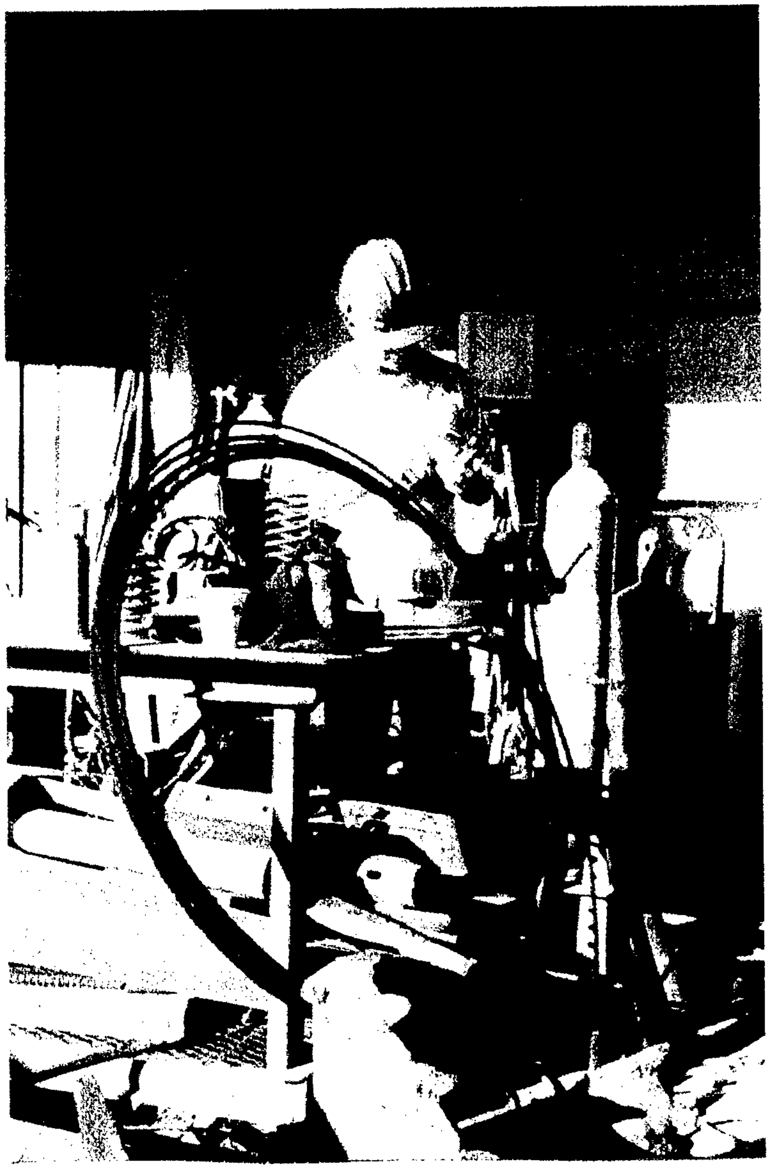

Figure 10.8 CFRP anchor preparation

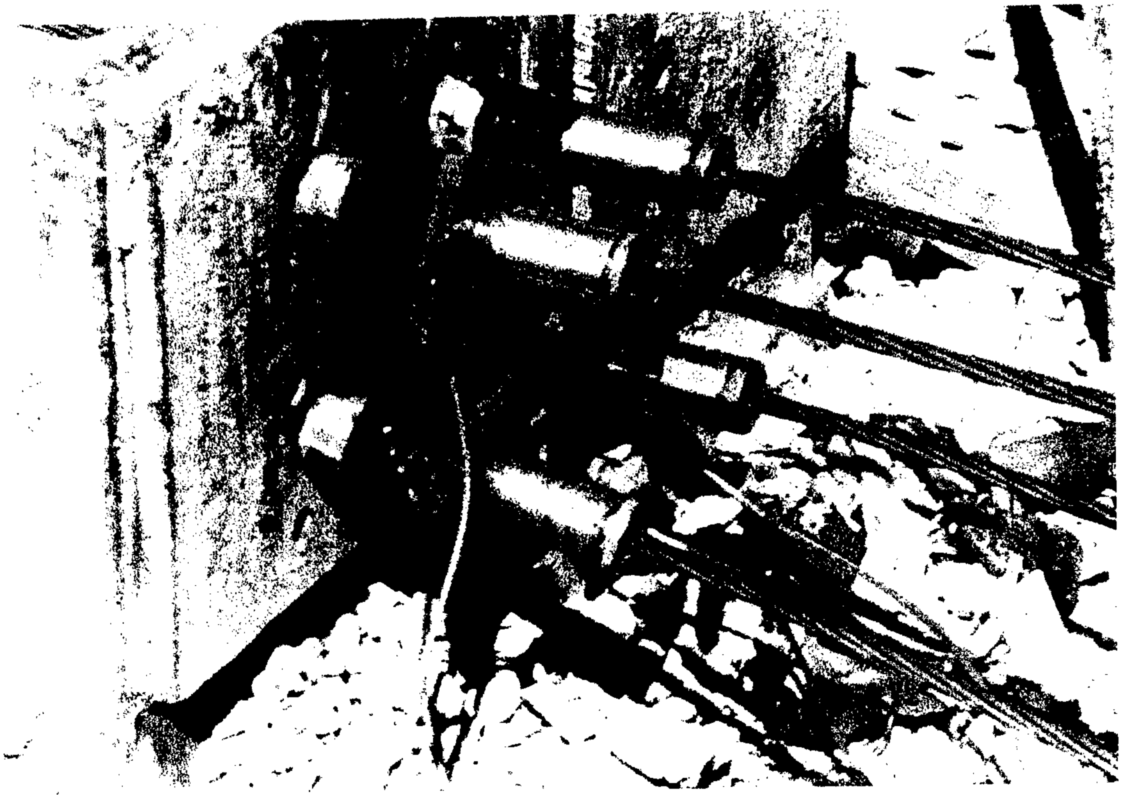

Figure 10.9 Load cell dead end configuration

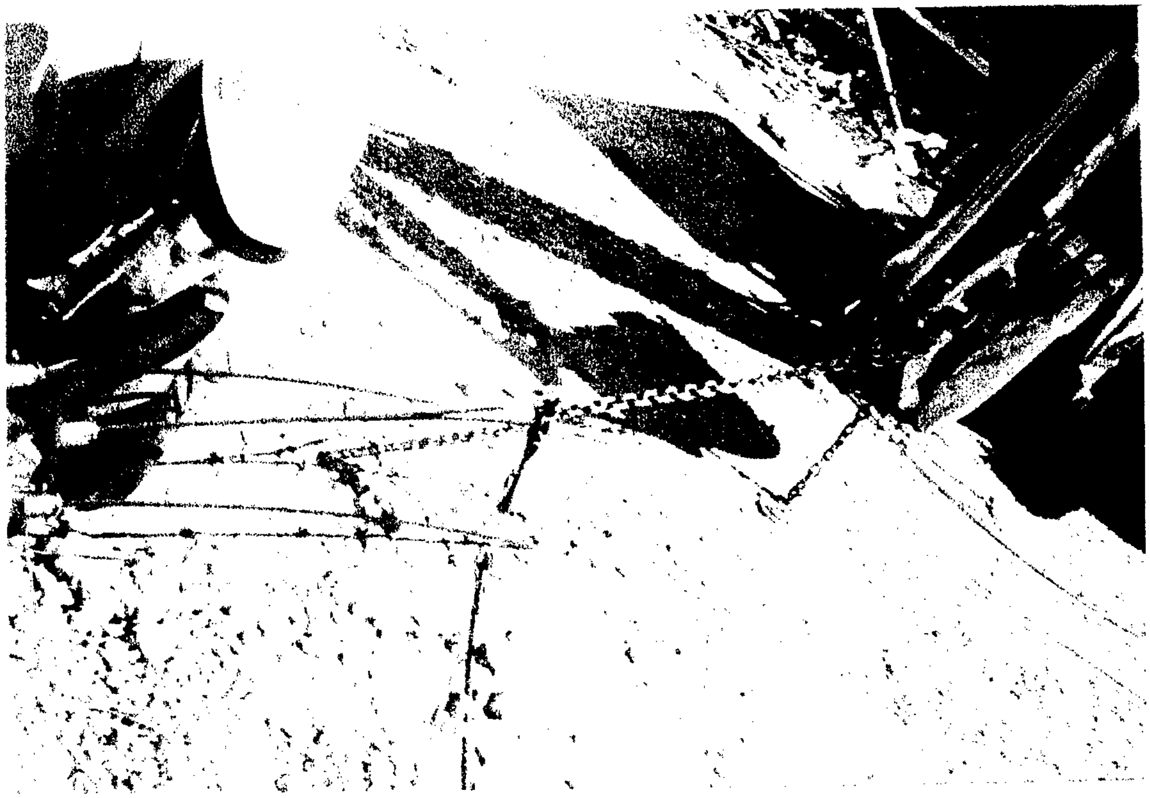

Figure 10.10 Tractor removing slack

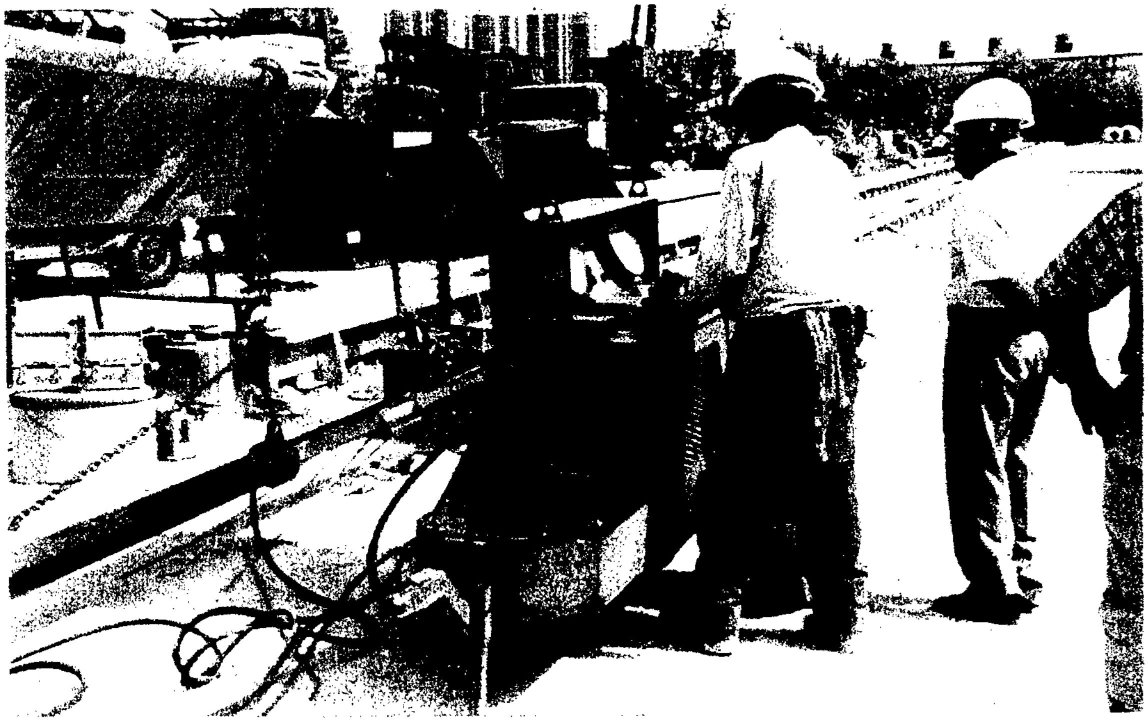

Figure 10.11 Stressing tendons

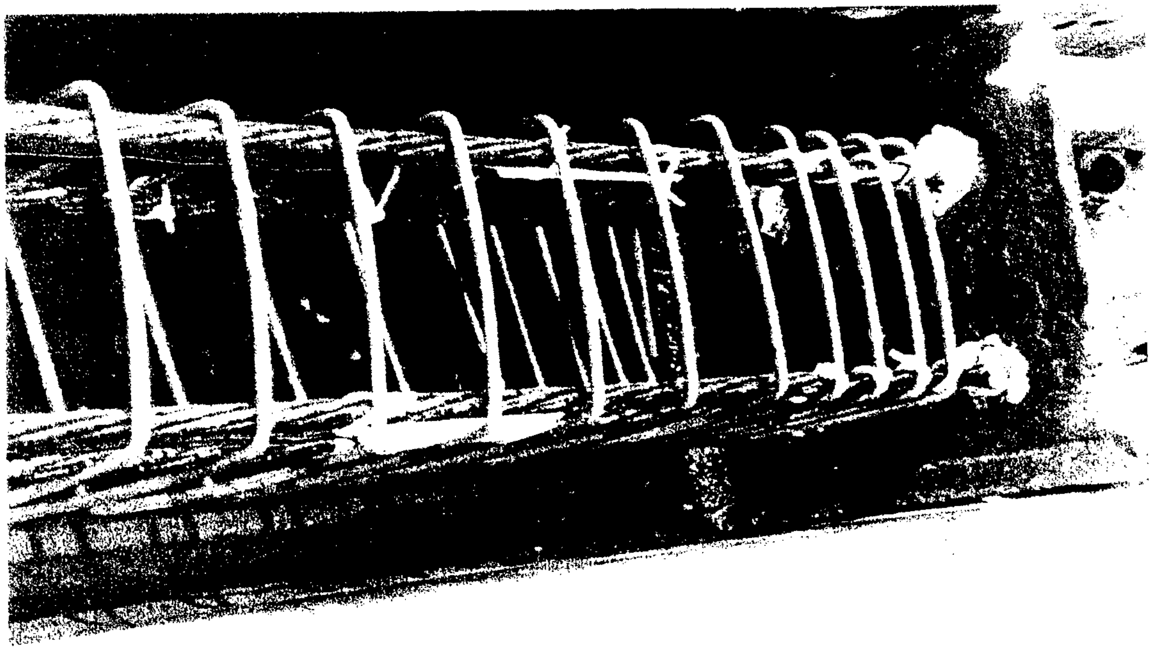

Figure 10.12 Embedded strain gage

Figure 10.13 Pile casting

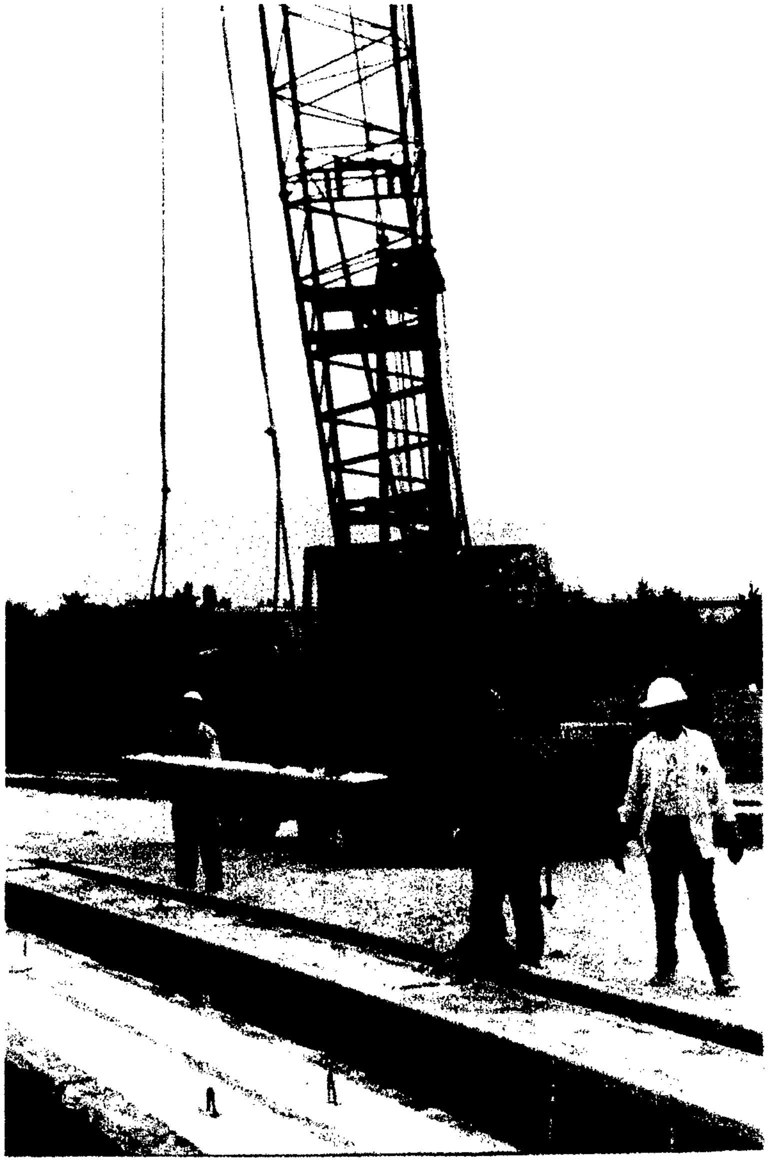

Figure 10.14 Removal of CFRP pretensioned concrete piles for storage

10.5 PRESTRESSING FORCES IN CFRP TENDONS DURING STRESSING AND RELEASE

10.5.1 Stresses and strains during prestressing stage

Using a Hercules hydraulic jack each CFRP tendon was tensioned approximately to a maximum of 88.9 kN (20 kips). The stress versus strain relationships of the CFRP tendons are shown in Fig. 10.15. The average value of Young's modulus for the four CFRP tendons is 144.6 GPa. The prestressing forces during stressing and casting for each tendon are given in Table 10.4. The specified ultimate load of the CFRP tendon by the manufacturer is 161 kN (36 kips) with a maximum strain of 1.6%. Based on load cell readings immediately after tensioning, the prestressing forces in the tendons were approximately 50%-63% of the ultimate load. After initial losses (three days after concrete casting) the prestressing forces in the CFRP strands were in the range of 48%-59% of the ultimate strength. The recorded strain data show that losses in the CFRP tendons three days after tensioning ranged between 1.1%-3.8% with an average value of 3.8 kN (850 lbs). The losses after tensioning could be attributed primarily to the anchor set and relaxation of the steel and CFRP tendons. The losses after 3 days from the date of casting averaged 2.4% , which could be attributed mainly to elastic shortening and shrinkage in concrete.

10.5.2 Transfer length

The surface electrical strain gages were attached to the end portions of two piles in order to determine the transfer length (Fig. 10.16). Six FLA-60 surface strain gages provided by Texas Measurements were used in the two piles. The gages were placed at a spacing of six inches along the center line of the piles for a distance of 36 inches. The concrete surface strains were measured before and after prestress release using a strain indicator. The strain distributions along the length of the two piles are shown in Fig.10.17. It is observed from the strain distribution that the transfer length is approximately 40 times the CFRP tendon diameter as compared to 29 and 38 times the bar diameter for fiber glass and steel tendons respectively. The comparison is based on an assumption of an effective prestress of 50% of the ultimate strength.

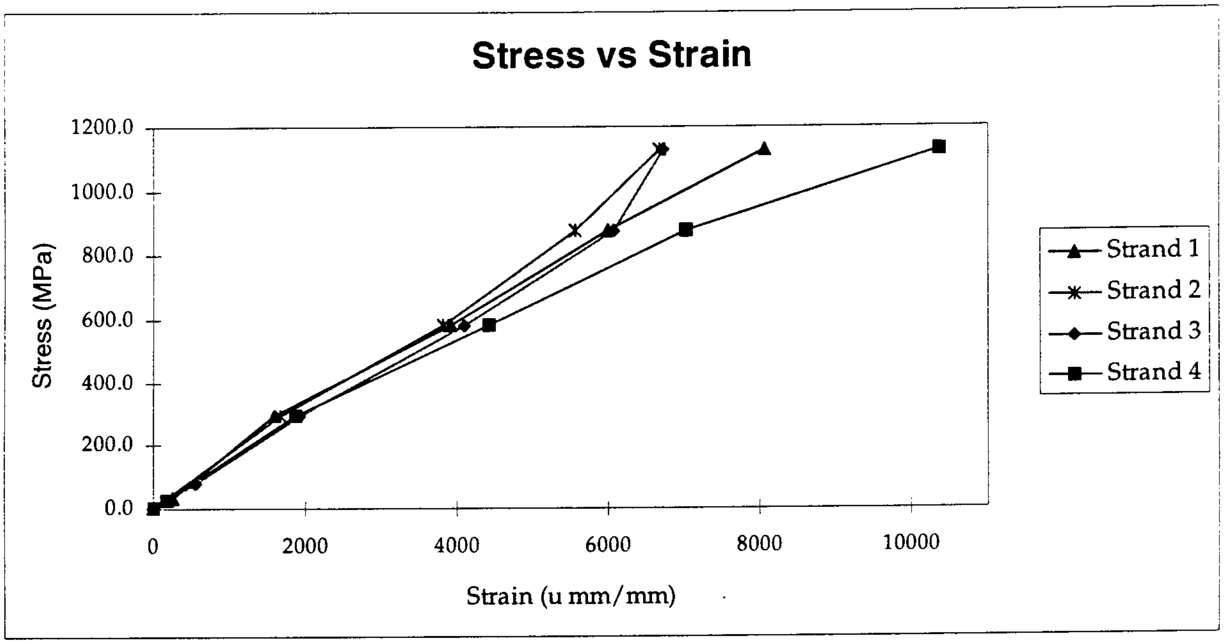

Figure 10.15 Stress vs. strain for CFRP tendons

Figure 10.16 Transfer length surface strain gages

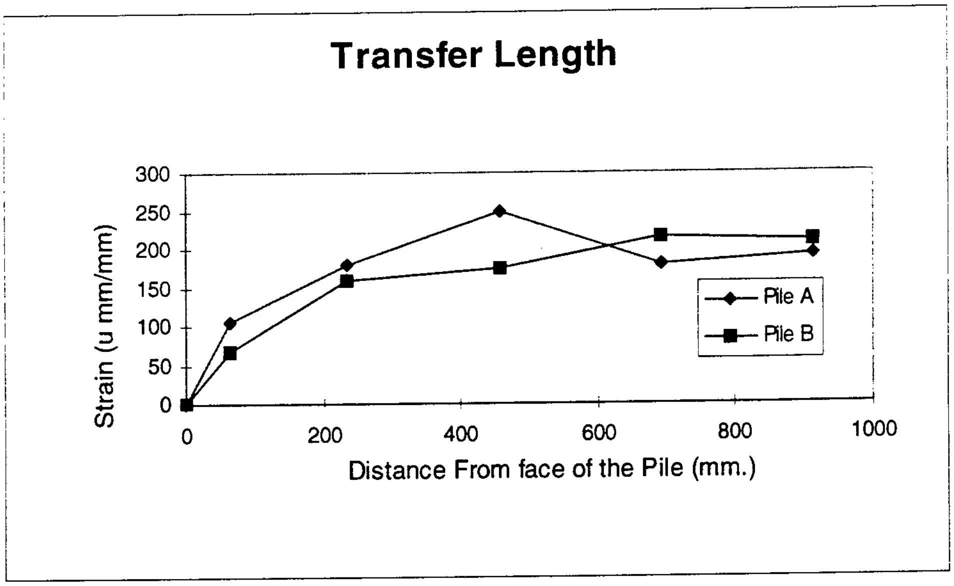

Figure 10.17 Stain variation along the pile length

CHAPTER 11

CFRP PRESTRESSED CONCRETE PILE DRIVING AND TESTING

11.1 INTRODUCTION

The field tests consisted of driving four concrete piles pretensioned with CFRP tendons. CFRP spiral reinforcements were used in piles A and B and steel spiral reinforcement in the piles C and D. The piles were instrumented as discussed in Chapter 10 and monitored during driving. The driving of the test piles, the results and discussions of the tests are presented in this chapter. The pile driving system and the hammer type used in this study are also presented in this chapter.

11.2 PILE DRIVING PROCEDURE

11.2.1 Pile driving equipment

The equipment necessary to drive a pile includes a piling frame and leaders, a crane supporting the hanging leaders, a pile helmet and hammer (Fig. 11.1). The piling frame has the function of guiding the pile with correct alignment from the stage of the first pitching in position to its final penetration. It also carries the hammer and maintains the hammer in position co-axially with the pile. Leaders consist of three types: fixed, semi-fixed, and swinging. The leader system provided by Curry Industries to drive the test piles was of the swinging leader type. The leaders are hung at the top by one line of the crane and the bottom is secured in the ground with spikes.

The piling crane is mounted on the base frame or carriage with one rope for handling the hammer and another for lifting the pile. The pile head is guided by a cap or helmet which has jaws on each side that engage with leaders. The hammer is similarly provided with jaws. The leaders are capable of adjustment in their relative positions to accommodate pile and hammers of various widths.

11.2.2 Pile driving hammer

The hammer is basically a weight which impacts the pile tip forcing penetration into the soil. The diesel hammer was selected for the test pile driving. The principle of the diesel hammer is that as the falling ram compresses air in the cylinder, diesel fuel is injected which is atomized by the impact of the ram on the concave base. The impact ignites the fuel and the resulting explosion adds an additional energy to the pile that is already moving down under the blow of the ram. The blow is sustained and imparts energy over a longer period than the drop or single acting hammer. As the ram rebounds after the explosion the excess fuel is expelled. The diesel hammer selected for the pile driving was the Delmag D12 type, the mass of the ram is 1220 kg (2690 lb) with a maximum energy of 31.25 kN-m (23 x 10^3 ft-lb) per blow and maximum striking rate of 40-60 blows per minute (Fig. 11.2).

11.2.3 Pile helmet

When driving the piles, a helmet is placed over the pile head for the purpose of retaining in position a cap block or 'dolly', which cushions the blow of the hammer and minimizes damage to the pile head. This dolly is placed in a void at the top of the helmet, which in turn is placed on the top of the pile. Five 19 mm (¾ in.) plywood sheets were used as cushion in the present study (Fig. 11.3).

11.2.4 Method of pile installation

The method employed to drive the piles is as follows: Leaders were first positioned in the soil by simply lifting the leader assembly and letting it free fall at the desired position. The pile was then dragged into the horizontal position close to the piling rig (Fig. 11.4). The diesel hammer was already attached to the leader and drawn up to the cathead. The pile was then lifted into the leaders using a line from the cathead and secured by bolts. The helmet, dolly and packing were then placed on the pile head and moved under the impact path of the hammer. The hammer was then lowered, positioned on the helmet to commence pile driving (Fig. 11.5).

11.3 DRIVING OF TEST PILES

The driving of the test piles was conducted on March 31, 1997. The four test piles were of 254 mm (10 in.) square sections, each with a length of 7.62 m (25 ft.). Pile-B, Pile-C, Pile-D, Pile-A were driven in that order at FDOT Maintenance Facility in Miami. The average specified drop height was 1.83 m (6 ft.) for all the piles. However, the drop height averaged 2.13 m (7 ft.) during driving based on the amount of energy transferred to the top of the piles. The driving logs and driving stresses at selected penetration depths are presented in the Tables 11.1 - 11.5. Figs. 11.6 - 11.9 show the blow count versus depth for each pile. Pile-A and Pile-B were driven to a depth of 7 m (23 ft.), Pile-C to a depth of 5.94 m (19.5 ft.) and Pile-D to a depth of 6.71 m (22 ft.). A soft layer was reached between 4.5 m (14.75 ft.) and 5 m (16.5 ft.) causing a decrease in blow count and the driving records were very similar for all the piles. The SPT values from the soil investigation of the test site are compared with the average blow count of the test piles (Fig. 11.10). The SPT values show reasonable correlation with the driving records of the piles.

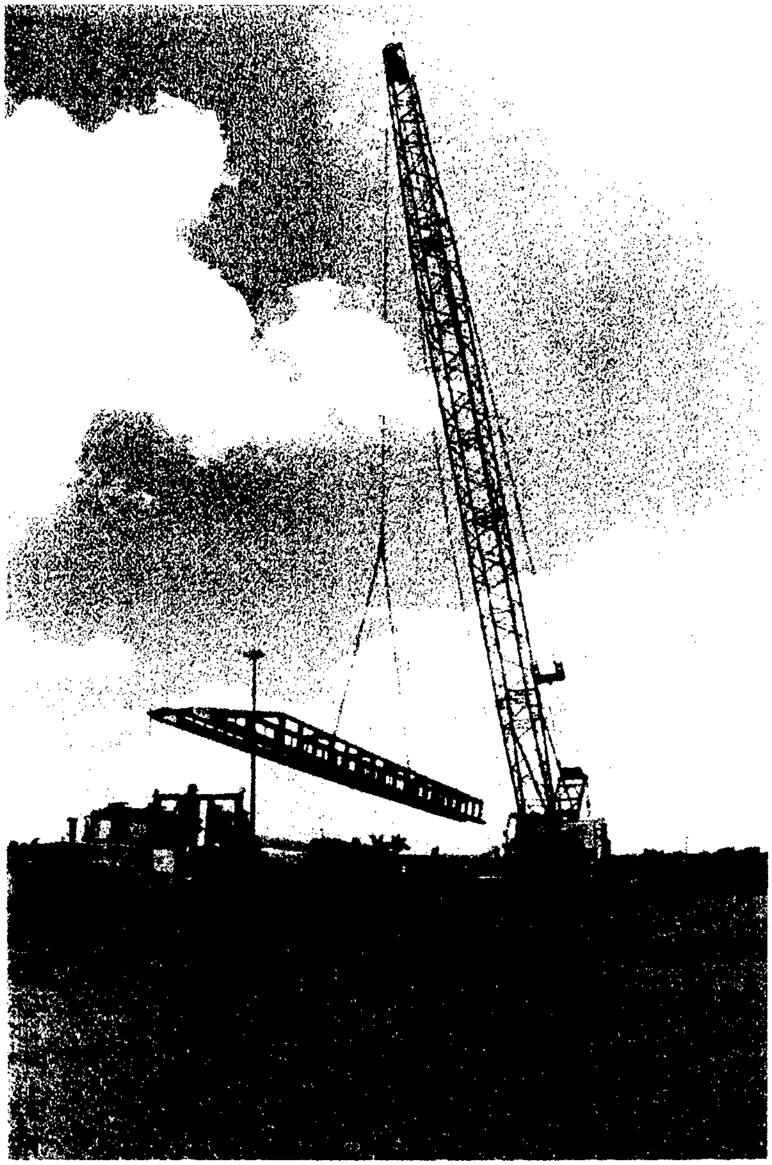

Figure 11.1 Pile driving equipment

Figure 11.2 Hammer, helmet and pile

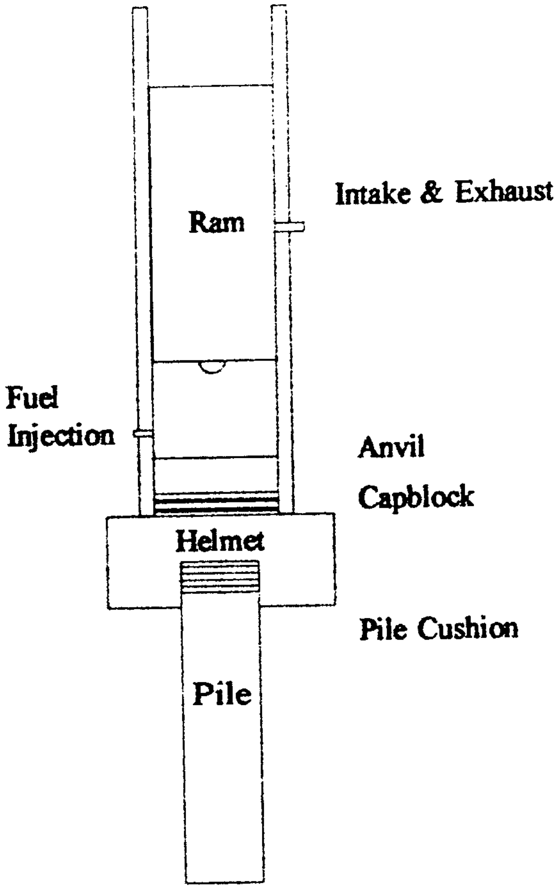

Figure 11.3 Schematic of diesel hammer and helmet

Figure 11.4 Positioning of CFRP pretensioned pile

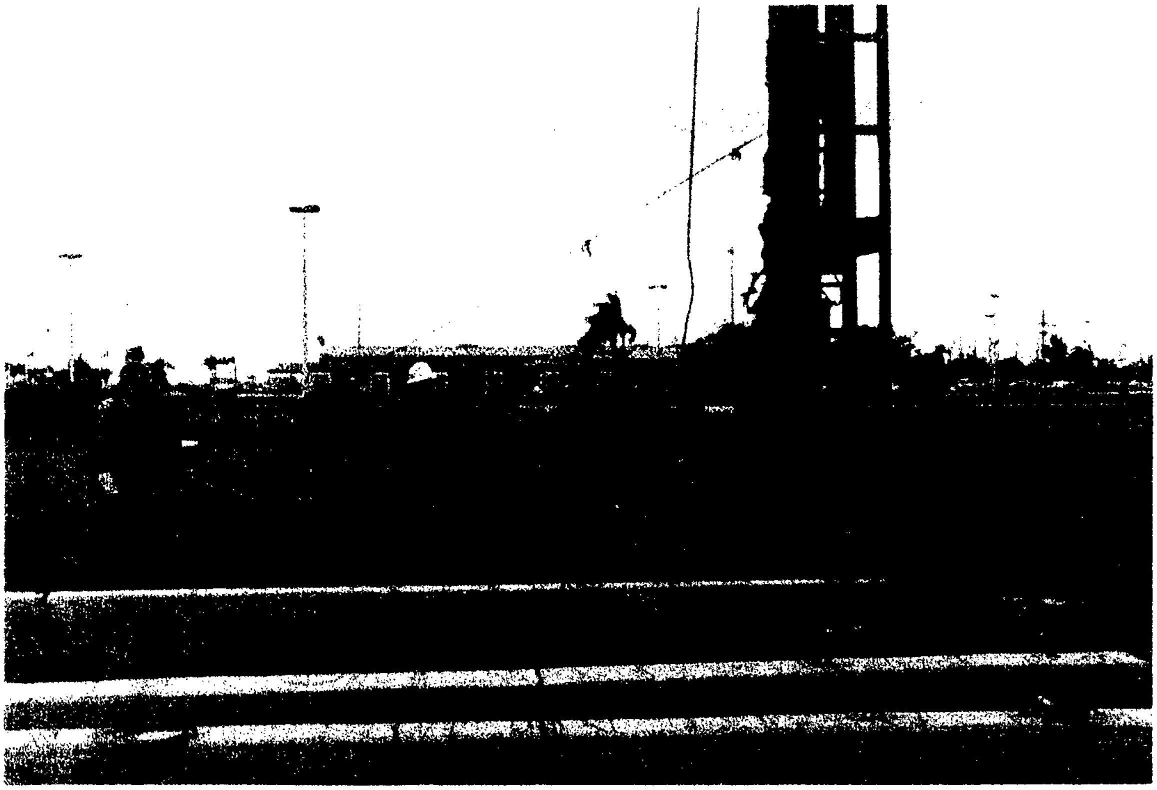

Figure 11.5 Driving of CFRP pretensioned concrete pile

Table 11.1 Driving log data

Depth (m)	Pile-A Blows/m	Pile-B Blows/m	Pile-C Blows/m	Pile-D Blows/m
0.30	13	16	20	26
0.61	10	16	20	30
0.91	23	23	46	59
1.22	30	49	125	52
1.52	30	43	75	49
1.83	43	36	16	59
2.13	33	30	13	36
2.44	26	30	16	66
2.74	26	46	13	30
3.05	30	92	23	56
3.35	59	79	36	49
3.66	46	26	30	72
3.96	56	33	52	85
4.27	56	66	52	75
4.57	26	23	62	43
4.88	26	46	52	39
5.18	23	66	56	26
5.49	43	66	59	62
5.79	66	66	85	82
6.10	89	157	558	125
6.40	171	89	-	39
6.71	177	39	-	46
7.01	164	36	-	-

Table 11.2 Pile-A driving stress data obtained from PDA

Depth (m)	Blows/m	Compressive stress (MPa)	Tensile stress (MPa)	Maximum transferred energy (kN-m)	Maximum capacity (kN)
0.30	13	8.89	0.55	3.53	125
0.61	10	8.54	0.41	2.58	138
0.91	23	9.44	1.38	2.99	174
1.22	30	10.61	0.41	3.39	209
1.52	30	7.85	1.31	3.53	218
1.83	43	14.68	0.28	8.69	374
2.13	33	16.47	0.00	8.69	543
2.44	26	16.26	0.00	8.14	575
2.74	26	15.02	1.31	7.60	468
3.05	30	14.06	0.34	7.19	343
3.35	59	11.09	0.90	6.24	192
3.66	46	9.51	1.38	5.70	143
3.96	56	9.71	1.03	4.48	361
4.27	56	12.26	0.41	6.24	303
4.57	26	12.68	0.07	6.52	316
4.88	26	13.64	0.07	6.24	445
5.18	23	14.12	0.00	7.19	387
5.49	43	11.16	1.65	5.70	183
5.79	66	10.13	1.52	5.70	151
6.10	89	14.74	0.21	7.06	419
6.40	171	17.91	1.38	8.96	1149
6.71	177	18.40	0.69	8.82	1332
7.01	164	19.57	1.86	9.37	1982

Table 11.3 Pile-B driving stress data obtained from PDA

Depth (m)	Blows/m	Compressive stress (MPa)	Tensile stress (MPa)	Maximum energy transferred (kN-m)	Maximum capacity (kN)
0.30	16	6.89	0.69	7.87	98
0.61	16	9.85	6.48	7.87	232
0.91	23	9.09	4.96	4.89	263
1.22	49	11.23	6.96	6.65	298
1.52	43	12.82	4.89	6.92	316
1.83	36	12.88	5.65	6.52	281
2.13	30	10.68	5.17	6.52	200
2.44	30	10.20	9.30	6.52	187
2.74	46	12.06	4.20	8.01	214
3.05	92	12.61	0.76	5.57	379
3.35	79	11.37	2.41	5.02	303
3.66	26	12.82	1.72	7.74	200
3.96	33	11.99	6.55	6.92	192
4.27	66	11.92	1.93	6.52	192
4.57	23	12.68	0.55	7.19	196
4.88	46	11.30	0.28	4.89	241
5.18	66	10.54	4.62	4.48	249
5.49	66	13.23	0.07	6.11	343
5.79	66	15.57	0.00	6.65	490
6.10	157	18.05	0.21	7.74	949
6.40	89	14.12	0.21	7.06	695
6.71	39	10.54	0.41	7.06	272
7.01	36	11.44	0.21	8.01	347

Table 11.4 Pile-C driving stress data obtained from PDA

Depth (m)	Blows/m	Compressive stress (MPa)	Tensile stress (MPa)	Maximum energy tansferred (kN-m)	Maximum capacity (kN)
0.30	20	7.30	3.93	6.65	125
0.61	20	10.40	9.37	7.87	254
0.91	46	11.92	10.20	6.38	334
1.22	125	13.71	5.58	6.92	432
1.52	75	10.89	6.75	6.92	196
1.83	16	8.06	8.27	7.74	0
2.13	13	8.20	9.30	8.01	4
2.44	16	10.40	11.30	6.79	192
2.74	13	9.37	9.65	5.29	200
3.05	23	10.54	7.37	7.19	254
3.35	36	10.40	9.09	7.19	209
3.66	30	11.85	2.96	6.24	303
3.96	52	12.54	3.86	6.38	374
4.27	52	12.61	3.31	6.65	356
4.57	62	11.37	2.00	5.70	263
4.88	52	11.02	7.44	5.43	285
5.18	56	11.51	0.48	5.70	281
5.49	59	12.95	0.07	6.79	361
5.79	85	15.92	0.00	7.74	530
5.94	558	20.81	1.24	9.91	1915

Table 11.5 Pile-D driving stress data obtained from PDA

Depth (m)	Blows/m	Compressive stress (MPa)	Tensile stress (MPa)	Maximum energy transferred (kN-m)	Maximum capacity (kN)
0.30	26	5.79	3.31	4.34	120
0.61	30	9.09	0.83	8.01	200
0.91	59	13.85	3.03	7.74	419
1.22	52	16.60	5.86	8.55	534
1.52	49	15.43	3.93	7.33	410
1.83	59	12.06	5.37	6.52	254
2.13	36	11.58	6.20	7.06	236
2.44	66	15.16	9.03	7.87	450
2.74	30	14.81	5.17	8.01	414
3.05	56	15.36	7.17	7.87	396
3.35	49	13.23	6.68	6.11	365
3.66	72	12.68	2.62	5.16	445
3.96	85	14.33	3.86	5.97	512
4.27	75	13.85	2.41	7.19	289
4.57	43	10.61	3.93	5.57	192
4.88	39	10.96	2.00	5.43	196
5.18	26	11.78	0.41	5.29	294
5.49	62	14.26	0.14	6.11	396
5.79	82	16.74	0.14	6.65	793
6.10	125	16.12	0.28	7.60	730
6.40	39	10.13	0.55	5.16	236
6.71	46	11.23	0.48	5.57	334

11.4 RESULTS AND DISCUSSIONS

The CFRP pretensioned concrete piles were subjected to driving stresses similar to that encountered during driving in a pile foundation for a bridge. The maximum compressive stress in the piles ranged between 16.74 to 20.81 MPa (2.43 to 3.02 ksi) and maximum tensile stress range was between 1.86 - 11.30 MPa (0.27 to 1.64 ksi) The actual stresses are consistent with the predicted stresses based on the wave equation. The predicted tensile and compressive stresses are in the range of 0.0 and 7.1 MPa (1.03 ksi) and 16.6 and 24.32 MPa (2.41 and 3.53 ksi) respectively. The predicted stresses compare well with the actual measured stresses shown in Table 11.6. The tensile stresses were maximum at the initial stage of driving whereas the maximum compressive stresses were at the end of the pile driving stage. Figs. 11.11 - 11.14 show the actual tensile and compressive stresses in the concrete for the test piles.

Table 11.6 —Summary of maximum pile driving stresses from PDA

Pile	Depth of penetration m (ft)	Tensile stress MPa (ksi)	Compressive stress MPa (ksi)	Maximum energy transfer kN-m (kip-ft)	Blow count blows/m (blows/ft)
Pile A	7.01 (23.0)	1.86 (0.27)	19.58 (2.84)	9.36 (6.9)	177 (54)
Pile B	7.01 (23.0)	9.31 (1.35)	18.07 (2.62)	8.00 (5.9)	157 (48)
Pile C	5.95 (19.5)	11.3 (1.64)	20.83 (3.02)	9.90 (7.3)	125 (38)
Pile D	6.71 (22.0)	9.03 (1.31)	16.75 (2.43)	8.00 (5.9)	125 (38)

Figs. 11.11 and 11.12 show the actual tensile and compressive stresses in pretensioned concrete piles with CFRP tendons together with CFRP hoops (Piles A and B). The maximum stresses obtained in both the piles (compressive stress of 19.58 MPa and tensile stress of 9.31 MPa) were less than the FDOT allowable stresses (S_{apc} and S_{apt}) given by:

$$S_{apc} = 0.7f'_c - 0.75f_{pe}$$
$$S_{apt} = 6.5\sqrt{f'c} + 1.05f_{pe} \qquad \text{............(11.1)}$$

where f'_c= concrete strength

f_{pe}= effective prestress

The observed tensile stresses in Pile A are much less, but the maximum tensile stress in Pile B almost approached the maximum allowable tensile stress, S_{apt} = 9.72 MPa (1.41 ksi), whereas maximum compressive stress in both the piles was much smaller than the allowable maximum stress, S_{apc} = 31.47 MPa (4.57 ksi). Figure 11.12 also shows a significant drop in the compressive stress at the same point where there was a significant increase in tensile stress. The high tensile stress developed in the pile at a depth of approximately 2.5 m (8.2 ft) correspond to the change in the soil strata, which was observed in the site soil investigation. The soil strata change can be observed from the change in SPT values and pile blow counts. The stresses in Piles C and D shown in Figs. 11.13 and 11.14 were similar but higher than those in piles A and B.

Figs 11.15 to 11.18 show the compressive and tensile stresses versus the depth of penetration of the piles based on strains measured by the data acquisition system (MEGADAC), which show good agreement with the stresses obtained from the PDA analyses. For the pile A, the tensile stress versus the depth of penetration was different from the results based on PDA, which showed negligible tensile stresses. However, MEGADAC data for pile A showed the same tendency as the other. It can be observed that the stresses obtained by the data acquisition system from the strain gages embedded at 0.3 m (1 ft) from the pile top were in good agreement with the PDA data based on the accelerometer and strain gage transducers. No concrete spalling or damage was observed in any of the test piles. Fig. 11.19 shows the test piles after completion of driving.

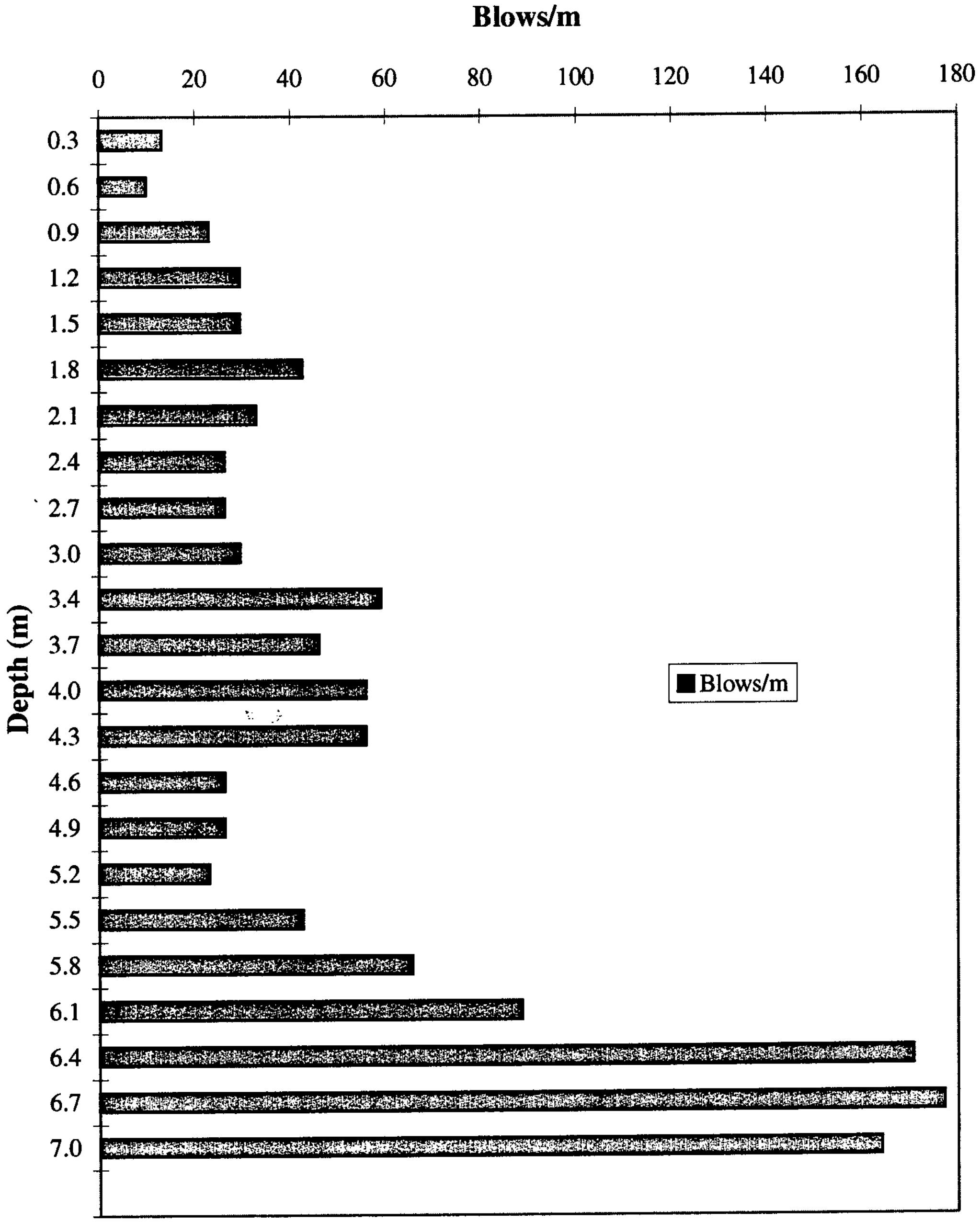

Figure 11.6 Pile-A Blow count vs. Depth

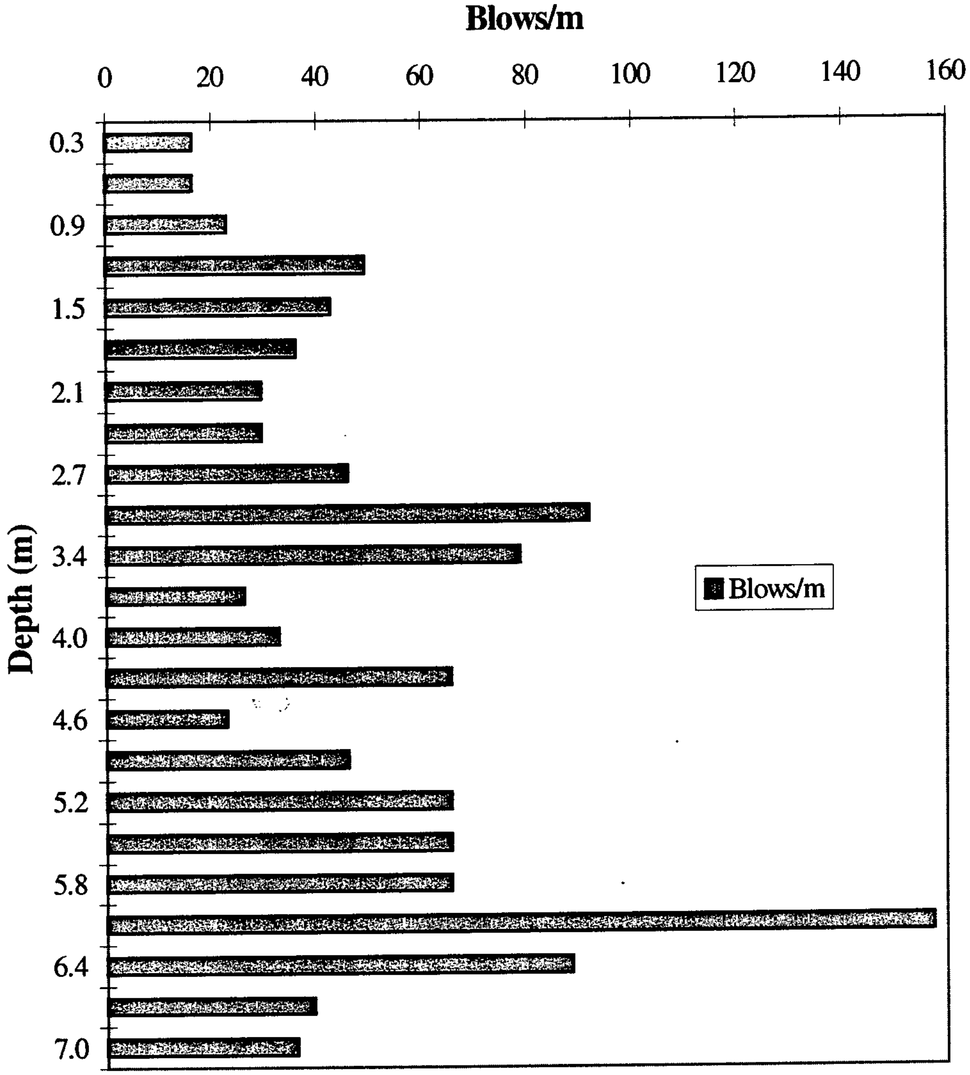

Figure 11.7 Pile-B Blow count vs. Depth

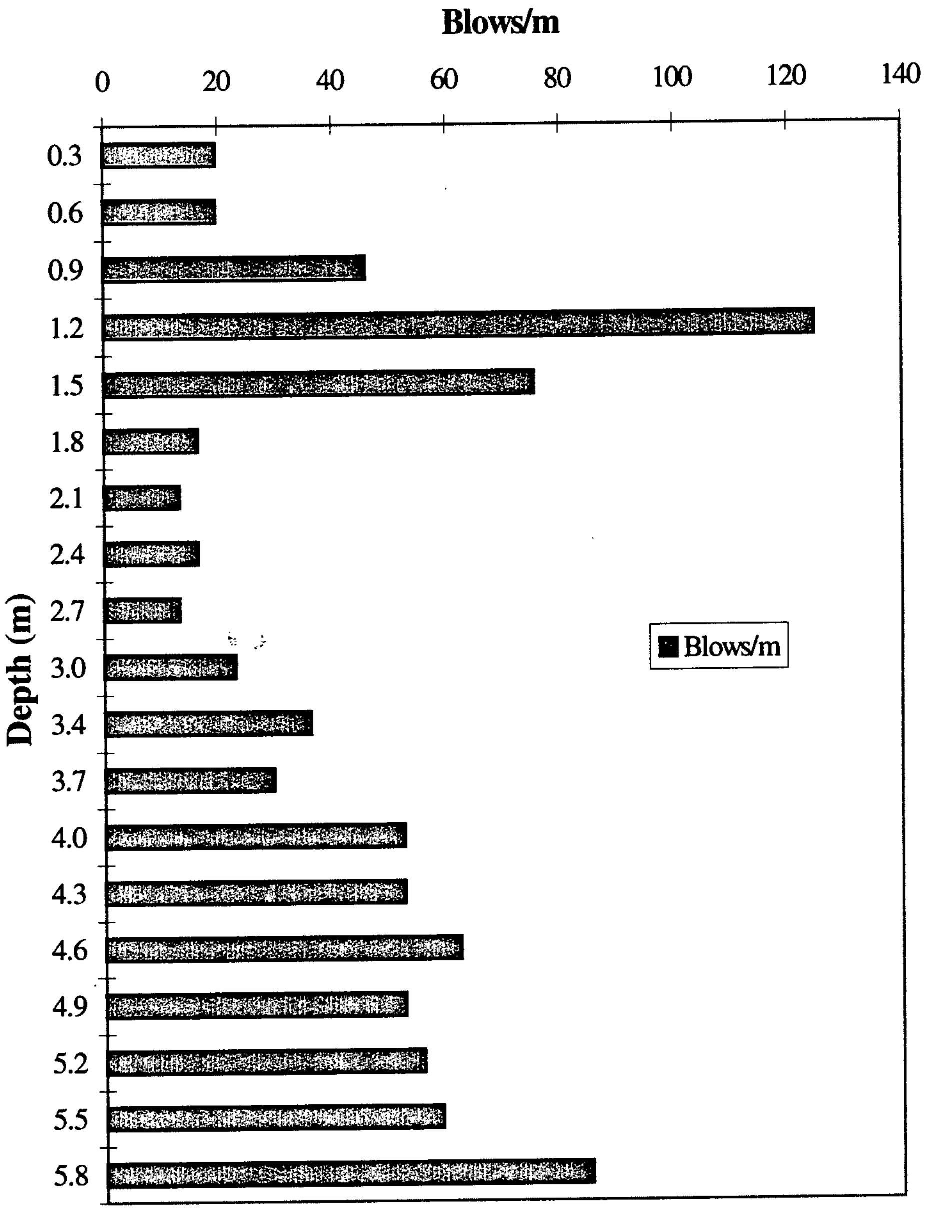

Figure 11.8 **Pile-C Blow count vs. Depth**

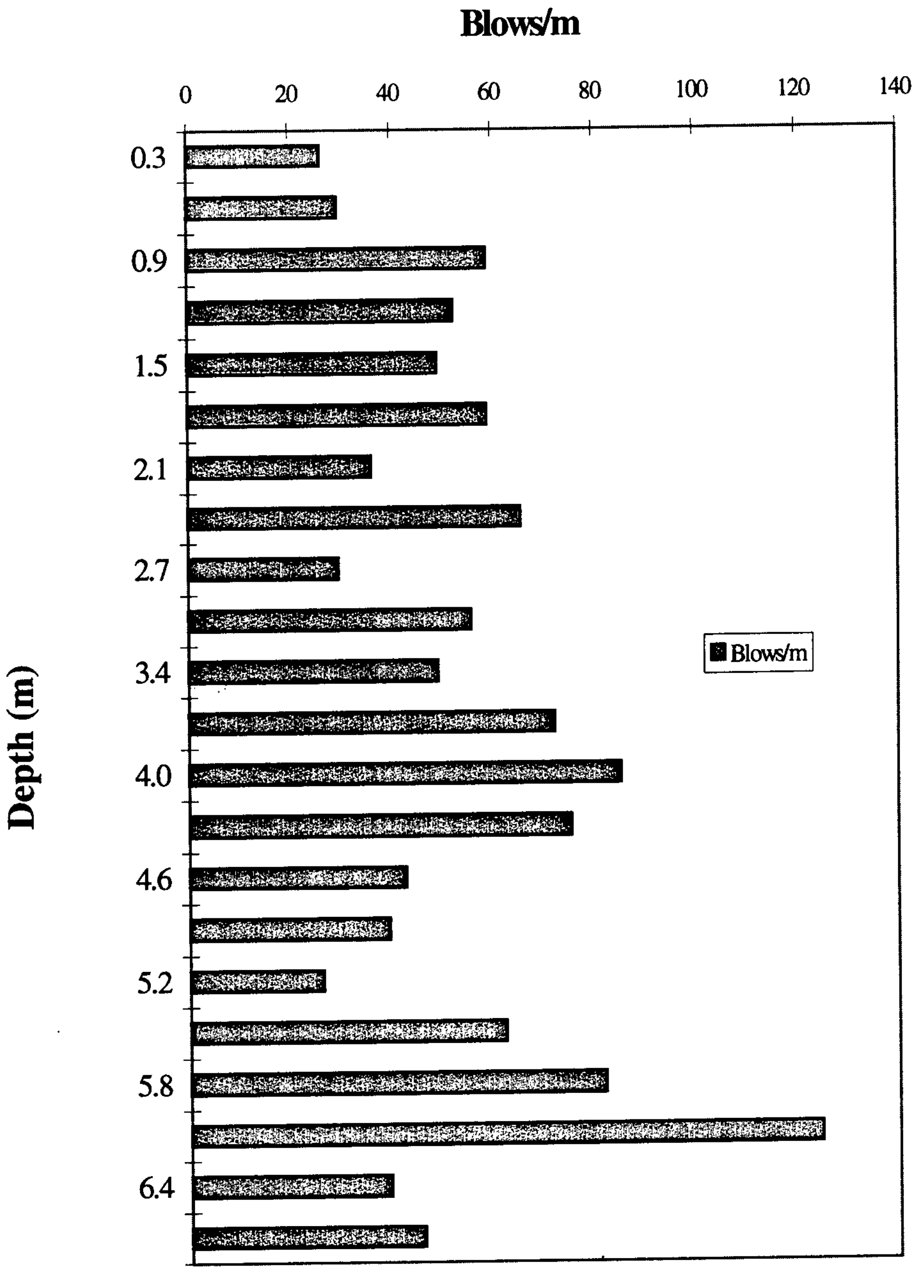

Figure 11.9 Pile-D Blow count vs. Depth

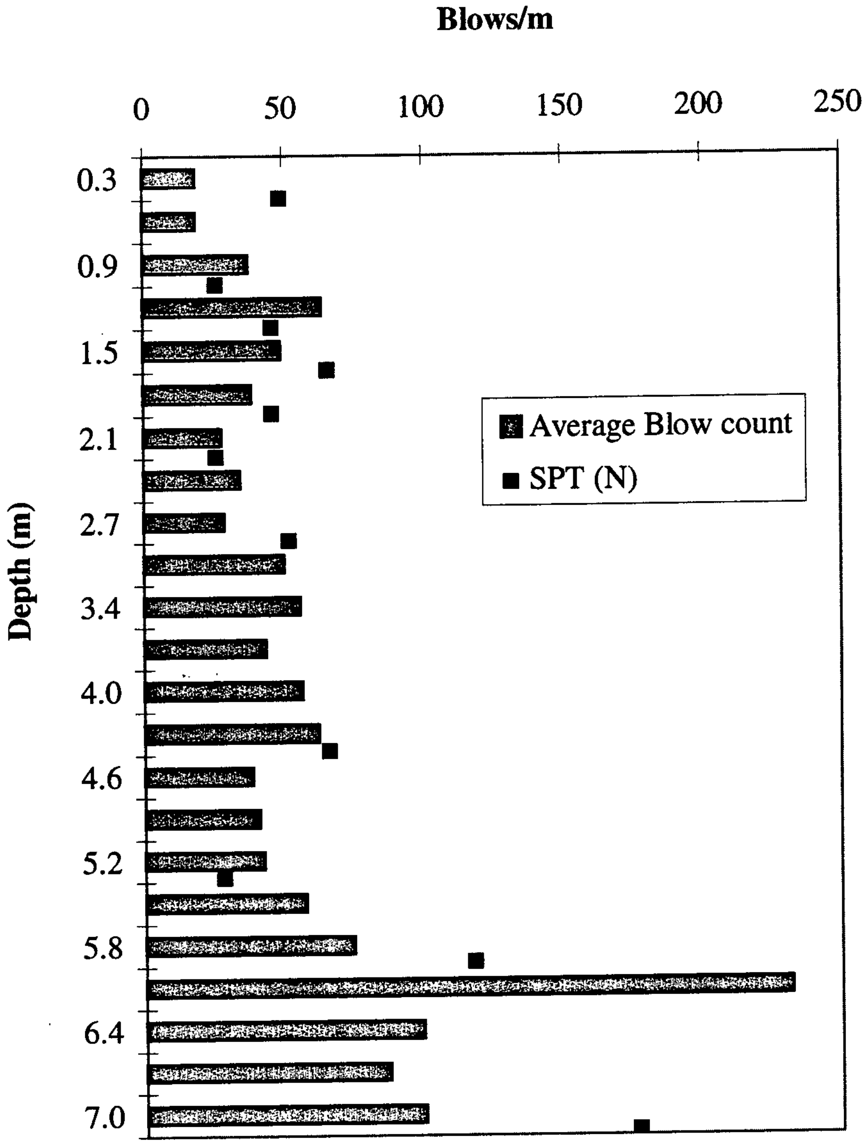

Figure 11.10 Comparison of SPT values to average blow count along the depth

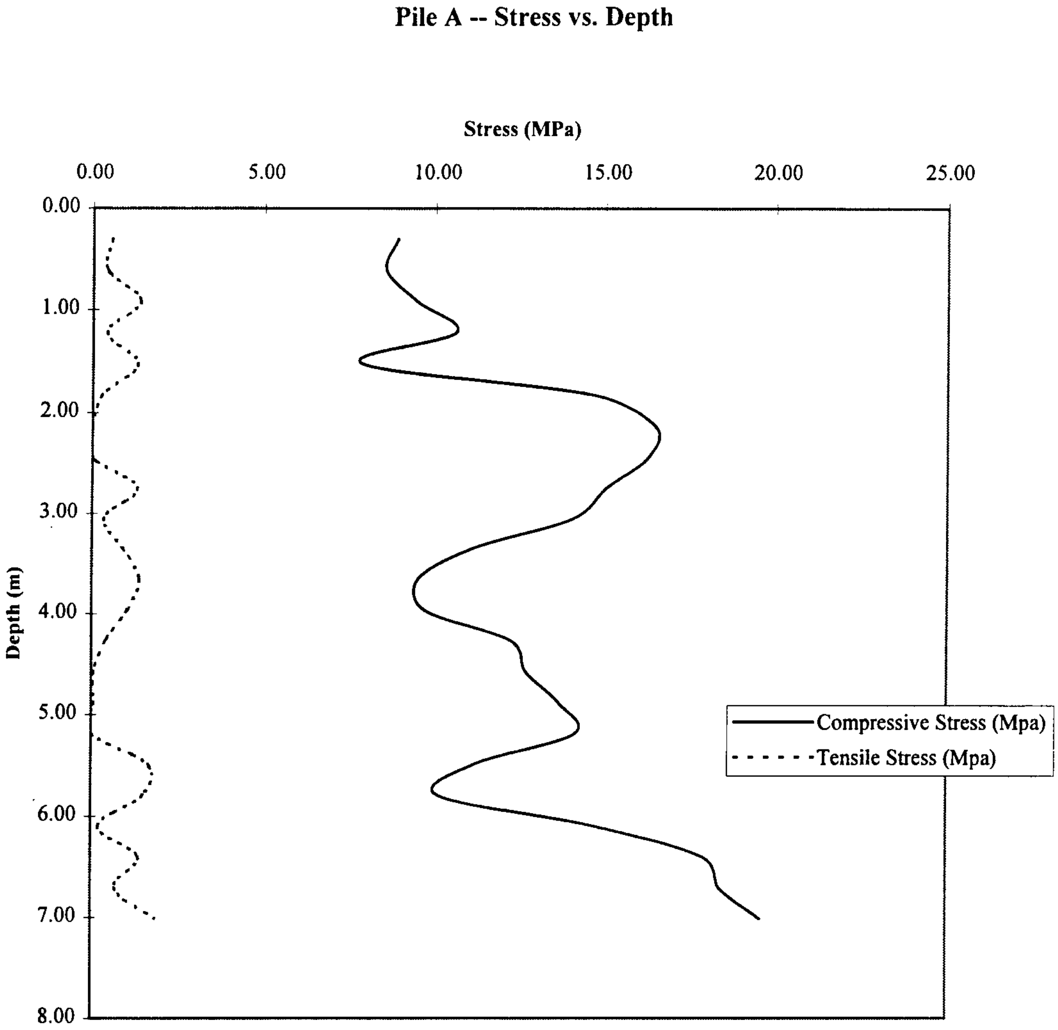

Figure 11.11 Driving stresses along the depth of penetration for Pile-A from PDA

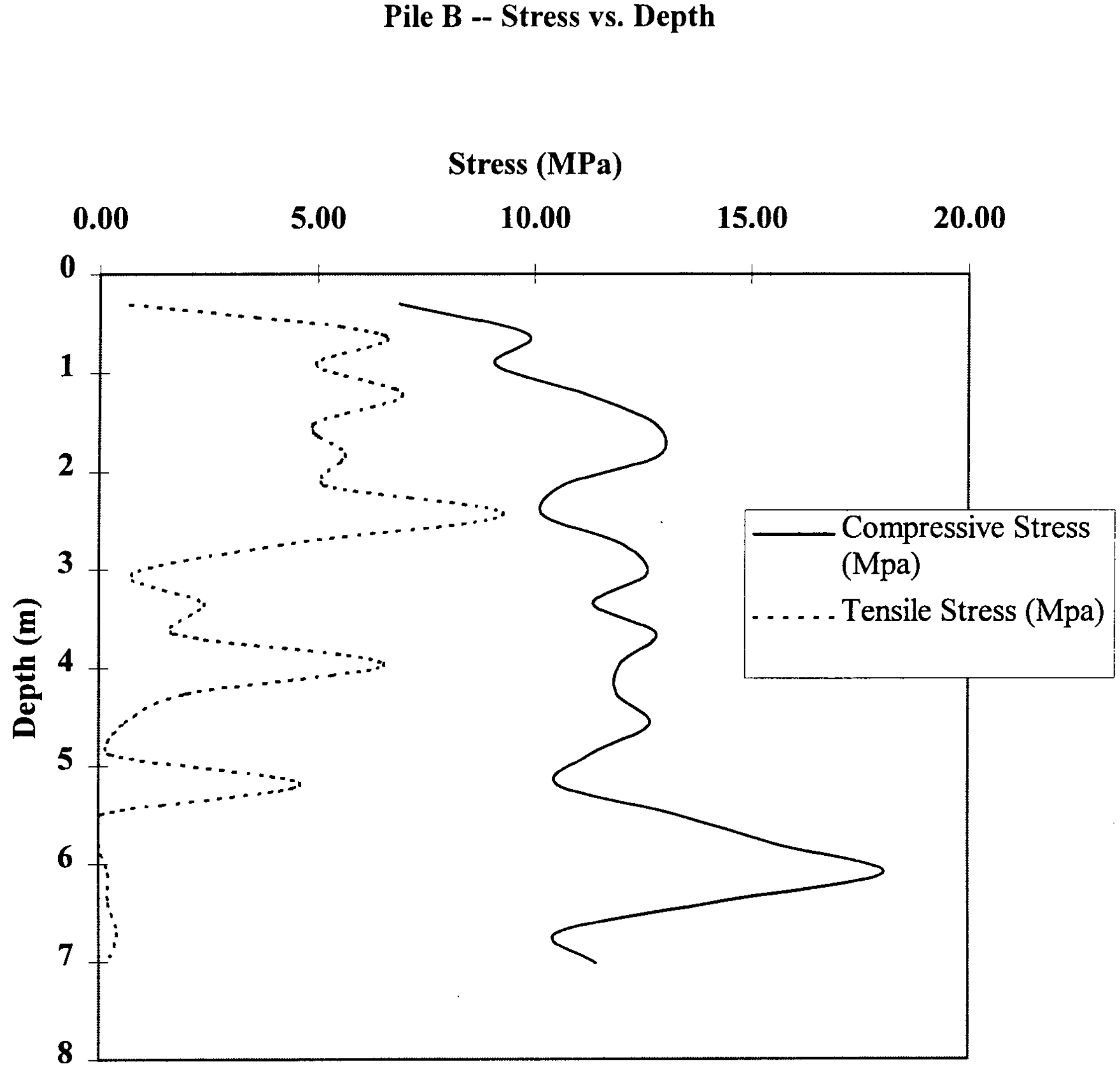

Figure 11.12 Driving stresses along the depth of penetration for Pile-B from PDA

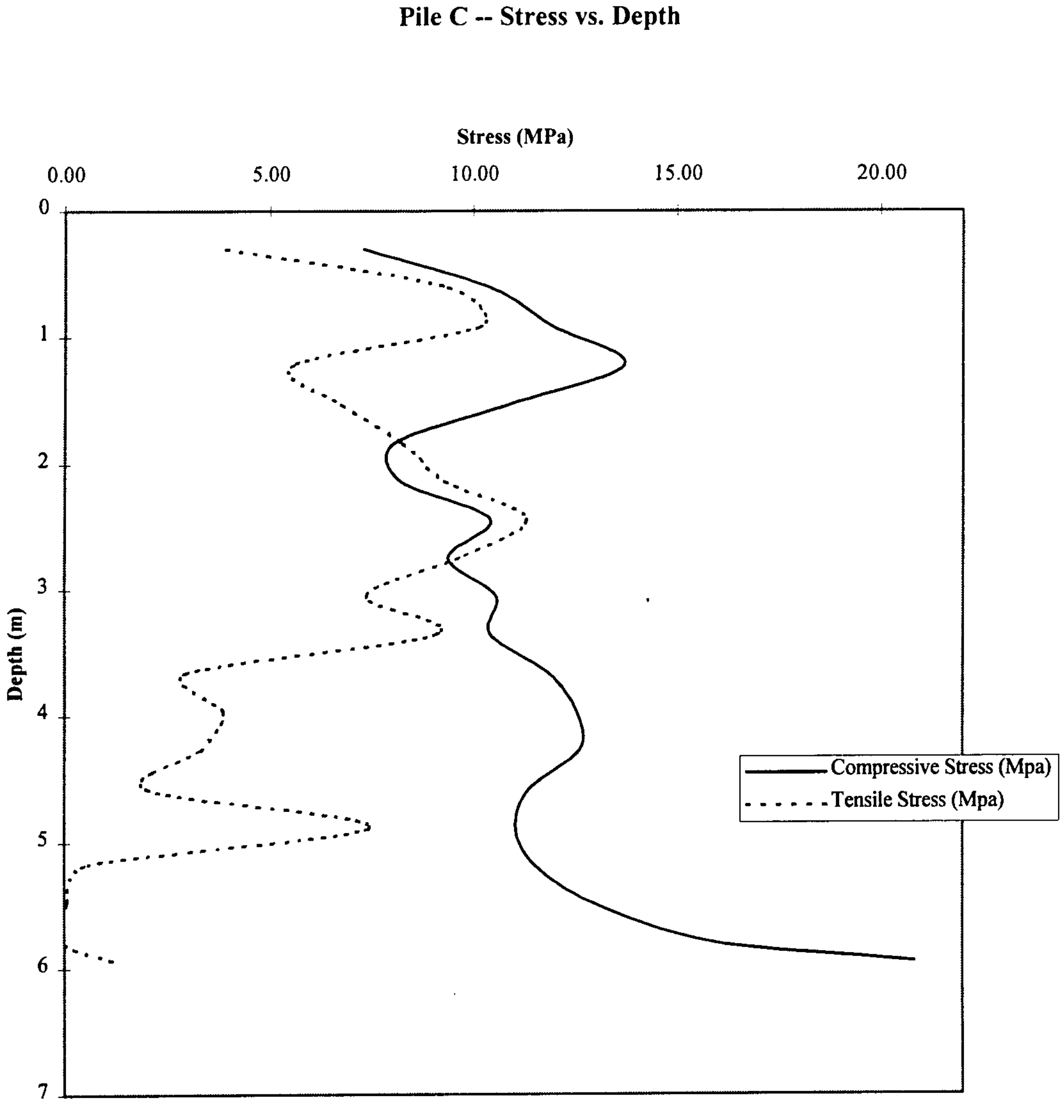

Figure 11.13 Driving stresses along the depth of penetration for Pile-C from PDA

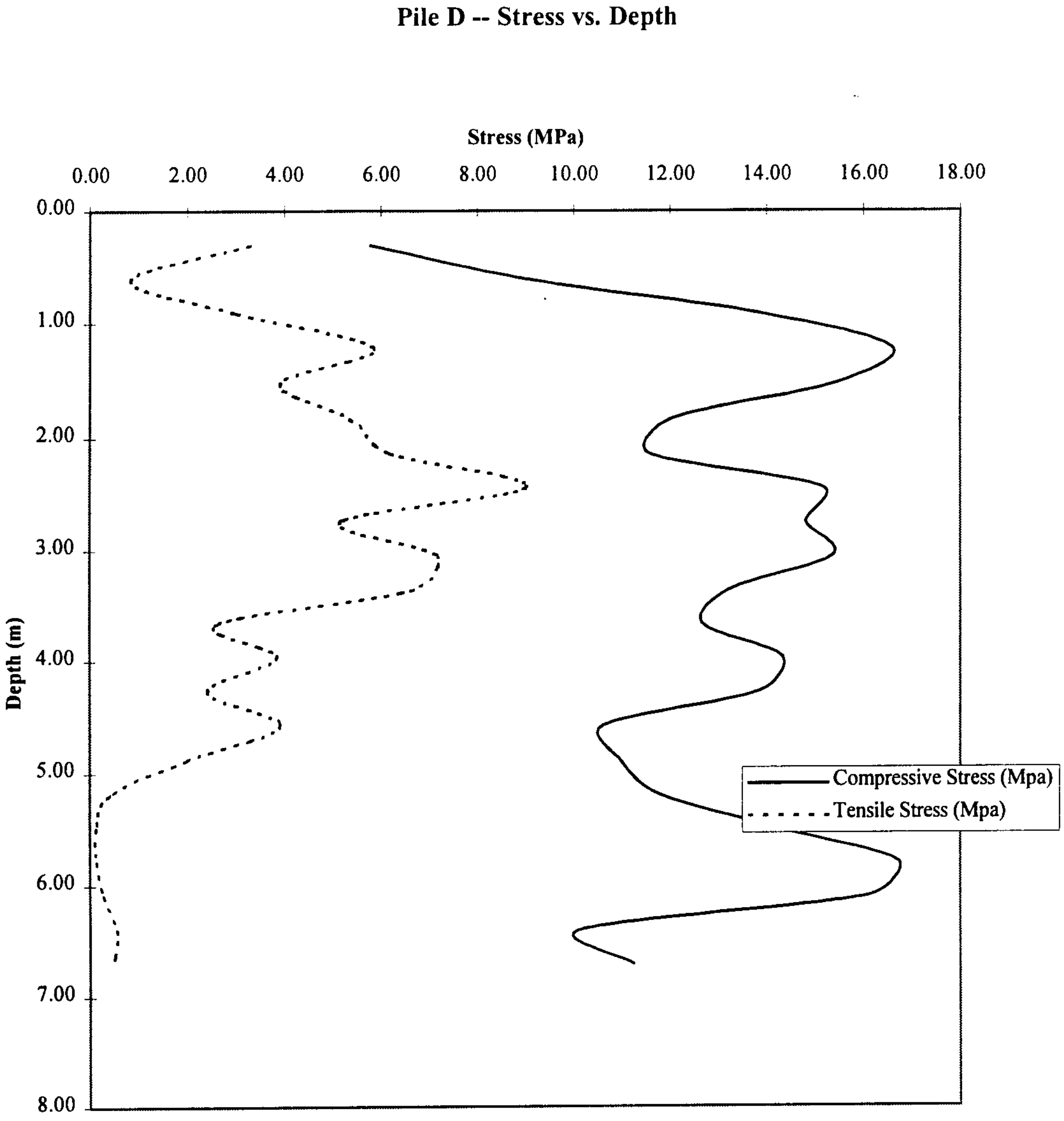

Figure 11.14 Driving stresses along the depth of penetration for Pile-D from PDA

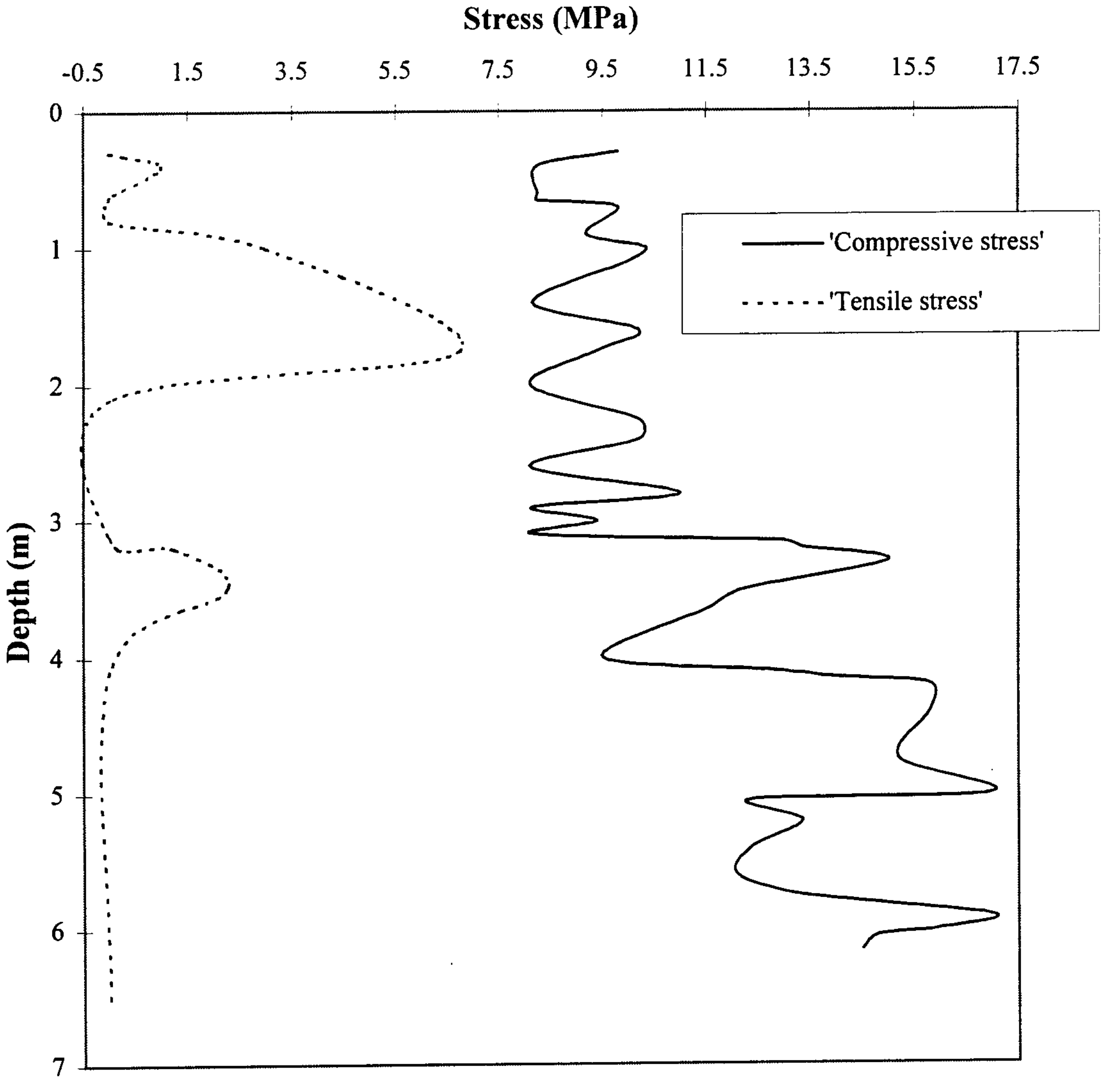

Figure 11.15 Driving stresses along the depth of penetration for Pile-A from data acquisition system

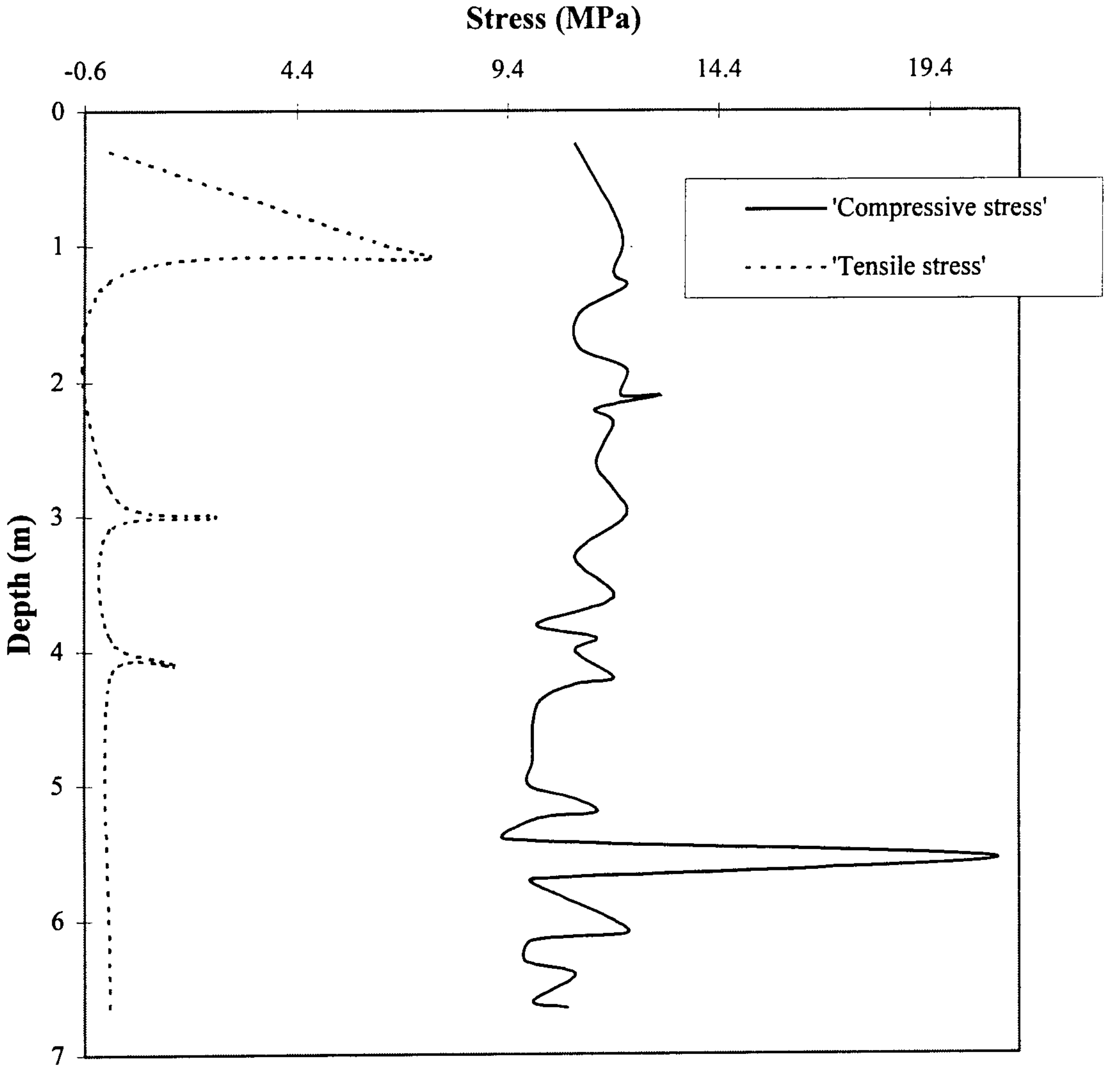

Figure 11.16 Driving stresses along the depth of penetration for Pile-B from data acquisition system

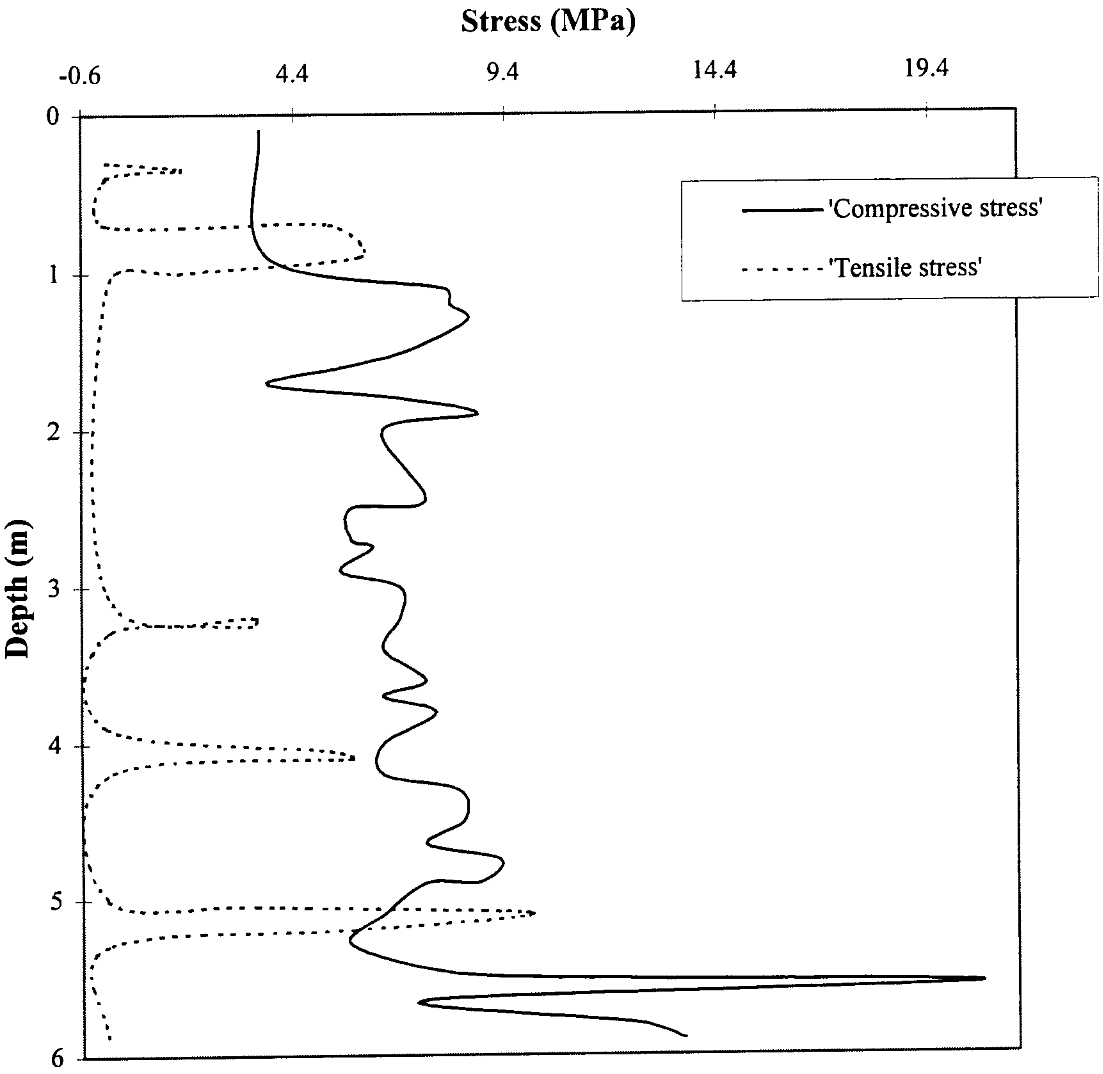

Figure 11.17 Driving stresses along the depth of penetration for Pile-C from data acquisition system

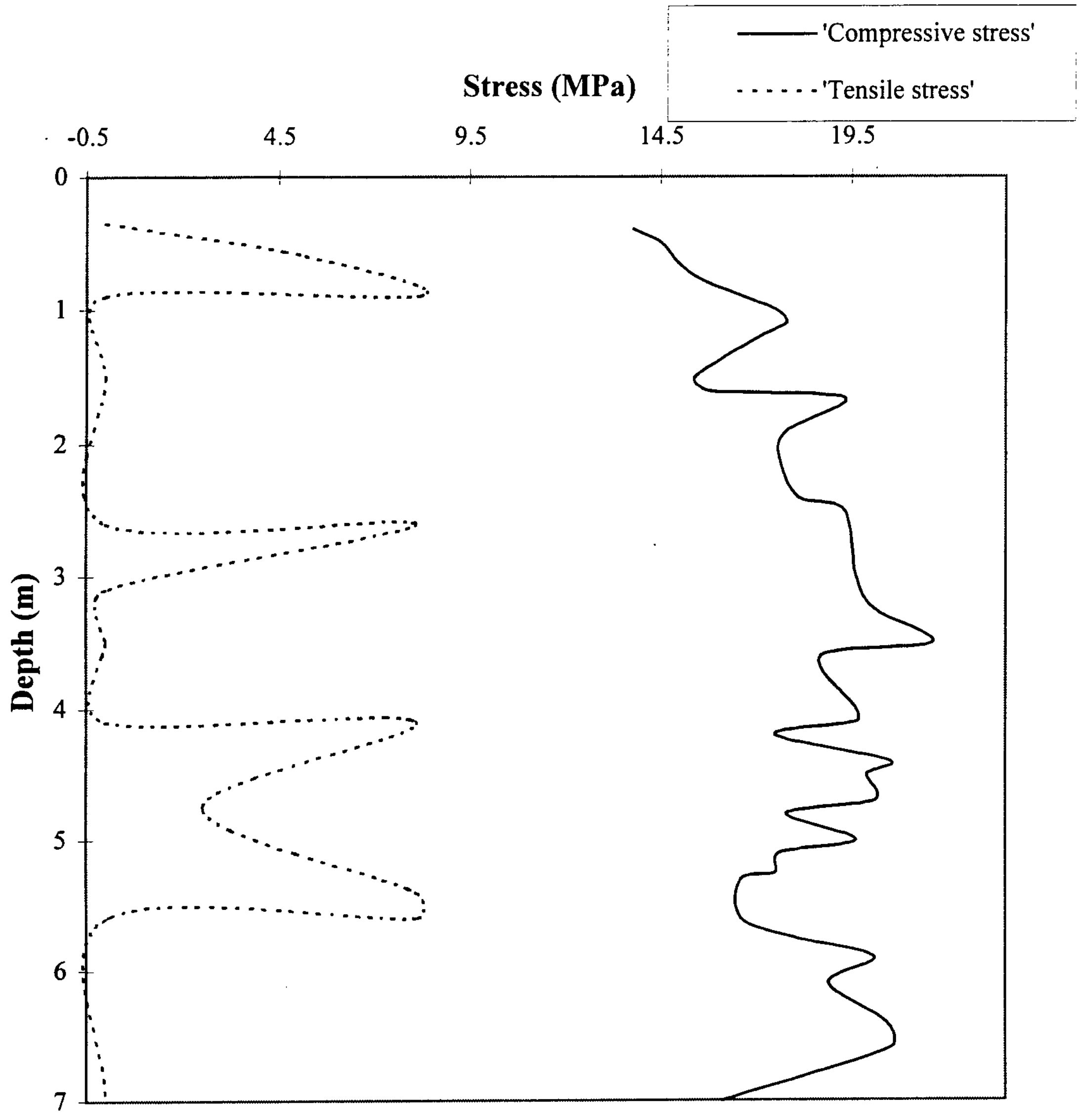

Figure 11.18 Driving stresses along the depth of penetration for Pile-D from data acquisition system

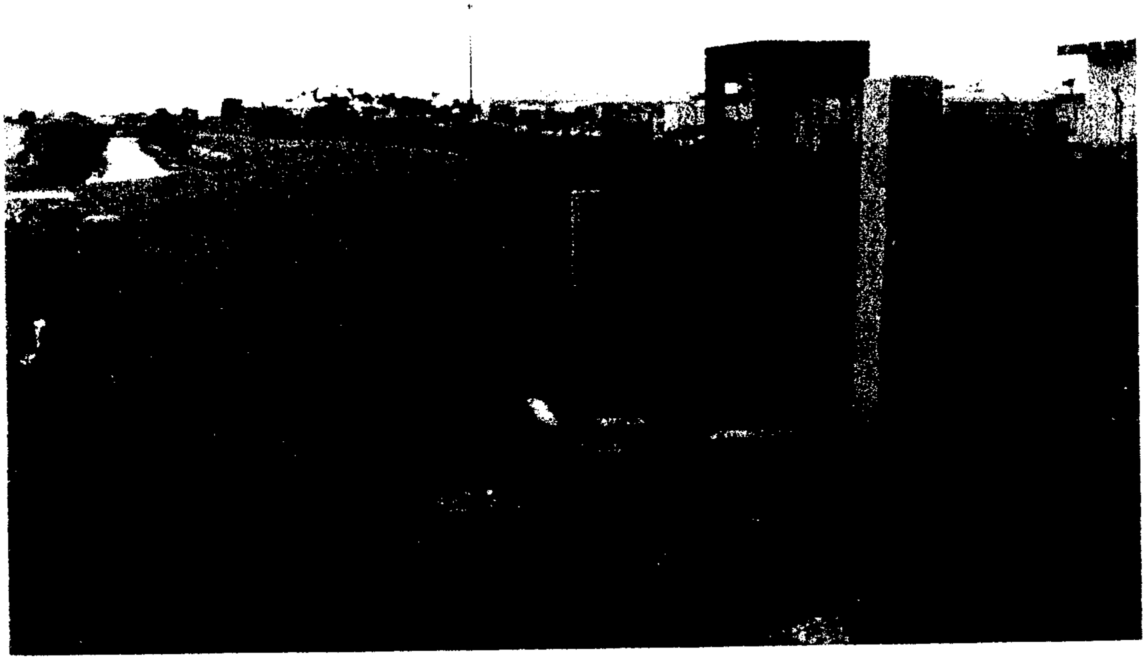

Figure 11.19 Piles after driving at the site

CHAPTER 12

CONFINEMENT EFFECTS IN REINFORCED CONCRETE COLUMNS WITH CFRP HOOP REINFORCEMENT

12.1 INTRODUCTION

Extensive research has been carried out in the area of confinement, mainly concrete confined with steel ties, hoops or spirals and jackets. It has been established that the lateral confinement would enhance both the strength and ductility of reinforced concrete members due to the development of triaxial stress field within the confined concrete. Very limited technical literature has been published related to CFRP reinforced concrete columns with CFRP hoops. The primary objectives of this study are the following:

i) to check the feasibility of CFRP hoops as transverse reinforcement in concrete columns under axial compression.
ii) to establish load - deformation characteristics of the concrete columns for different CFRP hoop spacings.
iii) to study the strength enhancement in the concrete columns due to the CFRP hoops as transverse reinforcement under ultimate loads.

This chapter presents the preparation, instrumentation and testing of the concrete column specimens confined with CFRP hoops. The specimens consist of four groups, each group having different hoop spacings of 50, 75, 100, and 150 mm. The columns in each group were tested to failure under axial compression.

12.2 EXPERIMENTAL WORK

12.2.1 Concrete column specimens

Eleven short column specimens of size 150 x 150 x 762 mm (6 x 6 x 30 in.), divided into four groups based on lateral CFRP hoop spacing were tested in axial compression (Table 12.1). The group CS2 consisted of two specimens with 50 mm hoop spacing, and the other three groups - CS3, CS4 and CS6 had three column specimens in each with 75, 100 and 150 mm hoop spacing respectively. The longitudinal reinforcement in each concrete column consisted of four 12.5 mm diameter CFRP seven wire strands placed symmetrically with a clear cover of 25 mm (Fig. 12.1).

12.2.2 Materials

12.2.2.1 Concrete

Concrete supplied by Tarmac Inc. Florida, was used in the casting of the column specimens. The 28 day cylinder compressive strength and modulus of elasticity of concrete used were 45 MPa (6,500 psi) and 31.73 GPa (4595.5 ksi) respectively. The maximum size of coarse aggregate was 19 mm and the cement: sand: aggregate ratio was 1: 1.31: 2.14.

12.2.2.2 Carbon FRP reinforcement

The materials used for manufacturing carbon FRP include the carbon fiber of the PAN base system and matrix resins (Table 5.1c). The properties of the carbon FRP reinforcements are presented in Table 12.2.

Table 12.1 Description of column specimens

Group	Column specimen	Spacing of CFRP hoop (mm)	Concrete cylinder strength at the time of testing (MPa)
CS6	CS61	150	40
	CS62	150	46
	CS63	150	46
CS4	CS41	100	41
	CS42	100	46
	CS43	100	46
CS3	CS31	75	46
	CS32	75	46
	CS33	75	46
CS2	CS21	50	40
	CS22	50	41

Table 12.2 Properties of carbon FRP reinforcement

Properties	Hoop reinforcment	Longitudinal reinforcement
Diameter of the FRP rod	7.5 mm (0.3 in.)	12.5 mm (0.5 in.)
Effective area of cross section	30.4 mm^2	76 mm^2
Modulus of elasticity	137.34 GPa (19.9 x 10^3 ksi.)	137.34 GPa (19.9 x 10^3 ksi.)

12.2.3 Fabrication and instrumentation of test column specimens

The column specimens were fabricated using detachable formwork. The formwork was made up of plywood, 762 mm (30 in.) long with an internal cross section of 150 x 150 mm. The end pieces with holes for housing the longitudinal CFRP tendons were mounted on both ends of the formwork. The formwork was waxed to facilitate easy removal of the specimens after casting. The CFRP hoops were placed in the form work along with the CFRP tendons through the end pieces. The longitudinal tendons were held in position by applying putty at the ends (Fig. 12.2). The hoops were tied along the length at predetermined spacings. To maintain the same cross section along the entire length, cross pieces were nailed at the center of the form work. Two embedded strain gages (PL-60) were tied to the longitudinal tendons and two to the lateral hoops (Fig. 12.3) in the middle 30 cm (1 ft.) portion of the specimens. Fig. 12.4 shows the concrete casting in progress. Ten standard concrete cylinders were also cast along with the column specimens to obtain the concrete strength. The specimens were initially cured daily for four days, and later stored for 10 days prior to testing. The curing was continued during the period of storage. Fig 12.5 show the specimen ready for testing.

12.2.4 Ultimate load tests

The columns were transported to Wingerter Laboratories Inc. in Miami for testing (Fig. 12.6). The end surfaces of the columns were prepared according ASTM capping standards to ensure uniform loading at the ends. The upper plate of the testing machine was arranged with steel spherical seating to minimize any eccentricity in the applied load (Fig. 12.7). Care was taken to load the columns axially so as to reduce any possible bending of the column. The column end surfaces were also filled to ensure uniform loading.

The columns were tested in a universal testing machine with a capacity of 1915 kN (430 kips) (Fig. 12.8). The embedded electrical strain gages were monitored using strain

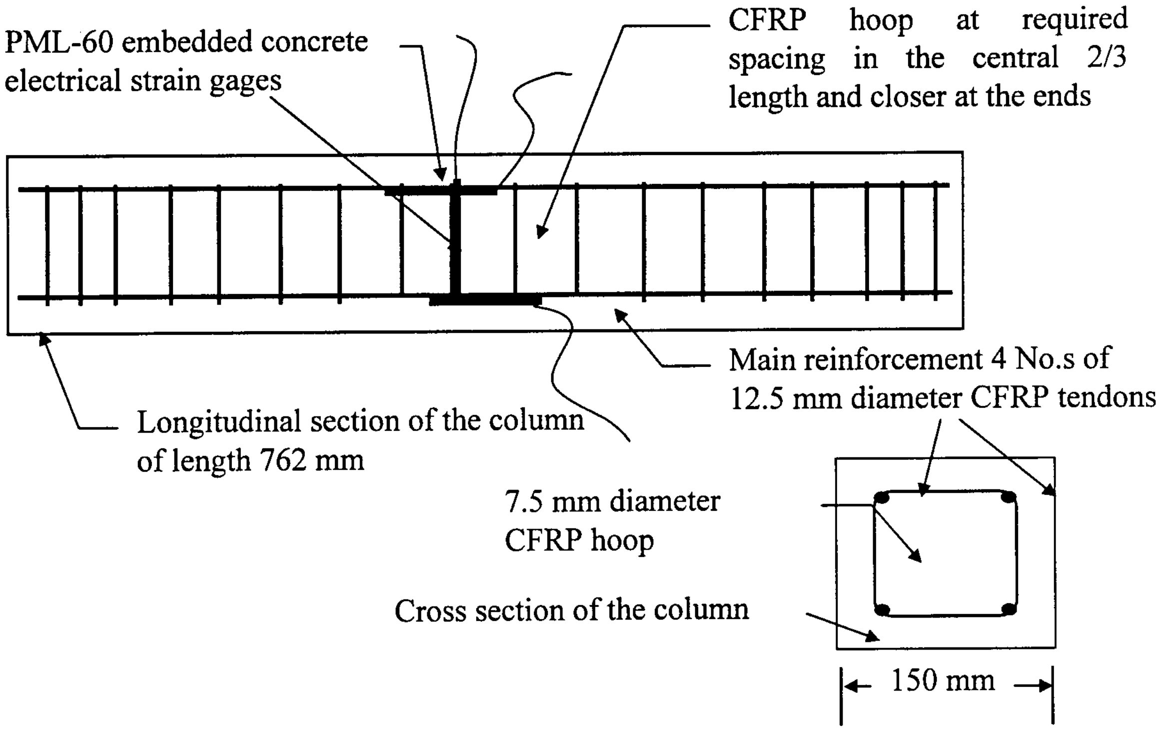

Figure 12.1 Sectional details of typical test column

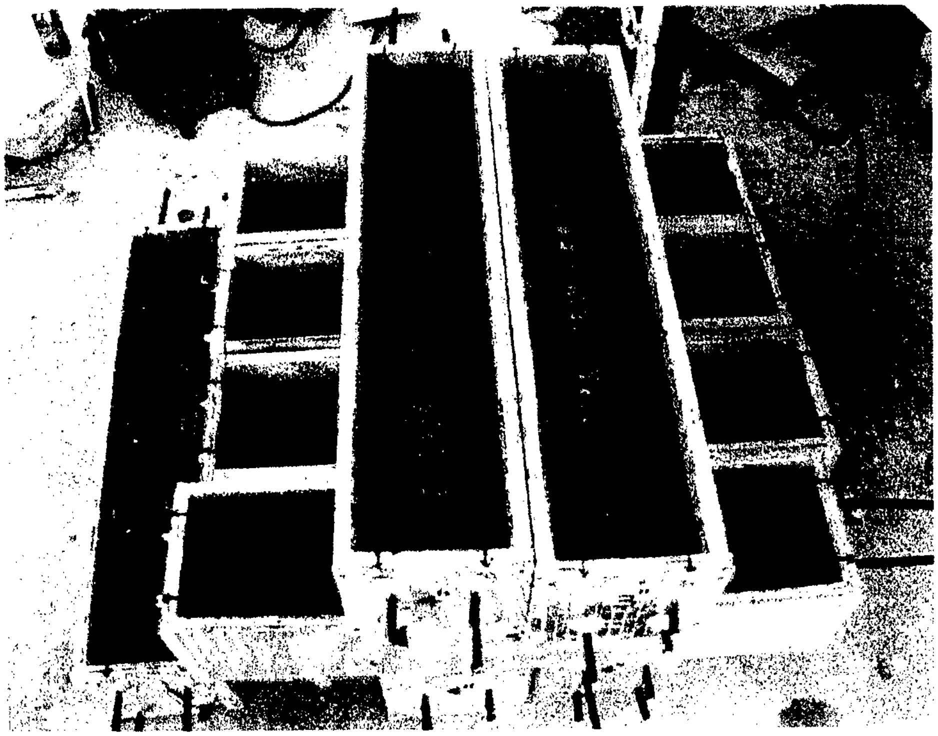

Figure 12.2 Form work for the test column specimen

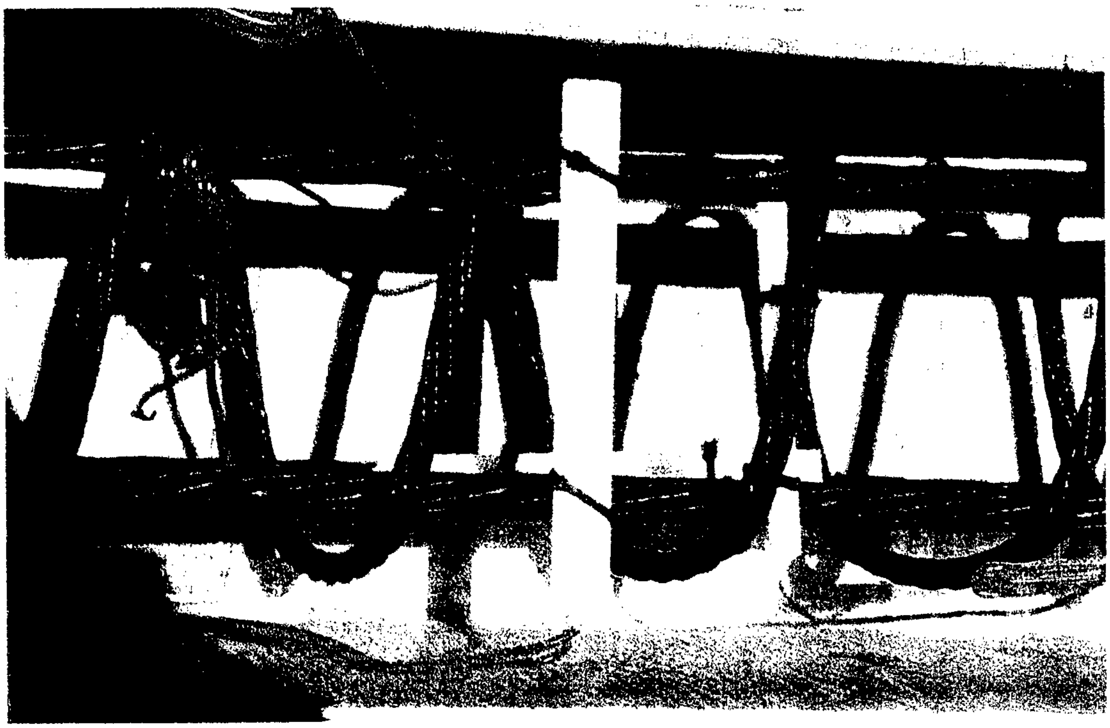

Figure 12.3 Embedded electrical strain gages

Figure 12.4 Concrete pouring in progress

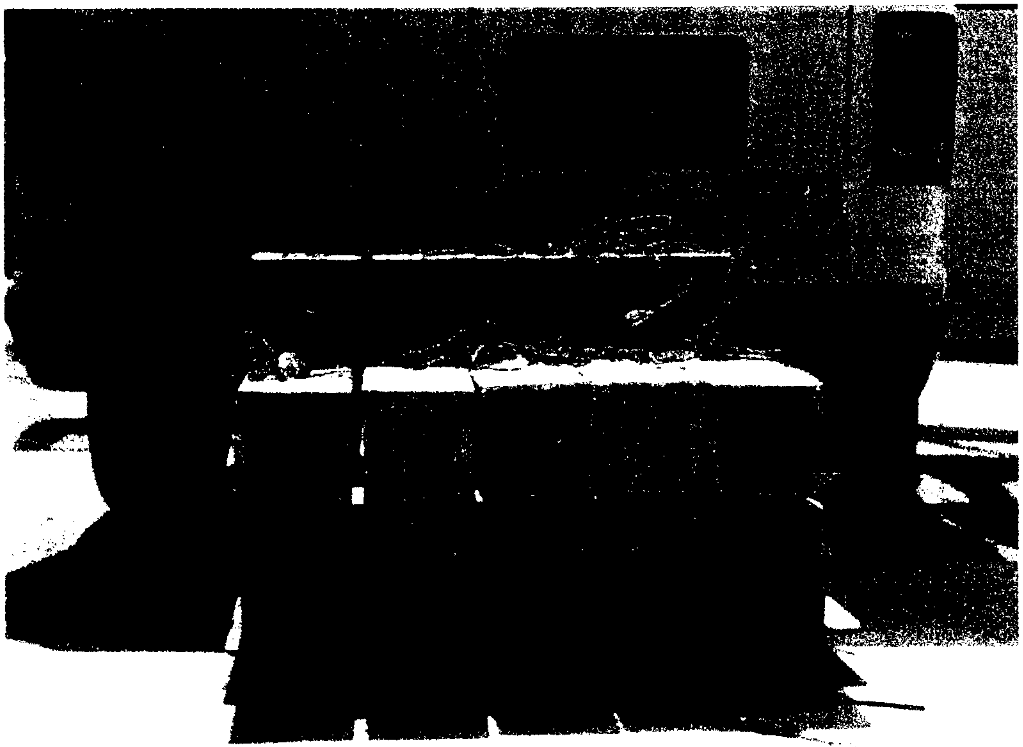

Figure 12.5 Concrete columns ready for testing

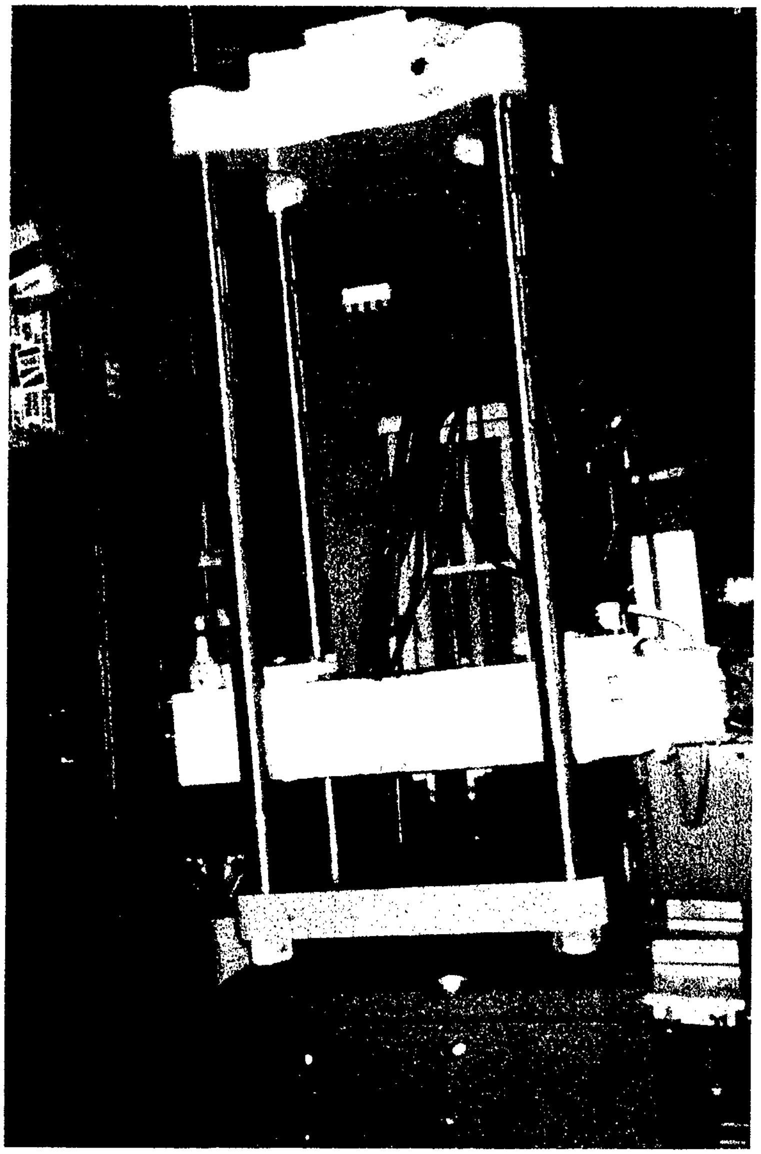

Figure 12.6 Testing facility used for ultimate load tests of concrete columns confined with CFRP hoops

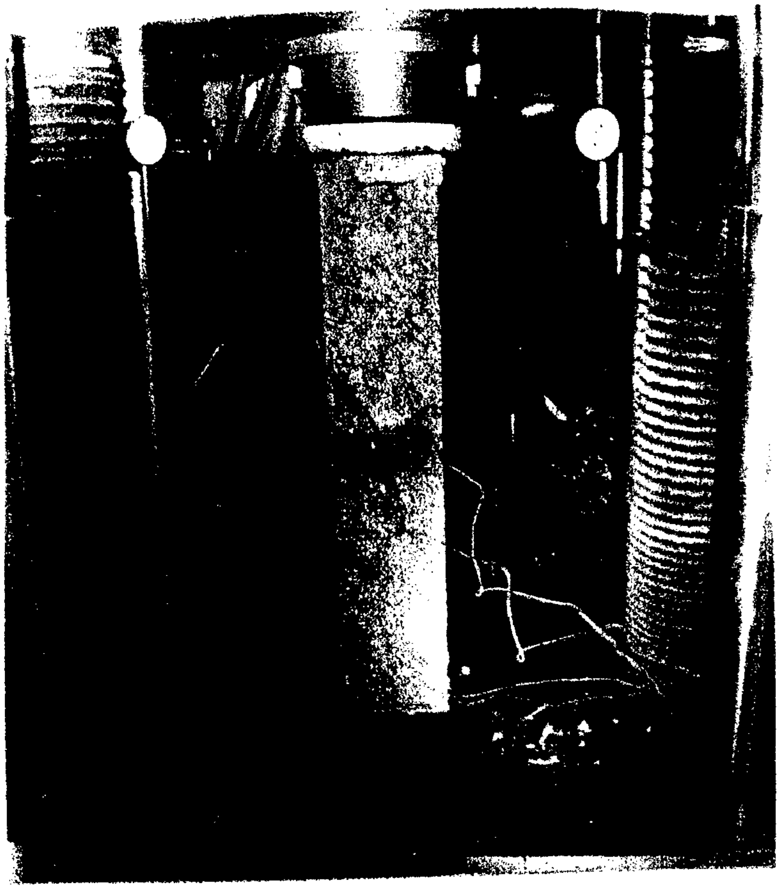

Figure 12.7 Test specimen ready for loading

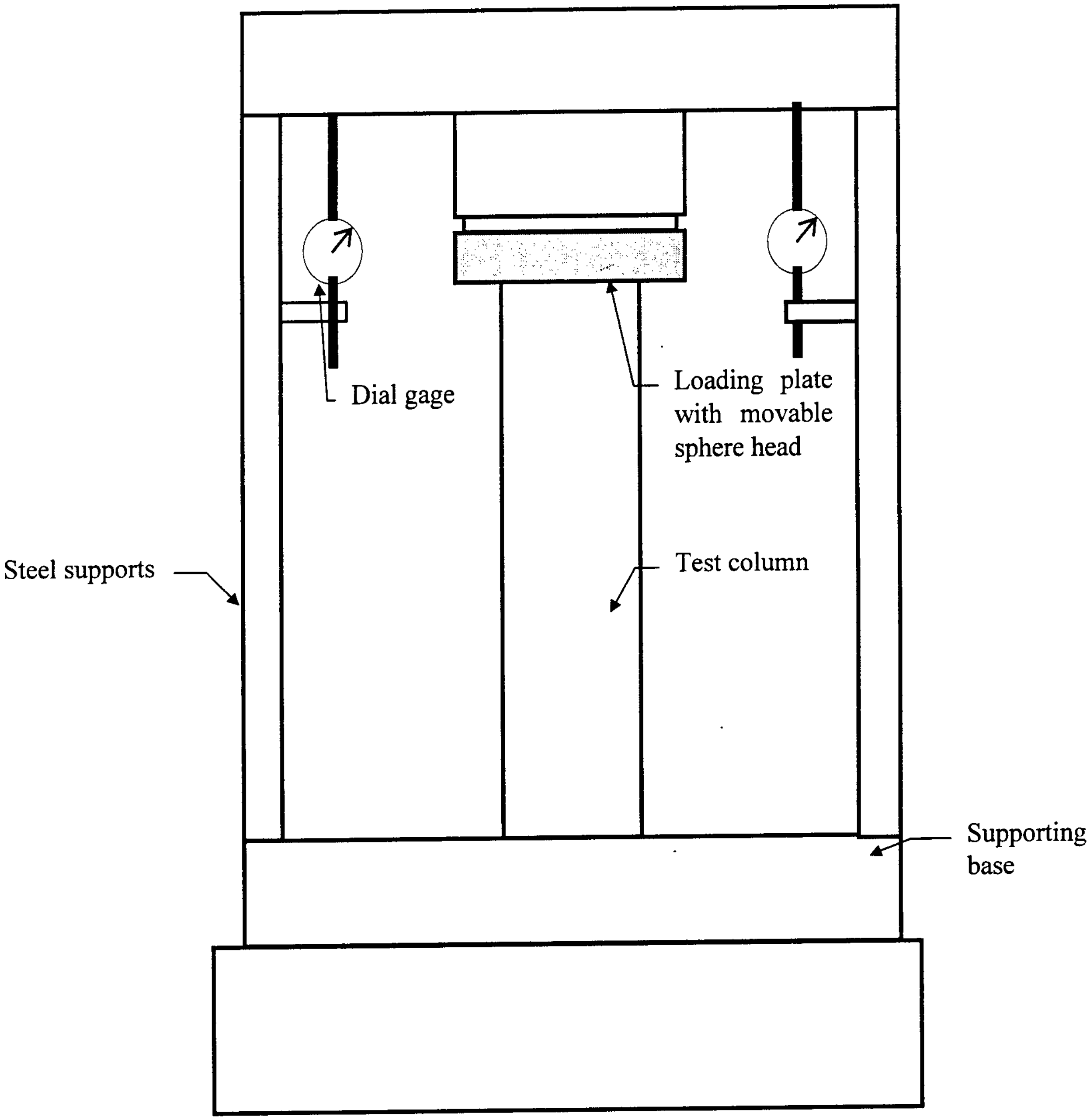

Figure 12.8 Schematic test set up of column confined with CFRP hoops

indicator. Two dial gages were fixed on either side of the specimen to monitor the relative movement of cross heads and determine the deformation in the concrete column during loading. The test set up mainly consisted of placing the column specimen concentric with the loading plate to avoid eccentricity, arranging the two dial gages and connecting the strain gages to the strain indicator (Fig 12.9). Initially a small load was applied and removed to check all the strain and dial gages. A loading rate of 110 kN/min as per ASTM standard loading rates was maintained for ultimate load tests of axially loaded columns.

The first column CS61with hoop spacing of 150 mm (6 in) was tested as a pilot test. The strain gage and dial gage readings were taken at every 66.72 kN (15 kips) interval initially and then at lower load intervals near the ultimate load. The specimen was carefully monitored for the longitudinal cracks and mode of failure. Premature failure was observed due to the buckling of the longitudinal CFRP reinforcement leading to ultimate failure of the column due to a hoop fracture in the damaged area (Fig. 12.10). This pilot test helped in developing a test procedure to avoid premature failure in the other specimens. This was achieved by drilling the ends of the CFRP tendons in the columns up to 25 mm to avoid direct contact of the loading plates (Fig. 12.11). This procedure aided in eliminating the buckling of longitudinal reinforcement.

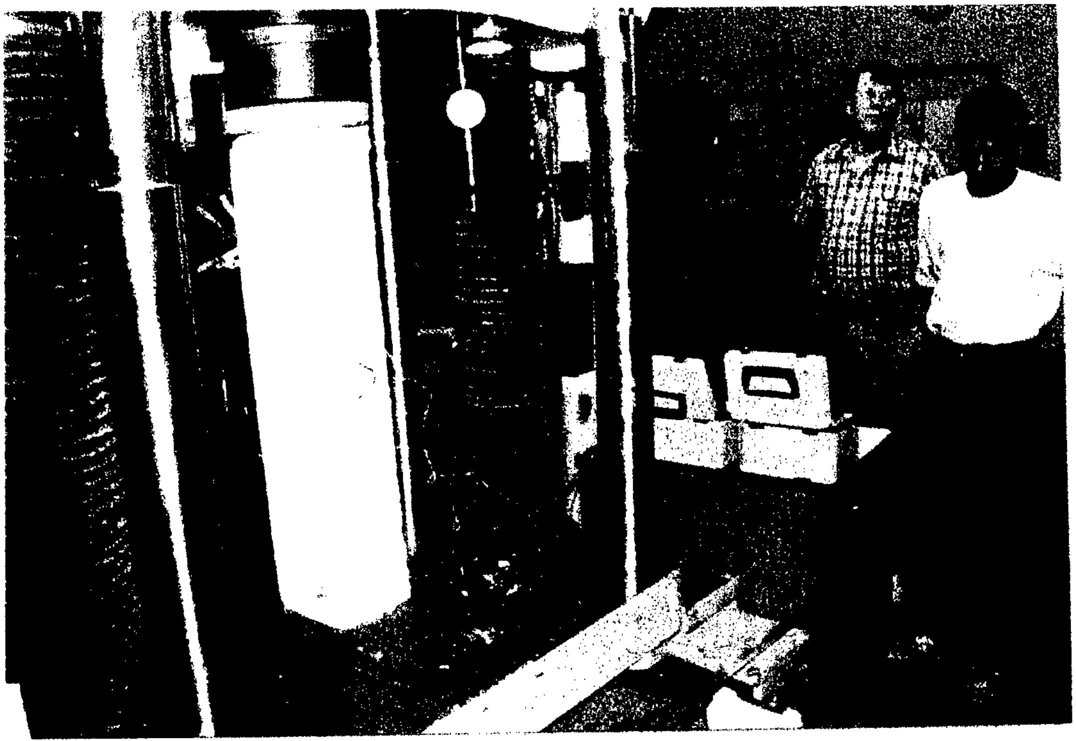

Figure 12.9 Strain gages attached to the strain indicator

Figure 12.10 View of fractured hoop near the damaged area

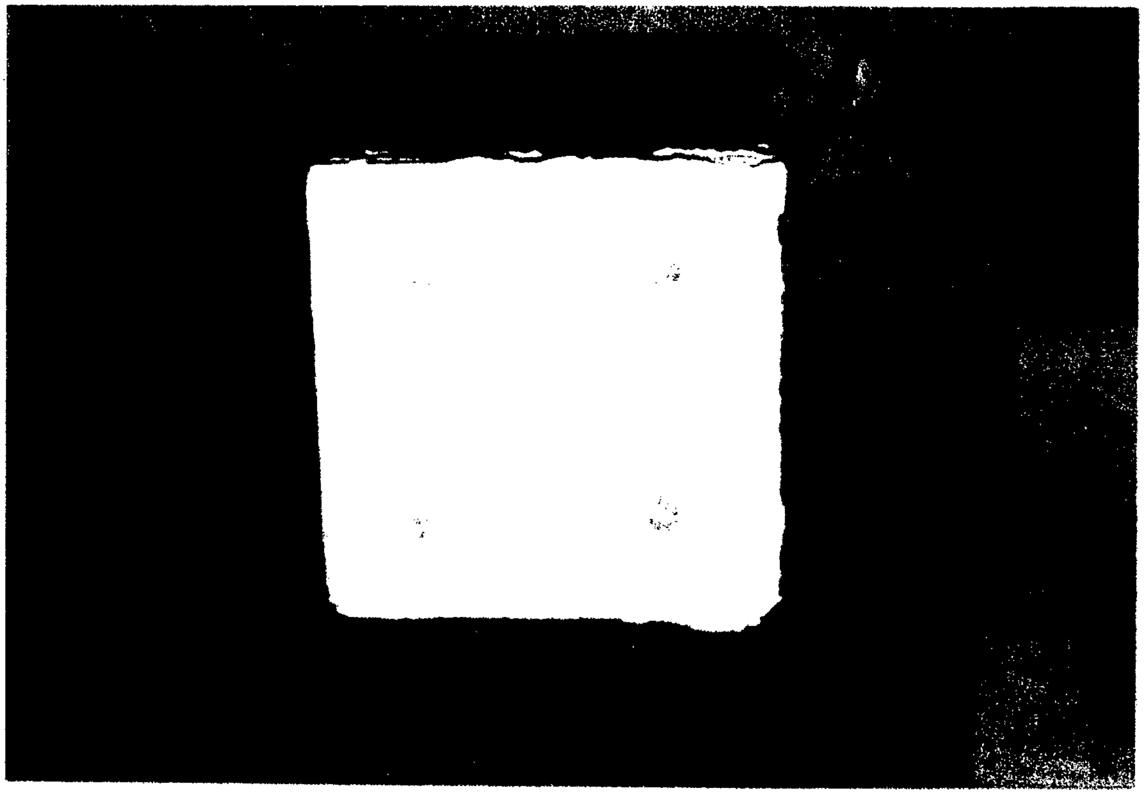

Figure 12.11 Longitudinal reinforcement drilled at the ends

12.3 RESULTS AND DISCUSSIONS

Strength enhancement due to CFRP hoop reinforcement

The strength enhancement in the column specimens due to CFRP hoop reinforcement is discussed based on the load vs. strain relationships. The concentric axial load capacity (P_o) of the specimens neglecting the area of the CFRP longitudinal reinforcement is given by

$$P_0 = 0.85 * f'_c * A \qquad \text{..............} (12.1)$$

where

f'_c = concrete cylinder strength

A = gross area of cross section of the column specimen

The ratios of the applied loads P to the axial load capacity P_o vs. the measured axial and lateral strains are shown in Figs. 12.12 - 12.22. Table 12.3 summarizes the observed ultimate load capacities and the percentage increases in strength of the CFRP reinforced concrete column specimens. The results presented in the table indicate less enhancement due to CFRP confinement than that reported in the literature for similar steel confinement.

Based on the observed behavior of the pilot column and the test results, the other two specimens in this group CS6 were modified, tested and carefully observed till failure. The test specimens CS62 and CS63 exhibited sudden failure. The failure was first initiated by spalling around the column near corners leading to the CFRP hoop fracture. The strength enhancement observed in both CS62 and CS63 specimens was **11.4 %**. Though no buckling of longitudinal reinforcement was observed, the failure was not gradual as observed in specimen CS61. This might be due to the larger spacing of the hoop reinforcement, which is almost equal to the lateral dimension of the specimen.

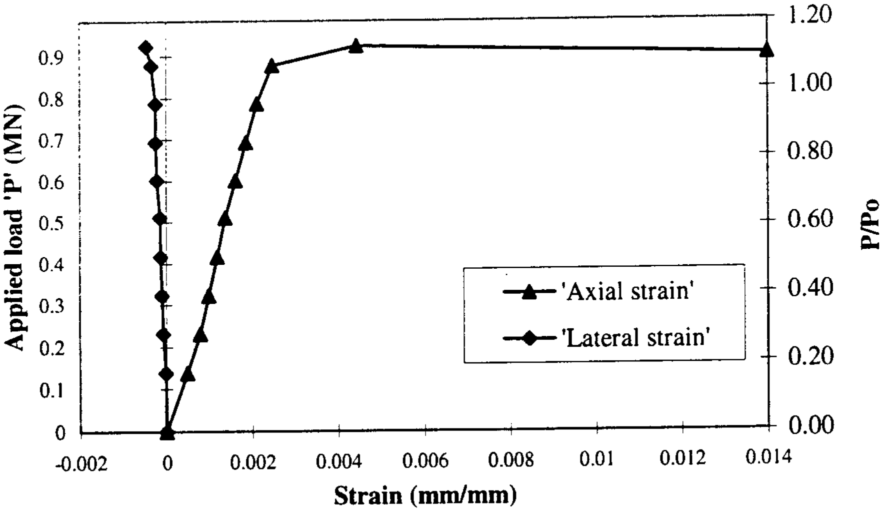

Figure 12.12 Load ratio vs. strain for column CS61

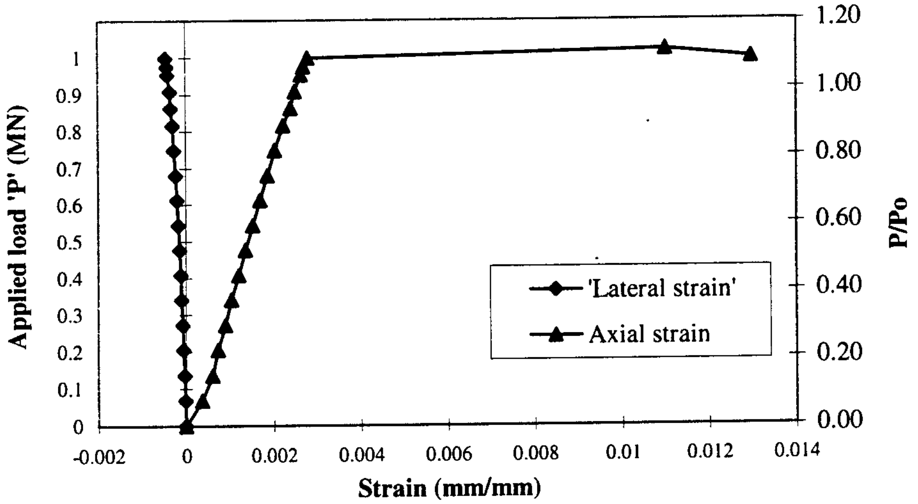

Figure 12.13 Load ratio vs. strain for column CS62

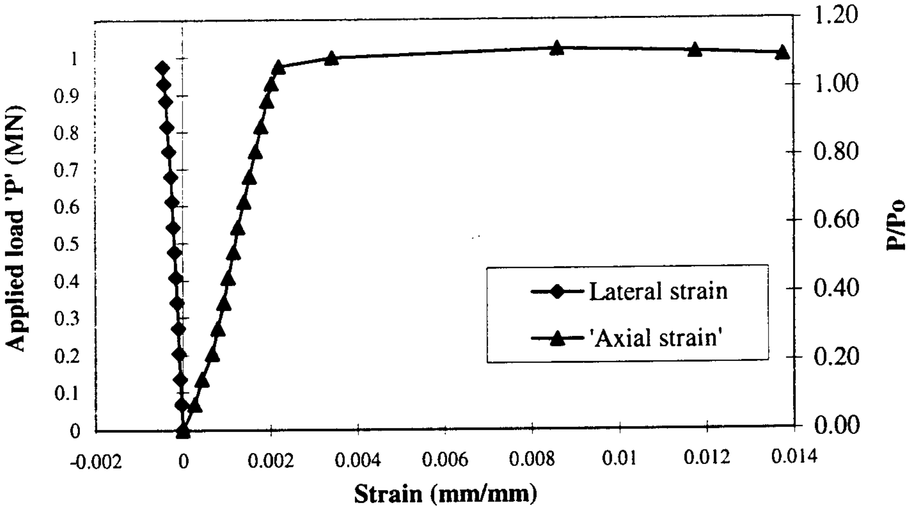

Figure 12.14 Load ratio vs. strain for column CS63

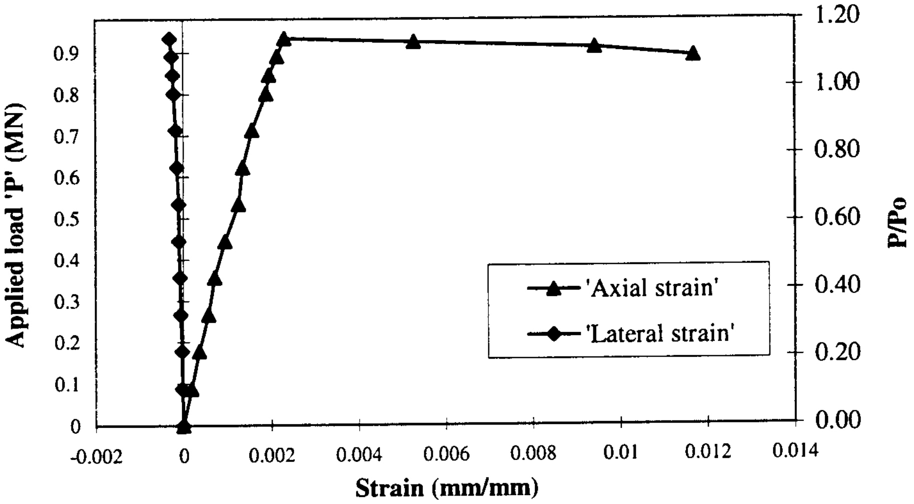

Figure 12.15 Load ratio vs. strain for column CS41

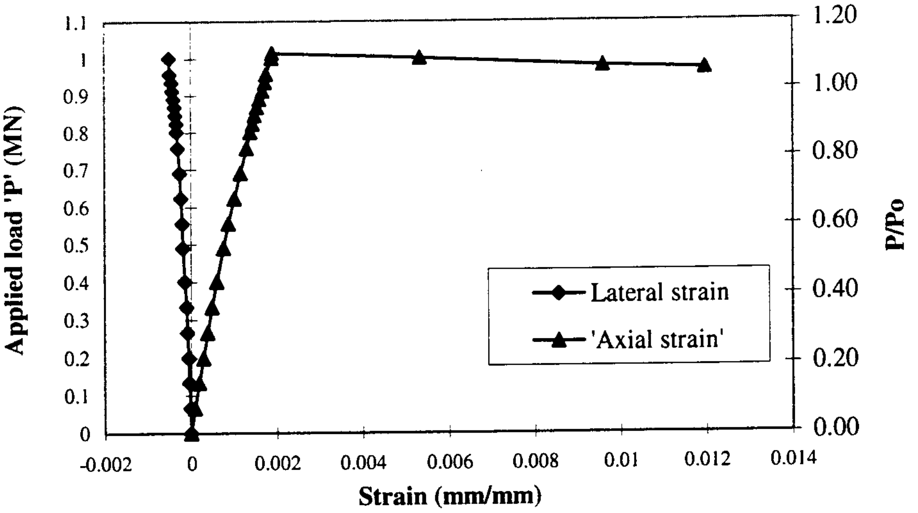

Figure 12.16 Load ratio vs. strain for column CS42

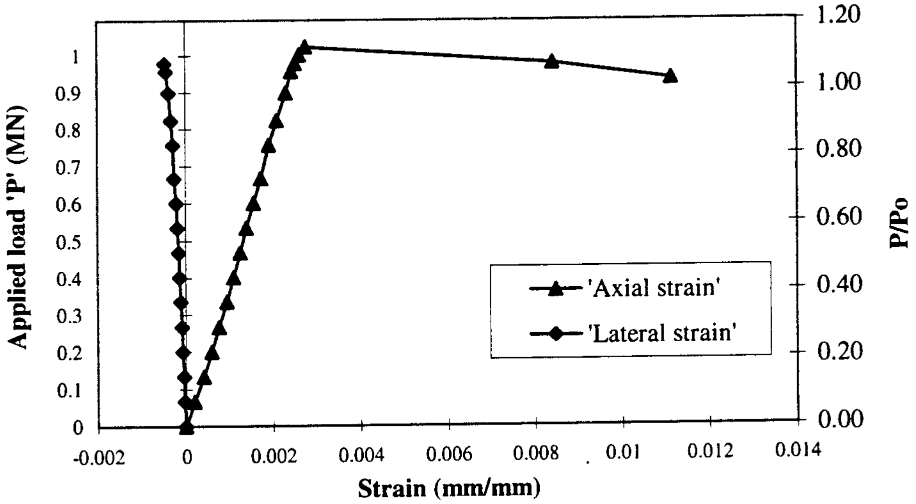

Figure 12.17 Load ratio vs. strain for column CS43

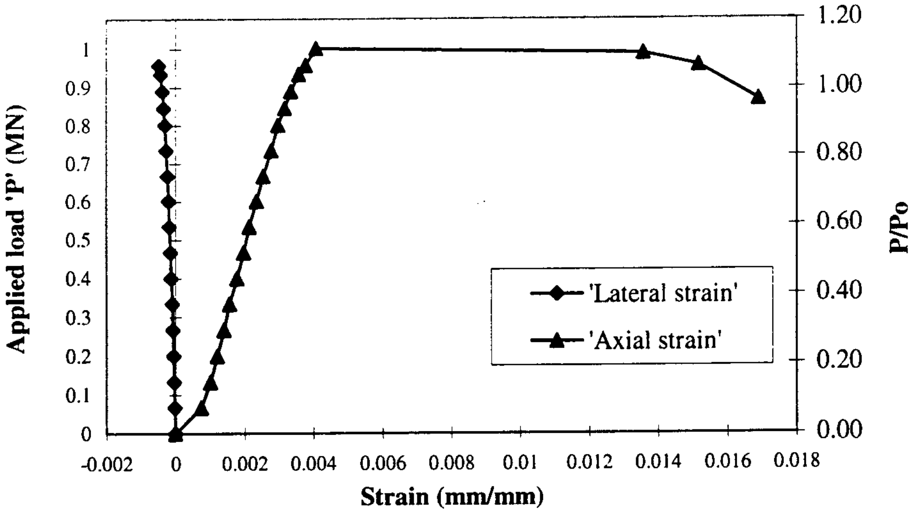

Figure 12.18 Load ratio vs. strain for column CS31

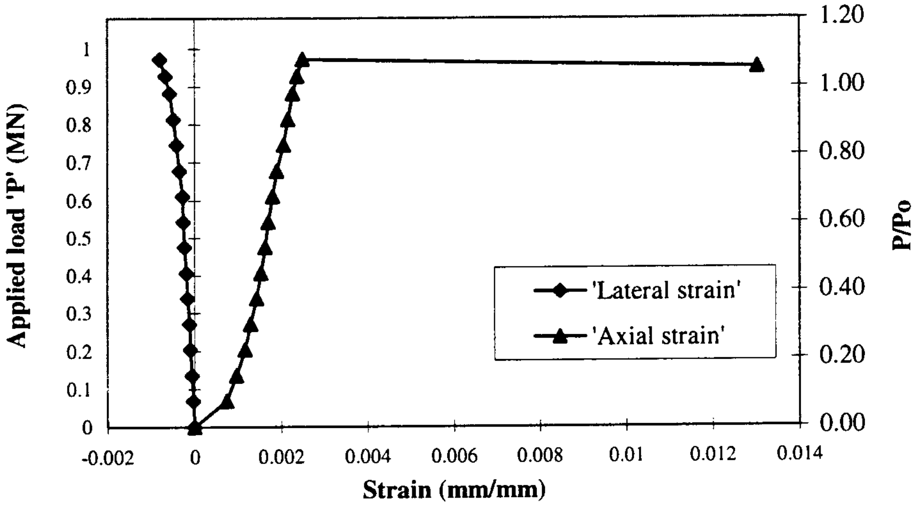

Figure 12.19 Load ratio vs. strain for column CS32

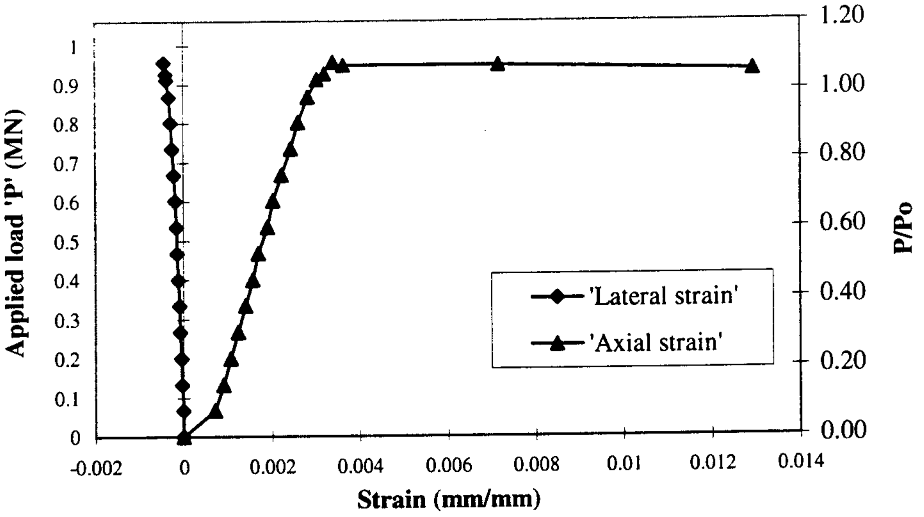

Figure 12.20 Load ratio vs. strain for column CS33

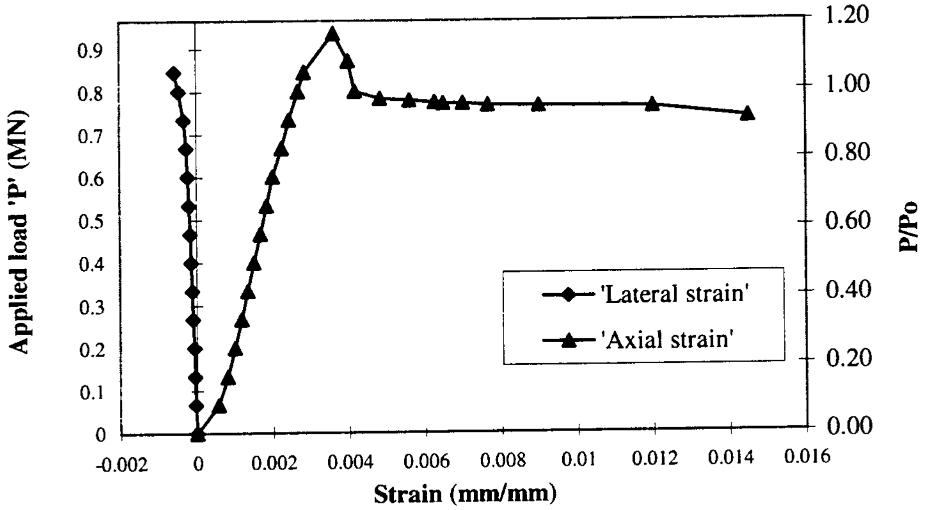

Figure 12.21 Load ratio vs. strain for column CS21

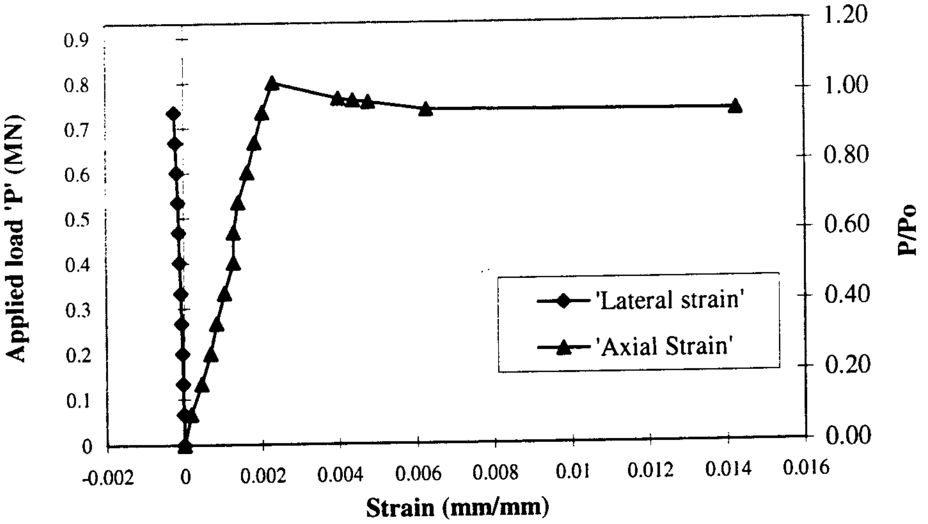

Figure12.22 Load ratio vs. strain for column CS22

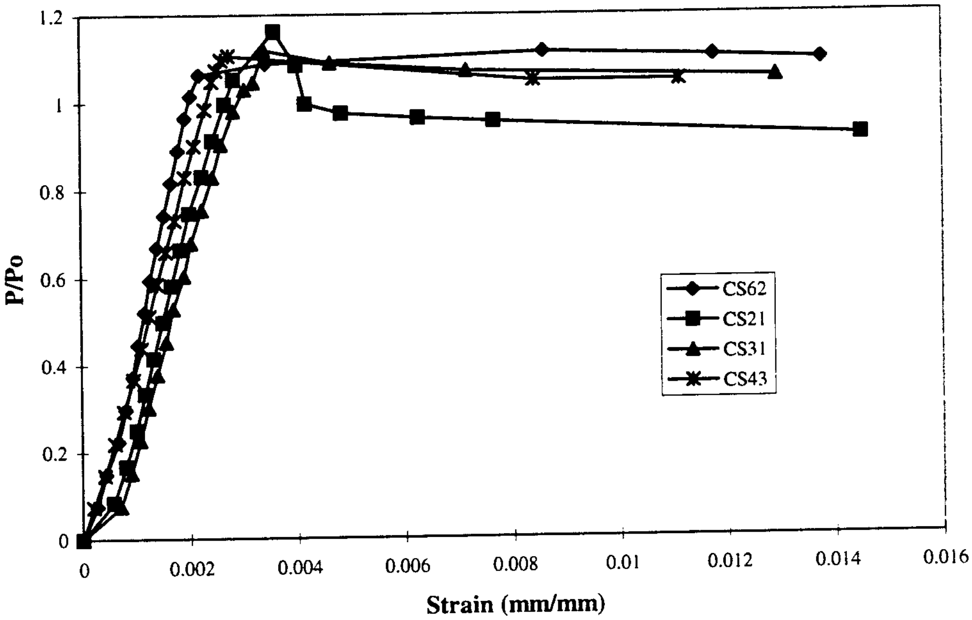

Figure 12.23 Load vs. strain relationships for typical columns

Table 12.3 Observed ultimate load capacity of column speciemns

Group	Column specimen	Concrete cylinder strength at the time of testing (MPa)	Ultimate load carried by the column, P_u (kN (kips))	Percentage increase in Strength $(P_u-P_o)/P_0$ %	Mode of ultimate failure
CS6	CS61	40	891 (200)	12.7	sudden (hoop fracture)
	CS62	46	1002 (225)	11.4	sudden (hoop fracture)
	CS63	46	1002 (225)	11.4	sudden (hoop fracture)
CS4	CS41	41	935 (210)	14.4	gradual
	CS42	46	1015 (228)	10.7	gradual
	CS43	46	1024 (230)	12.2	gradual
CS3	CS31	46	1002 (225)	11.4	gradual
	CS32	46	958 (215)	8.1	gradual
	CS33	46	958 (215)	8.1	gradual
CS2	CS21	40	935 (210)	16.3	very gradual
	CS22	41	802 (180)	3.2	very gradual

The specimens in the second group CS4 with a hoop spacing of 100 mm were prepared by drilling the longitudinal reinforcement to a depth of 25 mm on both ends to avoid buckling of the CFRP tendons. The first specimen CS41 was tested at an earlier age than the other two. This specimen showed a **14.4 %** strength enhancement with gradual failure (Fig. 12.15). The initiation of cracks started at the corners near the ends followed by concrete spalling. The ultimate failure was due to the crushing of the core concrete as well as the fracture of the CFRP hoop (Fig. 12.24). The other two specimens CS42 and CS43 tested at a later age showed **10.7 %** and **12.2 %** strength enhancement respectively with gradual failure (Figs. 12.16 & 12.17). The failure of the specimen CS43 initiated at one end of the column and propagated towards mid-section (Fig. 12.25), whereas failure was localized in the specimen CS42 in the mid regions (Fig. 12.26).

The specimens in the third group CS3 with a hoop spacing of 75 mm were prepared in the same manner as the specimens in group CS4 and tested to failure. The failure modes observed in CS32 and CS33 were similar to those in group CS4. The specimen CS31 showed a strength enhancement of **11.4 %** with gradual ductile failure (Fig. 12.18). The initiation of cracks started at the corners near the ends of the columns and propagated along the length followed by the shearing of the CFRP hoop (Fig. 12.27).

The specimens in the fourth group CS2 with a hoop spacing of 50 mm were tested at an early age than the other groups. The first specimen CS21 showed a strength enhancement of **16.32 %** (Fig 12.21). However, only **3.2 %** strength enhancement was observed in the second specimen CS22 (Fig. 12.22). This low strength enhancement in the specimen CS22 can be attributed to insufficient compaction of fresh concrete due to the very close spacing of the CFRP hoops. Insufficient compaction was necessitated to avoid damage to the CFRP hoop reinforcement. Fig. 12.28 shows the progressive failure of concrete in the specimen CS21. But both the column specimens showed enough ductility before ultimate failure.

Figure12.23 shows the load vs. axial strain for typical columns with different CFRP hoop spacings. It can be observed that both the peak loads and the corresponding strains increase with the decrease in the hoop spacing. The observed ultimate axial strain in all the groups was around 0.011 - 0.015, which is smaller than the value (0.03 to 0.04) reported for columns reinforced with steel hoops.

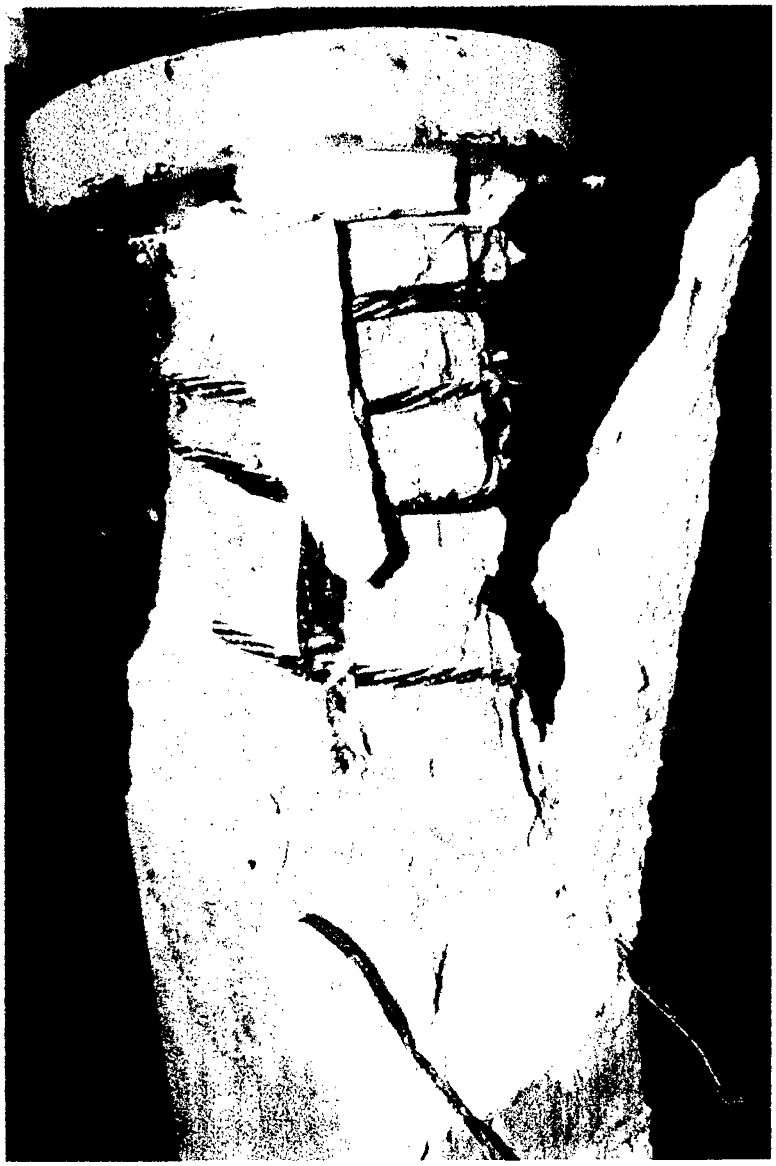

Figure 12.24 Failure of the column CS41 at the ultimate load

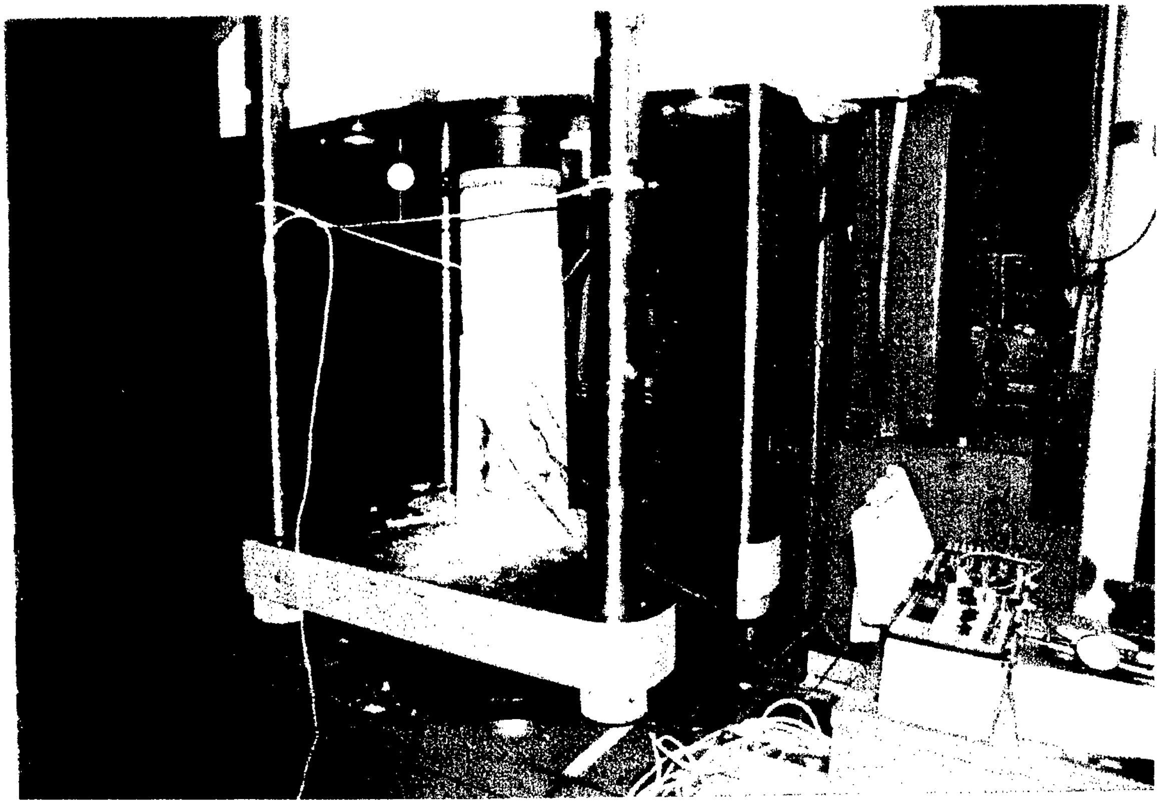

Figure 12.25 Failure starting at the end of the column (CS43)

Figure 12.26 Failure initiated in the middle (CS42)

Figure 12.27 Shearing of the CFRP hoop

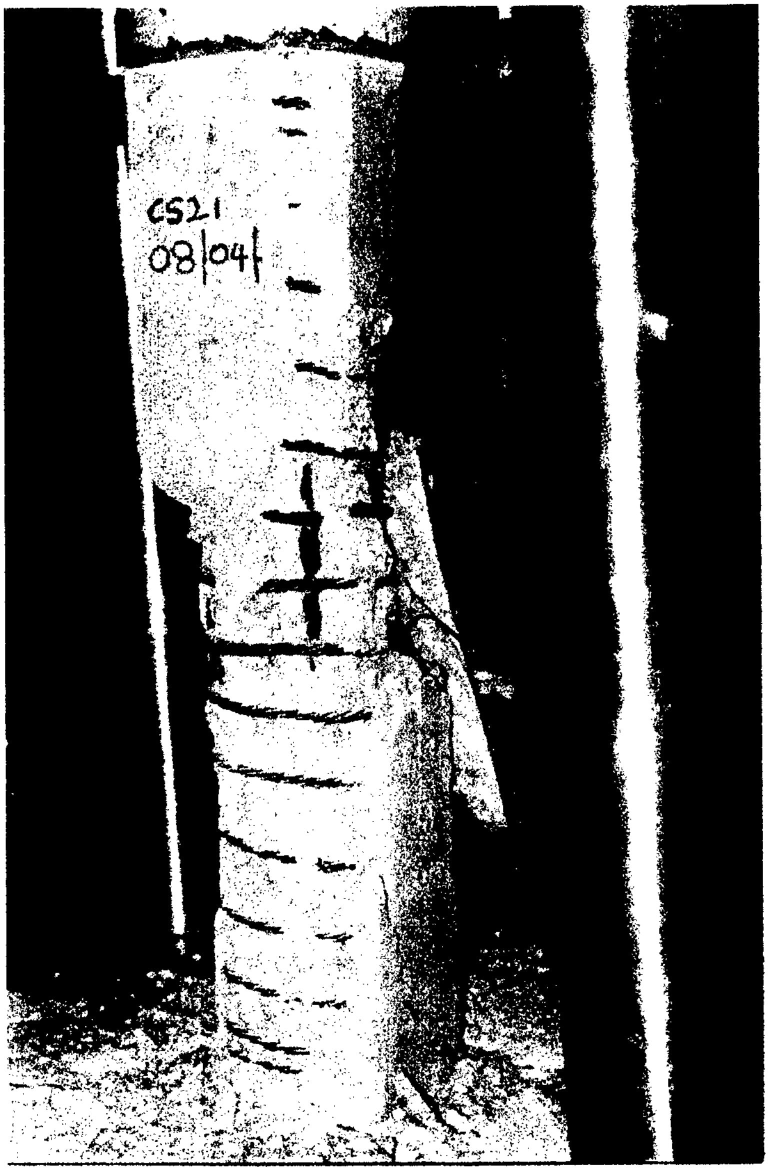

Figure 12.28 Progressive concrete cover spalling in column specimen CS21

12.4 ANALYTICAL MODEL FOR STRESS-STRAIN RELATIONSHIP OF REINFORCED CONCRETE COLUMNS CONFINED WITH CFRP HOOPS

The inelastic deformability of reinforced concrete columns is essential for overall strength and stability of structures subjected to lateral loads. Deformability of columns can be achieved through proper confinement of the core concrete. The requirements for confinement steel are currently available for design of columns. However, the behavior of reinforced concrete columns with CFRP hoops is not yet well understood. Existing theoretical models on confined concrete with i) steel lateral reinforcement and ii) FRP laminates are presented in Chapter 2. The analytical model and experimental stress-strain relationships of the reinforced concrete column specimens with CFRP hoop reinforcement are presented in this section.

Proposed Theoretical Model

The fractional equation for stress-strain relationship for confined concrete (Eqn. 2.8, Ahmad, 1982) is modified replacing f'_c and ε'_c by f'_{cc} and ε'_{cu} and rewritten as

$$f_c = \left\{ \frac{A\left(\varepsilon_c / \varepsilon'_{cu}\right) + (B-1)\left(\varepsilon_c / \varepsilon'_{cu}\right)^2}{1 + (A-2)\left(\varepsilon_c / \varepsilon'_{cu}\right) + B\left(\varepsilon_c / \varepsilon'_{cu}\right)^2} \right\} f'_{cc} \qquad \text{.................. (12.2)}$$

where f_c is the stress at strain ε_c, f'_{cc} is the peak stress and ε'_{cu} is the ultimate strain of the concrete confined with CFRP hoops. The constants A and B are chosen by iterative process based on the experimental stress-strain data from the column specimens (Table 12.4). The ultimate strain, ε'_{cu} from the regression analysis of the experimental results is given by

$\varepsilon'_{cu} = 0.0012 + 0.0002 * f'_{cc}$ (R-squared value of 83.5 %) .... (12.2a)

Table 12.4 Values of constants A and B

Spacing of the CFRP hoop, s (mm)	f'_c (MPa)	A	B
150	40	6.0	2.0
100	45	6.0	2.0
75	45	6.5	2.0
50	40	7.0	2.0

Linear model for f'_{cc}

The peak stress f'_{cc} is determined based on Eqn. 2.4 given by

$$f'_{cc} = f'_c + 4.1\sigma_p \qquad \text{.....................} (2.4)$$

where

$$\sigma_p = (2\, k f_{hu} A_h)/(s\, D) \qquad \text{.....................} (12.2b)$$

where f_{hu} = ultimate stress of CFRP hoop in MPa

A_h = area of cross section of CFRP hoop in sq. mm

s = spacing of CFRP hoop in mm

D = lateral dimension of the CFRP hoop in mm

The CFRP stress reduction coefficient, k depends on the spacing and is calculated as a ratio of the actual stress developed in the CFRP hoop at the time of ultimate column failure, f_h to the ultimate stress of the CFRP hoop, f_{hu} (2116 MPa). The values of k obtained from the column test specimens are given in Table 12.5. The variation of the stress reduction coefficient , k with s/D ratio is shown in Fig. 12.29 and expressed as a linear function in Eqn. 12.2c. It can be observed that the stress in the CFRP hoop reaches approximately 72.5% of the ultimate stress in the specimens with widely spaced hoops.

The CFRP hoop reinforcement is weak in shear to resist the lateral forces exerted by the coarse aggregate in the concrete and hence the premature rupture of the CFRP hoops.

Table 12.5 Calculated values of lateral stress (f_h) and the ratio $k=f_h/f_{hu}$

s (mm)	σ_p MPa	f_h MPa	$k=f_h/f_{hu}$
50	9.710	549.505	0.25969
50	9.502	537.772	0.25415
75	9.117	773.945	0.36576
75	8.109	688.331	0.32530
75	8.109	688.331	0.32530
100	8.949	1012.878	0.47868
100	8.720	986.928	0.46641
100	8.949	1012.878	0.47868
150	8.093	1373.970	0.64932
150	8.949	1519.318	0.71801
150	9.033	1533.604	0.72477

$$k = 0.4675 * s/D \qquad \text{(R-squared value of 97.88 \%)} \ldots\ldots.(12.2c)$$

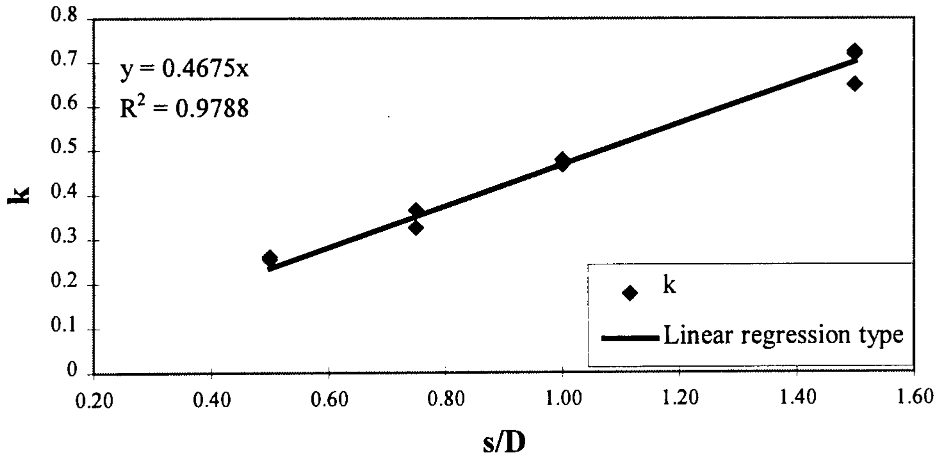

Figure 12.29 Variation of CFRP stress reduction coefficient with s/D ratio

The stress-strain model developed from the Eqns. 12.2 - 12.2c is compared with the experimental results of the uniaxial compression tests (Figs. 12.30-12.40). The stresses in concrete of the test column specimens are calculated based on the actual concrete area (which may range from A_{gross} to A_{core}) corresponding to the applied load. The theoretical predictions show good correlation with experimental results.

Non-linear model for f'_{cc}

An existing non-linear model (Eqn. 12.3) was used to predict the maximum confined concrete stress f'_{cc} [Mirmiran and Shahawy, 1996].

$$f'_{cc} = f'_c + 4.269\sigma_p^{\ 0.587} \qquad \ldots\ldots\ldots\ldots\ldots\ldots\ (12.3)$$

where

$$\sigma_p = (2\ f_{hu}\ A_h)/(s\ D) \qquad \ldots\ldots\ldots\ldots\ldots\ldots\ (12.3a)$$

This model was used in predicting the stress-strain relationship proposed in Eqn. 12.2, which also shows good correlation with the experimental results (Fig. 12.41-12.44).

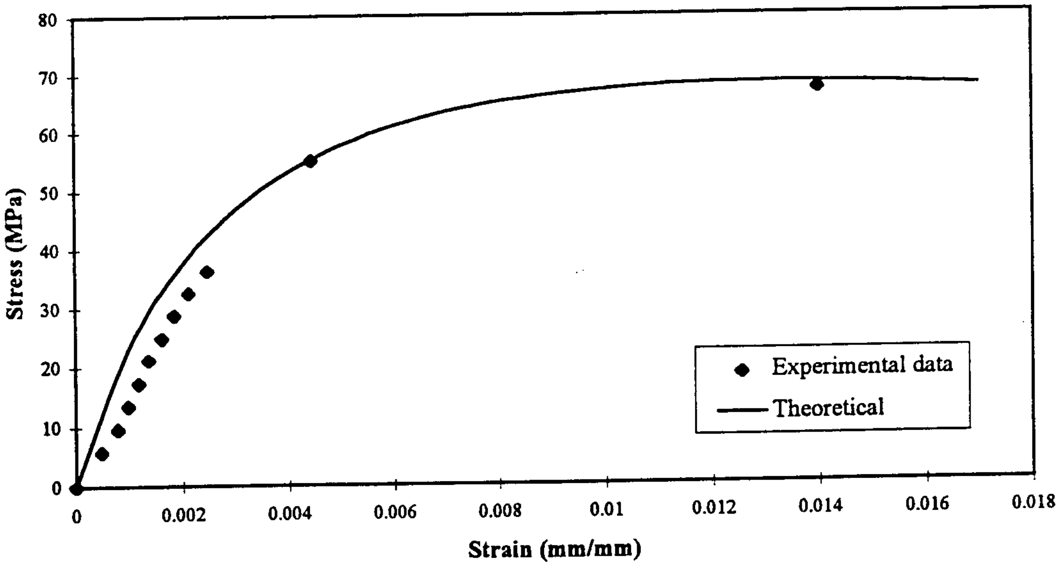

Figure 12.30 Stress - strain relationship for the column CS61 (s=150 mm)

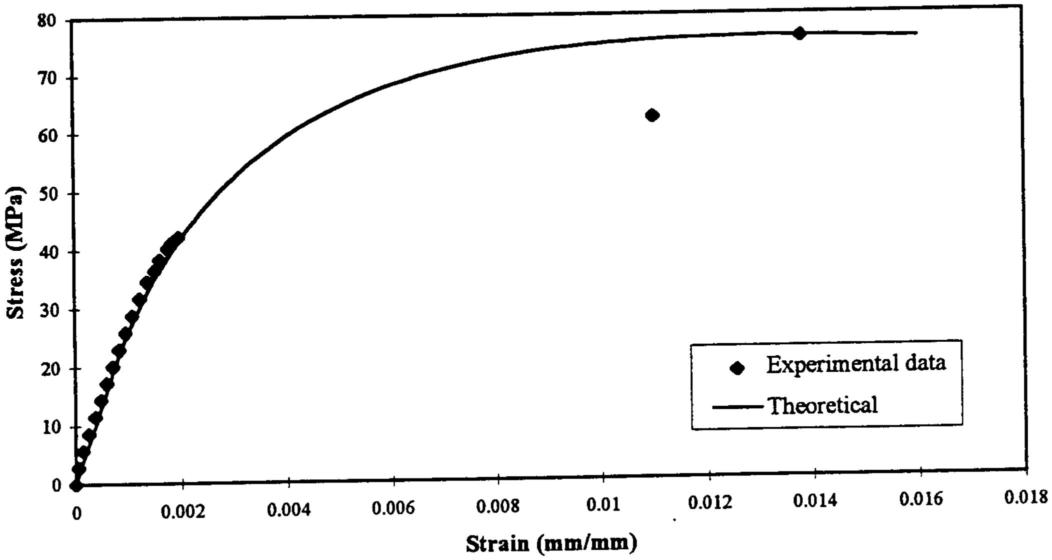

Figure 12.31 Stress - strain relationship for the column CS62 (s=150 mm)

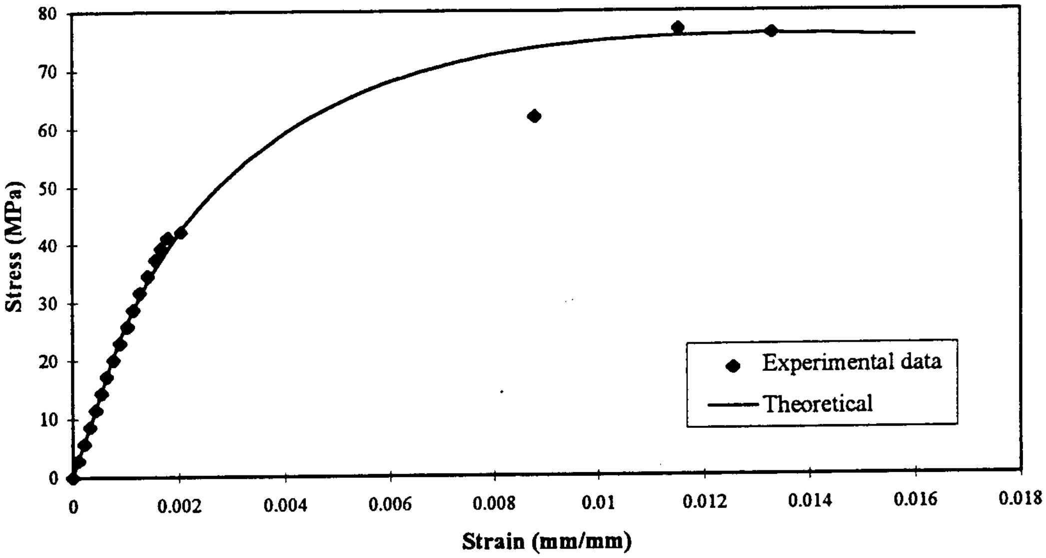

Figure 12.32 Stress - strain relationship for the column CS63 (s=150 mm)

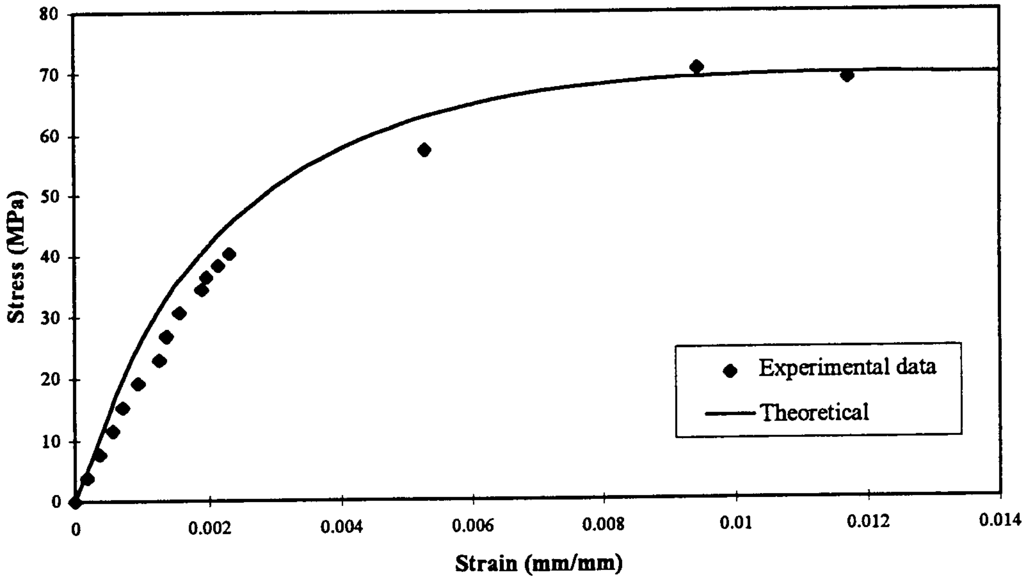

Figure 12.33 Stress - strain relationships for the column CS41 (s=100 mm)

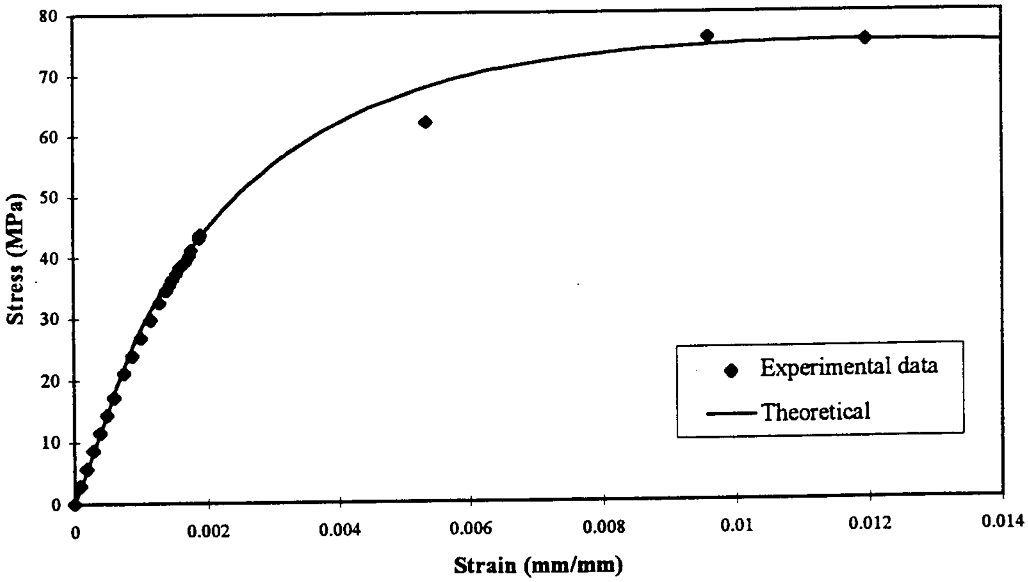

Figure 12.34 Stress - strain relationships for the column CS42 (s=100 mm)

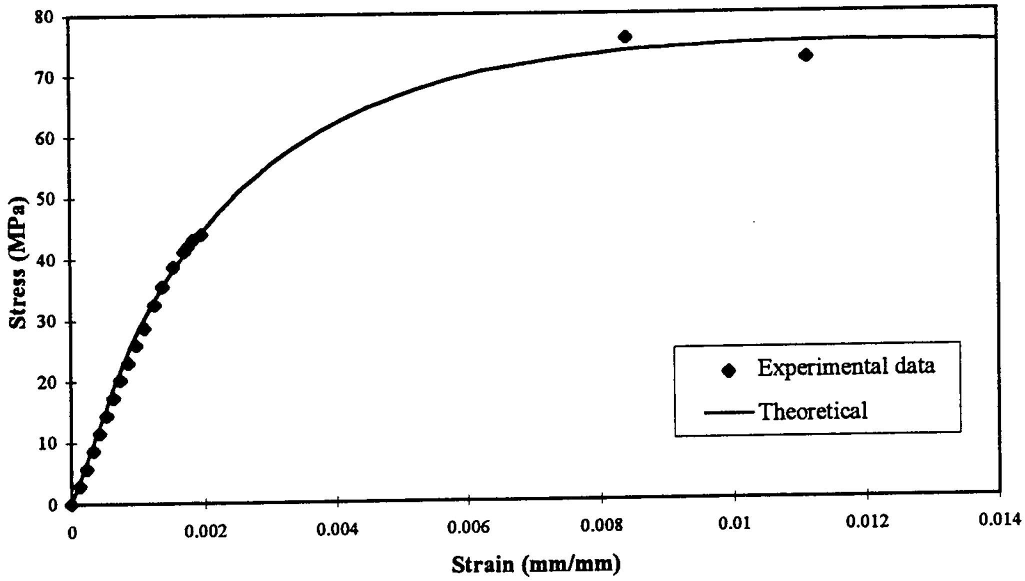

Figure 12.35 Stress - strain relationships for the column CS43 (s=100 mm)

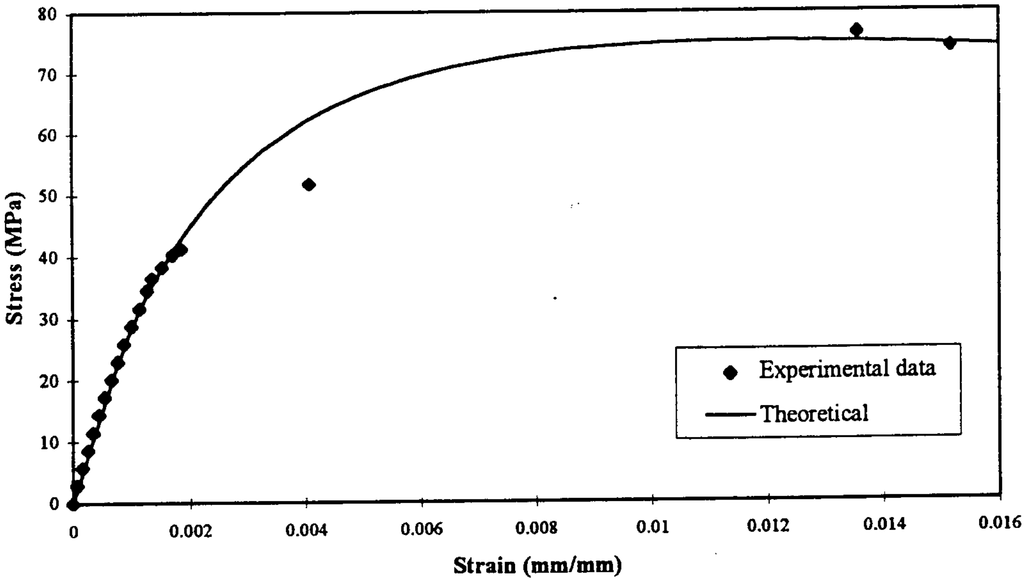

Figure 12.36 Stress - strain relationships for the column CS31 (s=75 mm)

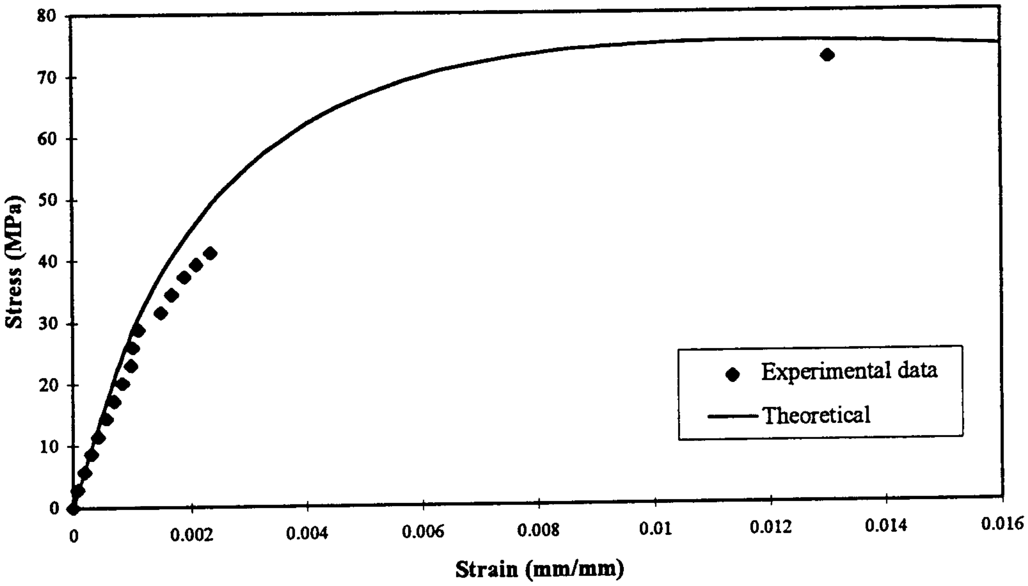

Figure 12.37 Stress - strain relationships for the column CS32 (s=75 mm)

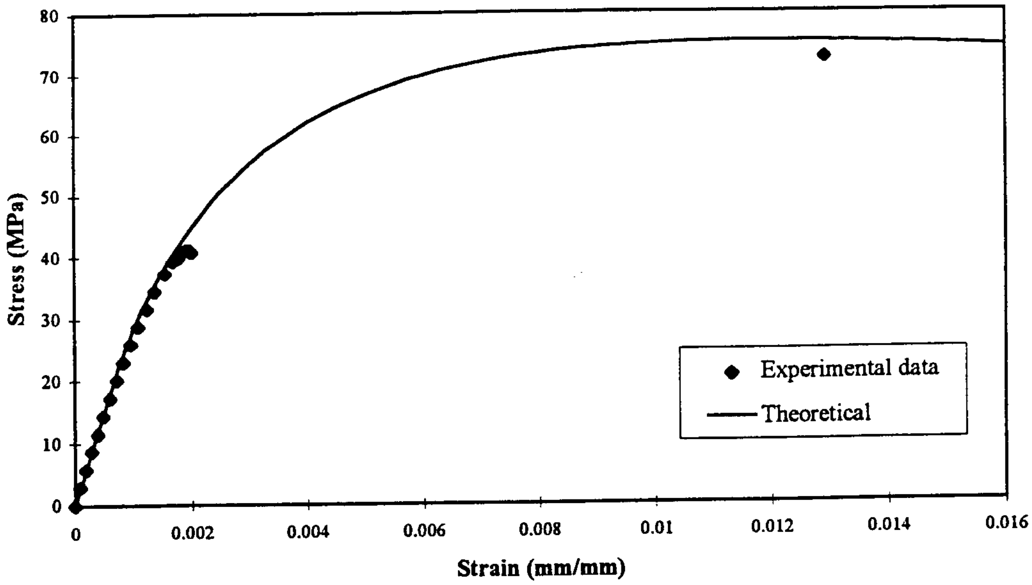

Figure 12.38 Stress - strain relationships for the column CS33 (s=75 mm)

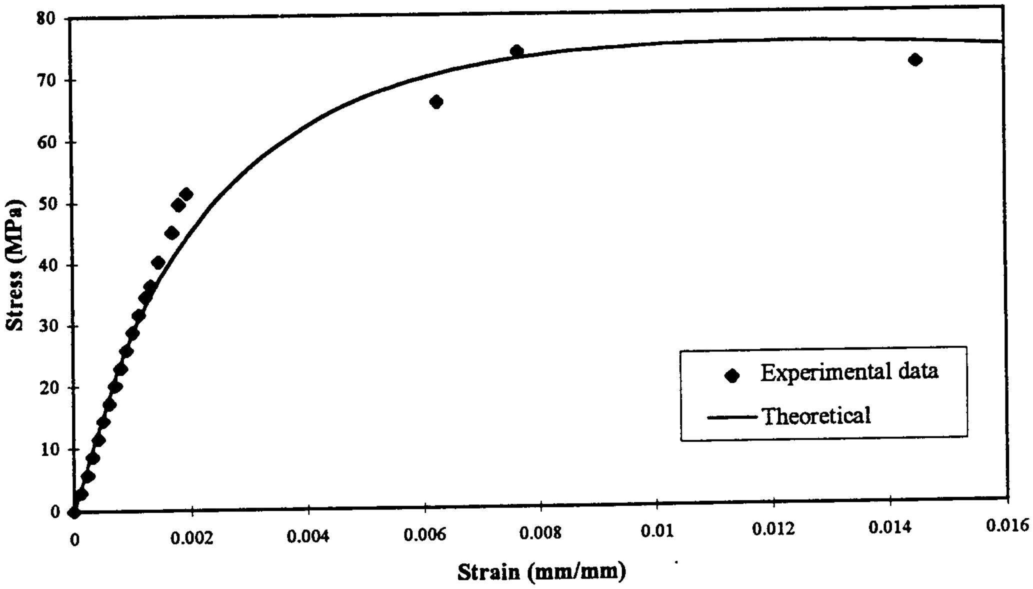

Figure 12.39 Stress - strain relationships for the column CS21 (s=50 mm)

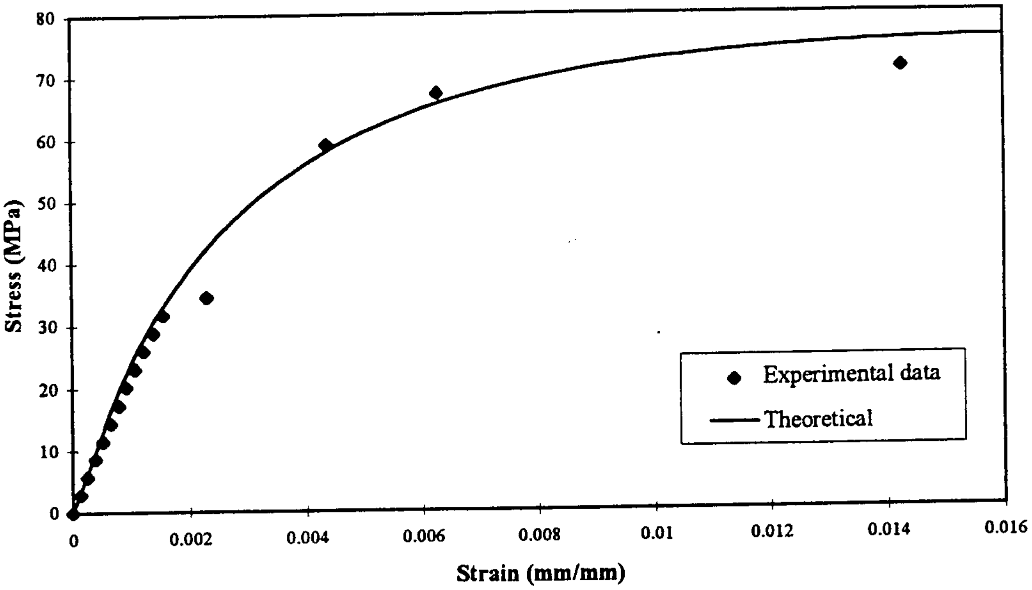

Figure 12.40 Stress - strain relationships for the column CS22 (s=50 mm)

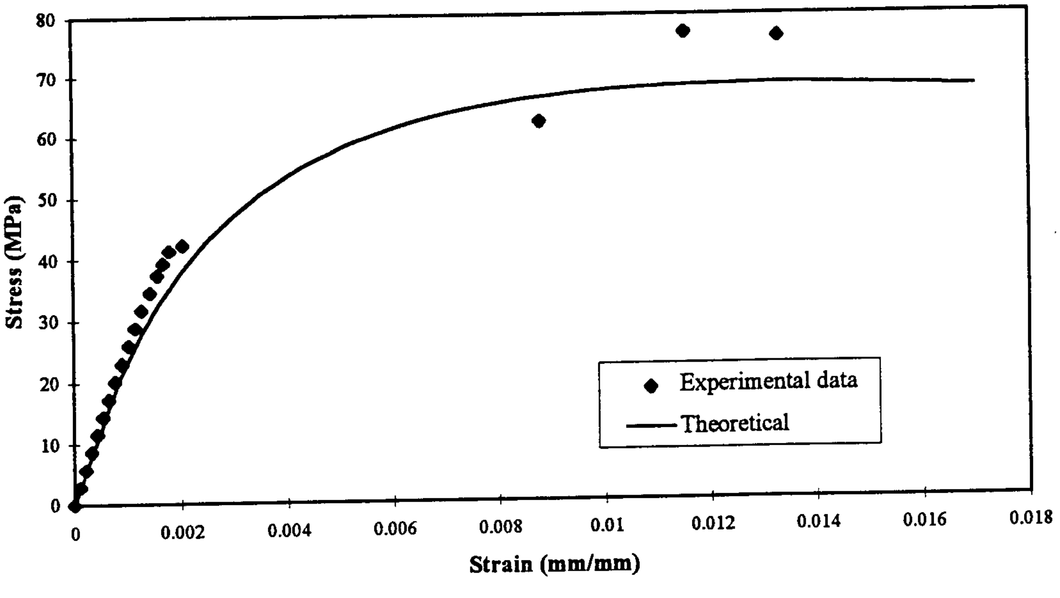

Figure 12.41 Stress - strain relationships for the column CS61 (s=150 mm) (using non-linear model for f'_{cc})

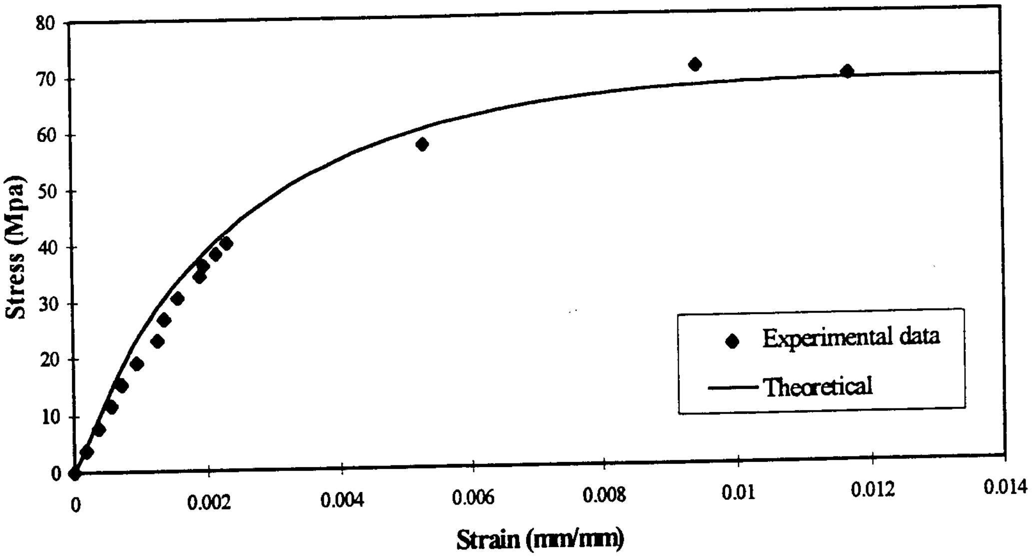

Figure 12.42 Stress - strain relationships for the column CS41 (s=100 mm) (using non-linear model for f'_{cc})

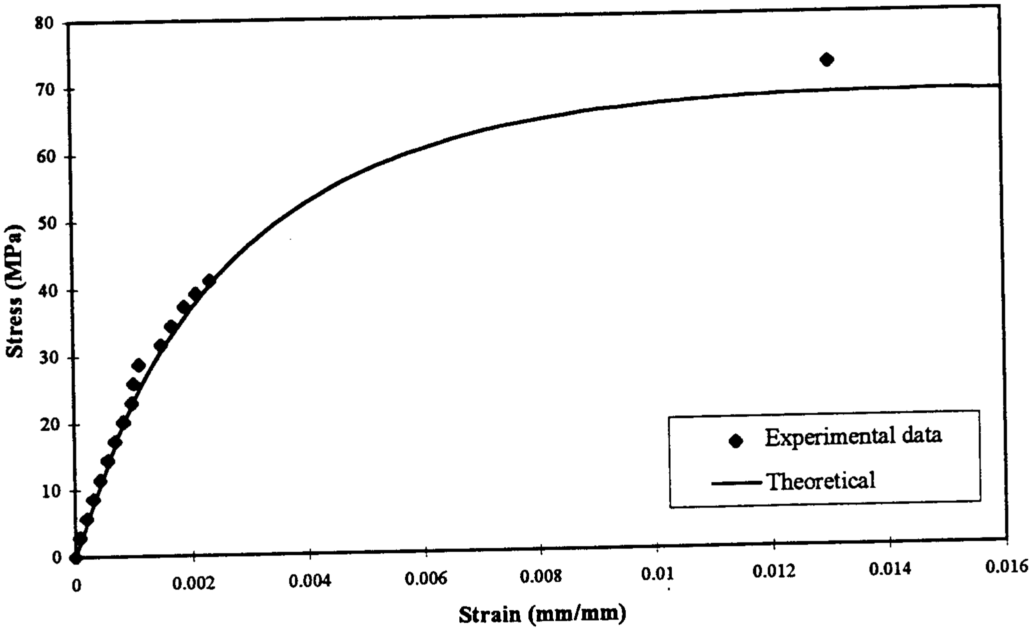

Figure 12.43 Stress - strain relationships for the column CS32 (s=75 mm) (using non-linear model for f'_{cc})

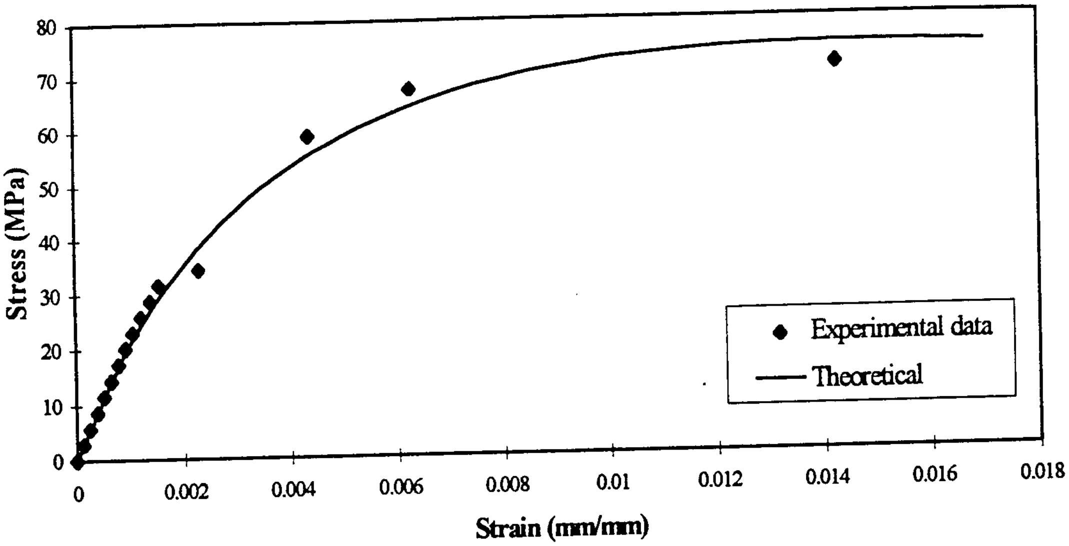

Figure 12.44 Stress - strain relationships for the column CS22 (s=50 mm) (using non-linear model for f'_{cc})

CHAPTER 13

SUMMARY AND CONCLUSIONS

13.1 SUMMARY

The available literature on mechanical properties of CFRP reinforcement, durability of FRP rods and tendons, service and ultimate load, and time dependent behavior of FRP reinforced concrete columns, existing models on confined concrete reinforced with steel ties and hoops, and pile driving are first reviewed in this study. An experimental program was carried out to study the durability of CFRP tendons exposed to air, seawater and alkaline solutions for different time duration. The ultimate strength analysis of CFRP reinforced concrete slender columns was made utilizing the moment magnification method and the CFRP stress – strain characteristics. An experimental investigation on the ultimate load behavior of eight CFRP reinforced concrete slender columns was carried out and the results compared with the theoretical values.

An analytical and experimental investigation was made on the long term behavior of CFRP reinforced concrete beams and columns under sustained loading. Four concrete beams and four concrete columns were subjected to sustained uniform load intensity for two years. An analytical method to predict the total deformations of CFRP reinforced concrete members at any time is proposed considering the instantaneous and time dependent deformations.

The feasibility of using pretensioned concrete piles with CFRP tendons in marine environment was examined based on analytical and experimental studies. Prior to fabrication and driving the test piles, an investigation of the pile driving site and equipment was made in order to determine the pile driving stresses using the wave equation analysis. The design, instrumentation, fabrication and driving of pretensioned concrete piles with CFRP tendons were carried out successfully in the study. The pile driving test results of the CFRP pretensioned concrete piles are discussed and compared with those of the concrete piles pretensioned with steel.

The load deformation characteristics of the concrete columns are established for different CFRP hoop spacing based on testing eleven concrete column specimens. The strength enhancement due to the CFRP hoops is evaluated using a proposed stress vs. strain model for confined concrete.

13.2 CONCLUSIONS

The following conclusions are made from the experimental and analytical results:

13.2.1 Environmental studies of CFRP tendons

i) The untensioned CFRP tendons immersed in alkali solution and seawater for different periods of exposure do not show strength degradation.

ii) The ultimate strengths of tensioned CFRP specimens exposed to air, seawater and alkali environments remain the same without any strength reduction.

13.2.2 Ultimate strength behavior of CFRP reinforced concrete slender columns

i) The moment magnification method developed for slender steel reinforced concrete columns has been shown to be applicable for the analysis of CFRP reinforced concrete columns as well as developing the load - moment interaction diagram.

ii) The load - deflection and the moment - curvature relationships are linear in the initial stage. As the eccentricity decreases, both the deflection and curvature appear to increase considerably with relatively small increase in the load and moment.

iii) The failure modes and crack patterns show ductile behavior of the CFRP reinforced concrete slender columns with sufficient warning before failure.

iv) The predicted first crack and ultimate loads based on the analytical method are approximately within 11.0 % of the observed loads.

13.2.3 Long-term behavior of concrete beams and columns reinforced with CFRP reinforcement

i) The time-dependent deflection, strain and curvature increase with the increase in the applied moment in the beams. The increases in deformations of the cracked beams are much higher than those of the uncracked beams.

ii) The rate of increase in deformations was higher in the initial period of loading and tends to reduce with time under sustained loading. The deformations increased as much as twice the instantaneous value in the first year and tend to reach a constant value thereafter.

iii) The age adjusted elastic modulus method used in the study appears to be realistic in predicting the long-term behavior of concrete beams and columns reinforced with CFRP. The deformations calculated based on the ACI and CEB creep and shrinkage coefficients were in reasonable agreement with the measured values.

iv) The time dependent deflections of beams reinforced with CFRP are computed using a simplified procedure based on the age of loading and the CFRP compression reinforcement ratio.

13.2.4 CFRP pretensioned concrete piles

i) The measured driving stresses from the PDA and data acquisition system MEGADAC are comparable for the CFRP pretensioned concrete piles with CFRP or steel hoops.

ii) The measured maximum tensile and compressive stresses during pile driving compare reasonably with stresses from the wave equation analysis.

iii) The wave equation analysis for prediction of driving stresses in steel pretensioned concrete piles can also be used for CFRP pretensioned pile analysis.

iv) The maximum observed stresses in the CFRP pretensioned concrete piles with CFRP hoops (compressive stress of 19.58 MPa (2.84 ksi) and tensile stress of 9.31 MPa (1.35 ksi)) were within the FDOT allowable stresses in compression, S_{apc} = 31.47 MPa (4.57 ksi) and tension, S_{apt} = 9.72 MPa (1.41 ksi).

13.2.5 Concrete columns confined with CFRP hoops

i) The failure of the specimens initiated by the spalling of the concrete cover at the peak stress. This was followed by buckling of longitudinal reinforcement and subsequent rupture of the hoops in the specimens with large hoop spacing.

ii) For specimens with close hoop spacing, the ultimate failure was due to the crushing of the core concrete as well as the fracture of the CFRP hoop.

iii) The CFRP hoop spacing affected the ductility of the specimen more than the strength enhancement of the column. The closer spacing of the hoop appears to increase the ductility of the specimen.

iv) It was observed that the stress in the CFRP hoop at failure was approximately 72.5% of its ultimate strength in the specimens with widely spaced hoops. The CFRP tendons have relatively low resistance to lateral loads and the rupture of the CFRP hoop reinforcement by shear are due to dilation of concrete in lateral direction.

v) A model to predict the stress - strain relationship of the concrete columns confined with CFRP hoops is proposed by modifying an existing model. The proposed model utilizes the peak stress and the ultimate strain in the concrete confined with CFRP hoops.

vi) A CFRP stress reduction coefficient, k has been introduced for determining the lateral stress. The coefficient, k depends on the hoop spacing and its lateral dimension.

vii) The proposed theoretical model shows good correlation with the experimental results.

REFERENCES

ACI, " Prediction of Creep, Shrinkage, and Temperature Effects in Concrete Structures", Committee 209, American Concrete Institute, Detroit, Mich. (1992)

ACI , " State-of-the-Art Report on Fiber Reinforced Plastic Rinforcement for Concrete Structures" Committee 440, Am. Conc. Inst., Detroit, Mich. (1996)

Ahmad, S. H. and Shah, S. P., " Stress-Strain Curves of Concrete Confined by Spiral Reinforcement", ACI Journal 1982, 79(6), pp. 484-490

Ahmad, S. H., Khaloo, A. R., and Irshaid, A., " Behavior of Concrete Spiral Confined by Fiberglass Filaments", Magazine of Concrete Research 1991, 43 (156), pp. 143-148

Amer, A., " Structural Behavior of Concrete Structures Pretensioned with Fiberglass Tendons", Ph.D. Thesis, University of Illinois, Chicago (1993)

Arockiasamy, M., and Sandepudi, K., " Active Deformation Control on Bridges Prestressed with Aramid Fiber Reinforced Plastics (AFRP) Cables", Final Report submitted to US and Florida Department of Transportation, August 1994.

Balaguru, P., and Nawy, E. G., " Evaluation of Creep Strains and Stress Redistribution in RC Columns", SP 76-12, Designing for Creep and Shrinkage, ACI, American Concrete Institute, Detroit, Mich, pp. 309-324 (1982).

Bazant, Z. P., " Mathematical Models for Creep and Shrinkage of Concrete", Creep and Shrinkage in Concrete Structures , Wiley. New York, NY, pp. 163-258 (1982).

Branson, D. E., “Design Procedures for Computing Deflections,” Journal of the American Concrete Institute, Proc. Vol. 65, September 1968, pp. 730-742.

CEB-FIP; “Evaluation of the Time Dependent Behavior of Concrete”, Laussane, Switzerland (1990)

Chan, W. W. L., “ The Ultimate Strength and Deformation of Plastic Hinges in Reinforced Concrete Frameworks”, Magazine of Concrete Research, 1955, 7 (21), pp. 121-132

Considère, A., “ Resistance a Compression du béton armé et du béton fretté”, Genie Civil, 1933. See also translation “ Experimental Researches on Reinforced Concrete," by L. S. Moisseiff, 1936

Currier, J., Dolan, C., and O'Neil, E., " Deflection Control of Fiber Reinforced Plastic Pretensioned Concrete Beams", Proc. of Second International Symposium on Non-Metallic (FRP) Reinforcement for Concrete Structures (FRPRCS-2), Ghent, Belgium, August 1995, pp. 413-420.

Fardis, M. N. and Khalili, H. H., “ FRP-Encased Concrete as a Structural Material”, Magazine of Concrete Research 1982., 34 (121), pp. 191-202

Fellenius, B., Editor, Third International Conference, Application of Stress Wave Theory, Ottawa, Canada, 1988.

“ Florida Department of Transportation (FDOT) Standard Specifications, Structures and Foundations”, Section 455, 1989.

FDOT Bulletin 121 A "SPT Drilling Data Correlation" Pile Foundations

Florida Department of Transportation Structures Design Office Static Pile Bearing Capacity Analysis Program SP94 - Version 1.1 February, 1995

FDOT, " Structures Design Guidelines", Florida Department of Transportation, Tallahassee, Florida, 1995

Ghali, A. and Favre, R., " Concrete Structures: Stresses and Deformations", E & FN Spon. (1994)

GRL & Associates, " Report on Dynamic Pile Tests for New Edison Bridge, Lee County, Florida", Orlando, FL, 1991.

Howie and Karbhari, V.M., " Effect of Materials Architecture on Strengthening Efficiency of Composite Wraps for Deteriorating Columns in the North-East," Proceedings of ASCE Third Materials Engineering Conference, Infrastructure: New Materials and Methods of Repair, San Diego, Nov. 13-16, 1994, p199

Issa, M. A, and Amer, A. (1995), " Prestress Losses in Fiberglass Pretensioned Concrete Compression Members", Materials and Structures, RILEM, 330-339.

Iyer, S.L., Silvakumar, R.(1994), " Graphite Prestressed Piles and Fiberglass Prestressed Pilecaps for U.S. Navy Pier in California," Infrastructure: New Materials and Methods for Repair, 3rd Materials Engineering Conference, SanDiego, CA, pp.392-399.

JSCE, " Application of Continuous Fiber Reinforcing Materials to Concrete Structures", JSCE No. 19, June 1992

Katawaki K., I. Nishizaki and I. Sasaki " Evaluation of the Durability of Advanced Composites for Applications to Prestressed Concrete Bridge," First International

Conference on Advanced Composite Materials in Bridges and Structures, Sherbrooke, Quebec, 1992 , p119

Katsuki, F., and Uomoto, T., " Prediction of Deterioration of FRP Rods due to Alkali Attack", Proceedings of the International RILEM Symposium (FRPRCS-2), Ghent, 82-89.(1995)

Mander, J. B., Priestly, M. J. N., and Park, R., " Observed Stress-Strain Behavior of Confined Concrete", Jr. of the Structural Div., ASCE, V.114(8), August 1988, pp. 1804-1826.

Priestley M. J. N. and F. Seible "Column Seismic Retrofit Using Fiberglass / Epoxy Jackets," First International Conference on Advanced Composite Materials in Bridges and Structures, Sherbrooke, Quebec, 1992 , p287

Mander, J. B., Priestley, M. J. N. and Park, P., " Seismic Design of Bridge Piers", Research Report No. 84-2, University of Canterbury, New Zealand, 1984

Mirmiran A., Shahawy Mohsen, "New Concrete-Filled Hollow FRP Composite Column", Composites Part B: Engineering V. 27, No. 3-4, 1996, pp. 263-268.

Morales, S. M., Nilson, A. H. and Slate, F. O., " Spiral-Reinforced High-Strength Concrete Columns", Report No. 82-10, Dept. of Structural Engineering, Cornell University, Ithaca, NY, 1982

Richart, F. E. and Brandtzaeg, A., "Failure of Plain and Spirally Reinforced Concrete in Compression," Engineering Experiment Station Bulletin No.190, University of Illinois, Apr.1929, pp.74

Richart, F. E., Brandtzaeg, A., and Brown, R. L., "A Study of Failure of Concrete Under Combined Compressive Stresses", Engineering Experiment Station Bulletin No. 185, Urbana, IL, 1928

Saadatmanesh, H., Ehsani, M. R. and Li, M. W., " Behavior of Externally Confined Concrete Columns", International Symposium, FRP Reinforcement for Concrete Structures, ACI SP-138, American Concrete Institute, Detroit, MI, 1993, pp. 249-265

Saeed Daniali and Noel S. Paramananantham " Concrete Columns Reinforced with Fiber Reinforced Plastic Rebars," Proceedings of ASCE Third Materials Engineering Conference, Infrastructure: New Materials and Methods of Repair, San Diego, Nov. 13-16, 1994, p567

Samra, R. M., " Creep Model for Reinforced Concrete Columns", J. Am. Conc. Inst., 86(1), 77-82 (1989)

Samra, R. M., " Creep Model for Reinforced Concrete Columns", J. Am. Conc. Inst., 86(1), 77-82 (1989)

Sen, R., Issa, M. and Mariscal, D., " Feasibility of Fiberglass Pretensioned Piles in a Marine Environment Final report CEM/ST/92/1, contract c-3321, Florida Department of Transportation, August 1992

Sen, R., Shahawy, M., Rosas, J., and Sukumar, S., " Durability of Aramid and Carbon Pretensioned Elements", Proc. of Second International Symposium on Non-Metallic

(FRP) Reinforcement for Concrete Structures (FRPRCS-2), Ghent, Belgium, August 1995.

Sen, R., Mariscal, D., and Shahawy, M., " Durability of Fiberglass Pretensioned Beams", ACI Structural Journal, sept-Oct. 1993, pp. 525-533.

Sen, R., Iyer, S., Issa, M., and Shahawy, M.," Fiberglass Pretensioned Piles for Marine Environment", Advanced Composites Materials in Civil Engineering Structures, ACSE, Jan 1991, p. 348.

Sen, R., S. Iyer, M. Issa and M. Shahawy "Fiberglass Pretensioned Piles for Marine Environment," Proceedings of Specialty Conference ASCE, Advanced Composites Materials in Civil Engineering Structures, Jan 31 - Feb. 1, 1991, Las Vegas, p348

Sen, R., Iyer, S., Issa, M., Patricia Wadsack and Shahawy, M., " Driving Stresses in Fiberglass Pretensioned Piles", ACI Structural Journal, V.90, No. 6, 1993, pp. 666-674

Smith, E. A. L., " Pile-Driving Analysis by the Wave Equation", Journal of the Soil Mechanics and Foundations Division, ASCE, Vol 86, No. EM 4, August 1960.

Smith, E. A. L., "Pile Driving Impact", Proceedings, Industrial Computation Seminar, September 1950, International Business Machines Corp., New York, NY, 1951

Talbot, A. N., " Tests of Concrete and Reinforced Concrete Columns", series of 1936. Engineering Experiment Station Bulletin No. 0, University of Illinois, Urbana, IL, 1936

Taniguchi, H., Mutsuyoshi, H., Kita, K. and Machida, A., " Ductile Behavior of Beams using FRP as Tendons and Transverse Reinforcement", International Symposium, FRP Reinforcement for Concrete Structures, ACI SP-138, American Concrete Institute, Detroit, MI, 1993, pp. 51-67

Tokyo Rope MFG. Co. Ltd. "CFCC Technical Data", October 1993.

Thomas, M. Gurtowski and Ming-Jiun Wu, “Compression Load Tests on Concrete Piles in Alluvium”, Proceedings of Symposium, Analysis and Design of Pile Foundations, ASCE, NY, 1984. pp. 138-153

APPENDIX A

A.1 CREEP COEFFICIENT AND SHRINKAGE STRAIN

The creep coefficient and shrinkage strain for the calculation of the long-term deformations for the beams and columns are based on ACI and CEB (1990) approaches.

A.1.1 ACI Committee 209 approach

Based on the extensive research work of Branson (1968), the ACI committee 209 [1] recommended the following expressions for creep and shrinkage of concrete:

$$\phi(t, t_0) = \frac{(t - t_0)^{0.6}}{10 + (t - t_0)^{0.6}} \phi_u \tag{A.1}$$

where

$$\text{Ultimate creep } \phi_u = 2.35\, K_c K_H K_T K_S K_F K_A \tag{A.2}$$

$$K_c = \begin{cases} 1.25 t_0^{-0.118} & \text{for moist cured cocrete} \\ 1.13 t_0^{-0.094} & \text{for steam cured concrete} \end{cases} \tag{A.3}$$

$$K_H = 1.27 - 0.0067\, h_e \quad h_e \geq 40\ \% \tag{A.4}$$

$$K_T = \begin{cases} 1.14 - 0.023 T_m & \text{for} \leq 1\,\text{year} \\ 1.10 - 0.017 T_m & \text{for ultimate value} \end{cases} \tag{A.5}$$

$$K_S = 0.82 + 0.067\, S_c \tag{A.6}$$

$$K_F = 0.88 + 0.0024\,F_a \tag{A.7}$$

$$K_A = \begin{cases} 1.00 & \text{for } A_c \le 6\% \\ 0.46 + 0.09A_c & \text{for } A_c > 6\% \end{cases} \tag{A.8}$$

Aging coefficient $\chi(t, t_0)$ is calculated from the Bazant's table, the value of χ depends on $(t - t_0)$, $\phi(t_\infty, 7)$ and initial loading age t_0, where

$$\phi(t_\infty, 7) = \frac{\varphi_u}{1.25 t_0^{-0.118}} \tag{A.9}$$

Free shrinkage is given by

$$\varepsilon_{cs}(t, t_s) = \frac{t - t_s}{35 + (t - t_s)}\,(\varepsilon_{cs})_u \tag{A.10}$$

where

Ultimate shrinkage coefficient $(\varepsilon_{cs})_u = 0.000780\, S_H S_T S_S S_B S_F S_A$ (A.11)

$$S_H = \begin{cases} 1.40 - 0.01h_e & 40\% \le h_e \le 80\% \\ 3.00 - 0.03h_e & 80\% \le h_e \le 100\% \end{cases} \tag{A.12}$$

$$S_T = \begin{cases} 1.23 - 0.038T_m & \text{for} \le 1\,\text{year} \\ 1.17 - 0.029T_m & \text{for ultimate value} \end{cases} \tag{A.13}$$

$$S_S = 0.89 + 0.041\,S_c \tag{A.14}$$

$$S_B = 0.75 + 0.034\,B_s \tag{A.15}$$

$$S_F = \begin{cases} 0.30 + 0.014F_a & \text{for } F_a \leq 50\% \\ 0.90 + 0.002F_a & \text{for } F_a \geq 50\% \end{cases} \quad \text{(A.16)}$$

$$S_A = 0.95 + 0.00880\ A_c \quad \text{(A.17)}$$

where

h_e = relative humidity (in %)

T_m = minimum thickness (in inches)

S_c = slump (in inches)

F_a = fine aggregate percent by weight

A_c = air content in percent of volume of concrete

B_s = number of 94- lb sacks of cement per cubic yard of concrete

A.1.2 CEB-FIP approach

The creep coefficient according to CEB-FIP is given by

$$\phi\,(t, t_0) = \phi_{RH} \cdot \beta(f_{cm}) \cdot \beta(t_0) \cdot \beta_c(t-t_0) \quad \text{(A.18)}$$

where

$$\phi_{RH} = 1 + \left[\frac{1 - \dfrac{RH}{RH_0}}{0.46.(h/h_0)^{1/3}} \right] \quad \text{(A.19)}$$

$$\beta(f_{cm}) = \frac{5.3}{\left(f_{cm}/f_{cm0} \right)^{0.5}} \quad \text{(A.20)}$$

$$\beta(t_0) = \frac{1}{0.1 + \left(t_0/t_1 \right)^{0.2}} \quad \text{(A.21)}$$

$$\beta_c(t-t_0) = \left[\frac{(t-t_0)/t_1}{\beta_H + (t-t_0)/t_1}\right]^{0.3} \tag{A.22}$$

$$\beta_H = 150.\left[1+\left(1.2.\frac{RH}{RH_0}\right)^{18}\right].\frac{h}{h_0} + 250 \le 1500 \tag{A.23}$$

The strain due to shrinkage or swelling according to CEB-FIP is given by

$$\varepsilon_{cs}(t, t_s) = \varepsilon_{cs0}.\ \beta_s(t - t_s) \tag{A.24}$$

where

$$\varepsilon_{cs0} = \varepsilon_s(f_{cm}).\ \beta_{RH} \tag{A.25}$$

$$\varepsilon_s(f_{cm}) = [\ 160 + 10.\ \beta_{sc}.\ (9 - f_{cm} / f_{cm0})].10^{-6} \tag{A.26}$$

β_{sc} = coefficient which depends on type of cement

$$\beta_{sc} = \begin{cases} 4 \text{ for slowly hardening cement, SL} \\ 5 \text{ for normal or rapid hardening cement, NR} \\ 8 \text{ for rapid hardening high strength cement, RS} \end{cases} \tag{A.27}$$

$$\beta_{RH} = \begin{cases} -1.55.\beta_{sRH} & \text{for } 40\% \le RH \le 99\% \\ +0.25 & \text{for } RH \ge 99\% \end{cases} \tag{A.28}$$

$$\beta_{sRH} = 1 - \left(\frac{RH}{RH_0}\right)^3 \tag{A.29}$$

$$\beta_s(t-t_s) = \left[\frac{(t-t_s)/t_1}{\beta_{sH} + (t-t_s)/t_1}\right]^{0.5} \qquad \text{(A.30)}$$

$$\beta_{sH} = 350 \, . \, (h/h_0)^2 \qquad \text{(A.31)}$$

where

RH = relative humidity of the ambient environment (in %)

h = $2A_c / u$;

A_c = cross-section of the structural member (in mm^2)

u =perimeter of the structural member in contact with the atmosphere

f_{cm} = mean compressive strength of concrete at the age of 28 days (in MPa)

t = age of concrete at the moment considered (in days)

t_0 = age of concrete at loading (in days)

RH_0 = 100 %

h_0 = 100 mm

f_{cm0} =10 MPa

t_1 = 1 day

A.2 AGING COEFFICIENT

The age-adjusted elastic modulus at time t is given by

$$\overline{E}_c(t,t_0) = \frac{E_c(t_0)}{1+\lambda\varphi(t,t_0)} \qquad \text{(A.32)}$$

where

λ = aging coefficient (Bazant 1972) (Table A.1)

Table A.1 Aging coefficient $\lambda(t,t_0)$ [Bazant, 1982]

$(t-t_0)$	$\varphi(t_\infty, 7)$	Value of λ			
		$t_0^* = 10$	$t_0^* = 10^2$	$t_0^* = 10^3$	$t_0^* = 10^4$
10 days	0.5	0.525	0.804	0.811	0.809
	1.5	0.720	0.826	0.825	0.820
	2.5	0.774	0.842	0.837	0.830
	3.5	0.806	0.856	0.848	0.839
10^2 days	0.5	0.505	0.888	0.916	0.915
	1.5	0.739	0.919	0.932	0.928
	2.5	0.804	0.935	0.943	0.938
	3.5	0.839	0.946	0.951	0.946
10^3 days	0.5	0.511	0.912	0.973	0.981
	1.5	0.732	0.943	0.981	0.985
	2.5	0.795	0.956	0.985	0.988
	3.5	0.830	0.964	0.987	0.990
10^4 days	0.5	0.461	0.887	0.956	0.965
	1.5	0.702	0.924	0.966	0.972
	2.5	0.770	0.940	0.972	0.976
	3.5	0.808	0.950	0.977	0.980

t_0^* expressed in days

where

$$\varphi(t_\infty,7) = \frac{\varphi(t_\infty,t_0)}{1.25t_0^{-0.118}}$$ for moist cured concrete

$\varphi(t_\infty, t_0) = \varphi_u$ the ultimate creep